EXPERIMENTAL AND ANALYTICAL STUDY OF THE DYNAMIC RESPONSE OF STEEL BEAMS AND COLUMNS TO BLAST LOADING

EXPERIMENTAL AND ANALYTICAL STUDY OF THE DYNAMIC RESPONSE OF STEEL BEAMS AND COLUMNS TO BLAST LOADING

By

Amr Abobakr Aly Mohamed Nassr

B.Sc., M.A.Sc.

A Thesis Submitted to the School of Graduate Studies
in Partial Fulfillment of the Requirements for the Degree
Doctor of Philosophy

McMaster University

July 2012

Doctor of Philosophy (2012) McMaster University
(Civil Engineering) Hamilton, Ontario

TITLE:	Experimental and Analytical Study of The Dynamic Response of Steel Beams and Columns to Blast Loading
AUTHOR:	Amr A. Nassr
	M.A.Sc. (McMaster University)
	B.Sc. (Assiut University)
SUPERVISORS:	Prof. A. Ghani Razaqpur
	Dr. Michael Tait
NUMBER OF PAGES:	xii, 275

Abstract

In this thesis the dynamic response of wide-flange steel beams and columns to blast loading was experimentally evaluated. A total of twenty six steel members were field tested using live explosives, where the charge size ranged from 50 to 250 kg of ANFO and the ground stand-off distance from 7.0 to 10.3 m. Blast wave characteristics, including incident and reflected pressures were recorded. In addition, time-dependant displacements, accelerations, and strains at different locations along the steel members were measured, and the post-blast damage and mode of failure of the test specimens were observed. This study also presented detailed analysis of the experimental data. The blast load characteristics were compared with those obtained using the Technical Manual UFC 3-340-02 model (UFCM). The spatial and temporal variations of strain rate were computed from the recorded strain time histories and analyzed. In addition, time-dependant deformations were analyzed to study the contributing modes of vibration in the dynamic response using Power Spectral Density (PSD) function. Moreover, the effect of the axial load on the maximum deformations, vibration periods, strain rates, and contributing modes in the dynamic response were study by comparing the beam results with the column results tested in the same blast shots.

The experimental results were compared with those obtained from an equivalent Single-Degree-of-Freedom (SDOF) model, which included material nonlinearity, strain rate effect, and P-δ effect. To account for strain rate effect on member stiffness and strength, its full moment-curvature response is determined by dividing its cross-section into a number of layers and a strain rate-dependent stress-strain relationship, based on the Cowper-Symonds strain rate model, was used to capture the nonlinear stress distribution over the section. The P-δ effect was modelled using the equivalent lateral load (ELL) method to simulate the secondary moment due to axial load. To determine the effects of higher modes of vibration and the variation of steel member mechanical properties along its length

on its dynamic response, the test steel members were also analyzed using Multi-Degree-of-Freedom (MDOF) models, based on Finite Element Modelling (FEM). These dynamic models were also used to investigate the effect of axial-bending interaction and dynamic stability of columns. In addition, the results of the dynamic models were used to evaluate the results of the Moment Magnification Factor (MMF) commonly used in the interaction formulas to design steel beam columns under blast. Moreover, the effect of strain rate caused by the blast loading on the local stability of steel columns was also evaluated insofar as it might lead to a shift in the governing mode of failure.

Results showed the UFCM pressure predictions compared reasonably well with the measured pressure in the positive phase in terms of both the peak pressure and overall time variations. Results also showed that when proper accounting for secondary-moment due to axial load and strain rate effect on the member resistance function, the SDOF model adequately captured both the overall response, such as the time-dependant deformations and internal forces, and instability behaviour of steel columns under blast loading. It is also shown that using MMF method overestimates the column capacity for ductility ratios μ greater than one, irrespective of the axial load to Euler elastic buckling load ratio (P/P_e). Also for $P/Pe > 0.5$, even if $\mu > 1.0$, the UFC method still overestimates the actual column capacity. The results of the dynamic models were used to generate stability diagrams for the assessment of the critical load and Pressure-Impulse (PI) diagrams for checking the column performance against the allowable deflection limits, which can be implemented in design standard of steel structures under blast loading.

KEYWORDS: Blast loads; Buckling; Damage; Dynamics; Experimental results; Explosions; Field tests; Finite element analysis; Single-degree-of-freedom model; Stability; Steel beams; Steel columns; Strain rate; Moment-curvature relationships; Multi-degree-of-freedom model; Nonlinear time-history analysis.

Acknowledgements

I wish to express my deepest gratitude and appreciation to my supervisors Dr. Ghani Razaqpur and Dr. Michael Tait for their encouragement and endless support throughout my research steps. This research would not have been successfully completed in this form without their advice and support. I appreciate the opportunity to work in such a professional environment. They gave me the opportunity to grow as a researcher and treated me more like a research partner rather than their student.

Special thanks are due to Dr. Manuel Campidelli for his help and support throughout all my research phases.

I also would like to extend my sincere thanks and appreciation to my committee members, Dr. K.S. Sivakumaran and Dr. J. McDermid, for their valuable advices and suggestions. Their helpful comments and discussions during our meetings are greatly appreciated.

A word of thanks is due to Mr. Bert von Rosen, Mr. Rick Guilbeault, Mr. Don Wilson, Mr. David Perrett, and Mr. Kent Wheeler for their assistance during the experimental phase of this study. I would like also to thank my friends and colleagues at McMaster University Ahmed Mostafa, Badr AbouZeid, Marwan Shedid, Mohamed Mostafa, Mohamed Negm, Mostafa El-Sayed, for their help and valuable discussion during my studies.

The following organizations are gratefully acknowledged for their support towards this study: the Chemical, Biological, Radiological/Nuclear and Explosives Research and Technology Initiative (CRTI project 06-015TD), Public Works and Government Services Canada, the Centre for Effective Design of Structures (CEDS) at McMaster University, and the Natural Sciences and Engineering Research Council (NSERC) of Canada for their financial support, the Canadian Explosives Research Laboratory (CERL) for assisting with the blast tests, and the Canadian Armed Forces for the use of their test range. CEDS

received funding through the Ontario Research and Development Challenge Fund, a program of the Ministry of Research and Innovation of Ontario.

Finally, I am would like to express my sincere gratitude to my family for their continuous support and encouragement. This thesis is dedicated to my parents, Magda and Abobakr, and my brothers, Mohamed and Ahmed, for their unconditional love, care, patience, and support.

Co-Authorship

This thesis has been prepared in accordance with the regulations for a sandwich thesis format or as a compilation of research papers stipulated by the faculty of graduate studies at McMaster University. This thesis consists of the following papers:

Paper I

Nassr, A.A., Razaqpur, A.G., Tait, M.J., Campidelli, M., and Foo, S. "***Experimental Performance of Steel Beams under Blast Loading***" ASCE's Journal of Performance of Constructed Facilities, accepted in Sept. 23, 2011. Available online. DOI: 10.1061/(ASCE)CF.1943-5509.0000289.

Design of experimental program and analysis of experimental data were performed by Amr A. Nassr. Paper I was written by Amr Nassr. Dr. Razaqpur, Dr. Tait, Dr. Campidelli, and Dr. Foo supervised the research work; reviewed and revised the journal paper.

Paper II

Nassr, A.A., Razaqpur, A.G., Tait, M.J., Campidelli, M., and Foo, S. (2012) "***Single and Multi Degree of Freedom Analysis of Steel Beams under Blast Loading***" Nuclear Engineering and Design, 242(1), 63-77. DOI:10.1016/j.nucengdes.2011.10.020.

Analyses using SDOF model, MDOF model, and Power Spectral Density function were performed by Amr A. Nassr. Paper II was written by Amr A. Nassr. Dr. Razaqpur, Dr. Tait, Dr. Campidelli, and Foo supervised the research work; reviewed and revised the journal paper.

Paper III

Nassr, A.A., Razaqpur, A.G., Tait, M.J., Campidelli, M., and Foo, S. "***Dynamic response of wide flange steel columns subjected to blast loading: Experimental results***" Submitted to ASCE's Journal of Structural Engineering in Oct. 2011.

Design of experimental program and analysis of the experimental data were performed by Amr A. Nassr. Paper III was written by Amr Nassr. Dr. Razaqpur, Dr. Tait, Dr. Campidelli, and Dr. Foo supervised the research work; reviewed and revised the journal paper.

Paper IV

Nassr, A.A., Razaqpur, A.G., Tait, M.J., Campidelli, M., and Foo, S. "***Strength and Stability of Steel Beam Columns under Blast Load***" Submitted to International Journal of Impact Engineering in March 2012.

Analyses using SDOF model and FEM model to study the strength and stability of steel beam columns under blast load were performed by Amr A. Nassr. Paper IV was written by Amr A. Nassr. Dr. Razaqpur, Dr. Tait, Dr. Campidelli, and Dr. Foo supervised the research work; reviewed and revised the journal paper.

Table of Contents

Chapter 1: Introduction

1.1 Background

Several disasters such as the bombings of the World Trade Centre in New York (1993), the Federal Building in Oklahoma City (1995), the Khobar Tower in Saudi Arabia (1996), the U.S. embassies in Nairobi, Kenya and Dar El-salaam, Tanzania (1998), and more recent bombing in Oslo (2011) have prompted the need for the examination of the behaviour of some potentially vulnerable structures to blast loads. Furthermore, modern steel buildings designed under the provisions of current codes and practices, particularly those in urban environments, may be incapable of maintaining their structural integrity under the influence of severe blast loads. None of the existing steel design codes, including the Canadian standard CAN/CSA-S16-09 standard (CISC, 2011) have any provision related to design against blast loads, therefore, their automatic extension to design of steel structures subjected to blast may not be warranted. Blast loads induce strain rate related response behaviour in steel that is characterized, among other effects, by an increase in its yield strength compared to its static strength but without significant change in the elastic modulus. Also, steel members may respond differently to blast loads with short or long positive pressure duration. Therefore, the need exists for a better understanding of steel member behaviour under blast loads.

1.2 Motivation

The prediction of dynamic response and failure of steel members and structures subjected to blast loading is a complex problem involving nonlinear response in both geometry and material properties. In addition, the actual strain rate experienced by steel members under realistic blast loads has not been properly quantified and the effect of these high strain rates on material properties has not

been fully investigated. Therefore, there is need for experimental data to verify the results of analytical methods pertaining to dynamic response of steel members and structures under such an extreme load. While analytical and numerical methods are available to predict the response of steel members under blast loading, experimental data is scarce. Experimental data obtained from full scale blast loads will furnish the necessary basis for design specifications of steel structures under blast loads.

1.3 Objectives of the research

The objectives of this research are as follows:

(1) To experimentally investigate the dynamic response of steel members during field testing of steel beams and columns subjected to blast loads caused by detonations of real explosives involving different charge weights and stand-off distances.

(2) To develop simple design oriented dynamic models for computing the response of steel beams and columns. The proposed models will include the effect of high strain rates. The results of the dynamic models will be compared to the experimental data to check the validity and accuracy of the dynamic models.

(3) To study, through parametric analysis, the relation between key steel beams and columns structural properties and blast load characteristics and to use the results in order to establish safe/unsafe domains for blast resistant design of steel members.

1.4 Organization of the dissertation

This dissertation describes a combination of experimental and analytical research used to investigate and document the dynamic response of steel beams and columns to blast loading. The information presented in this dissertation aims at providing a better understanding of the dynamic response of steel members to

blast loading and developing simple yet accurate tools that can be used for blast resistant design. The content of the dissertation as follows:

- The motivation and objectives of the dissertation as well as background information pertaining to blast loads, blast-structure interactions, and methods of analysis are presented in Chapter 1.
- Chapter 2 contains a description of the experimental program, test matrix, test setup, and instrumentation of testing steel beams under blast loading.
- Chapter 3 contains detailed analyses of the dynamic response of test beams as well as comparisons between the experimentally measured time-dependant deformation responses and the corresponding responses predicted by Single- and Multi-Degree-of-Freedom models. The contributing modes of vibrations in the response are determined and discussed.
- The experimental results of steel columns under blast loading are presented in Chapter 4. The effect of the axial load on the maximum deformations, vibration periods, strain rates, and contributing modes in the dynamic response are studied.
- Chapter 5 presents analytical study on strength and stability of beam columns. Practical design curves for beam columns are developed and presented.
- The thesis summary, major conclusions and recommendations for future research are presented in Chapter 6.

1.5 Literature review

The literature review of this study attempts to cover some aspects of blast loading characteristics, including explosion phenomena, pressure time profile, and blast-structure interaction. The influence of high strain rates, caused by blast loading, on the mechanical properties of steel and the failure modes of steel members is also presented. This is followed by a discussion of the analysis techniques used to

determine the dynamic response of steel members to blast loading. Although some numerical or analytical studies have been performed by others to study the effects of blast loading on the response of steel structures, these are not reviewed in detail because the reported responses are often influenced by certain assumptions that are not necessarily satisfied by real structures. In the case of steel columns, many studies have focused on the effect of dynamic or impulse axial loads while in the current study the axial load is assumed to be statically applied.

1.5.1 Blast loading

An explosion is a large-scale and sudden release of energy that generally generates high temperature and a large amount of gas (Baker et al. 1983). For a conventional explosive, such as trinitrotoluene (TNT), the energy release is associated with the rearrangement of its atoms, while in nuclear explosive the reaction between protons and neutrons releases the energy (Baker et al. 1983). In general, explosions can be classified into four basic types; a vapor cloud explosion, a vessel explosion, a dust explosion and a condensed phase explosion (ASCE, 1997). In a vapor cloud explosion, a flammable material, such as liquefied gases, ignites under certain conditions of pressure and temperature and may produce a fire ball. In a vessel explosion, a rapid combustion or release of energy occurs in an airtight space like a room or pressure vessel. In a dust explosion, similar to a vapor cloud explosion, a combustible material is dispersed in the air forming a flammable cloud and a flame propagates through it. Generally, explosion against structures are condensed phase explosions. High pressure and waves accompany the detonation of high explosive materials.

An oxidation reaction occurs during the explosion which is called combustion. When explosive materials decompose at a rate below the speed of sound (subsonic), the combustion process is called *deflagration*. On the contrary, *detonation*, such as explosion of TNT, occurs more rapidly and produces a high intensity shock wave with the reaction rate being 4-25 times faster than the speed

of sound (supersonic) (Smith and Hetherington 1994). The detonation is accompanied by large pressure up to 300 kilobar and temperature of about 3000-4000 ^{o}C. The hot gas expands forcing out the surrounding air and occupying the associated volume. As a consequence, a blast wave forms in front of this gas volume containing most of the energy released by the explosion.

1.5.1.1 Pressure time profile

After an explosion, the blast wave or shock front generates an instantaneous rise in pressure from ambient pressure P_o to a peak incident pressure (or side-on overpressure) P_s . The pressure subsequently decays first to ambient level at time t_d, then to an under-pressure $\overline{P}_s$ before eventually returning to ambient pressure at time $t_d + \bar{t}_d$. Figure 1.1 shows the typical pressure time profile of a blast wave in air (USDOD 2008). The loading profile consists of two main phases; the portion above ambient pressure is called positive phase with duration, t_d, while the portion below ambient is called the negative phase with duration $\bar{t}_d$. The negative phase has longer duration and lower intensity than the positive phase.

An important characteristic of the pressure time profile to be defined is the *impulse*. The positive impulse, i is the area beneath the pressure time curve from arrival at time t_a to the end of the positive phase (Baker et al. 1983), and it is given by

$$i = \int_{t_a}^{t_a+t_d} P(t)dt \tag{1.1}$$

Similarly, the negative impulse can be given as (Baker et al. 1983)

$$\bar{i} = \int_{t_a+t_d}^{t_a+t_d+\bar{t}_d} P(t)dt \tag{1.2}$$

When the shock wave encounters a solid surface such as a building, it is stopped abruptly, causing the pressure to increase above the values observed in the

incident blast wave. This process of magnifying the blast wave is known as reflection. The reflected pressure, P_r, is of primary interest because it produces the maximum load on structures.

Some investigators have suggested certain relationships to represent the pressure time-history $P(t)$ of the ideal blast wave, generally emphasizing only the positive phase. The simplest form assumes a linear decay given by Baker (1973) as

$$P(t) = P_o + P_s\left(1 - \frac{t}{t_d}\right) \tag{1.3}$$

where t is the time after the pressure wave arrival. Others have suggested an exponential decay, such as the modified Frielander equation by Baker (1973) as

$$P(t) = P_o + P_s\left(1 - \frac{t}{t_d}\right)e^{-\beta\frac{t}{t_d}} \tag{1.4}$$

where β is the decay parameter coefficient. A somewhat more complex model has been proposed (Baker 1973) as

$$P(t) = P_o + P_s\left(1 - \frac{t}{t_d}\right)ae^{-b\frac{t}{t_d}} + (1-a)e^{-c\frac{t}{t_d}} \tag{1.5}$$

in which *a*, *b*, and *c* are constants obtained from experimental data.

The negative phase duration, with its relatively low amplitude, has often been ignored. This is either because of the difficulty associated with measuring or computing the characteristics of the negative phase, or because most researchers consider it relatively unimportant compared to the positive phase (Baker 1973). The negative phase pressure variation can be expressed as follows (Baker 1973)

$$P(t) = P_0 - \overline{P}_s\left(\frac{t}{t_d^-}\right)\left(1 - \frac{t}{t_d^-}\right)e^{-4\frac{t}{t_d^-}} \tag{1.6}$$

1.5.1.2 Scaling laws and scaled-distance

Scaling laws are commonly used to predict air-blast characteristics, such as time of arrival, peak pressure, duration, and impulse for a given charge size at a given distance from ground zero. The most widely used approach to blast wave scaling law is Hopkinson scaling law (Baker et al. 1983), which is commonly described as the cube-root scaling law. This law states that two explosions will have identical blast wave characteristics provided they have equal scaled-distances *Z*. The scaled-distance is defined as

$$Z = \frac{R}{W^{1/3}} \tag{1.7}$$

where *R* is the distance from the charge centre in meters, and *W* is the weight of the explosive materials in kilograms.

1.5.1.3 TNT equivalence

Most of the data pertaining to explosions are introduced in terms of the output of an equivalent TNT explosive. Therefore, it is convenient to relate any explosive to its TNT equivalent. A number of approaches have been introduced to convert the explosive mass to a TNT equivalent mass. For chemical explosives, the mass of an explosive can be related to an equivalent TNT mass using the heat of combustion ratio (Henrych 1979) as

$$w_{TNT} = \frac{H_{Exp}}{H_{TNT}} w_{Exp} \tag{1.8}$$

where w_{TNT} is the equivalent TNT mass, H_{TNT} is the heat of combustion for TNT, H_{Exp} and w_{Exp} are the heat of combustion and mass of the explosive under consideration respectively. Another more accurate method to relate any explosive to an equivalent TNT is to perform tests and compare the pressure and impulse from that explosive with those obtained from TNT with the same mass. Such TNT equivalency factors can be found in various sources (Baker et al. 1983; Smith and

Hetherington 1994). Table 1.1 shows the conversion factors for a number of common explosives (Baker et al. 1983).

1.5.1.4 Dynamic pressure

In addition to the incident pressure, the high velocity wind due to the rapidly moving air behind the shock front results in another pressure known as the dynamic pressure q (Smith and Hetherington 1994). The dynamic pressure q can be given in terms of incident pressure P_s, ambient pressure P_o, and specific heat ratio γ as

$$q = \frac{P_s^2}{\left[2\gamma P_o + (\gamma - 1)P_s\right]} \tag{1.9}$$

The dynamic pressure is relevant in reflected pressure calculations as it will be shown in a subsequent section.

1.5.1.5 Blast load predictions

The response of a structure or element to a blast event is strongly dependent on the spatial and temporal distributions of the blast pressure and its magnitude. Therefore, the relatively accurate prediction of these quantities is important for assessing a member's response to a blast event. Blast load parameters are in practice often determined by using a set of empirical relations that are plotted in the form of charts or fitted into equations. Software , such as CONWEP (Hyde, 1990) and ATBLAST (2007), are also available to predict blast load parameters, which are based on experimental data collected from blast tests. In Figure 1.2, the peak reflected pressure P_r, peak incident pressure P_s, reflected impulse i_r, incident impulse i_s, time of arrival t_a, and positive phase duration are shown depending on the scaled-distance Z (USDOD 2008). There are also some closed-form semi-empirical expressions available that can be used to estimate the blast parameters.

Kinney and Graham (1985) proposed the following semi-empirical equation for the reflected pressure P_r expressed in kPa

$$P_r = 0.20P_s\left(\frac{7P_o + 4P_s}{7P_o + P_s}\right) \tag{1.10}$$

in which P_o is the atmospheric pressure and P_s is the incident overpressure which is given in terms of Z as (Kinney and Graham 1985)

$$\frac{P_s}{P_o} = \frac{808\left[1+\left(\frac{Z}{4.5}\right)^2\right]}{\sqrt{1+\left(\frac{Z}{0.048}\right)^2}\sqrt{1+\left(\frac{Z}{0.32}\right)^2}\sqrt{1+\left(\frac{Z}{1.35}\right)^2}} \tag{1.11}$$

Similarly, the positive phase duration t_d, expressed in milliseconds (ms), was given as (Kinney and Graham 1985)

$$\frac{t_d}{W} = \frac{980\left[1+\left(\frac{Z}{0.54}\right)^{10}\right]}{\left[1+\left(\frac{Z}{0.02}\right)^3\right]+\left[1+\left(\frac{Z}{0.74}\right)^6\right]+\sqrt{1+\left(\frac{Z}{6.9}\right)^2}} \tag{1.12}$$

On the other hand, Prugh (1999) expressed positive reflected impulse I_r in kPa.ms as follows

$$\frac{I_r}{W^{1/3}} = 8.97\left(\frac{200}{Z^{1.5}} + \frac{125}{Z}\right) \tag{1.13}$$

Alternatively, numerical methods based on laws of conservation of energy, mass and momentum and a given equation of state may be used within the framework of computational fluid dynamics to obtain the blast load parameters (Lee et al. 2009). However, the latter is not widely used in structural engineering applications, particularly in the case of simple geometries such as the one in the present tests. In this study, the predictions of two blast load models will be investigated.

It is important to experimentally assess the accuracy of the predictions of these approaches, the reflected pressure, positive impulse and positive phase

duration obtained from experimental data need to be compared with the corresponding values by some well established methods.

1.5.2 Blast-structure interaction

As mentioned, the blast wave is characterized by a rapidly rising peak pressure followed by decay towards a peak negative pressure and finally returning to ambient conditions. The true load applied to structures may deviate from these conditions in some cases. The actual net load acting on the structure depends on the size of the charge, the location of the charge relative to the structures, as well as the structure shape and orientation (Baker et al. 1983; Smith and Hetherington 1994; USDOD 2008).

1.5.2.1 Blast waves impinging on an infinite rigid plane

As the blast wave travels outward, it is reflected when it encounters an infinite, rigid solid surface. The reflected wave travels back through the atmosphere at a higher velocity and pressure. Because the incident wave and the reflected wave coincide, the pressure on the rigid plane is higher than the incident pressure and is denoted as $P_r(t)$. The associated reflected impulse is denoted as $i_r(t)$. The ratio of the reflected and the incident pressure is called reflection coefficient $C_{r\alpha}$.

The reflected pressure and impulse are dependent on the angle of incidence α_i, which is the angle between the direction of the moving plane blast wave and the normal to the target surface. If the angle is 90^o, the blast wave travels alongside the target surface and the pressure acting on the surface is equal to the incident pressure (side-on pressure). The reflection coefficients $C_{r\alpha}$ for angles of incidence α_i between 0^o and 90^o are shown in Figure 1.3. Starting at an angle of incidence of approximately 40^o, the reflection coefficient increases and has a local maximum which is sometimes higher than the reflection coefficient at 0^o. This is due to Mach reflection, which occurs when the interaction of the

reflected wave and the incident wave produce an enhanced shock front known as the Mach front or Mach stem (Baker et al. 1983; USDOD 2008).

1.5.2.2 Blast wave impinging on a structure

If a blast wave hits a structure, the structure is loaded by pressure, which consists of two parts: the first part is due to blast wave pressure and the second part due to the dynamic pressure. The effect of these parameters on an object is shown in Figure 1.4. Depending on the size of the object compared to the positive phase duration of the blast t_d, the incident pressure surrounds the objects with positive pressure as shown in Figure 1.4(a). The dynamic pressure is the result of the movement of air away from the explosion source. The blast wind causes a positive pressure on the front of a structure and a negative pressure (suction) at the back as shown in Figure 1.4(b). Due to the translational nature, dynamic wind pressure, it is also called drag pressure. The drag pressure on a structure is equal to the dynamic pressure multiplied by a drag factor C_d. The drag factor is a function of the shape of the structural member. A list of drag factors are given in Baker et al. (1983) and USDOD (2008).

For a structure with a relatively small dimension in one direction, the incident pressure on the front and back of the building are approximately equal and hence the translational pressure (net pressure) is approximately zero as shown in Figure 1.5(a). Due to the small dimensions of the front or face of the structure, no reflections occur. The structure is only loaded with the translational pressure due to the dynamic pressure (Smith and Hetherington 1994). For larger objects or building, the front of the object is loaded with the reflected pressure. The sides and top (roof) are loaded with the side-on pressure, with the two side pressure acting in opposite directions with net zero translational pressure. Due to the large local pressure difference between the front and sides of the structures, the blast wave diffracts around the building. When the diffraction from the front to the sides of the building is completed, the reflected pressure on the front is decreased

from the reflected pressure to incident pressure. Similarly, pressure differences cause the blast wave to diffract from the sides to the back of the building. If the diffraction (clearing) time is smaller than the positive phase duration, the structure is loaded by translational pressures due to incident pressure and dynamic pressure as shown in Figure 1.5(b). If the diffraction time is larger than the positive phase duration of the blast, the structure is sequentially loaded as shown in Figure 1.5(c). The structure feels pressure either at the front, at the sides, or at the back. The diffraction (clearing time) for the rectangular faces can be estimated using (Smith and Hetherington 1994)

$$t_c = \left(\frac{2S + D}{U_x} \right) \tag{1.14}$$

where S is the height or the half breadth of the face, whichever is smaller, D is the distance from the point of interest to the structure's edge. U_x is the speed of the incident shock.

1.5.3 Structural response

1.5.3.1 Strain rate effect

It is well know that structural components subjected to high rate of loading exhibit an increase in the strength of the material compared to an identical material subjected to static loading (Campbell and Duby 1956; Henrych 1979; USDOD 2008). Several experiments have been conducted in an effort to determine the dynamic properties of different materials subjected to dynamic tension, compression, shear, bending, or a combination of these loads with different strain rates (Aspden and Campbell 1966; Campbell and Duby 1956; Krafft et al. 1954; Jones 1988; Lamarche and Tremblay 2011). The principal variables measured in these investigations include the stresses and strains at various rates of load applications. The influence of material strain rate sensitivity manifests itself as a strengthening effect in structures. This might suggest that it is a beneficial

phenomenon since it provides an additional safety factor. In many cases, however, a structural resistance mode change occurs which causes larger and not smaller associated deformations (Jones 1988).

It should be noted that material strain rate sensitivity is a material effect and is independent of the structural geometry (Jones 1988) and the carbon content of steel (Itabashi and Kawata 1999). In order to account for the effect of strain rate, a ratio of material dynamic strength to static strength is usually used and it is referred to as Dynamic Increase Factor (DIF). This ratio is given as a function of strain rate either graphically or mathematically (Soroushian and Choi 1987; USDOD 2008). The behaviour of steel under various dynamic actions (tension, compression, shear, and bending) is discussed in the following sections.

1.5.3.1.1 Tension

The properties of metals under dynamic tension have been studied in many investigations (Soroushian and Choi 1987; Bassim and Panic 1999; Lamarche and Tremblay 2011). The objective of most tests have been either to determine the complete stress-strain relationship or to measure certain mechanical properties of the material under the action of strain rates higher than encountered in similar static tests. The specific properties include the elastic modulus, yield stress, ultimate strength, change in cross-sectional area, and fracture energy. The majority of the rapid loading experiments have been conducted by single impacts leading to specimen failure or by modifying the ordinary tensile testing machines to provide faster motion of the driving head which pulls one end of the specimen (Goldsmith 1960). Figure 1.6 shows a typical stress-strain curve for a low carbon structural steel as adopted from the technical manual UFC 3-340-02 (USDOD 2008). The solid line represents the standard tensile static test, while the dashed one represents a rapid strain rate test. As it can be seen, the yield stress significantly increases at rapid strain. Also, the ultimate stress, to a lesser extent

increases with strain rate. The ultimate strain and the modulus of elasticity, on the other hand, remain practically unchanged.

One of the early investigations on the mechanical properties of steel under dynamic tension was conducted by Manjoine and Pittsuburgh (1944). They conducted some tensile testes on carbon steel using a high-speed machine. Their experimental results indicated that the yield stress and ultimate tensile stress increased with an increase in strain rate. Also, it was found that the mechanical properties of steel with lower yield strength are more strain rate sensitive. Soroushian and Choi (1987) reported the results of dynamic monotonic tensile tests on structural steel, deformed reinforcing bars, and deformed wires conducted with different strain rates up to 10 /s. The results of these tests showed that all the characteristics of the stress strain relationship increased with increasing strain rate. The yield strength is more strain rate sensitive than the ultimate strength, while the steel modulus of elasticity is independent of the rate of straining. No significant difference among the strain rate-dependent response of structural steel, deformed reinforcing bars, and deformed wires was reported, which confirms the fact that strain rate sensitivity is independent of structural geometry. Based on the results of these experiments, a strain rate sensitive constitutive model with strain hardening for steel was proposed.

Similar tests conducted on mild steel at various strain rate up to 100 sec^{-1} were reported by Jones (1988) and are illustrated in Figure 1.7. The results showed that the upper and lower yield stress increase with increase in strain rate as observed by Manjoine and Pittsuburgh (1944). However, the ultimate tensile stress increased more slowly. Therefore, this study concluded that the strain hardening becomes less important for mild steel with large tensile strains and large strain rates. Malvar (1998) proposed relationships that give the DIF for both yield and ultimate stress as function of the strain rate. These relationships were based on dynamic tensile tests on reinforcing bars. The adopted DIF formulations were as follows

$$DIF = \left(\frac{\dot{\varepsilon}}{10^{-4}} \right)^{\alpha} \tag{1.15}$$

where

$\alpha = 0.074 - 0.040 \frac{\sigma_y}{414}$ for yield stress, or

$\alpha = 0.019 - 0.009 \frac{\sigma_u}{414}$ for ultimate stress

$\dot{\varepsilon}$ is the strain rate in s^{-1}, σ_y and σ_u are the yield and ultimate stress in MPa. This formulation is valid for yield stresses between 290 and 710 MPa and for strain rates between 10^{-4} and 10 /s. Many other constitutive equations for the strain rate-sensitive behaviour have been proposed in the literature. Jones (1988) reported one equation for rigid plastic materials and it is given by

$$DIF = \frac{\sigma'_y}{\sigma_y} = 1 + \left(\frac{\dot{\varepsilon}}{D} \right)^{1/q} \tag{1.16}$$

where σ'_y and σ_y are the dynamic and static yield stresses. $\dot{\varepsilon}$ is the strain rate in s^{-1}. D and q are constants for a particular material. For mild steel, D=40, and q= 5. The above equation shows that the dynamic yield stress for mild steel at the strain rate double of $40\,s^{-1}$ is double its static yield stress.

1.5.3.1.2 Compression

The dynamic compressive experiments are typically carried out with devices compressing the specimen between two movable anvils which approach each other at a constant rate. Other dynamic compressive tests use an impact technique by dropping a weight, or impact by a bullet, or by projection of the test piece against a hard target. Generally, the dynamic behaviour of metals in tension and compression is similar (Goldsmith 1960). However, the tensile specimen may fail either by necking or brittle fracture, while the compressive specimen fails by barrelling, column action, or shear effect (Goldsmith 1960). Jones (1988) reported

the results of the uni-axial compressive test on mild steel, titanium, and aluminum with different rates of strain. The results showed a significant increase in the upper yield stress of the mild steel with increase of strain rate as shown in Figure 1.8. Material strain hardening decreased with the increase of strain rate. Titanium and aluminum, on the other hand, exhibited less sensitivity to strain rate than mild steel.

1.5.3.1.3 Bending

The influence of the strain rate presented in previous sections was investigated by producing a uniform stress state in the test specimens. However, dynamic bending moments do not cause a uniform state of stress across the thickness of structural members. The dynamic behaviour of mild steel beams with rectangular cross-section subjected to a uniform bending moment was investigated by Rawlings (1963). The maximum strain rate produced by the experimental arrangement was only about 1.0 /s. The experimental yield stresses in Figure 1.9 show a significant increase with increase in strain rate. The results of this study were compared with some other experimental results of dynamic uni-axial load which were used to derive curves of bending moment against angle of bend.

Aspden and Campbell (1966) tested carbon steel specimens under pure bending with maximum strain rate up to 20 /s. The static and dynamic bending moments versus bending angle curves for different bending angle rates are shown in Figure 1.10. In addition to the dynamic flexure tests, they conducted dynamic compression testes on the same material. This is to correlate the results of the dynamic flexure tests with those obtained from dynamic axial tests. The results of bending tests showed that the curvature rate had a large influence on the behaviour of steel beams as the dynamic upper yield moment at strain rate of 12 /s increased by 80% compared to the static yield moment. This study suggested that the dynamic flexure behaviour cannot be fully explained by using the data

obtained from the compression tests in calculations based on the elementary theory of plastic bending. Such calculations gave a smaller upper yield moment.

In order to derive a relationship between rate sensitivity bending moment and curvature, a material rate-sensitivity or DIF relationships (Eq. (1.15) or Eq. (1.16)) should be employed based on the following assumptions (Aspden and Campbell 1966):

(i) the strain distribution is linear across the section;

(ii) the strain is uniform along the beam length;

(iii) the curvature rate is constant;

(iv) the material behaviour is the same in tension and compression;

(v) the changes in cross-sectional geometry are negligible.

Considering a rectangular cross-section with breadth *b* and depth *d*, the dynamic plastic bending moment can be obtained from the following

$$M' = 2\int_0^{d/2} z\sigma(\varepsilon,\dot{\varepsilon})b \; dz \tag{1.17}$$

where *z* is the distance from the neutral axis, and $\sigma(\varepsilon,\dot{\varepsilon})$ is the stress at strain ε and strain rate $\dot{\varepsilon}$. From the above assumptions, the strain can be related to the curvature, $\varepsilon = \kappa z$. Therefore, Eq. (1.17) can be rewritten as

$$M' = 2b\int_0^{d/2} z\sigma(\kappa z,\dot{\kappa} z) \; dz \tag{1.18}$$

in which κ and $\dot{\kappa}$ are the curvature and curvature rate, respectively

It should be noted that the use of the DIF to enhance the material strength in calculating the dynamic resistance of structural members is recommended by well known design guidelines, including the Technical Manual UFC 3-340-02 (USDOD 2008), and ASCE (1997). However, the DIF value suggested by these guidelines is based on averaged strain rates over a given cross-section, even though the actual strain rate profile varies over the depth of the section. The suggested values are independent of the actual strain rates that may be experienced by a member under a given blast scenario and are presumably

conservative, but the degree of conservatism is not always evident. In reality the use of a fixed value might result in overestimating the effect of the strain rate, especially in the case of wide flange sections with a high web-area to flange-area ratio. In addition, the DIF is assumed to be constant for all sections along the member length, without regard for the strain rate variation along the member, e.g. diminishing strain rate close to the ends of simply supported beams. This may result in unconservative design, particularly when designing for shear and/or end connections.

In addition, the strain rate range of 100-1000 /s is often cited for blast in the literature (Bischoff and Perry 1991). However, to date in the open literature, there is scant strain rate data obtained from blast tests on reasonable size steel members to confirm the validity of the above rates in far range blast scenarios. Therefore, experimental tests with a wide range of scaled-distances are needed to establish the range of strain rates experienced by steel structures during unconfined explosions. Such data would assist in deriving realistic dynamic increase factors for design purposes.

1.5.3.2 Analysis techniques

1.5.3.2.1 Single-degree-of-freedom (SDOF) system

A large number of approximate solution techniques are available in the literature to predict the structural behaviour under different dynamic loads. Most of these techniques are based on transforming the structural elements into discrete systems with a certain number of nodes (lumped masses). The most basic dynamic system that allows easy response calculation is the equivalent Single-Degree-Of-Freedom (SDOF) system (i.e. mass-spring-damper system). In this method of analysis, the member mass is lumped at one point along its length and only the displacement of this point is traced during the dynamic event. Biggs (1964) gives a thorough presentation of to SDOF method, which is also incorporated in the Technical

Manual UFC 3-340-02 (USDOD 2008). Biggs (1964) suggested a list of required transformation factors to equate the equivalent SDOF system to the real structural element and they are derived so that the deflection obtained by analyzing the equivalent SDOF represents the actual deflection of the structural member at one significant point on the structure (e.g. the mid-span of a beam). As shown in Figure 1.11, the real beam is transformed to an equivalent SDOF system which consists of an equivalent concentrated mass, damper, spring, and a time varying concentrated force.

The equivalent mass *M*, stiffness *K* of the system, and equivalent force *F* on the system is calculated by equating the total energy of the SDOF system at any time to the total energy of the beam assuming a predetermined displacement shape. The lumped mass of the SDOF is made equivalent to the distributed mass of the beam by assuming that both have the same kinetic energy. The spring stiffness in the SDOF system can be made equivalent to the bending stiffness by assuming that both have the same strain energy. The concentrated force on SDOF system can be made equivalent to the distributed force on the beam, by assuming that the works done by the two forces are equal. The energy equivalence results in mass factor, K_M, resistance factor, K_R, and load factor, K_L for equivalent mass, resistance, and force in the SDOF system. The load factor is found to be approximately equal to the resistance factor (Mays and Smith 1995). Thus, these factors can be expressed mathematically as follows

$$K_R = K_L = \frac{\int_0^L p\phi(x)dx}{pL} \tag{1.19}$$

$$K_M = \frac{\int_0^L m\phi^2(x)dx}{mL} \tag{1.20}$$

where m and p are the mass and load per unit length of the member, $\phi(x)$ is the assumed mode or displaced shape of the member, and L is the member length.

Different deformed shapes $\phi(x)$ are assumed for different response stages (e.g. elastic, elastic-plastic, or fully plastic conditions). For each response stage, new transformation factors are applied. A list of these transformation factors for each response and boundary conditions is given in Biggs (1964). The equation of motion can be formulated for the equivalent SDOF system by satisfying the force equilibrium of the system and can be written as

$$K_M M \ddot{y} + K_L R(y) = K_L P(t) \tag{1.21}$$

or

$$K_{LM} M \ddot{y} + R(y) = P(t) \tag{1.22}$$

where $\ddot{y}$ is the equivalent mass acceleration and is equal to the actual beam mid-span acceleration, M, $R(y)$, and $P(t)$ are the beam total mass, resistance, and load, respectively. K_{LM} is the so-called load-mass factor given by $K_{LM}=K_M/K_L$, and its values for simply supported beam under uniform pressure as listed by Biggs (1964) are 0.78 and 0.66 for elastic and plastic stages, respectively. The static load-deflection relationship of the structural member should be used as the resistance-displacement function $R(y)$. For linear elastic system with stiffness K, the natural frequency of vibration f of the SDOF system is equal to

$$f = \frac{1}{2\pi}\sqrt{\frac{K}{K_{LM} M}} \tag{1.23}$$

The damping is usually not considered in impulsive loading problems such as blast and impact as the maximum response usually occurs during the first vibration cycle when damping has minimum contribution to the dynamic response (Smith and Hetherington, 1994).

In this investigation the accuracy and limitations of the SDOF model will be examined by comparing its results with corresponding experimental data from tests on full scale steel beams and columns.

1.5.3.2.1.1 Response of SDOF system to idealized blast pressure

In this section, the response of the SDOF system is determined. For simplicity, blast pressure time profiles are usually idealized as a triangular pulse with peak force F_m and duration t_d as shown in Fig. 1.12. There are other forcing functions of the blast pressure time profiles included in the literature such as rectangular and exponential decaying pulses (Li and Meng 2002a; Li and Meng 2002b). For convenience, the following dimensionless parameters are defined (Li and Meng 2002a; Li and Meng 2002b).

$$\begin{aligned} &\overline{F}_m = \frac{F_m}{R_m} \qquad \overline{t}_d = \omega_1 t_d \qquad \overline{t} = \omega_1 t \\ &\overline{I} = \overline{F}_m \int_0^{\overline{t}_d} \overline{F}(t)\, d\overline{t} \qquad \overline{y} = \frac{y}{y_m} \qquad \overline{F} = \frac{F}{F_m} \end{aligned} \tag{1.24}$$

where $\overline{F}_m$, $\overline{y}$, $\overline{t}$, and $\overline{t}_d$ are the non-dimensional quantities for maximum force, displacement, time, and load duration. ω_1 is the circular frequency and is equal to $2\pi f$, where f is the frequency of vibration. The force function can be expressed in non-dimensional form as

$$\overline{F}(t) = \left(1 - \frac{\overline{t}}{\overline{t}_d}\right) \tag{1.25}$$

The response of the SDOF to the idealized triangular load can be given using the convolution integral (Biggs 1964) as follows

$$\overline{y}(\overline{t}, \overline{t}_d) = \overline{F}_m \int_0^{\overline{t}} \overline{F}(\tau)\sin(\overline{t} - \tau)\, d\tau = \overline{F}_m \begin{cases} -\dfrac{\overline{t}}{\overline{t}_d} + 1 - \cos\overline{t} + \dfrac{\sin\overline{t}}{\overline{t}_d} & \text{if } \overline{t} \le \overline{t}_d \\ -\cos\overline{t} + \dfrac{\sin\overline{t}}{\overline{t}_d} - \dfrac{\sin(\overline{t} - \overline{t}_d)}{\overline{t}_d} & \text{if } \overline{t}_d > \overline{t}_d \end{cases} \tag{1.26}$$

Response for different $\overline{t}_d$, which is equivalent to the $\frac{t_d}{T}$ ratio, is shown in Fig. 1.13. As this ratio becomes greater, more oscillations occur during the presence of the forced vibration. If $\overline{t}_d$ is small, no displacement peak develops during the forced vibration.

1.5.3.2.1.2 Dynamic load factor (DLF) and DLF-$\overline{t}_d$ diagram

The dynamic load factor (DLF) is the ratio of the maximum dynamic response to the static deformation. DLF-$\overline{t}_d$ diagram is obtained by calculating maximum response corresponding to different $\overline{t}_d$ values. Therefore, DLF can be calculated from

$$DLF = \frac{y_m}{y_{st}} = \frac{y_m K}{y_{st} K} = \frac{\overline{y}_m}{\overline{F}_m} \tag{1.27}$$

Figure 1.14 shows DLF-$\overline{t}_d$ diagram for the idealized triangular pulse. To interpret the DLF-$\overline{t}_d$ diagram, it is useful to look at the limits of DLF-$\overline{t}_d$ diagram. When $\overline{t}_d \to 0$, the duration of the blast is very short compared to the natural period of the structure. An impulse has exactly this property, so to evaluate this limit, DLF is determined assuming the dynamic load to be imparted to the structures as an impulse *I*. Impulse response is given as (Chopra 2001)

$$y(t) = \frac{I}{M\omega_1} \sin \omega_1 t \tag{1.28}$$

In a non-dimensional form, it can be rewritten as

$$\overline{y} = \overline{I} \sin \overline{t} \tag{1.29}$$

where $\overline{I}$ is the non-dimensional impulse $\overline{I} = \overline{F}_m \Delta \overline{t}$. Therefore, DLF at $\overline{t}_d \to 0$ is obtained from

$$DLF = \frac{\overline{y}}{\overline{F}_m} = \frac{\overline{t}_d}{2} \tag{1.30}$$

The impulsive asymptote is independent of the pressure time profile. The other limit is where $\overline{t}_d \to \infty$ and the blast load becomes a step force and DLF can be obtain from convolution integral as follows

$$\overline{F}(t) = 1 \quad \to \quad DLF = \int_0^{\overline{t}} \sin(\overline{t} - \overline{\tau}) d\overline{\tau} = 1 - \cos \overline{t} \quad \to \quad DLF = 2 \tag{1.31}$$

The quasi-static asymptote is determined to be 2. Both the quasi-static asymptote and impulsive asymptote can be identified from DLF-$\overline{t}_d$ diagram as shown in Fig. 1.14. Baker et al.(1983) divided the DLF-$\overline{t}_d$ diagram into three distinct regimes:

- The quasi-static regime: In this regime the duration of the load is very large compared to the structure's natural period (i.e. $\overline{t}_d$ is greater than 40). In other words, the load dissipates very little before maximum displacement occurs. The pressure time-history has no effect on the response as the response only depends on the peak force F_m and structural stiffness K, and not on the load duration t_d or the structural mass M. The maximum dynamic deflection is twice the static deflection (DLF=2.0).
- The impulsive regime: The duration of the load is small relative to the structure period; the load is imparted to the structure and removed before the structure undergoes significant deformation (i.e. $\overline{t}_d$ is less than 0.40). The pressure time-history does not affect the response. The response is directly proportional to the impulse, the area under the load-time-history. Any combination of peak loads and duration with the same impulse will result in the same maximum deformation. Both structural stiffness and mass has an influence on the response.
- The dynamic regime: The response is affected by both the load and the impulse. The response depends on the stiffness and the mass. The load duration is of the same order of magnitude as the structural period (i.e. $0.40 < \overline{t}_d < 40$). In this case, transient analysis is required to obtain the structural response.

1.5.3.2.1.3 Pressure-impulse diagrams

Pressure-impulse (P-I) diagrams are widely used in structural blast resistant design to establish safe response limits for given blast loading scenarios (USDOD 2008). The P-I diagram is an iso-damage curve for a structural element (i.e. each

combination of pressure and impulse produces the same damage level in a structural element loaded with a particular blast loading history). P-I diagrams were first derived to assess the houses damaged by bombs dropped on United Kingdom in the Second World War (Jarrett 1968; Mays and Smith 1995). The damage level to the houses was quantified by a series of P-I diagrams, such as complete demolition, severe damage, relatively minor structural damage. These iso-damage P-I diagrams have been applied not only to predict structural damage (Smith and Hetherington 1994), but also to predict blast-induced human injuries (Baker et al. 1983; Mays and Smith 1995; Smith and Hetherington 1994).

Figure 1.15 shows the primary features of a P-I diagram. The two asymptotes, one for pressure and the other for impulse, define limiting values for each parameter. Thus, loads with very short duration, compared to the structure natural period, are called impulsive loading and the structure response is insensitive to the peak pressure but very sensitive to the associated impulse. This forms the impulsive asymptote that defines the minimum required impulse to reach a particular damage level. On the other hand, as the load duration becomes longer compared to the natural period of the structural element, the load is termed quasi-static loading and the response becomes sensitive to peak pressure but not to the associated impulse of the pulse. Thus, the other asymptote represents the minimum level of required peak pressure to reach the particular damage level. The transition regime connecting the impulsive asymptote to the quasi-static asymptote is termed as the dynamic regime. In this regime, the structural response depends on both pressure and impulse. The load duration is of the same order of magnitude as the structural natural period.

As shown in Fig. 1.15, the P-I curve divides the pressure-impulse space into two distinct regions. Combinations of pressure and impulse that fall above and to the right of the curve will produce damage in excess of the specific limit, while those below and to the left will not induce less damage than the specified damage level. The P-I diagrams could also be presented as a set of P-I curves,

forming threshold contours, with different damage levels, such as low-, medium-, and high-damage.

1.5.3.2.1.4 Pressure-impulse diagram for elastic system

The P-I for elastic system is a modification of the DLF-$\bar{t}_d$ diagram. The *x*- and *y*-axes are labeled with *P* and *I*. These parameters are given by

$$P = \bar{F}_m = \frac{1}{\bar{D}_m} = \frac{F_m}{y_m K} \tag{1.32}$$

$$I = \frac{P\bar{t}_d}{2} \tag{1.33}$$

Therefore, the impulsive regime becomes a vertical asymptote instead of linear in DLF-$\bar{t}_d$ diagram and it is modified as follows

$$\begin{aligned} &\bar{D}_m = \frac{\bar{t}_d}{2}, && I = \frac{P\bar{t}_d}{2} = 1 \\ &P = \frac{2}{\bar{t}_d} \to \infty && \bar{t}_d \to 0 \end{aligned} \tag{1.34}$$

The quasi-static regime remains horizontal asymptote and it is modified as follows

$$\begin{aligned} &\bar{D}_m = 2, && P = \frac{1}{2} \\ &I = \frac{P\bar{t}_d}{2} \to \infty && \bar{t}_d \to \infty \end{aligned} \tag{1.35}$$

Figure 1.16 shows the P-I diagram for the elastic system. The three previously defined loading regimes can be identified in this figure. The vertical asymptote is the impulsive regime and has a limiting value of 1.0. The horizontal asymptote is the quasi-static regime and has a limiting value of 0.5. The transition curve is the dynamic regime connecting the two asymptotes.

P-I diagrams can also be developed using the energy balance method (Baker et al. 1983). The impulsive asymptote can be obtained by equating the total strain energy stored in the system at its maximum response to the kinetic

energy imparted to the system. On the other hand, the quasi-static asymptote can be obtained by equating the work done by load to the total strain energy gained by the system. Expressing these approaches mathematically

$$\text{K.E. = S.E. impulsive asymptote,} \tag{1.36}$$

$$\text{W.E. = S.E. quasi-static asymptote} \tag{1.37}$$

where K.E. is the kinetic energy of the system at time zero, S.E. is the strain energy of the system at maximum displacement, and W.E. is the work done by the load to displace the system from rest to its maximum displaced position. For the case of elastic system, the energy expressions are given by

$$K.E. = \frac{I^2}{2M} \tag{1.38}$$

$$W.E. = F_m y \tag{1.39}$$

$$S.E. = \frac{1}{2} K y^2 \tag{1.40}$$

Baker et al. (1983) recommended the following hyperbolic tangent relationship to connect the impulsive asymptote to quasi-static asymptote

$$S.E. = W.E. \tanh^2 \left(\frac{K.E.}{W.E.} \right)^{1/2} \tag{1.41}$$

Baker et al. (1983) reported that less than 1% error is introduced when the pervious approximation is used to obtain the transition regime for the elastic system. Figure 1.16 shows also a comparison between the P-I diagram based on the energy balance method and SDOF system. The figure shows that hyperbolic tangent relationship gives a good approximation for the P-I diagram for the elastic system.

1.5.3.2.1.5 Pressure-impulse diagram for elastic-plastic system

The P-I for elastic perfectly plastic SDOF system were developed by Li and Meng (2002b). The material model was assumed as bilinear resistance function. They used the inverse ductility ratio α, i.e. the ratio of maximum elastic displacement

y_{el} to the maximum displacement y_{m}, as a deformation criterion. Thus, the inverse ductility ratio can be written as

$$\alpha = \frac{y_{el}}{y_{\mathrm{m}}} \tag{1.42}$$

Figure 1.17 shows the P-I diagram for an elastic-plastic SDOF using the dimensionless parameters of P and I (Eq. 1.35) for various α values (Li and Meng 2002b). The difference between the curves increases with increased α values, but the difference is less between the curves in the quasi-static regime compared to the impulsive regime. The P-I diagram for elastic-plastic system can also be obtained using energy balance method. The energy parameters for the system are as follows

$$K.E. = \frac{I^2}{2M} \tag{1.43}$$

$$W.E. = F_m y \tag{1.44}$$

$$S.E. = \frac{1}{2} K y_{el}^{\ 2} + K y_{el}(y_m - y_{el}) \tag{1.45}$$

Figure 1.17 shows also a comparison between P-I obtained from the SDOF analysis and the ones obtained from the hyperbolic approximation proposed by Baker et al. (1983). Again, good agreements can be observed for different ductility ratios.

1.5.3.2.1.6 Effect of axial load

The response of laterally loaded steel members is greatly affected by the magnitude of axial load as it affects the lateral bending stiffness, bending moment, displacement, and frequencies of vibration. This interaction between the two loads is commonly known as *P*-δ effect.

The axial load P magnifies the maximum deflection and moment. For an elastic and simply supported column of length L that is subjected to a uniform

static load q, mid-span displacement and moment are given by (Timoshenko and Gere 1961)

$$\delta_{z=L/2} = \frac{5qL^4}{384EI}\left[\frac{12(2\sec(u)-2-u^2)}{5u^4}\right] \tag{1.46}$$

$$M_{z=L/2} = \frac{qL^2}{8}\left[\frac{2(1-\cos(u)}{u^2\cos(u)}\right] \tag{1.47}$$

where $u = \frac{\pi}{2}\sqrt{\frac{P}{P_{cr}}}$, $P_{cr} = \frac{\pi EI}{L^2}$ is the Euler elastic buckling load, and EI is the flexural rigidly of the steel column. The factor outside the square brackets in each equation represents the response due to the lateral load while the term within the brackets is an amplification factor that accounts for the secondary moment (P-δ) due to axial load. The above equations can be approximated by

$$\delta = \frac{5qL^4}{384EI}\left[\frac{1}{1-P/P_{cr}}\right] \tag{1.48}$$

and

$$M = \frac{qL^2}{8}\left[\frac{1}{1-P/P_{cr}}\right] \tag{1.49}$$

If P/P_{cr} is less than 0.6, the error in the approximate expressions is 2% (Timoshenko and Gere, 1961). The above equations show that the lateral stiffness, defined as $K = qL/\delta$, approaches zero as the load P approaches the critical buckling load P_{cr}.

In dynamic response, the frequencies are affected by the axial load. The frequencies for nth mode of vibration for a simply supported column with axial load P is given by (Bazant and Cedolin 1991)

$$f_n = \frac{n^2\pi}{2L^2}\sqrt{\frac{EI}{m}}\sqrt{1-\frac{P}{n^2P_{cr}}} \qquad n=1, 2, 3,\ldots \tag{1.50}$$

where m is the mass per unit length. The first factor is the frequency for member in the absence of the axial load while the term in brackets accounts for the axial load. The above equation shows that the fundamental frequency decreases as P/P_{cr} increases, or, in other words, the increase of the axial load leads to elongation of member natural period. The fundamental frequency goes to zero as P approaches P_{cr}. The effect of the axial load on the higher frequencies, however, is less significant. For instance, an axial load of P/P_{cr} =0.9 reduces the frequency of first mode by 70% while it reduces the third frequency mode by only 5%.

1.5.3.2.2 Finite Element Modelling (FEM)

Finite element modelling (FEM) is considered a robust tool to perform nonlinear dynamic analysis of structures with complex geometry, loading, and boundary conditions and it is capable of handling both geometric and material nonlinearities. Furthermore, the effect of the strain rate, axial load, and strain hardening can be included in the dynamic analysis. At least three commercial finite element softwares are available to model the behaviour of structures under blast load, including ABAQUS (Hibbett Karlsson and Sorenson, 2000), AUTODYNE (Century Dynamics, 2003), and LS-DYNA ((Hallquist, 2006 and LSTC. 2007).

1.5.3.2.3 Dynamic models in the literature

Symonds (1980) derived SDOF formulation for a clamped-clamped beam subjected to impulsive loading and constrained against axial displacement. SDOF technique allowed axial tension to develop during the response. The study divided the response into three phases: elastic; rigid-plastic with small displacements; and rigid-plastic with large displacements. The axial tension was neglected during the elastic and rigid-plastic, small displacement phases. However, the axial force was significant for large deflections as membrane action took over. The results were compared with test data of impulsively loaded beams and showed good

agreement. The study showed that the rigid plastic model gives poor results when the ratio of initial kinetic energy of the pulse to the total elastic energy capacity is less than six. This suggested that the elastic strain energy should be included in column analysis when the ratio is in this range.

Shope (2006) presented detailed derivation of two SDOF approaches that included the effects of the axial loading in the impulsive response of W-section steel columns. The first approach used a bilinear resistance function based on the assumption of sudden formation of plastic hinges during the response. The resistance function was derived in general form with different boundary conditions and failure modes. The second SDOF approach introduced a nonlinear resistance function accounting for gradual yielding in the member during the dynamic response. The effect of the strain rate was not considered in these approaches. Both SDOF models were compared with finite element model results and the comparison indicated that the nonlinear SDOF and finite element model were in good agreement, while a lack of agreement was observed between bilinear and finite element model. The study attributed this deviation to the strain energy overestimation of bilinear SDOF model.

The inelastic response of beams under combined axial load and lateral dynamic load was investigated by Rao and Raghavan (1987) using the finite element method. Uniform impulse loads were modelled as short duration pulse loads acting for a duration of one-tenth of the fundamental period of the member. They recommended that the influence of the compressive axial load should be included when its magnitude exceeds ten percent of the critical buckling load. They found that for any given axial load, there exists a certain lateral load beyond which the response would be unbounded.

The finite element software ABAQUS (2004) was used by Shope (2006) to model the W-section steel column subjected to constant axial and lateral blast loads. The response and plastic hinge formations with different level of axial loads, slenderness ratios, and boundary conditions were investigated. Major axis,

minor axis, and biaxial bending were examined in this study. The study only focused on impulse blast loading with short duration (impulsive regime). The concept of critical impulse was introduced in this study. The critical impulse is an impulse that causes either the column to collapse or exceeding the deflection limit. The results for each column configuration were presented as a set of curves showing the critical impulse versus the axial load. The critical impulse significantly decreased with the increase of the axial load level.

Recently, Lee et al. (2009) used LS-DYNA (2005) software to simulate the blast loads based on computational fluid dynamics (CFD). The software was used also to model the W-shaped steel columns. The simulated blast load profile was compared with those obtained from available blast load softwares CONWEP (Hyde, 1990) and ATBLAST (2007). Similar results were obtained for the peak pressures and durations, while CFD model had a significant rise time compared to the almost negligible rise time assumed in CONWEP and ATBLAST. Difference in the reflected impulse distribution along the column was also observed. The authors attributed the discrepancy in the pressure time profile and the impulse distribution to the difference in surface rigidities of the two models, as the web surface of the CFD model had more flexibility than the rigid surface assumed by ATBLAST and CONWEP. The response of three column sizes with different boundary conditions was obtained based on CFD simulation blast load and CONWEP load.

The P-I diagrams for elastic and elastic-perfectly-plastic SDOF systems were conducted by Li and Meng (2002a; 2002b) for three different pulse loading shapes: rectangular, linear decaying (triangular), and exponential decaying. In the dynamic regime, they showed that the P-I curves are sensitive to the pulse shape. Empirical equations were also proposed to generate the P-I curves taking into account the pulse shape and inverse ductility ratios. The effect of material hardening and softening on P-I diagrams are described in Fallah and Louca (2007). The hardening and softening index was introduced to generalize the

solutions. Parametric studies were conducted on the effect of the inverse ductility and hardening and softening index on P-I diagrams. Recently, P-I diagrams for combined failure modes of rigid plastic beams was proposed by Ma et al. (2007). In this study, closed-form solutions for P-I diagrams of simply supported and fully clamped rigid-plastic beams subjected to a rectangular pulse were developed.

Although some of the above-mentioned design approaches and numerical techniques are widely relied on, there is lack of detailed empirical data from actual blast tests on full scale steel members to corroborate their predictions, especially when the response over the inelastic range is concerned. For instance, it is important that phenomena such as spatial and temporal variation of member strains be captured during the tests and compared with their predicted variations, in order to confirm that the simple displacement function assumed in the derivation of SDOF models yields a sufficiently accurate representation of the strain variation.

1.5.3.3 Current design approaches

1.5.3.3.1 Beams

The Technical Manual UFC 3-340-02 (USDOD 2008) has adopted the SDOF method presented in Biggs (1964) for the design of beams. The strain rate effect is considered in the design by scaling up the yield stress by a constant value and in most cases; it is assumed that the beam will experience plastic deformation. The design procedure involves computing the SDOF response and limiting the maximum deflection to some limiting value. This limiting criterion is defined in terms of maximum rotation at the end supports maximum and maximum ductility ratio. A maximum ductility ratio of 10 and a maximum support rotation of two degrees are prescribed for structures where safety of personnel and equipment are concerned.

1.5.3.3.2 Columns

According to UFC 3-340-02 (USDOD 2008), the resistance of a beam column subjected to combined axial load and bending about the x-axis can be calculated using the following interaction formulas, provided all other failure modes are prevented

$$\frac{P}{P_u}+\frac{C_{mx}M_x}{M_{px}\left(1-\frac{P}{P_{ex}}\right)}\le 1.0 \tag{1.51}$$

$$\frac{P}{P_P}+\frac{M_x}{1.18M_{Px}}\le 1.0 \text{ for } \frac{P}{P_P}\ge 0.15 \tag{1.52}$$

$$\frac{M_x}{M_{Px}}\le 1.0 \text{ for } \frac{P}{P_P}\le 0.15 \tag{1.53}$$

Equations (1.52) and (1.53) neglect the *P-δ* effect which means that they are based on the assumption that column failure is instigated by the section reaching its full plastic capacity without experiencing instability. Equation (1.53) permits neglecting the effect of axial load on the column resistance for values of $P/P_p \le$ 0.15. These requirements are identical in form to those in AISC (1994) for beam columns under static loads, but the moment M_x in the case of blast loads must be obtained from a dynamic analysis and the maximum resistance or capacity of the section must be calculated based on its dynamic material properties. The term $C_m/(1-P/P_e)$ is the moment magnification factor (MMF) and it accounts for the for the *P-δ* effect. Equations (1.51) to (1.53) cannot be applied to columns with μ > 1.0 because they are derived based on the assumption of $\mu \le 1.0$. In the derivation of all three equations, it is implicitly assumed that the column flexural stiffness is constant and equal to its elastic stiffness. In the ASCE Standard (2011), for beam columns with compact section maximum ductility ratio of 3 is permitted while for non-compact sections it is limited to 0.85. Therefore, the problem arises when the UFC formulas are applied to compact sections with $\mu >$ 1.0. This issue will be addressed in this thesis.

1.5.4 Experimental blast tests for steel members

Based on the information available in the open literature, most research programs and government sponsored tests have focused on understanding the response of reinforced concrete and masonry structures to blast loading (Magnusson 2007; Schenker et al. 2008; Oesterle et al. 2009). The response of Fibre Reinforced Polymer (FRP) retrofitted concrete structure and masonry structures to blast loading has been also experimentally investigated (Davidson et al. 2004; Razaqpur et al. 2007; Tan and Patoary 2009; Wu et al. 2009). Magallanes et al. (2006) investigated the behaviour of a W360X347 column with a clear height of 5730 mm (18'-9") subjected to 1818 kg (4000 pounds) of TNT-equivalent ANFO with a ground stand-off distance of 4750 mm (15'-6"). Only the peak residual deformation of the column above its base in the strong axis direction was reported after the test. Detailed experimental data for steel members subjected to blast loading is lacking partly due to security concerns in some countries and the desire to limit the dissemination of such information and partly due to the difficulty of obtaining reliable and detailed data in blast tests which are inherently destructive and make it difficult to protect the instrumentation (Jama et al. 2009). This lack of detailed experimental data makes it difficult to judge the validity and/or limitations of the assumptions made in various theoretical and numerical models. However, detailed data is necessary to validate the common assumptions in blast analysis by all types of models, particularly in SDOF model, which are inherently simple and yet most commonly used in practice.

In the light of the above state the art, the objective of this thesis is to perform blast tests on full scale steel beams and columns specimens using explosives in order to capture their dynamic response with a relatively large array of instruments. The observed responses will be compared with predictions of both SDOF and MDOF models to check some of the assumptions in the formulations of the models used in these types of analyses.

1.6 References

ASCE. (2011). "Blast Protection of Buildings: ASCE/SEI 59-11." American Society of Civil Engineers.

ASCE. (1997). "Design of blast resistant buildings in petrochemical facilities." Task Committee on Blast Resistant Design, ASCE, New York.

AISC. (1994). "Manual of steel construction. Load and resistance factor design (LRFD)." American Institute of Steel Construction, Chicago, IL.

Aspden, R. J., and Campbell, J. D. (1966). The effect of loading rate on the elasto-plastic flexure of steel beams." Proceedings of the Royal Society of London. Series A, Mathematical and Physical Sciences, 290(1421), 266-285.

ATBLAST. (2007). "A computer software by Protective Glazing Council." Applied Research Associates (ARA), Inc., USA.

Baker, W. E. (1973). "Explosions in air." University of Texas Press, Austin,.

Baker, W. E., Cox, P. A., Westine, P. S., Kulesz, J. J., and Strehlow , R. A. (1983). Explosion hazards and evaluation, Elsevier Scientific Pub. Co., Amsterdam; New York.

Bassim, N. and Panic, N. (1999). "High strain rate effects on the strain of alloy steels." Journal of Material Processing Technology, 92-93, 481-485.

Bazant, Z. P., and Cedolin, L. (1991). "Stability of structures: elastic, inelastic, fracture, and damage theories." Oxford University Press, New York.

Biggs, J. M. (1964). "Introduction to structural dynamics." McGraw-Hill Book Company, New York.

Bischoff, P., and Perry, S. (1991). "Compressive behaviour of concrete at high strain rates." Materials and Structures, 24(6), 425-450.

Campbell, J. D., and Duby, J. (1956). "The Yield Behaviour of Mild Steel in Dynamic Compression." Proceedings of the Royal Society of London. Series A, Mathematical and Physical Sciences, 236(1204), 24-40.

Century Dynamics Ltd. (2003). "2-D and 3-D user's manual." Horsham, UK.

Chopra, A. K. (2001). Dynamics of structures : theory and applications to earthquake engineering, Prentice Hall, Upper Saddle River, NJ.

CISC. (2011). "Handbook of steel construction, Canadian Institute of Steel Construction." Willowdale, Canada.

Davidson, J. S., Porter, J. R., Dinan, R. J., Hammons, M. I., and Connell, J. D. (2004). "Explosive testing of polymer retrofit masonry walls." Journal of Performance of Constructed Facilities, 18(2), 100-106.

Jama, H. H., Bambach, M. R., Nurick, G. N., Grzebieta, R. H., and Zhao, X. L. (2009). "Numerical modelling of square tubular steel beams subjected to transverse blast loads." Thin-Walled Structures, 47(12), 1523-1534.

Fallah, A. S., and Louca, L. A. (2007). "Pressure-impulse diagrams for elastic-plastic-hardening and softening single-degree-of-freedom models subjected to blast loading." International Journal of Impact Engineering, 34(4), 823-842.

Goldsmith, W. (1960). "Impact: the theory and physical behaviour of colliding solids." E. Arnold, London.

Hallquist, J.O. (2006). "Ls-Dyna theory manual." Livermore Software Technology

Henrych, J. (1979). "The dynamics of explosion and its use." Elsevier Scientific Publishing Company, New York, USA.

Hibbett Karlsson and Sorenson Inc. (2000). "Getting started with ABAQUS/explicit." Version 6.1.

Hyde, D.W., 1990. "Conventional weapons effect (CONWEP)." Application of TM5-855-1. US Army Engineer Waterways Experiment Station, Vicksburg, USA.

Itabashi, M. and Kawata, K. (2000). "Carbon content effect on high-strain-rate tensile properties for carbon steels." International Journal of Impact Engineering, 24(2), 117-131.

Jarrett, D. E. (1968). "Derivation of the British explosives safety distances." Ann. NY Acad. Sci., 152(1), 18-35.

Jones, N. (1988). "Structural impact." Cambridge University Press, Cambridge ; New York.

Krafft, J. M., Sullivan, A. M., and Tipper, C. F. (1954). "The effect of static and dynamic loading and temperature on the yield stress of iron and mild steel in compression." Proceedings of the Royal Society of London. Series A, Mathematical and Physical Sciences, 221(1144), 114-127.

Lamarche, C. and Tremblay, R. (2011). " Seismically induced cyclic buckling of steel columns including residual-stress and strain-rate effects" Journal of Constructed Steel Research, 67(9), 1401-1410.

Lee, K., Kim, T., and Kim, J. (2009). "Local response of W-shaped steel columns under blast loading." Structural Engineering and Mechanics, 31(1), 25-38.

Li, Q. M., and Meng, H. (2002a). "Pressure-impulse diagram for blast loads based on dimensional analysis and single-degree-of-freedom model." Journal of Engineering Mechanics, 128(1), 87-92.

Li, Q. M., and Meng, H. (2002b). "Pulse loading shape effects on pressure-impulse diagram of an elastic-plastic, single-degree-of-freedom structural model." International Journal of Mechanical Sciences, 44(9), 1985-1998.

LSTC. (2007). "Ls-Dyna keyword user's manual. Version 971." Livermore Software Technology Corporation (LSTC), Livermore, California.

Ma, G. W., Shi, H. J., and Shu, D. W. (2007). "P-I diagram method for combined failure modes of rigid-plastic beams." International Journal of Impact Engineering, 34(6), 1081-1094.

Magallanes, J. M., Martinez, R., and Koening, J. (2006). "Experimental results of the AISC full-scale column blast test. Report TR-06-20.2," The American Institute of steel construction, Chicago.

Magnusson, J. (2007). "Structural concrete elements subjected to air blast loading." PhD Thesis, Royal Institute of Technology, Sweden.

Malvar, L. J. (1998). "Review of static and dynamic properties of steel reinforcing bars." ACI Materials Journal, 95(5), 609-616.

Manjoine, M. J., and Pittsuburgh, E. (1944). "Influence of rate of strain and temperature on yield stresses of mild steel." Journal of Applied Mechanics, 11, 211-18.

Mays, G. C., and Smith, P. D. (1995). "Blast effects on buildings: design of buildings to optimize resistance to blast loading. " Thomas Telford, London.

Oesterle, M. G., Hegemier, G. A., and Morrill, K. B. "Response of concrete masonry walls to simulated blast loads. " Austin, Texas, 140-140.

Prugh, R.W. (1999). "The effects of explosive blast on structures and personnel" Process Safety Progress 18(1), 5-16

Rao, S. S., and Raghavan, K. S. (1987). "Finite-element dynamic inelastic analysis of beams and plates under combined loading." Computers & Structures, 25(3), 355-364.

Rawlings, B. (1963). "The dynamic behaviour of mild steel in pure flexure." Proceedings of the Royal Society of London. Series A, Mathematical and Physical Sciences(275), 528-43.

Razaqpur, A.G., Tolba, A., and Contestabile, E. (2007) "Blast loading response of reinforced concrete panels reinforced with externally bonded GFRP laminates." Composites Part B: Engineering, 38(5-6), 535-546.

Schenker, A., Anteby, I., Gal, E., Kivity, Y., Nizri, E., Sadot, O., Michaelis, R., Levintant, O., and Ben-Dor, G. (2008). "Full-scale field tests of concrete slabs subjected to blast loads." International Journal of Impact Engineering, 35(3), 184-198.

Shope, R. L. (2006). "Response of wide flange steel columns subjected to constant axial load and lateral blast load." Virginia Polytechnic Institute, Virginia, USA.

Smith, P. D., and Hetherington, J. G. (1994). "Blast and ballistic loading of structures." Butterworth-Heinemann, Oxford; Boston.

Soroushian, P., and Choi, K.-B. (1987). "Steel mechanical properties at different strain rates." Journal of Structural Engineering, 113(4), 663-672.

Symonds, P. S. (1980). "Finite elastic and plastic deformations of pulse loaded structures by an extended mode technique." Int. J. Mech. Sci., 22, 597-605.

Tan, K. H., and Patoary, M. K. H. (2009). "Blast Resistance of FRP-strengthened masonry walls. I: approximate analysis and field explosion tests." Journal of Composites for Construction, 13(5), 422-430.

Timoshenko, S.P., and Gere, J.M. (1961). "Theory of elastic stability." McGraw-Hill Inc., New York.

USDOD, (2008). "Structures to resist the effects of accidental explosions." Document No. UFC 3-340-02. US Department of Defense (USDOD), Washington, DC.

Wu, C., Oehlers, D. J., Rebentrost, M., Leach, J., and Whittaker, A. S. (2009). "Blast testing of ultra-high performance fibre and FRP-retrofitted concrete slabs." Engineering Structures, 31(9), 2060-2069.

Table 1.1: Conversions factors for common explosives (Baker et al. 1983)

Explosive	**Mass specific energy Qs (KJ/Kg)**	**TNT equivalent (Qs/Q_{TNT})**
Compound B (60% RDX, 40% TNT)	5190	1.148
RDX (Cyclonite)	5360	1.185
HMX	5680	1.256
Nitroglycerine (liquid)	6700	1.481
TNT	4520	1.000
ANFO	3228	0.670
Blasting Gelatine	4520	1.000
Semtex	5660	1.250

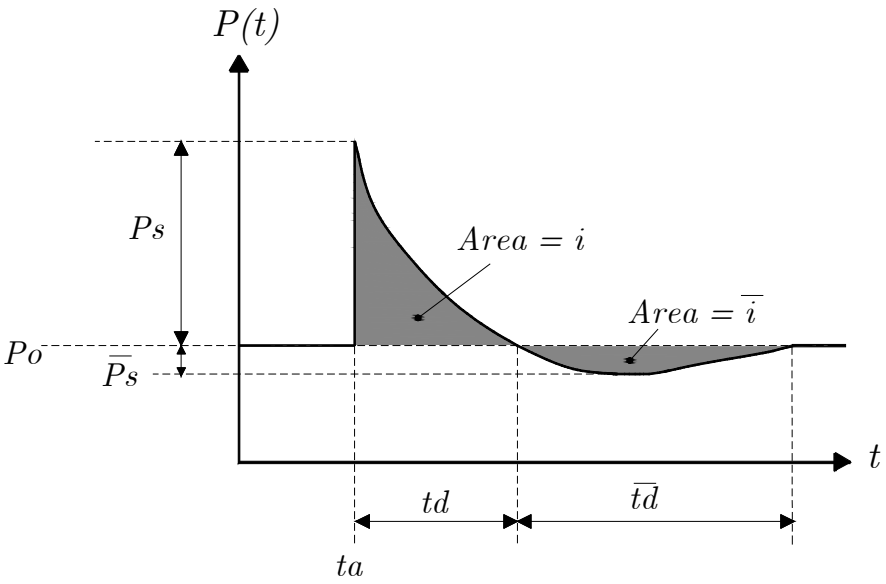

Fig. 1.1: Blast wave pressure time profile (USDOD 2008)

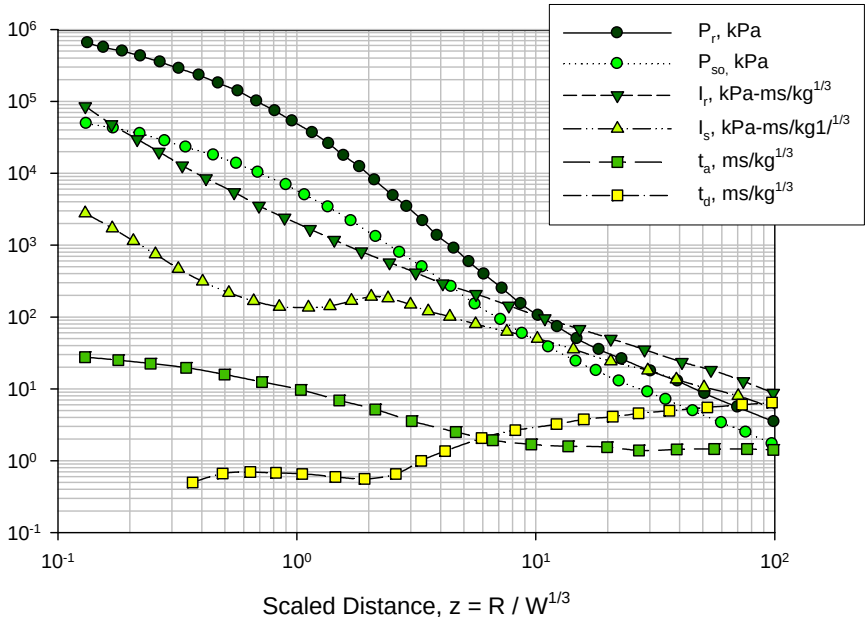

Fig. 1.2: Surface blast parameter as a function of scaled-distance profile (USDOD 2008)

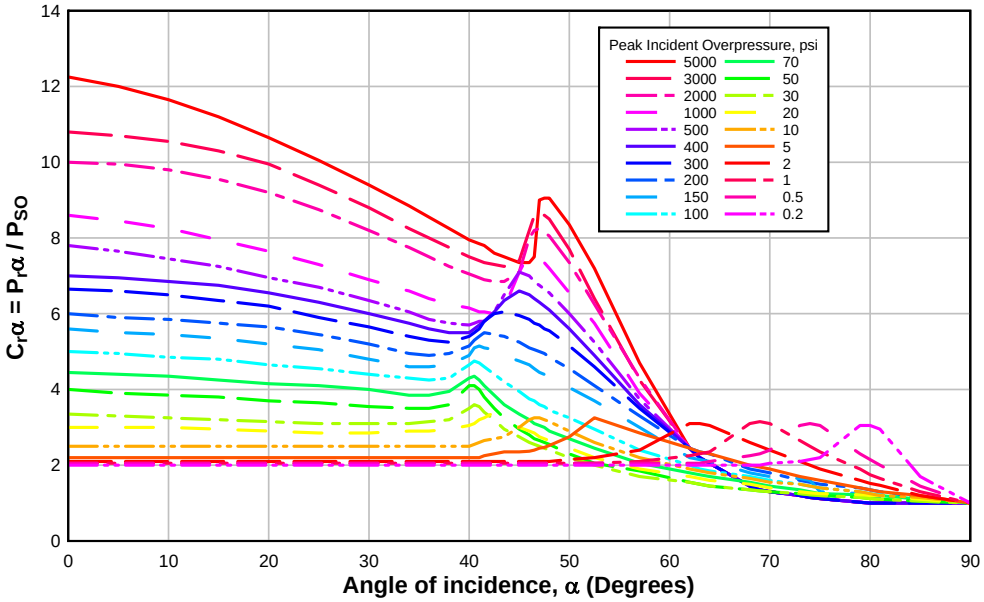

Fig. 1.3: Reflection coefficient versus angle of incidence for a detonation (USDOD 2008)

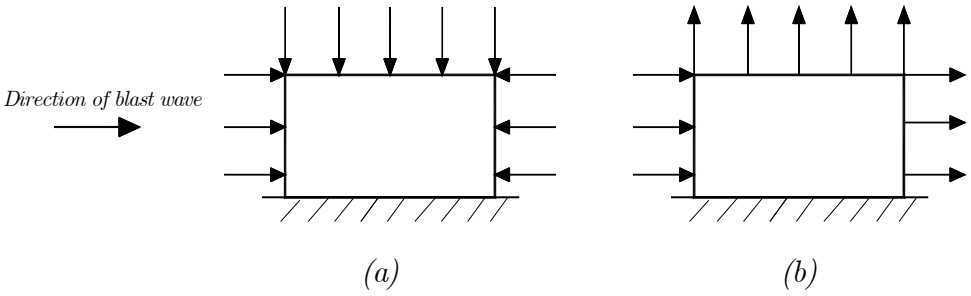

Fig. 1.4: Effect of (a) overpressure, and (b) dynamic pressure on structure

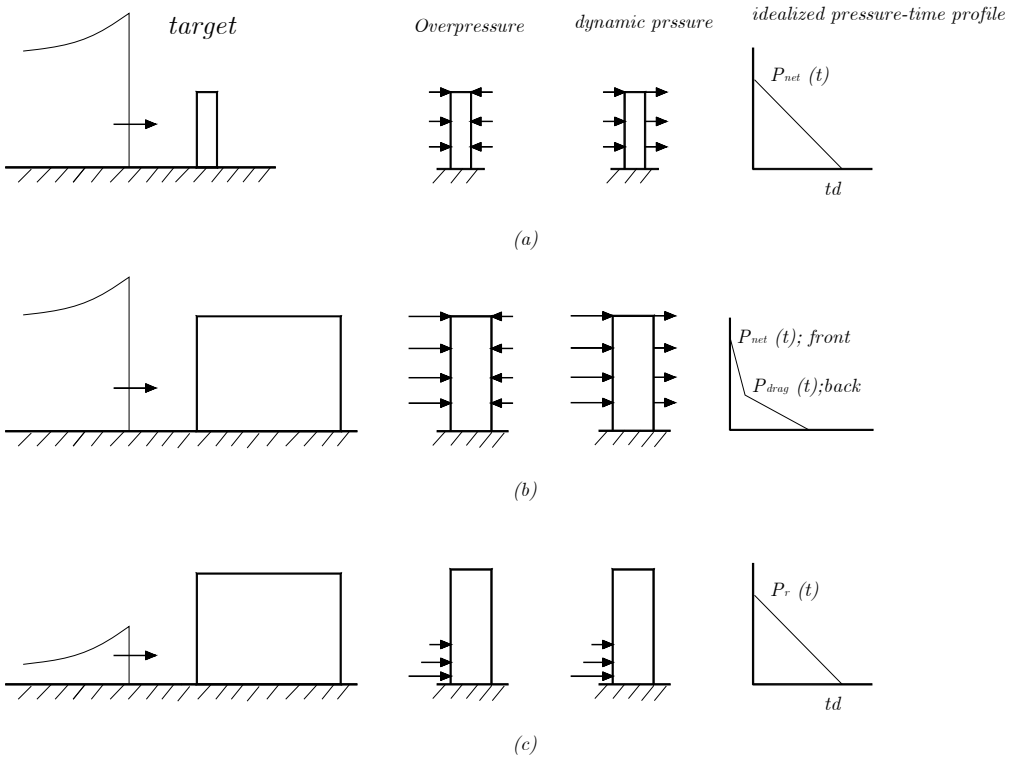

Fig. 1.5: Blast-structure interaction

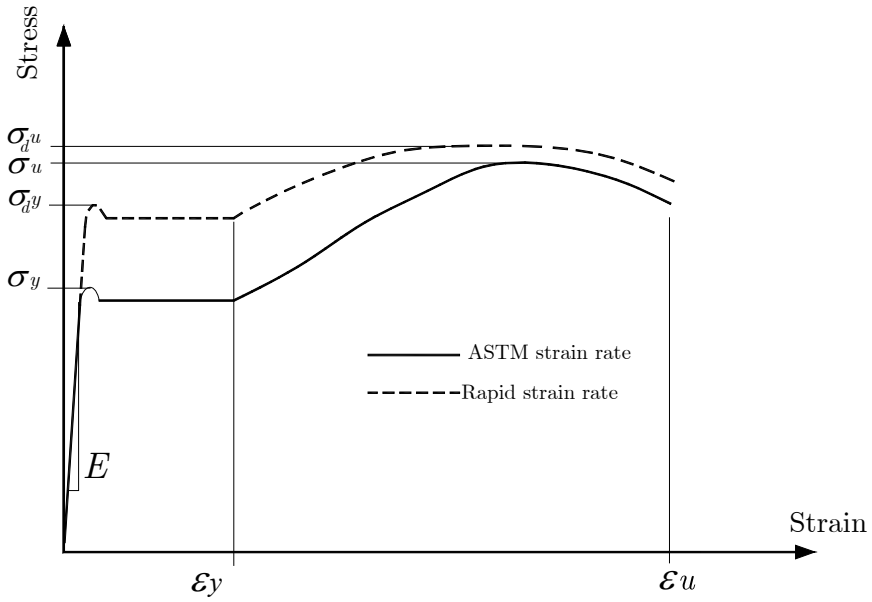

Fig. 1.6: Effect of strain rate for low carbon steel (USDOD 2008)

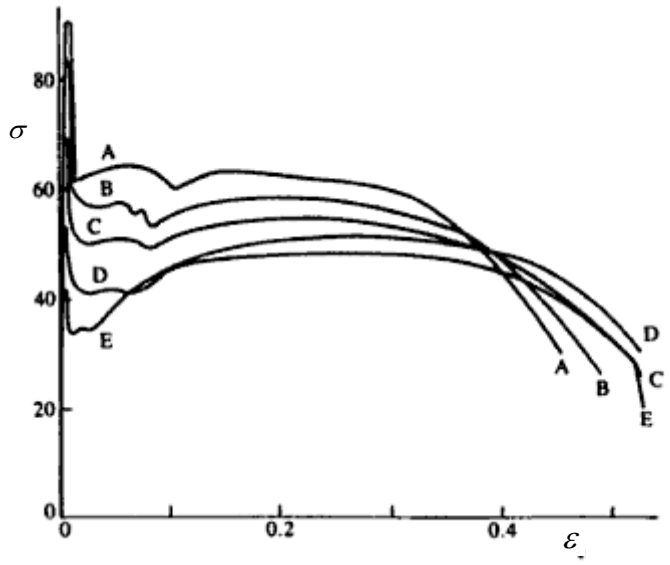

Fig. 1.7: Dynamic tensile on mild steel at various strain rates. A: $\dot{\varepsilon}$ =106 s^{-1}, B: $\dot{\varepsilon}$ =55 s^{-1}, C: $\dot{\varepsilon}$ =2 s^{-1}, D: $\dot{\varepsilon}$ =0.22 s^{-1}, E: $\dot{\varepsilon}$ =0.001 s^{-1} (Jones 1988)

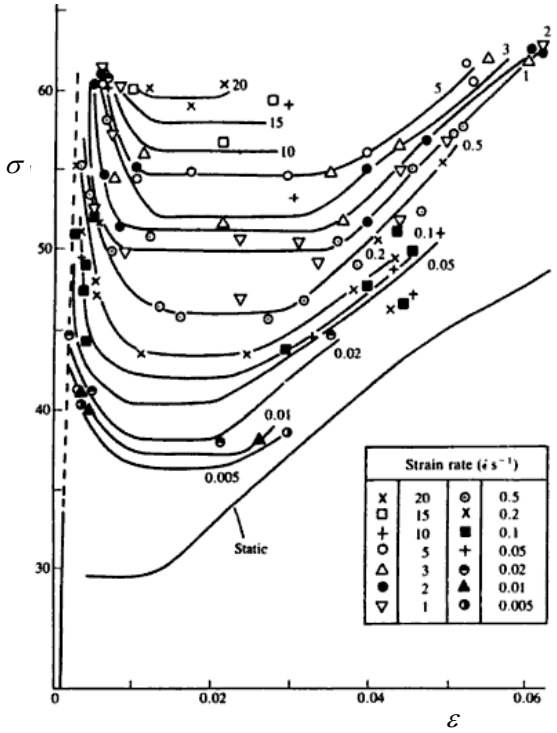

Fig. 1.8: Stress-strain curves for mild steel at various uni-axial compressive strain (Jones 1988)

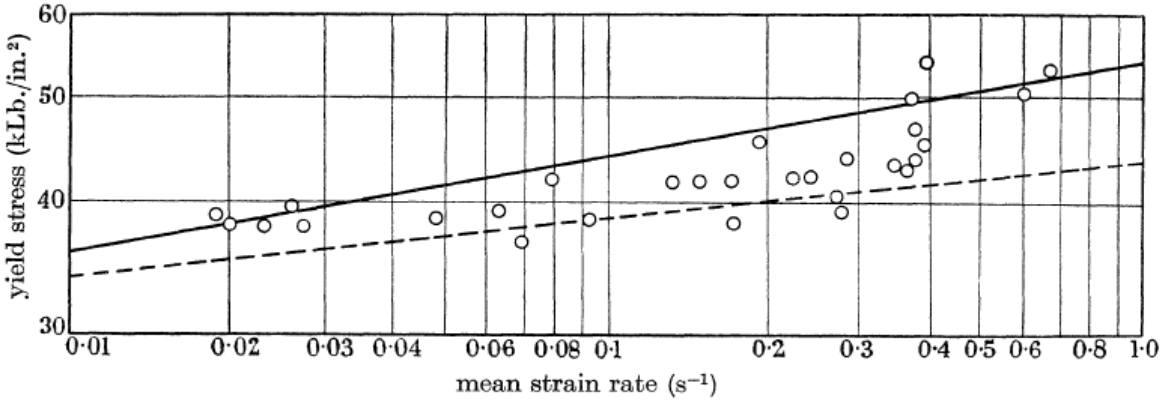

Fig. 1.9: o, Lower yield stresses from dynamic tests (Rawlings 1963); dashed line results of Manjoine and Pittsuburgh (1944); solid line, results of other investigators.

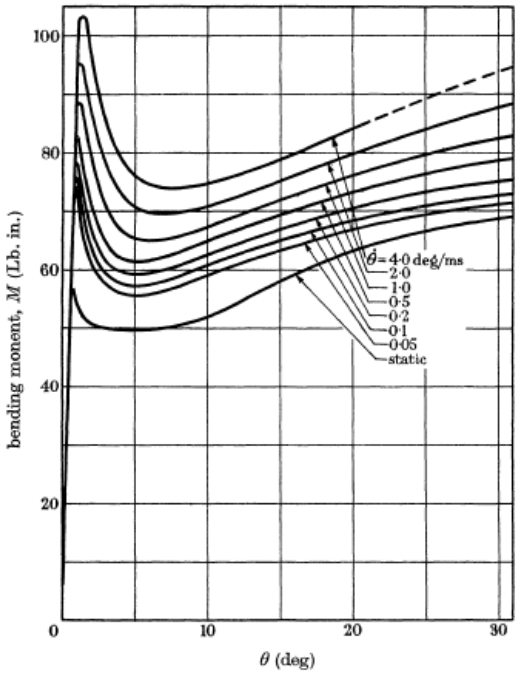

Fig. 1.10: Dynamic bending moment-rotation curves for different values of rotation rates (Aspden and Campbell 1966)

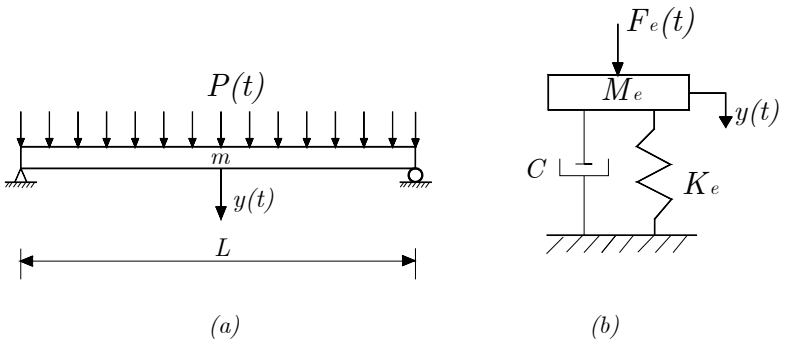

Fig. 1.11: Equivalent SDOF system, (a) real structure, (b) equivalent system

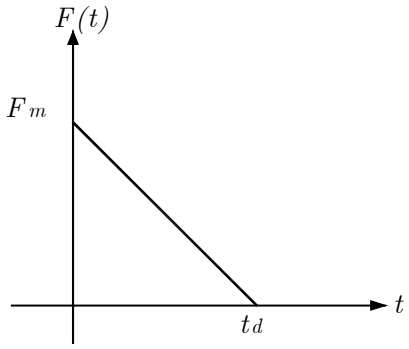

Fig. 1.12: Idealized blast pressure profile

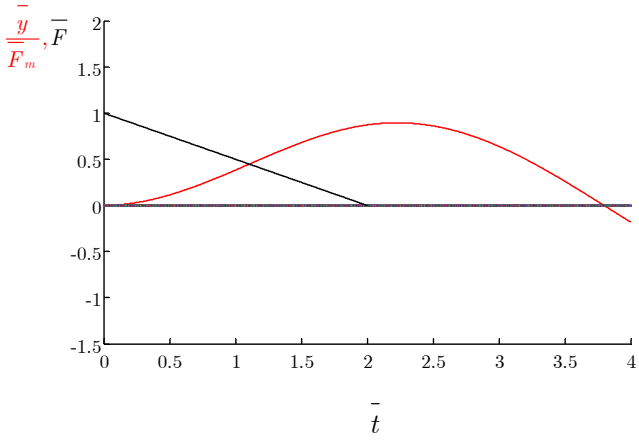

(a) $\bar{t}_d = 2$

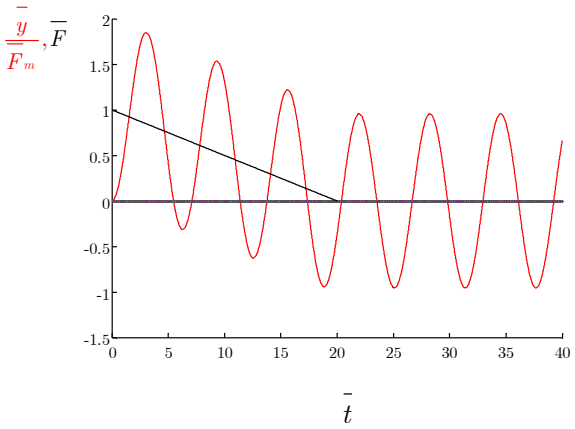

(b) $\bar{t}_d = 20$

Fig. 1.13: SDOF response to idealized triangular load for different $\bar{t}_d$

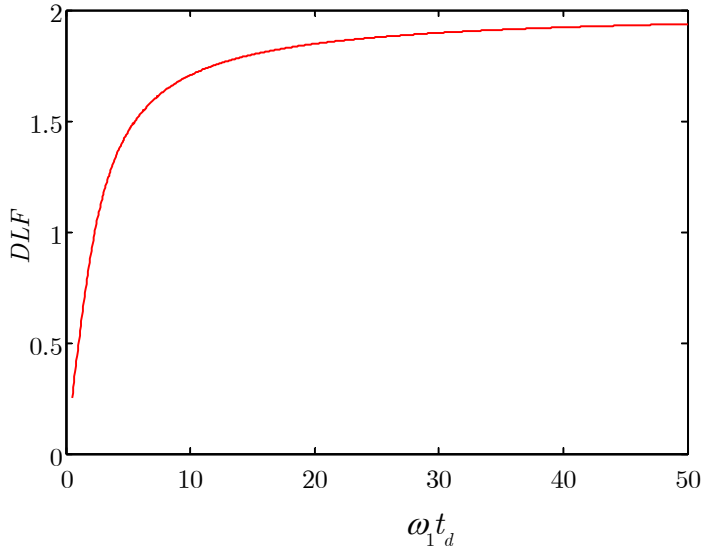

Fig. 1.14: DLF-$\overline{t}_d$ diagram for triangular pulse

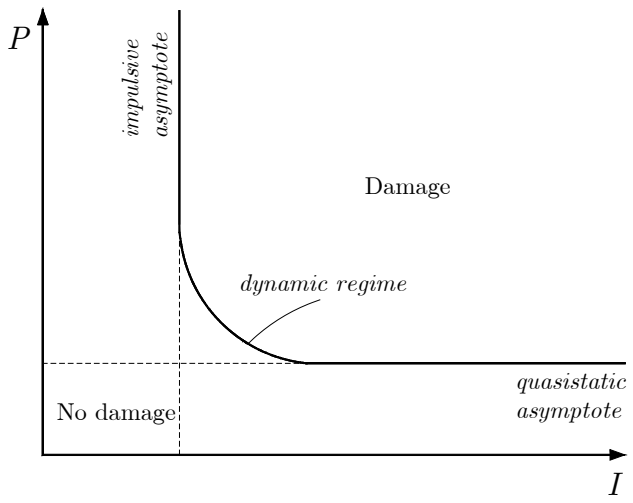

Fig. 1.15: Sketch of a typical pressure-impulse diagram

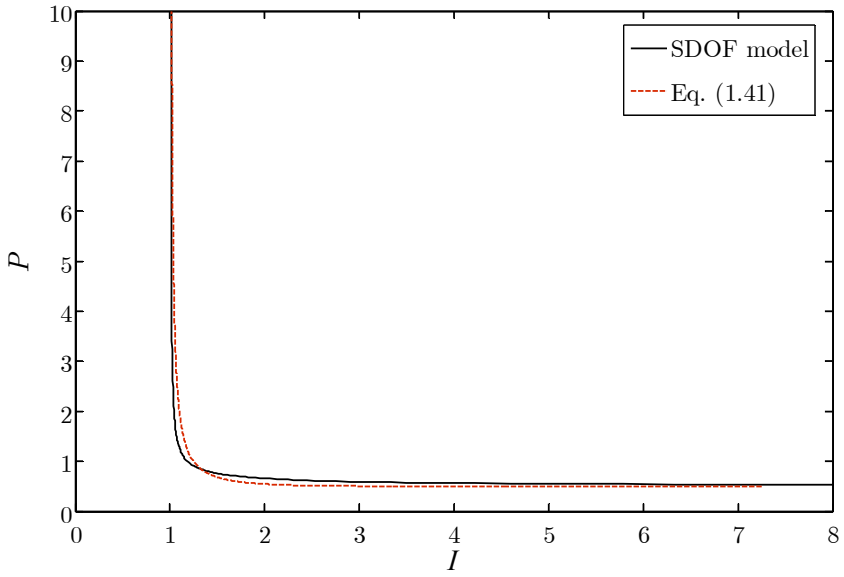

Fig. 1.16: Comparison of P-I diagram for elastic system between the SDOF system and hyperbolic tangent relationship approximation

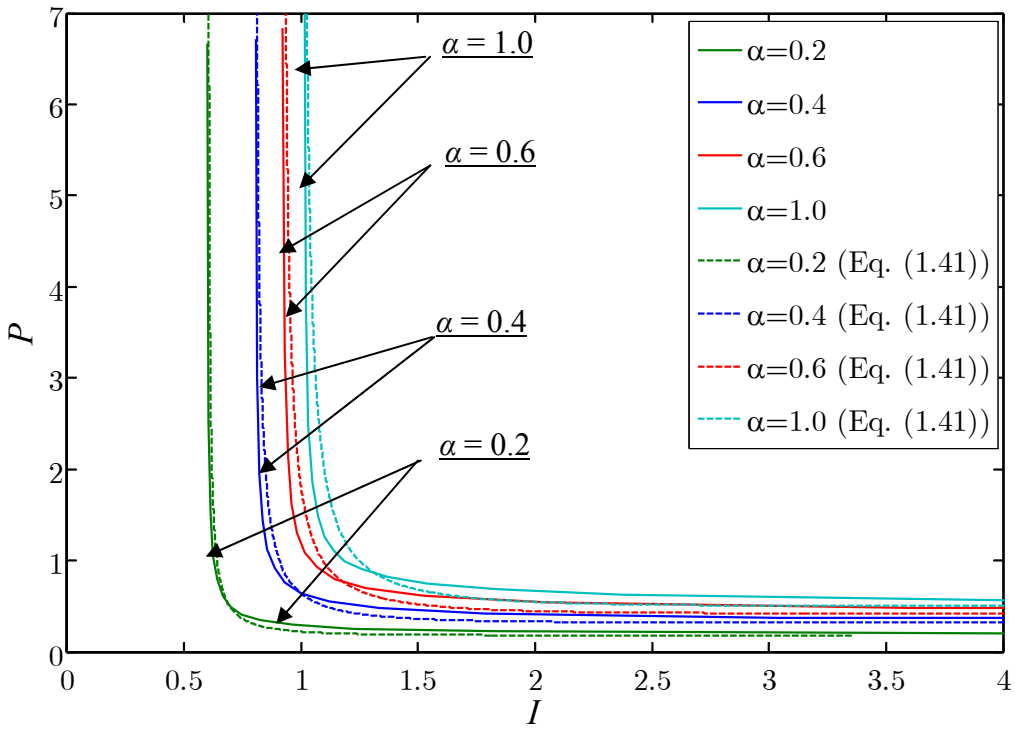

Fig. 1.17: Comparison of P-I diagram for elastic system between the SDOF system and hyperbolic tangent relationship approximation

Chapter 2: Experimental Performance of Steel Beams under Blast Loading

2.1 Abstract

In this study the dynamic response of typical wide-flange steel beams was experimentally evaluated under blast loading. A total of thirteen beams were field tested using live explosives, where the charge size ranged from 50 to 250 kg of ANFO and the ground stand-off distance from 7.0 to 10.3 m. Blast wave characteristics, including incident and reflected pressures were recorded. In addition, time-dependant displacements, accelerations, and strains at different locations along the steel members were measured, and the post-blast damage and mode of failure of the test specimens were observed. The blast load characteristics were compared with those obtained using the Technical Manual UFC 3-340-02 results. The displacement response results were used to validate the results obtained from a nonlinear dynamic analysis based on Single-Degree-of-Freedom (SDOF) model. Results showed that the UFC 3-340-02 pressure predictions compare reasonably well with the measured pressure in the positive phase in terms of both the peak pressure and overall time variations. The SDOF model predicted reasonably well the maximum displacements of beams in the elastic range, but it overestimated them in the plastic range.

Keywords: Blast loads; Damage; Dynamics; Explosions; Steel beams; Strain rate; Field tests

2.2 Introduction

Recent world events have prompted the need for the examination of the behaviour of structures to blast and high impact loads. Modern steel buildings designed under the provisions of current codes, particularly lighter frame structures with non-moment resisting connections, may be incapable of maintaining structural integrity under severe blast loads. In addition, as a result of a blast risk assessment, some structures, such as embassy buildings, major commercial centres, important government buildings, and some critical industrial facilities, may require blast-resistant design. To ensure the safety of these structures, it is important to design them for levels of strength and ductility which would be adequate to resist the expected design-based threat level. The attainment of this goal requires the development of suitable blast-resistant design procedures and construction techniques.

Currently, practical blast-resistant design is generally based on simplified models involving Single-Degree-of-Freedom (SDOF) dynamic analysis. Many studies have been conducted over the years to investigate the dynamic analysis of structural members under blast loading, focusing on the prediction of the structural response by assuming the first mode of vibration to dominate the dynamic behaviour of these members (Biggs 1964; Krauthammer et al. 1986; Krauthammer et al. 1990; Boutros 2000; Schleyer and Hsu 2000). However, there is not sufficient empirical data available in the open literature to corroborate the generality of this assumption or its limitations, particularly in the inelastic and plastic deformation ranges. Other analytical and numerical models with various degrees of sophistication are also available to analyze the dynamic response of steel members under blast loading, but detailed experimental data needed to validate these methods are scarce in the open literature. Therefore, to validate theoretical and numerical models, it is important to obtain, through field tests, detailed quantitative load and response data using realistic structural members and blast loading scenarios.

To date, based on the information available in the open literature, most research programs and government sponsored tests have focused on understanding the response of reinforced concrete and masonry structures to blast loading (Magnusson 2007; Schenker et al. 2008; Oesterle et al. 2009). The response of Fibre Reinforced Polymer (FRP) retrofitted concrete structure and masonry structures to blast loading has been also experimentally investigated (Davidson et al. 2004; Razaqpur et al. 2007; Tan and Patoary 2009; Wu et al. 2009). However, there are fewer studies that have experimentally investigated the resistance of structural steel members under blast loading (Lawver et al. 2003). Despite the simple behaviour of steel members in pure bending, which can be modelled by an elasto-plastic resistance function, the effect of other blast related phenomena on their complete dynamic response still need investigations, e.g. the coupling of strain rate effect with global and local buckling (Liew 2008). Aspden and Campbell (1966) pointed out that the dynamic flexural behaviour of steel beams cannot be fully explained on the basis of the data from uni-axial compression tests, which would lead to strain rate dependent moment curvature diagrams largely different from those produced by dynamic bending tests. For instance, smaller values of the upper yield moment and constant moment resistance before work-hardening onset would be obtained. Magallanes et al. (2006) investigated the behaviour of a W360×347 column with a clear height of 5730 mm (18'-9") subjected to 1818 kg (4000 pounds) of TNT-equivalent ANFO with a ground stand-off distance of 4750 mm (15'-6"). Only the peak residual deformation of the column above its base in the strong axis direction was reported after the test. Generally, because of the destructive nature of blast testing, protecting the instrumentation, such as displacement transducers and accelerometers to record the full time-dependent response of test members is a difficult task; therefore, limited information is normally reported after the performance of such experiments (Jama et al. 2009). This makes it difficult to

compare in detail the results of analytical/numerical models with the corresponding quantities in the experiment.

Blast loads induce strain rate dependant stresses and deformations that differ in several respects from those caused by other types of dynamic loads, including seismic and wind loads. Several research investigations have been conducted to study the effect of strain rate caused by dynamic uni-axial tensile or compressive loads on the mechanical properties of steel (Manjoine and Pittsuburgh 1944; Krafft et al. 1954; Soroushian and Choi 1987; Malvar 1998; Bassim and Panic 1999). These studies have shown that, under high strain rate, the yield strength exhibits a noticeable increase, the ultimate tensile strength shows relatively smaller increase; while the elastic modulus generally remains insensitive to the strain rate. The Dynamic Increase Factor (DIF) is generally defined as the ratio of the steel dynamic strength to its static strength and it is typically used to account for the effect of the strain rate on the mechanical properties of steel. Different DIF formulations are given in the literature as a function of the strain rate using rate sensitive models (Jones 1988; Malvar 1998), which are based on experimental data obtained from uni-axial tensile tests of steel specimens under various strain rates. The use of the DIF to enhance the material strength in calculating the resistance of structural members is recommended by widely known design guidelines, which can be found in the Technical Manual UFC 3-340-02 (USDOD 2008), and in ASCE (1997). However, the DIF value suggested by these guidelines is based on averaged strain rates over a given cross-section, even though the actual strain rate profile varies over the depth of the section. The suggested values are independent of the actual strain rates that may be experienced by a member under a given blast scenario and are presumably conservative, but the degree of conservatism is not always evident. In reality the use of a fixed value might result in overestimating the effect of the strain rate, especially in the case of wide flange sections with a high web-area to flange-area ratio. In addition, the DIF is assumed to be constant for all sections along the

member length, without regard for the strain rate variation along the member, e.g. diminishing strain rate close to the ends of simply supported beams. This may result in unconservative design, particularly when designing for shear and/or end connections.

This paper describes full-scale blast tests on wide-flange steel beams. The first objective of these tests is to study the blast response of steel beams via the analysis of detailed time-dependant data records, including the displacements, strains, and accelerations measured during the different blast shots. The second objective is to examine the accuracy of the SDOF model used to model the flexural response of beams under blast loads by comparing its predictions with the experimental data obtained in these tests.

2.3 Experimental program

2.3.1 Field blast test

A total of thirteen steel beams, each with span length of 2413 mm (95 inches) were tested, Fig. 2.1(a). As shown in Fig. 2.1(b), two different section sizes, W150×24 and W200×71, were investigated, sizes that are typical of those used in steel buildings. Members of each section size were obtained from the same production batch to minimize variation in material properties. The static nominal yield stress and ultimate strength, as specified by the manufacturer, of the W150×24 section were 393 and 537 MPa, respectively, and those of the W200×71 section were 362 and 474 MPa, respectively. These sections conform to Canadian standard CSA G40.21 specifications and satisfy Class 1 section classification according to CAN/CSA-S16-09 standard (CISC 2011), a class that permits the attainment of the section plastic moment capacity prior to local failure due to flange or web buckling.

2.3.1.1 Test matrix

Each beam was subjected to one of the five blast shots generated by different combinations of stand-off distance and charge weight as shown in Table 2.1. For convenience, the beams were tested in the vertical position and simply supported. They were subjected mainly to bending caused by the blast pressure as the axial stress due to self-weight was practically negligible. All the blast shots were conducted in the field, where the maximum charge size used was limited to 250 kg of ANFO. It is worth mentioning that extremely high pressures can be achieved by close-in explosions of small size, but such blast-scenarios would involve local failure modes, such as breaching and cratering, that were not intended to be the focus of this investigation. The objective was to investigate the behaviour of full size beam specimens subjected to reasonably plane shock waves and essentially uniform pressure. These conditions would comply with the assumptions made in the development of the common Single Degree of Freedom (SDOF) model. Consequently, a minimum stand-off distance of several meters had to be maintained.

The ground stand-off distance ranged from 7 to 10.3 meters while the charge size varied from 50 to 250 kg. The stand-off distance and charge weight combinations were designed to achieve different levels of response and ductility ratio in the test beams. Three W150×24 beams were tested in shots 1, 2, 3, and 4 and one W200×71 beam in shot 5. The test parameters included the strong and weak axes orientation of the steel sections with respect to the direction of blast wave propagation. Table 2.1 shows the test matrix including the charge mass, ground stand-off distance, scaled-distance, section designation and orientation, and the test beams designations.

2.3.1.2 Test setup

Figures 2.2(a) and (b) show the front and side view of the test setup for shots 1 to 4 in the test program. A reinforced concrete (RC) supporting frame with clear opening of 2.36×2.81 m was used to support the steel specimens during the blast test. The supporting frame consisted of 2 RC beams and 2 RC columns joined together at the 4 corners by steel sockets. Due to its large size, the supporting frame was built in such way that it could be assembled on site.

In order to confine the specimens and to prevent the wrap around of the pressure wave, an ISO steel container was placed behind the frame. The wrap around phenomenon has a pronounced effect on the pressure and impulse acting on a target with relatively small dimensions because shock waves would engulf the target before the pressure substantially drops on the target surface facing the charge. For convenience, the chosen steel container was a standard shipping container with nominal dimensions of 20 ft (6.1 m) long, 8 ft (2.4 m) wide, and 8 ft (2.4 m) high. The container also provided safe housing for the instrumentation and wiring during each blast event. In addition, plywood panels were placed between the test specimens to simulate building cladding and to prevent the pressure from wrapping around the specimens during the blast. As shown in Fig. 2.2(a), concrete block wing walls were erected around the RC frame which provided a total reflecting surface with outer dimensions approximately equal to 5.42×3.72 m, as depicted in Fig. 2.3. This setup provided reasonably uniform peak pressure and impulse over the test beams by minimizing the clearing effect, which is known to be due to rarefaction waves travelling back from the edges of the reflecting surface and causing considerable pressure relief, which, in turn, leads to a significant loss of total specific impulse (Smith and Hetherington 1994). Figure 2.3 shows key dimensions of the test setup, including the frame dimensions, dimensions of the overall reflecting surface, and beam spacing. This setup was used for shots 1 to 4 and each shot involved the testing of six W150×24

members, which included 3 beams and 3 columns. Only the results related to the test beams are presented and discussed in this paper.

Due to the greater resistance of the W200×71 section and the maximum charge size limitation, in order to be able to induce reasonable amount of stress in this member under the blast load, it became necessary to enhance the pressure acting on it by using a steel curtain interposed between the specimen and the explosive charge, which had the effect of a wider tributary area capable of collecting and transferring a greater load to the samples. The curtain consisted of twelve 1180 mm long structural steel elements made of a HSS 254×152×6.4 mm section. These elements were strung by aircraft cables and cladded on one face with a thin metal sheet. The cables were firmly secured to steel rods at the top of the curtain, and the rods were supported at their ends on steel brackets welded to the reaction frame ceiling. Figures 2.2(c) and (d) show the front and back views of the steel curtain. This support system allowed the whole curtain to swing freely Due to its particular design; the curtain had very high stiffness in the horizontal direction but negligible stiffness in the vertical direction. The high horizontal stiffness allowed for an efficient load transfer without significant energy dissipation through plastic deformation of the curtain elements while the low vertical stiffness enabled the curtain to follow the test sample deformed shape without interfering with its stiffness.

All the steel specimens were pinned at the top and roller supported at the bottom. Each member had a 24.5 mm (1 inch) thick steel plate welded to its end. The pin connection consisted of a steel pin connecting the beam end to the RC frame, as shown in Fig. 2.4(b) and (c). The roller support was formed by welding a round bar to the bottom of the beam and butting against a bracket welded to the bottom of the supporting frame. In addition, a steel chain was used to prevent the bottom of the beam from swinging freely during the negative or rebound phase of the motion. A 100 mm gap was left between the bottom end of the beams and the support frame to allow free axial displacement.

The charge was placed at a given stand-off distance from the centre of the supporting frame, as shown in Fig. 2.2(a) and 2.4 (a). The charge was made of several 25 kg bags of Ammonium Nitrate-Fuel Oil mixture (ANFO) and arranged in a prismatic shape. Note that theoretically the charge shape will not have significant effect on the planarity of the pressure wave at large distances. The chemical composition of the explosive charge was of 5.7% fuel oil and 94.3% ammonium nitrate. The explosive energy of ANFO is approximately 3717 kJ/kg, which is 82% of the energy of one kilogram of TNT.

2.3.1.3 Instrumentations

During the blast tests, incident and reflected pressures, strains, accelerations, and displacements were measured. Incident pressure was measured at four to six different locations during each shot. The distance of the transducers from the charge centre ranged from 6 to 15 meters, as indicated in Table 2.2. The free field transducers were installed on tripods located along a line parallel to direction of the blast wave, and they are labeled FF1 to FF6. The reflected pressure was measured by five pressure transducers that were installed at different positions on the RC frame and are labeled as P1 to P5 in Fig. 2.3. These gauges were coated with silicon rubber to minimize the effects of heat radiation during the explosion. All the pressure transducers were of a capacity of 6950 kPa, a resolution of 0.021 kPa, a low frequency response of 0.5 Hz, and a resonant frequency of 500 kHz.

The displacement time-history along each test specimen was recorded using a number of linear potentiometers. The chosen potentiometers had a maximum stroke of 600 mm, a repeatability of less than 0.01 mm, and a maximum operating speed of 5 m/s. The potentiometers were supported by wooden posts inside the test frame at one end and to the specimen back flange at the other end. The end in contact with the specimen was clamped to allow measurement of inbound and rebound displacements. Due to the destruction of the displacement potentiometers during some shots, only the mid-span displacement

time-history for beams 1B3, 2B3, 3B3, 4B3, 5B1 were recorded. The displacement transducers were designated as 1-D1, 2-D1, 3-D1, 4-D1, and 5-D1, respectively. In addition, a number of electrical strain gauges of nominal resistance of 120 ohms were used to capture the strain time-history at a number of locations along each beam as shown in Fig. 2.5. Six different strain gauge arrangements were used to capture the variation of strain over the cross-section and along the span. Each strain gauge was given a designation to indicate the shot number and its location according to the particular arrangement, i.e. strain gauge 6 in shot 3 was designated as 3-S6.

Mid-span acceleration-time-history was recorded for beam 5B1 using an accelerometer with a frequency range from 0.5 to 35000 Hz. This accelerometer was designated as 5-A1. A high speed camera was used to record a close-in view for blast event in shot 3 and an overview of blast shot 4. The high speed camera could capture high-quality video at 3000 frames per second. A junction box was used to connect the strain gauge end wires to the data acquisition system and the box was buried under the steel container to protect it during the blast. All the data were automatically recorded at a sampling rate of 1×10^6 /s, and the data acquisition equipment was located at a safe distance of approximately 25 m from the test frame.

2.3.2 Static tests

In addition to the field tests, the experimental program included static testing of six control beams in the laboratory. The six specimens were divided into three groups of two beams each. Group I and Group II beams were made of W150×24 sections. The beams in Group I, designated as CS1W150_x-x and CS2W150_x-x, were tested about their strong axes, while those in Group II, designated as CS1W150_y-y and CS2W150_y-y, were tested about their weak axes. Beams in Group III, designated as CS1W200_x-x and CS2W200_x-x, were made of a W200×71 section and were tested about their strong axes. The static tests were

conducted under four-point bending, as shown in Fig. 2.6. The load was applied monotonically for all tests and the mid-span deflection and strain were measured. The results of the static tests will be used to compare the static and dynamic strengths of the beams.

2.4 Experimental results

2.4.1 Static tests

To facilitate discussion of the blast response of the test specimens, the static test results will be first presented. The load versus mid-span deflection curves for specimens of Group I are shown in Fig. 2.7(a), which, as expected, are linear up to the yield load, P_y, with an average value of 140 kN. Beyond the yield load, the stiffness of the beams gradually decreased, but due to further plasticization of the section and subsequent strain hardening, the beams continued to carry additional load until they reached their ultimate capacity. The average ultimate load was measured to be 150 kN, beyond which the load decreased as the displacement increased. The curve descended steeply as the beams experienced out-of-plane deformations. The corresponding yield moment M_y and ultimate moment M_u were found to be 67 and 72 kN.m, respectively.

Figure 2.7(b) shows the load mid-span displacement curves for the two specimens of Group II. Due to fact that these beams were tested about the weak axis and since in this orientation most of the material of the section is concentrated close to the neutral axis, these beams exhibited a continuous increase in load as the displacement increased and before the section became fully plastic. The test, however, was terminated at a displacement approximately equal to $10\Delta_y$, where Δ_y is the mid-span displacement under the yield load. The average yield load P_y and average ultimate load P_u were measured to be 35 kN and 47 kN, respectively. The corresponding yield moment M_y and ultimate moment, M_u were 17 and 22 kN.m, respectively. Fig. 2.7(c) shows the load mid-span displacement curves of the specimens in Group III, which exhibit the same basic characteristics

as the corresponding curves of the beams in Group I. For these specimens, the average P_y, P_u, M_y, and M_u were determined to be 595, 651, 285 and 311 kN.m, respectively.

The strain was measured for each beam using a strain gauge mounted on the mid-span sections on the tension face of the beam. The average value of this strain corresponding to the yield load was found to be 2010, 2284, and 2047 $\mu\varepsilon$ for the beams in Group I, II, and III, respectively. The elastic bending stiffness parameter *EI/L* for each beam was calculated from the slope of the linear portion of its load deflection curve, where *E*, *I*, and *L* are the beam elastic modulus, moment of inertia and span length, respectively. The average bending stiffness parameters for Group I, II, and III were calculated to be 1001, 148, and 5017 kN.m, respectively. The elastic bending stiffness parameter *EI/L* was used to calculate the slope of the resistance function of the SDOF model in the loading and unloading stages, while the ultimate moment was used to calculate the maximum resistance. Table 2.3 gives a summary of the static resistance properties of test specimens where the stiffness *K* and resistance *R* values in this table will be discussed later.

2.4.2 Blast tests

2.4.2.1 Post-blast observations

The steel beams were carefully checked after each shot and the post-blast damage and mode of failure of each specimen were recorded. The response of the beams in shots 1, 2, 3, and 5 appeared to be purely flexural. The beams in shots 1 and 3 experienced only elastic deformations as no permanent deformations were observed in either in-plane or out-of-plane directions. The beams in shots 2 and 5 experienced yielding and plastic deformations, particularly visible at the mid-span section; however, no out-of-plan deformations were observed in these beams. On the other hand, in shot 4, the beams sustained yielding and plastic deformation in

both the in-plane and out-of-plane directions. None of the sections exhibited any noticeable twist. Furthermore, none of the beams exhibited local buckling or fracture at any section, including at the K-line region on the interior of the section that is characterized by reduced ductility as a result of the steel milling process and the residual stresses, or at the front flange at the mid-span which was subjected to large deformations. Both flanges deformed in a uniform pattern as they were not folded inward towards the interior of the section.

Post-blast residual in-plane and out-of-plane deformations along all the test beams were measured using an accurate surveying instrument (total station). The maximum permanent deflection for beams in shot 2 was found to be 2.9 mm at the mid-span section of 2B3 (see Table 2.1 for each beam characteristics). Beams 2B1 and 2B2 experienced less permanent deflection than 2B3 and their maximum deflections were measured to be 2.2 and 2.4 mm, respectively. Figure 2.8(a) shows the in-plane post-blast deflected shapes of the beams in shot 2, which appear to be reasonably symmetrical about the longitudinal centreline of the beam. Figure 2.8(b) shows the peak permanent deflection of 5B1 to be 30.7 mm at the mid-span section. The maximum in-plane and out-of-plane deflection of beams in shot 4 were 3.8 and 17 mm, respectively. The full post-blast deflected shape of the beams in shot 4, in both in-plane and out-of-plane directions, are plotted in Fig. 2.8(c) and (d), respectively. The difference among the deflected shapes of nominally identical beams in the same shot can be attributed to the slight variations in the stand-off distance of the beams and to the slight non-uniformity of the blast pressure caused by random variations in the parameters governing blast waves. As the scaled-distance gets smaller, the blast pressure wave begins to deviate from a purely plane shape and this will affect the blast pressure distribution on the target surface. This is more evident in shot 4 with its smaller scaled-distance. Moreover, higher permanent deformations were observed close to the bottom of the test beams due to the non-uniform distribution of the

pressure over the beam length and the decrease of the reflected pressure from the bottom to the top of the test frame.

2.4.2.2 Pressure time-history

The reflected and incident pressure time histories were recorded during all blast shots. Figures 2.9(a) and (b) show the typical incident pressure histories captured by free-field pressure transducers during shots 1 and 2, respectively. The measured pressure profiles showed the typical features of a blast pressure wave, including zero rise time, exponential decay, and positive and negative pressure phases (Baker 1983). With reference to Fig. 2.9(a), the peak incident pressure P_{so} recorded in shot 1 decreased from 351 kPa at stand-off distance SD = 6.0 m to 115 kPa at SD = 10.0 m. The peak incident pressure decreased further to 50 kPa at SD = 15.0 m, i.e. a reduction of 85% compared to the peak pressure at SD = 6.0 m. The area beneath the pressure time curve from the time of arrival t_a to the end of the positive phase was used to determine the positive impulse. The maximum positive impulse decreased with the distance from the centre of explosion, but with a slower rate, due to the increase in the pressure duration as the stand-off distance increased. It decreased from I_s = 435 kPa.ms at SD = 6.0 m to I_s = 270 kPa.ms at SD = 10.0 m. The maximum impulse decreased further to I_s =205 kPa.ms at SD = 16.0 m, i.e. a reduction of 52% compared to the maximum impulse at SD = 6.0 m. With reference to Fig. 2.9(b), similar observations can be made regarding incident pressure time histories captured during shot 2.

Due to wave reflection from the surface of the flanges and test frame, the initial waves were reinforced and magnified, causing the pressure to increase above the incident blast pressure. This reflected pressure represents the actual pressure acting on the test specimens. Figures 2.10(a) and (b) show the typical reflected pressure time histories recorded in shots 1 and 2, as captured by the reflected pressure transducers mounted on the test frame, and it can be noticed that they have the same basic shape as the incident pressure profiles. The enlarged

insets in Fig. 2.10(a) and (b) show the measured positive phase of the pressure histories in shots 1 and 2, respectively, and their comparison with the positive pressure profile obtained using an empirical relationship by fitting a high order polynomial to the data points reported in UFC-3-340-02 (USDOD 2008). This relationship gives results that are practically identical to those given by the relationships developed by Kingery and Bulmash (1984), which is the basis for the well known blast prediction software CONWEP (Hyde 1990). For the sake of clarity, the relationship used in this study will be referred to as the UFC-Model (UFCM). As shown in Fig. 2.10, the UFCM pressure profiles compare reasonably well with the measured pressure during the positive phase in terms of both peak pressure and overall time variation.

In order to extract the blast pressure wave parameters, such as peak pressure, impulse, and positive phase duration, the measured positive pressure profiles were fitted to the modified Friedlander equation through nonlinear regression analysis. The modified Friedlander equation is given as (Baker et al. 1983):

$$P(t) = P_{\max}\left(1-\frac{t}{t_d}\right)\exp\left(-\gamma\frac{t}{t_d}\right) \tag{2.1}$$

where $P(t)$ is the pressure variation with time, P_{max} is the peak pressure, γ is a shape parameter, t_d is the positive load duration, and t is the time. All the positive pressure phases captured by the incident and reflected pressure transducers were fitted using the above equation. The enlarged inserts in Figures 2.10(a) and (b) show typical fitted pressure profile of measured pressure time-history in shots 1 and 2, respectively.

Tables 2.4 and 2.5 list all the incident and reflected peak pressures, impulses, and positive phase durations measured and their corresponding predicted values using UFCM. It can be noticed by considering the peak incident (Table 2.4) and peak reflected pressure (Table 2.5) values that the reflected pressure is two to five times higher than the incident or free field pressure. This

agrees with Baker et al. (1983) observation who stated that the reflected pressure may be at least twice and as high as eight times the incident pressure. The average of the measured peak reflected pressures, P_r, recorded by the different transducers in shots 1, 2, 3, 4, and 5 were 307, 623, 1560, 4283, and 2098 kPa, respectively, with differences of 3, 2, 18, 2, and 10% compared to the corresponding values predicted by UFCM. The average measured reflected impulse, I_r, based on the recorded pressure profiles in each shot were found to be 715, 1279, 2130, 3174, and 3144 kPa.ms for shots 1, 2, 3, 4, and 5, respectively, with differences of 6, 1, 8, 19, and 15% compared to the corresponding values predicted by UFCM. The positive phase duration was generally overestimated by UFCM by a range of 20 to 80%. With reference to the results in Table 2.5, it can be noticed that there are differences among the measured pressure and impulse values recorded by the different gauges in the same shot, e.g. the impulse P2 is larger than that measured by gauge P4 in shots 1, while the opposite is true for shot 3. These discrepancies and the differences may be partially attributed to the irregularities of the terrain, which presented what could be described as gentle upward and downward slopes known to enhance or weaken the shocks (Baker 1983). Such irregularities varied for each shot due to the use of heavy equipments needed to load and unload the test beams.

It should be noted that the difference between UFCM predictions and the measurements performed in this experimental program are to be expected since the data used in this model to generate empirical relationships were obtained from explosions of carefully shaped spherical or hemispherical charges. Therefore, these differences are not to be interpreted as evidence of lack of accuracy on the part of UFCM; rather, they should be construed as evidence that UFCM predictions can be reasonable for larger scale distances even if the charge shape deviates significantly from the ideal spherical shape. It must be recalled that real blast scenario may involve cased explosives, car bombs, and other unusual charge shapes which deviate significantly from the ideal spherical charge shapes.

2.4.2.3 Strain and strain rate time-history

The mid-span strain time histories for test beams during shot 1 to 4 are shown in Fig. 2.11; all strain time histories were recorded from the instant of initiation of the explosion. The histories for beams 1B1, 1B2, and 1B3 in shot 1, with maximum values of $559, 535, 552\ \mu\varepsilon$, are shown in Fig. 2.11(a), captured by gauges 1-S1, 1-S4, and 1-S6, respectively. These gauges were mounted on the back flange at the mid-section of each beam. The small differences among the maximum strain values may be attributed to the non-uniform distribution of the reflected pressure on these specimens, but the differences are practically inconsequential. The maximum strain in beams 1B1, 1B2, and 1B3 occurred at 16.8, 17.0, and 16.4 ms, respectively. By comparing these time lengths with the positive phase duration of the corresponding pressure histories, one can observe that the maximum strain occurred in the free vibration phase at a time greater than the positive phase duration, which is indicative of the impulsive nature of the present blast loads (Biggs 1964). The beams in this shot remained in the elastic range as the measured maximum strains were lower than the yield strain ε_y, obtained from the static testing of companion beams.

Beams in shots 2 and 3 experienced larger strains than those in shot 1. The strain responses for beams 2B2 and 2B3, captured by gauges 2-S4 and 2-S6 in shot 2, and for beams 3B2 and 3B3 captured by 3-S4 and 3-S6 in shot 3, are shown in Fig. 2.11(b) and (c), respectively. The maximum measured strains were $3435, 3378, 2370,$ and $2384\ \mu\varepsilon$ in beams 2B2, 2B3, 3B2, and 3B3, respectively. The maximum strain in beams 2B2 and 2B3 in shot 2 exceeded the yield strain and their residual values were found to be approximately $100\ \mu\varepsilon$ which was estimated by determining the neutral position of vibration of the last recorded cycle in the strain time-history (Biggs 1964). The strain history for beam 4B1 in shot 4 is shown in Fig. 2.11(d), with a maximum strain of $3610\ \mu\varepsilon$, which exceeded the yield strain. Figure 2.11(d) shows only the first two strain peaks recorded during shot 4 as a signal loss occurred after the second peak and this loss

is indicated in the remaining strain history by a sudden increase to a value of 10000 $\mu\varepsilon$, followed by a plateau to the end of the trace. The strain gauge at mid-span of beam 5B1 in shot 5 failed to capture any data. Therefore, instead the strain history at the section located at 1/3 of the span is presented in Fig. 2.11(e), which shows a maximum strain of 2536 $\mu\varepsilon$ and a residual strain of approximately 220 $\mu\varepsilon$. A summary of the maximum strain in each shot is reported in Table 2.6.

The strain rate time histories corresponding to each strain response are also plotted in Fig. 2.11. The strain rate time histories were obtained by differentiating the captured strain time histories using the central difference method. As shown in Fig. 2.11, the strain rates had their maximum values at time of zero strain. The strain rate decreased with increased strain and it approached zero at the time of maximum strain. The highest strain rate was 2.89 /s in shot 4 and the lowest rate was 0.28 /s in shot 1. The highest strain rates associated with shots 2, 3, and 5 were calculated to be 0.90, 1.70, and 1.40 /s, respectively. It is worth mentioning that these strain rates are significantly less than the strain rate range of 100-1000 /s often cited for blast in the literature (Bischoff and Perry 1991). However, to date in the open literature, there is scant strain rate data obtained from blast tests on reasonable size steel members to confirm the validity of the above range in far range blast analysis and design. Therefore, additional tests with a wide range of scaled-distances are needed to establish the range of strain rates experienced by steel structures during unconfined explosions. Such data would assist in deriving realistic dynamic increase factors for design purposes.

Figure 2.12(a) shows the variation at three points over the height of the cross-section of beam 1B1. A maximum tensile strain of 559 $\mu\varepsilon$ was recorded by gauge 1-S1, while the gauge 1-S3 recorded a compressive maximum strain of 333 $\mu\varepsilon$ as it was located closer to neutral axis. Although 1-S2 was at the mid-height of the cross-section, i.e. at the neutral axis, a maximum strain of 52 $\mu\varepsilon$ was measured. This small strain may be the result of axial pressure exerted by the

blast. Figure 2.12(b) shows the strain time-history at three points over the depth of beam 1B3. Figure 2.12(c) and (d) show the strain history captured by gauges 2-S6 and 2-S7 in beam 2B3 and by gauges 3-S6, 3-S7, and 3-S8 on beam 3B3 during shots 2 and 3, respectively. Using the measured strain values for the three points over the depth of the section, the strain and strain rate profiles are plotted in Figs. 2.13(a) and (b) for beam 1B1 at different instants of time. As can be observed, both the strain and strain rate profiles are linear, confirming the assumption that plane sections remain plane after bending.

The variations of strain at two or three points along the test beams were also monitored, as shown in Fig. 2.14. In Fig. 2.14(a), the tensile strain variations at two points along beam 1B3 are shown. Gauge 1-S6 was located at mid-span while gauge 1-S10 was situated at 1/6 of the span from the bottom end of the beam. It is quite clear that the strains at the two locations are in-phase throughout the vibration period. The strain varied along beam 1B3 from 552 $\mu\varepsilon$ at the location of gauge 1-S6 to 305 $\mu\varepsilon$ at the position of gauge 1-S10, with a total reduction of 45%. Figure 2.14(b) shows the variation of the longitudinal strain at three points along the length of beam 3B3. The maximum strain decreased from 2384 $\mu\varepsilon$ at location of gauge 3-S6 to 2050 $\mu\varepsilon$ at the position of gauge 3-S9, i.e. a reduction of 14%. The maximum strain decreased further to 1440 $\mu\varepsilon$ at the position of gauge 3-S10, which is 40% less than the strain measured at 3-S6. The variations of longitudinal strain at two points along beam 4B3 and 5B1 are shown in Fig. 2.14(c) and (d), respectively. The above strain variations along the test beams provide a good indication of the deflected shape during the vibration period. The deflected shapes at different time instants were obtained by integrating the curvature diagram, established from the measured strain at two or three points over the length of each beam. Figure 2.15(a) and (b) show the deflected shapes at different instants during the in-bound displacements of beam 1B3 and 3B3, respectively.

2.4.2.4 Displacement and acceleration-time histories

The mid-span displacements for beams 1B3, 2B3, 3B3, and 5B1 are shown in Fig. 2.16(a) to (d) as captured by displacement potentiometers 1-D1, 2-D1, 3-D1, and 5-D1, respectively. The maximum displacement for beam 1B3 was recorded to be 6.9 mm, as shown in Fig. 2.16(a). Due to the larger charge size used in shot 2 and the lower stiffness of the member involved, a maximum displacement of 40.8 mm was recorded for beam 2B3, as shown in Fig. 2.16(b). The maximum displacements for beams 3B3 and 5B1 were 33.2 and 62.8 mm, as shown in Fig. 2.16(c) and (d), respectively. Note that displacement transducer 4-D1 failed to capture any data because it was destroyed by the blast and falling debris. Table 2.6 summarizes the absolute maximum displacements recorded for each shot. The mid-span acceleration-time-history for beam 5B1 was recorded during shot 5. As shown in Fig. 2.17, under the effect of the blast pressure, the beam exhibited an increase in the acceleration to a maximum value of 1.92×10^3 m/s^2 at approximately 0.8 ms after the arrival time. A second acceleration peak of 3.8×10^3 m/s^2 can be observed at 5.5 ms after the arrival time. The second peak can be explained by a sudden jump in the velocity caused by the formation of the plastic hinge at mid-span (Magnusson 2007).

2.5 Comparison with the single degree of freedom (SDOF) model

The simplified SDOF analysis method used in this study is commonly employed in blast-resistant design practice (USDOD 2008; Dusenberry, 2010). The key assumption of this analysis is that a real beam can be represented by an equivalent SDOF spring-mass system. The dynamic response of the beam is approximated by its first mode shape, and the dynamic equation of motion of the system is solved assuming an elastic-perfectly plastic spring. The equation of motion for the equivalent SDOF system is written as

$$K_{LM} M\, \ddot{y} + R(y) = P(t) \tag{2.2}$$

where y and $\ddot{y}$ are the mid-span displacement and acceleration and K_{LM} is the so-called load-mass factor. A list of these factors can be found in Biggs (1964) and UFC 3-340-02 (USDOD 2008). M, $R(y)$, and $P(t)$ are the mass, resistance, and load of the real beam, respectively. It should be noted that the structural damping is typically neglected when calculating the response under blast loading since the maximum deformations often occurs during the first cycle of the response. The blast pressure is represented by an impulse-equivalent triangular pulse with zero rise time. Here, the peak reflected pressure and impulse values of the triangular pulses were calculated as the average of the peak pressure and impulse values measured by the pressure transducers fixed to the test frame as given in Table 2.5. The blast pressure was assumed to be uniformly distributed over the surface of the flange facing the blast wave in shots 1 to 4, or over the steel curtain face in shot 5. In general, the variation of the blast pressure in space and time is quite complex; however, all the related calculations can be greatly simplified by making the above assumptions, which are reasonable when simple geometries are involved and the definition of far range applies to the blast scenario involved (USDOD 2008). The bilinear resistance function of the equivalent elastic-plastic spring, R, is defined by its initial stiffness, K, and its maximum resistance R_m. Both the stiffness $K = \left(384/5L^2\right).\left(EI/L\right)$ and maximum resistance $R_m = 8M_u/L$ were obtained from the static test results described earlier and are listed in Table 2.3 for all test beams. In order to account for the strain rate effect in the dynamic response, the yield strength of the steel was increased by 24% as recommended by UFC 3-340-02 (USDOD 2008). Note that in the elastic range $R(y) = ky$, while in the plastic range $R(y) = R_m$.

A comparison of the measured mid-span displacement time histories of test beams in shots 1 to 5 and their corresponding calculated values using the SDOF model are shown in Fig. 2.16. The SDOF values agreed reasonably well in terms of the peak displacement and overall response with the corresponding

measured values in shots 1 and 3, which involved elastic deformations, as the maximum displacements obtained from SDOF model were computed to be 6.3 and 36.4 mm, differing by 9% for shots 1 and 3, respectively, from the corresponding experimental values. Greater discrepancy was found for shots 2 and 5, particularly, in the case of the beams undergoing plastic deformations, as the maximum displacements were computed to be 53.7 and 76.5, which are 30 and 17% higher than the corresponding experimental values, respectively.

The experimental mid-span acceleration-time-history of beam 5B1 in shot 5 is compared in Fig. 2.17 with the corresponding computed history based on the SDOF model. Reasonable agreement was achieved in terms of the second peak acceleration; however, there was less agreement between the first peak and overall time variation, as can be seen in Fig. 2.17. The flat part of the acceleration time-history predicted by SDOF in the free vibration phase, between 3 and 10 ms, is due to the simple resistance function assumed by SDOF model. When plastic deformation is attained during the free vibration phase, the acceleration is a function of the maximum resistance and mass of the system, which are both constants (Biggs 1964). Therefore, it can be argued that the elastic-perfectly plastic resistance function commonly assumed by SDOF model may not be sufficiently accurate to represent the actual acceleration response for members undergoing plastic deformations, as is evident in the present analysis. The difference between the experimental data and those obtained by SDOF model may be partly attributed to the effect of higher modes of vibration and negative pressure phase, which, in compliance with prevailing practice, are neglected in the model. In addition, the blast pressure is applied to the entire surface at the same time in the analysis, but the blast pressure first arrives close to the bottom of the test beams in the test. Moreover, the Dynamic Increase Factor (DIF) recommend by UFC 3-340-02 (USDOD 2008) as used in this analysis (DIF=1.24), is an estimated value based on an assumed average strain rate. However, this factor may not reflect the real effect of the strain rate and may underestimate the actual

strength increase. As stated earlier, in the present tests, the strain rate is maximum at the time of zero displacement, and it decreases with increased displacement. In order to achieve greater accuracy the influence of strain rate may need to be included in a more accurate manner, as will be shown below.

To study the variation of DIF with time in the present tests, the typical DIF-time histories, corresponding to the level of the strain rates reached during blast shots 2 and 4 are shown in Fig. 2.18(a) and (b), respectively. Two constitutive equations for the strain rate-sensitive behaviour were used to plot the above DIF-time histories. The first model was taken from Malvar (1998) who proposed the following equation based on results of dynamic tensile tests performed on steel rebars:

$$\text{DIF} = \left(\frac{\dot{\varepsilon}}{10^{-4}} \right)^{\alpha} \tag{2.3}$$

where $\alpha = 0.074 - 0.040 \frac{f_y}{414}, \dot{\varepsilon}$ = the strain rate in s^{-1}, and f_y = yield stress in (MPa). The second model was based on the work of Cowper and Symonds (Jones 1988), who proposed:

$$\text{DIF} = 1 + \left(\frac{\dot{\varepsilon}}{D} \right)^{1/q} \tag{2.4}$$

where D and q are constants for a particular material. These constant were taken for steel as D = 40, and q = 5 (Jones 1988). As shown in Fig. 2.18, the test members would experience variations in strain rates, and consequently the corresponding strength increase due to strain rate effect would also vary with time. The Cowper and Symonds model typically gave higher DIF values than the Malvar model. The maximum DIF values obtained from the Cowper and Symonds model were found to be 1.35, 1.48, 1.52, 1.62, 1.51 for shots 1, 2, 3, 4, and 5, respectively with average DIF values of 1.28, 1.38, 1.44, 1.46, and 1.42 for shots 1, 2, 3, 4, and 5, respectively. It can be noticed in Fig. 2.18 that the average DIFs achieved by all blast shots are higher than that suggested by UFC 3-340-02

(USDOD 2008). Table 2.6 summarizes deflection, strain, strain rate, and the maximum DIF according to the Cowper and Symonds model achieved in each shot.

The sensitivity of the SDOF predictions to the DIF was studied by comparing the measured displacement and acceleration-time histories with those obtained from SDOF model based on DIF=1, and on average DIF, calculated by using the actual strain rates, as shown in Fig. 2.16 and 17. DIF had no effect on the maximum displacement of beams in shot 1 as they remained in the elastic range, as shown in Fig. 2.16(a). Underestimating the effect of the strain rate in the SDOF model resulted in inelastic response for beams in shots 3, although the actual response of beams in shot 3 were in the elastic range, as shown in Fig. 2.16(c). The maximum displacements were generally significantly overestimated when the effect of strain rate was ignored (DIF=1.00), while they were in better agreement with the experimental displacements when the average DIF based on the actual strain rates was used. Again, using average DIF of the actual strain rate in the SDOF model gave better agreement with the measured acceleration when plastic deformation was attained, as shown in Fig. 2.17. Table 2.6 summarizes the measured and predicted SDOF predictions for the maximum displacements of each beam. It should be noted that using a fixed value of DIF, which is independent of the actual strain rate experienced by a member under a given blast scenario, is not always conservative as it might give a false estimate of the member capacity that, in turn, could result in unsafe design of the member connections or the supporting members.

Clearly the currently used SDOF models for blast resistance design (USDOD 2008) can be further refined in order to capture the observed behaviour of the tested beams. This includes the effect of the negative pressure and better representation of the dynamic increase factor due the effect of strain rate.

2.6 Summary and conclusions

In this study full-scale field tests were performed on wide flange steel beams to investigate their behaviour and resistance under blast loading. The effects of charge size and stand-off distance on their behaviour were investigated by measuring their response using a variety of measuring devices. None of the beams experienced local buckling or other type of local failure; instead, they all exhibited a ductile response under blast loading. The measured blast pressure magnitude and positive phase duration were compared with the corresponding values predicted by UFCM. The measured response values of the beams were compared with the corresponding predicted values using a SDOF elastic-plastic spring-mass model under the assumption of the constant strain rate over time and over the cross-section. Based on the results the following conclusions are reached:

(1) The UFCM was able to predict the peak blast pressures and impulses with differences of 18 and 19 % for the average reflected pressure and the average reflected impulse when compared with the experimental reflected pressure and impulse values. However, UFCM generally overestimated the positive phase duration.

(2) Assuming a DIF of 1.24, the SDOF model predicted the response of the current steel beams undergoing elastic deformation reasonably well, with a maximum difference of 9% between the measured and computed maximum displacements values. However, the maximum difference in the case of beams that experienced plastic deformation was 30%.

(3) Using a constant dynamic increase factor to estimate the material strength due to strain rate might not provide a realistic assessment of the actual effect of the strain rate on the dynamic response of beams, particularly if the actual response remains elastic while the predicted response is plastic. Therefore, the effect of the strain rate on a member response should be more accurately accounted for in SDOF analysis in order to achieve higher accuracy and better agreement with the experimental results.

(4) Underestimating the actual capacity of a member due to inaccurate consideration of strain rate effect is not always on the safe side for the design of the member connections or its supporting members.

2.7 Acknowledgements

The authors wish to gratefully acknowledge the following organizations for their support towards this study: the Chemical, Biological, Radiological/Nuclear and Explosives Research and Technology Initiative (CRTI project 06-015TD), Public Works and Government Services Canada, the Centre for Effective Design of Structures (CEDS) at McMaster University, and the Natural Sciences and Engineering Research Council of Canada for their financial support, the Canadian Explosives Research Laboratory (CERL) for assisting with the blast tests, and the Canadian Armed Forces for the use of their test range. CEDS received funding through the Ontario Research and Development Challenge Fund, a program of the Ministry of Research and Innovation of Ontario. The authors also appreciate the technical support of Messrs. Rick Guilbeault and Don Wilson of CERL during the experimental phase of this study.

2.8 Notation

The following symbols are used in this paper:

DIF = dynamic increase factor;

Δ_y = displacement at the yield load (mm);

$\dot{\varepsilon}$ = strain rate (1/s);

ε_y = yield strain;

f_y = yield stress (MPa);

K = stiffness (kN/m);

K_{LM} = load-mass factor;

I_s = incident impulse (kPa.ms);

I_r = reflected impulse (kPa.ms);

μ = ductility ratio;

M = mass (kg);

M_y = yield moment (kN.m);

M_u = ultimate moment (kN.m);

P_{so} = peak incident pressure (kPa);

P_r = peak reflected pressure (kPa);

R = resistance (kN);

t_a = arrival time of pressure wave (ms);

t_d = positive phase duration (ms);

y = mid-span displacement (mm);

$\ddot{y}$ = mid-span acceleration (m/s^2);

Z = scaled-distance (m/kg$^{1/3}$).

2.9 References

ASCE. (1997). "Design of blast resistant buildings in petrochemical facilities." Task Committee on Blast Resistant Design, ASCE, New York.

Aspden, R. J., and Campbell, J. D. (1966). "The effect of loading rate on the elasto-plastic flexure of steel beams." Proceedings of the Royal Society of London. Series A, Mathematical and Physical Sciences, 290(1421), 266-285.

Baker, W. E., Cox, P. A., Westine, P. S., Kulesz, J. J., and Strehlow , R. A. (1983). "Explosion hazards and evaluation" Elsevier Scientific Pub. Co., Amsterdam; New York.

Bassim, M. N., and Panic, N. (1999). "High strain rate effects on the strain of alloy steels." Journal of Materials Processing Technology, 92-93, 481-5.

Biggs, J. M. (1964). "Introduction to structural dynamics." McGraw-Hill Book Company, New York.

Bischoff, P., and Perry, S. (1991). "Compressive behaviour of concrete at high strain rates." Materials and Structures, 24(6), 425-450.

Boutros, M. K. (2000). "Elastic-plastic model of pinned beams subjected to impulsive loading." Journal of Engineering Mechanics, 126(9), 920-927.

CISC. (2011). "Handbook of steel construction." Canadian Institute of Steel Construction, Willowdale, Canada.

Hyde D.W., (1990). "Conventional weapons effect (CONWEP)" Application of TM5-855-1. US Army Engineer Waterways Experiment Station, Vicksburg, USA.

Davidson, J. S., Porter, J. R., Dinan, R. J., Hammons, M. I., and Connell, J. D. (2004). "Explosive testing of polymer retrofit masonry walls." Journal of Performance of Constructed Facilities, 18(2), 100-106.

Dusenberry, D. O. (2010). "Handbook for blast resistant design of buildings." J. Wiley, Hoboken, N.J.

Jama, H. H., Bambach, M. R., Nurick, G. N., Grzebieta, R. H., and Zhao, X. L. (2009). "Numerical modelling of square tubular steel beams subjected to transverse blast loads." Thin-Walled Structures, 47(12), 1523-1534.

Jones, N. (1988). "Structural impact." Cambridge University Press, Cambridge; New York.

Kingery, C.N. and Bulmash, G. (1984). "Airblast Parameters from TNT Spherical Air Burst and Hemispherical Sur-face Burst." Report ARBL-TR-02555. US Army Research and Development Centre – Ballistic Research Laboratory (BRL), Aberdeen Proving Ground, Aberdeen, MD.

Kinney, G.F., Graham, K.J., 1985. "Explosive shocks in air." Springer-Verlag, New York.

Krafft, J. M., Sullivan, A. M., and Tipper, C. F. (1954). "The effect of static and dynamic loading and temperature on the yield stress of iron and mild steel in compression." Proceedings of the Royal Society of London. Series A, Mathematical and Physical Sciences, 221(1144), 114-127.

Krauthammer, T., Bazeos, N., and Holmquist, T. J. (1986). "Modified SDOF analysis of RC box-type structures." Journal of Structural Engineering, 112(4), 726-744.

Krauthammer, T., Shahriar, S., and Shanaa, H. M. (1990). "Response of reinforced concrete elements to severe impulsive loads." Journal of Structural Engineering, 116(4), 1061-1079.

Lawver, D., Daddazio, R., Vaughan, D., Stanley, M., and Levine, W. (2003) "Response of AISC steel column sections to blast loading." Problems Involving Thermal-Hydraulics, Liquid Sloshing, and Extreme Loads on Structures, 2003 ASME Pressure Vessels and Piping Conference, ASME, NY, 139-148.

Liew, J. Y." Survivability of steel frame structures subject to blast and fire." Journal of Constructional Steel Research, 64 (7-8) 854–866.

Magallanes, J. M., Martinez, R., and Koening, J. (2006). "Experimental results of the AISC full-scale column blast test." Report TR-06-20.2, The American Institute of steel construction, Chicago.

Magnusson, J. (2007). "Structural concrete elements subjected to air blast loading," PhD Thesis, Royal Institute of Technology, Sweden.

Malvar, L. J. (1998). "Review of static and dynamic properties of steel reinforcing bars." ACI Materials Journal, 95(5), 609-616.

Manjoine, M. J., and Pittsuburgh, E. (1944). "Influence of rate of strain and temperature on yield stresses of mild steel." Journal of Applied Mechanics, 11, 211-18.

Oesterle, M. G., Hegemier, G. A., and Morrill, K. B. "Response of concrete masonry walls to simulated blast loads." Austin, Texas, 140-140.

Razaqpur, A. G., Tolba, A., and Contestabile, E. (2007). "Blast loading response of reinforced concrete panels reinforced with externally bonded GFRP laminates." Composites Part B: Engineering, 38(5-6), 535-546.

Schenker, A., Anteby, I., Gal, E., Kivity, Y., Nizri, E., Sadot, O., Michaelis, R., Levintant, O., and Ben-Dor, G. (2008). "Full-scale field tests of concrete slabs subjected to blast loads." International Journal of Impact Engineering, 35(3), 184-198.

Schleyer, G. K., and Hsu, S. S. (2000). "A modelling scheme for predicting the response of elastic-plastic structures to pulse pressure loading." International Journal of Impact Engineering, 24(8), 759-777.

Smith, P. D., and Hetherington, J. G. (1994). Blast and ballistic loading of structures, Butterworth-Heinemann, Oxford; Boston.

Soroushian, P., and Choi, K.-B. (1987). "Steel mechanical properties at different strain rates." Journal of Structural Engineering, 113(4), 663-672.

Tan, K. H., and Patoary, M. K. H. (2009). "Blast resistance of FRP-strengthened masonry walls. I: approximate analysis and field explosion tests." Journal of Composites for Construction, 13(5), 422-430.

USDOD (2008) "Structures to resist the effects of accidental explosions." Document No. UFC 3-340-02. US Department of Defense (USDOD), Washington, DC.

Wu, C., Oehlers, D. J., Rebentrost, M., Leach, J., and Whittaker, A. S. (2009). "Blast testing of ultra-high performance fibre and FRP-retrofitted concrete slabs." Engineering Structures, 31(9), 2060-2069.

2.10 List of figures

Table 2.1: Matrix of test specimens

Shot	Section designation	Charge mass (kg)	Stand-off distance (m)	Scaled-distance ($m/kg^{1/3}$)	Axis of bending	Test beams
1	W150X24	50	10.30	2.80	x-x	1B1, 1B2, 1B3
2	W150X24	100	10.30	2.22	y-y	2B1, 2B2, 2B3
3	W150X24	150	9.00	1.69	x-x	3B1, 3B2, 3B3
4	W150X24	250	7.00	1.11	x-x	4B1, 4B2, 4B3
5	W200X71	250	9.50	1.51	x-x	5B1

Table 2.2: Stand-off distance of pressure transducers

Shot	Charge (kg)	Incident Pressure Transducers						Reflected Pressure Transducers				
		FF1 (m)	FF2 (m)	FF3 (m)	FF4 (m)	FF5 (m)	FF6 (m)	P1 (m)	P2 (m)	P3 (m)	P4 (m)	P5 (m)
1	50	6.00	8.00	10.00	10.00	15.00	15.00	10.72	10.60	10.49	10.49	10.37
2	100	6.00	8.00	10.00	10.0	15.00	15.00	10.72	10.60	10.49	10.49	10.37
3	150	6.00	8.00	9.00	9.00	15.00	15.00	9.46	9.26	9.13	9.26	9.14
4	250	5.00	7.00	10.00	10.00	15.00	15.00	7.59	7.33	7.16	7.33	7.18
5	250	6.00	8.00	9.50	9.50	N/A	N/A[(1)]	9.94	9.75	9.62	9.76	9.63

(1) N/A= Not Available

`

Table 2.3: Static resistance parameters of tested beams

Group	Section	Orientation	M_y (kN.m)	M_u (kN.m)	ε_y (με)	EI/L (kN.m)	K (kN/m)	R_m(kN)
I	W150X24	x-x	67	72	2010	1001	13206	230
II	W150X24	y-y	17	22	2284	148	1955	65
III	W200X71	x-x	285	311	2047	5017	66179	988

Table 2.4: Recorded free field pressure data for test shots

Shot		FF1			FF2			FF3			FF4			FF5			FF6		
		P_{max} (kPa)	I (kPa-ms)	t_d (ms)	P_{max} (kPa)	I (kPa-ms)	t_d (ms)	P_{max} (kPa)	I (kPa-ms)	t_d (ms)	P_{max} (kPa)	I (kPa-ms)	t_d (ms)	P_{max} (kPa)	I (kPa-ms)	t_d (ms)	P_{max} (kPa)	I (kPa-ms)	t_d (ms)
1	Measured	351	435	3.6	NC	NC	NC	115	270	6.4	164	399	6.4	50	221	11.3	51	205	6.8
	UFCM	391	525	7.1	203	401	7.47	124	328	9.5	124	329	9.5	56	231	12.3	56	231	12.3
	Ratio[1]	0.90	0.83	0.51	--	--	--	0.93	0.82	0.67	1.32	1.21	0.67	0.89	0.96	0.92	0.91	0.89	0.55
2	Measured	688	661	4.1	400	583	5.4	207	469	6.1	236	546	6.0	86	368	12.1	77	289	6.8
	UFCM	665	820	9.6	343	627	8.9	206	509	9.4	206	509	9.4	87	356	13.7	87	356	13.7
	Ratio	1.03	0.81	0.43	1.17	0.93	0.61	1.01	0.92	0.64	1.14	1.07	0.64	0.99	1.03	0.89	0.89	0.81	0.50
3	Measured	NC[2]	NC	NC	651	954	7.9	350	672	7.6	370	728	5.2	105	408	10.2	NC	NC	NC
	UFCM	902	1047	10.8	469	816	10.5	357	730	10.2	357	730	10.2	114	458	14.1	114	457	14.1
	Ratio	--	--	--	1.39	1.17	0.76	0.98	0.92	0.75	1.04	1.00	0.51	0.92	0.89	0.72	--	--	--
4	Measured	NC	NC	NC	888	1109	9.2	350	673	7.6	370	729	5.2	200	774	10.6	137	409	8.06
	UFCM	935	1255	12.7	935	1255	12.7	415	921	12.2	415	921	12.2	165	631	13.9	165	631	13.9
	Ratio	--	--	--	0.95	0.88	0.72	0.84	0.73	0.62	0.89	0.79	0.41	1.21	1.23	0.77	0.83	0.65	0.58
5	Measured	1456	865	2.2	795	900	6.6	386	941	10.6	406	684	5.8	N/A[3]	N/A	N/A	N/A	N/A	N/A
	UFCM	1308	1363	2.8	693	1130	13.1	467	966	12.4	467	966	12.4	N/A	N/A	N/A	N/A	N/A	N/A
	Ratio	1.11	0.63	0.76	1.15	0.80	0.50	0.83	0.97	0.86	0.87	0.71	0.47	N/A	N/A	N/A	N/A	N/A	N/A

(1) Ratio= ratio of measured to predicted by UFCM

(2) NC= Not Captured

(3) N/A=Not Available

Table 2.5: Recorded reflected pressure data for test shots

Shot		P1			P2			P3			P4			P5		
		P_{max} (kPa)	I (kPa-ms)	t_d (ms)	P_{max} (kPa)	I (kPa-ms)	t_d (ms)	P_{max} (kPa)	I (kPa-ms)	t_d (ms)	P_{max} (kPa)	I (kPa-ms)	t_d (ms)	P_{max} (kPa)	I (kPa-ms)	t_d (ms)
1	Measured	267	770	7.9	329	742	7.2	318	712	7.1	310	629	7.2	311	721	6.8
	UFCM	301	742	10.1	310	752	10.0	319	761	9.9	319	761	9.9	328	771	9.8
	Ratio(1)	0.89	1.04	0.79	1.06	0.99	0.72	1.00	0.94	0.72	0.97	0.83	0.73	0.95	0.93	0.70
2	Measured	NC(2)	NC	NC	624	1176	6.8	NC	NC	NC	582	1320	6.3	662	1340	4.9
	UFCM	575	1233	9.8	603	1257	9.7	620	1271	9.6	606	1259	9.7	625	1276	9.6
	Ratio	--	--	--	1.04	0.94	0.70	--	--	--	0.96	1.05	0.65	1.06	1.05	0.51
3	Measured	1293	1877	6.7	1409	1765	6.8	1484	2688	6.1	1984	2250	6.3	1631	2058	4.9
	UFCM	1228	1924	10.1	1312	1976	10.1	1370	2011	10.1	1307	1973	10.1	1363	2007	10.1
	Ratio	1.05	0.98	0.66	1.07	0.89	0.67	1.08	1.34	0.60	1.52	1.14	0.63	1.20	1.03	0.49
4	Measured	3862	3109	2.18	NC	NC	NC	4704	3238	2.5	NC	NC	NC	NC	NC	NC
	UFCM	3999	3740	13.0	4746	4037	12.9	4724	4029	12.9	4448	3921	12.9	4716	4026	13.0
	Ratio	0.97	0.83	0.17	--	--	--	1.00	0.80	0.20	--	--	--	--	--	--
5	Measured	1947	2541	5.7	NC	NC	NC	2054	3881	8.9	2012	3240	10	2380	2915	5.2
	UFCM	1794	2662	12.2	1898	2725	12.3	1965	2764	12.3	1891	2721	12.3	1957	2759	12.3
	Ratio	1.09	0.95	0.47	--	--	--	1.05	1.40	0.72	1.06	1.19	0.81	1.22	1.06	0.43

(1) Ratio= ratio of measured to predicted by UFCM

(2) NC= Not Captured

Table 2.6: Summary of the maximum displacement, strain, strain rate, and DIF

Shot	Max. deflection (mm)				Max. strain ($\mu\varepsilon$)	Max. strain rate ($1/s$)	Max. DIF (Cowper and Symonds)
	Measured	SDOF (DIF=1.00)	SDOF (DIF=1.24)	SDOF (DIF based on test[2])			
1	6.9	6.3	6.3	6.3	559	0.28	1.35
2	40.8	57.0	53.7	47.4	3435	0.90	1.48
3	33.2	40.8	36.4	34.5	2384	1.70	1.52
4	NC[1]	40.0	35.8	33.7	3610	2.89	1.62
5	62.8	91.5	76.5	66.1	2536[3]	1.40	1.51

(1) NC= Not Captured

(2) Average DIF obtained from actual strain rates

(3)The strain was measured at 1/3 of the span from the bottom

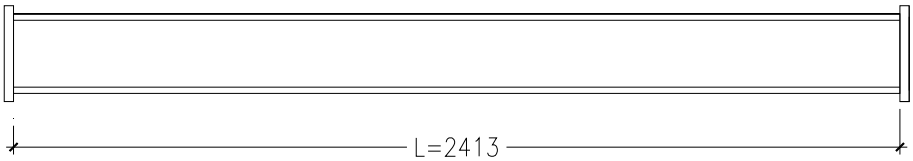

(a)

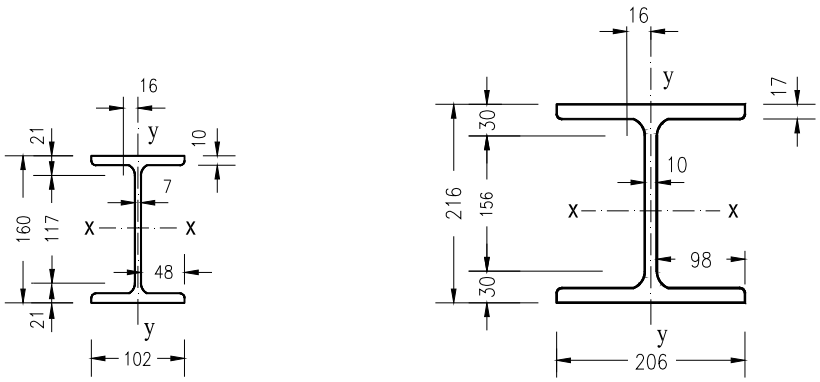

(b)

Fig. 2.1: (a) Typical test specimens and (b) cross-sections of the test specimens (all dimensions are in mm and the mass is in kg/m)

(a) Front view of test setup

(b) Side view of test setup

(c) Steel curtain (front view)

(d) Steel curtain (back view)

Fig. 2.2: Blast test setup

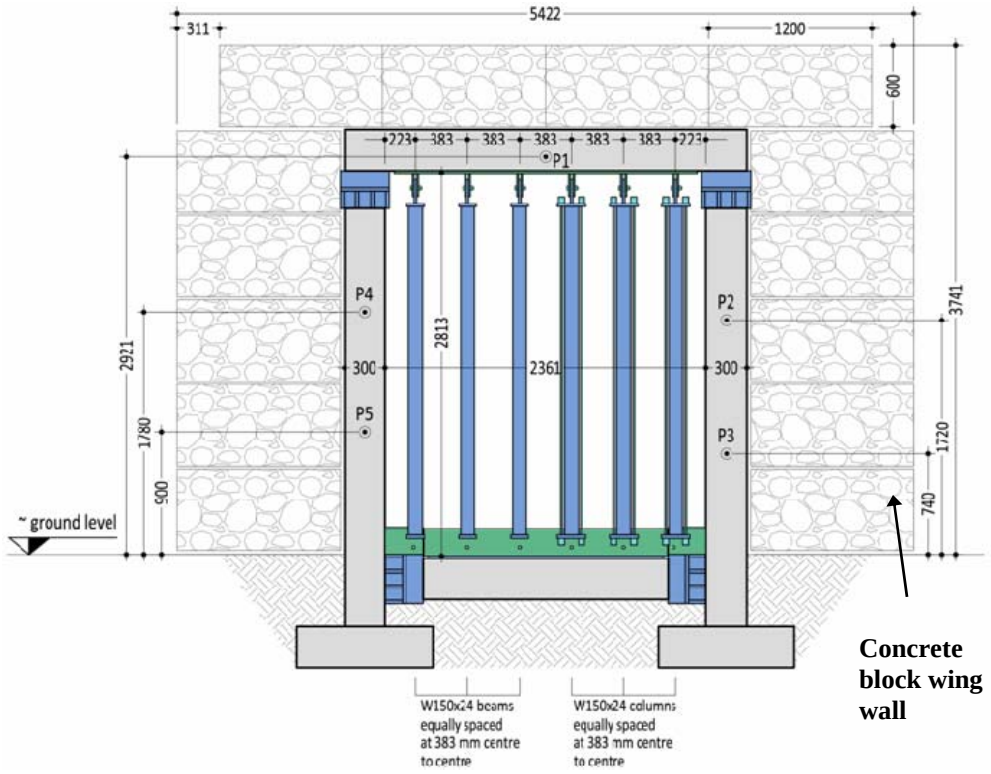

Fig. 2.3: Dimensions of the test frame and the reflecting surface (in mm)

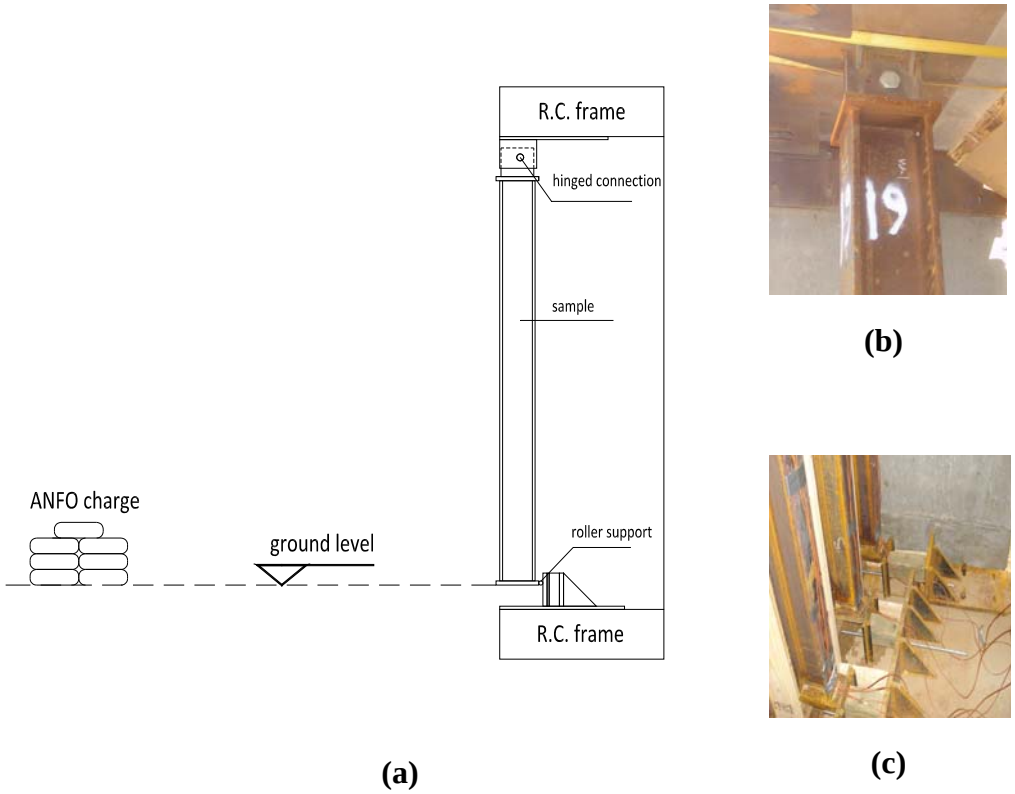

Fig. 2.4: (a) Schematic view of charge location, (b) beam hinged end, and (c) beam roller end

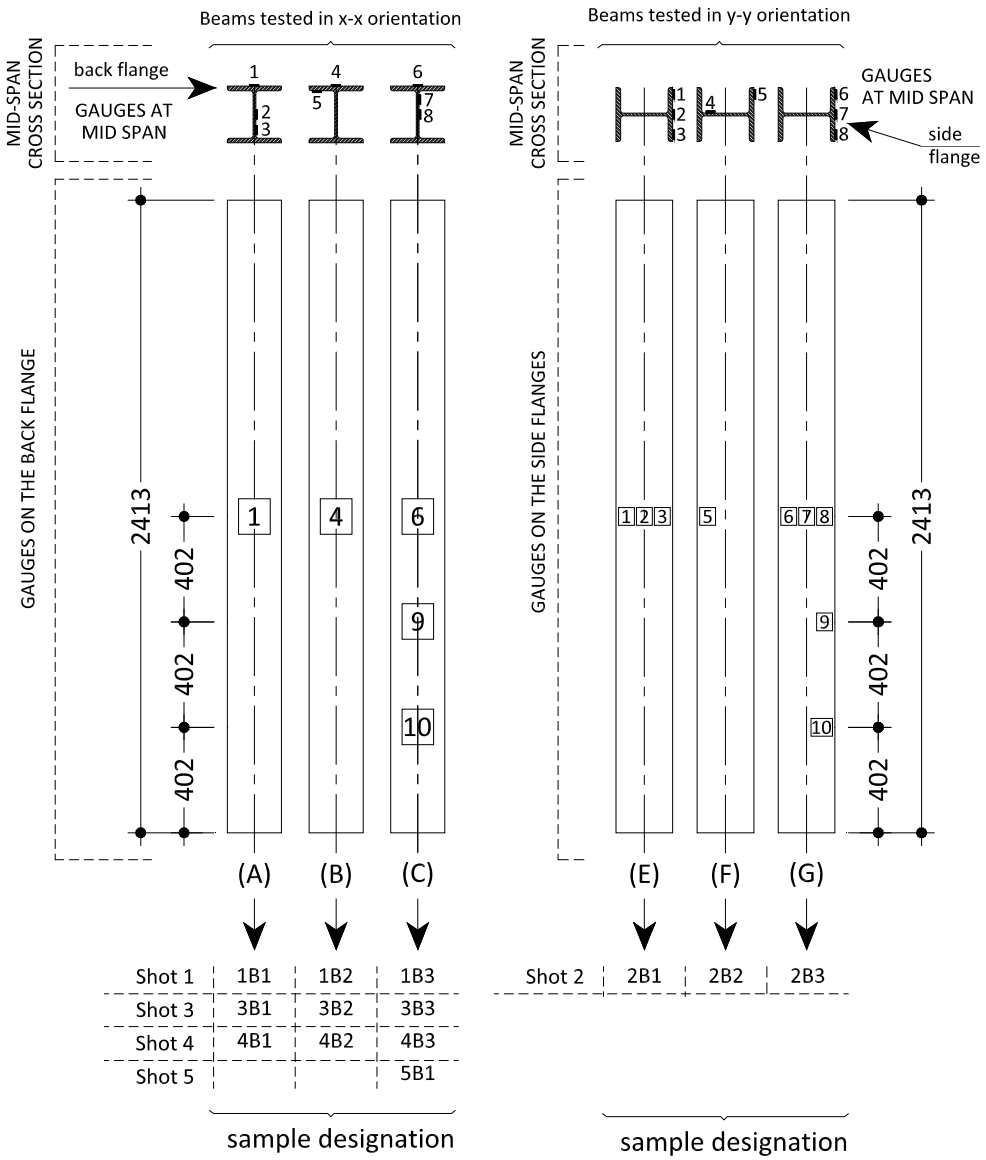

Fig. 2.5: The strain gauge layout arrangements

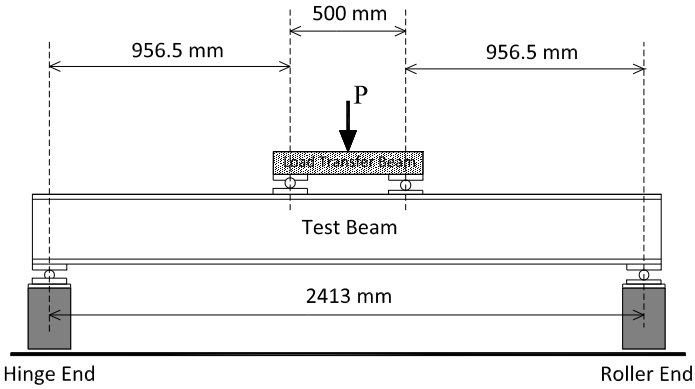

Fig. 2.6: Test setup for static testing

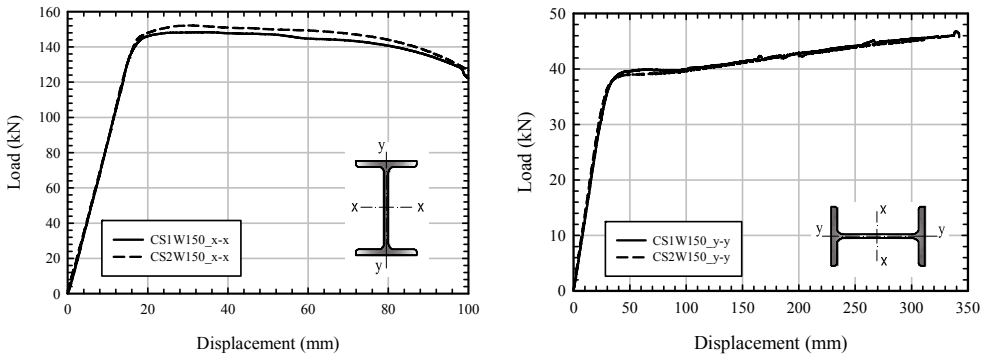

(a) Group I (b) Group II

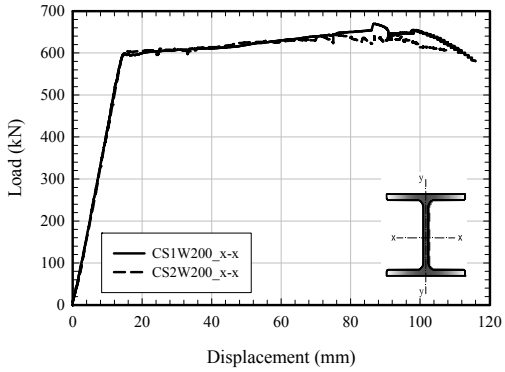

(c) Group III

Fig. 2.7: Static behaviour of test beams

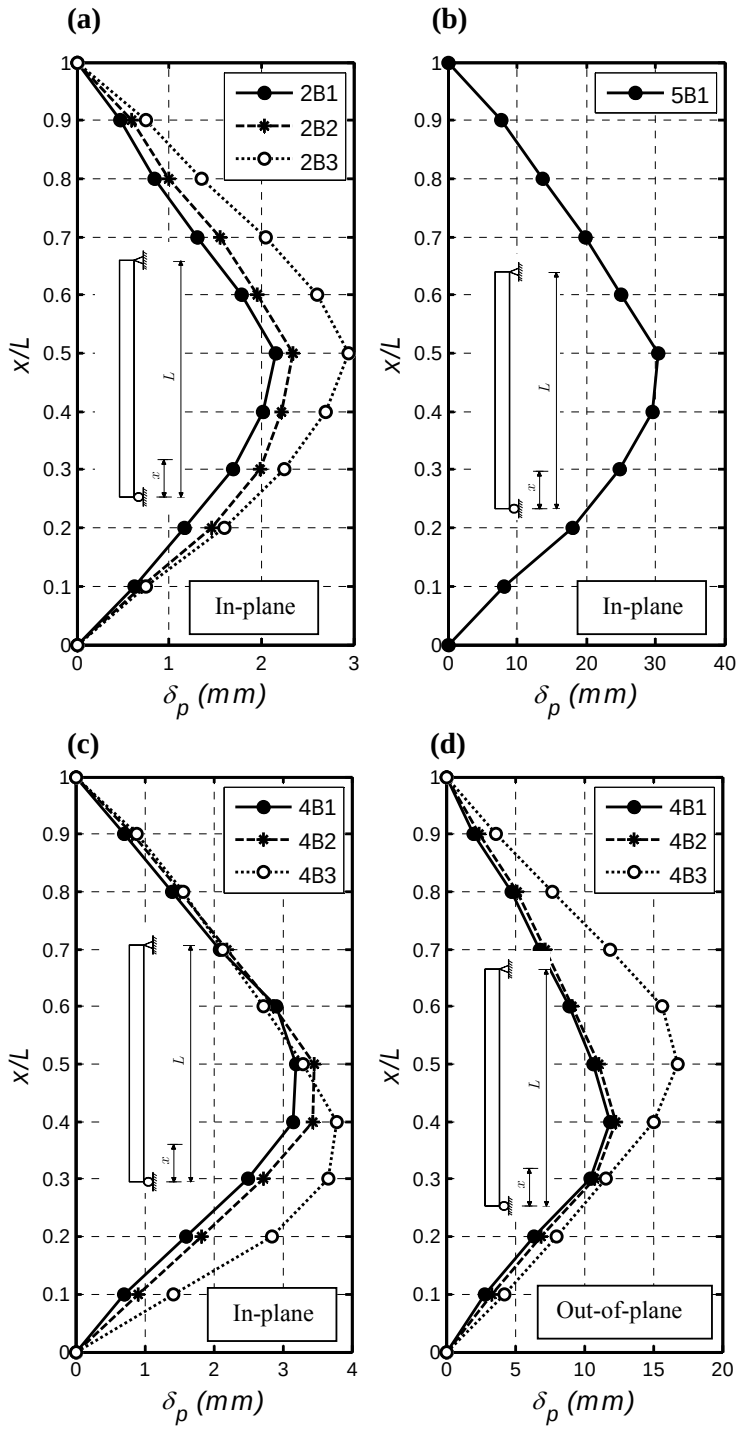

Fig. 2.8: Permanent deflected shape of steel beams after the blast tests

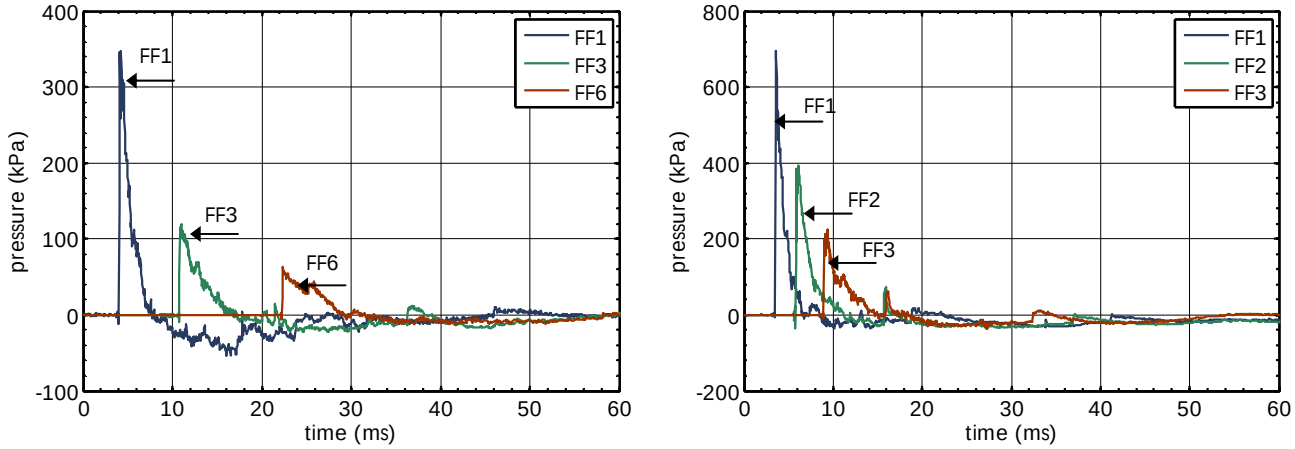

(a) Shot 1 (b) Shot 2

Fig. 2.9: Typical incident pressure obtained from free field gauges

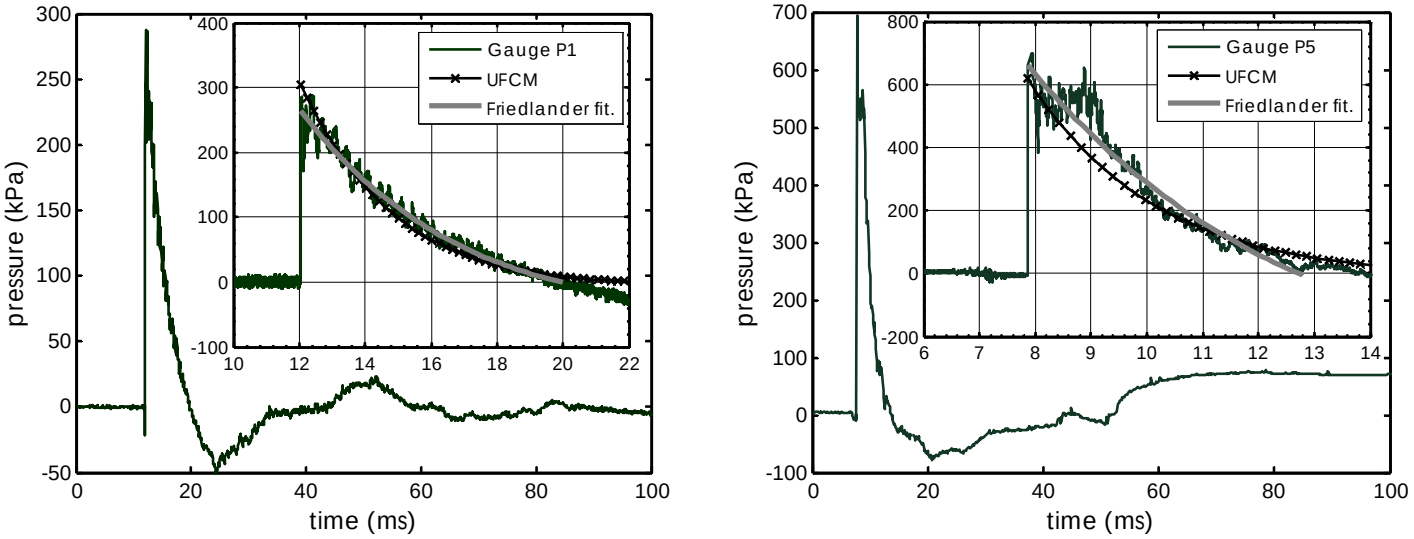

(a) Shot 1 (b) Shot 2

Fig. 2.10: Typical reflected pressure for blast shots

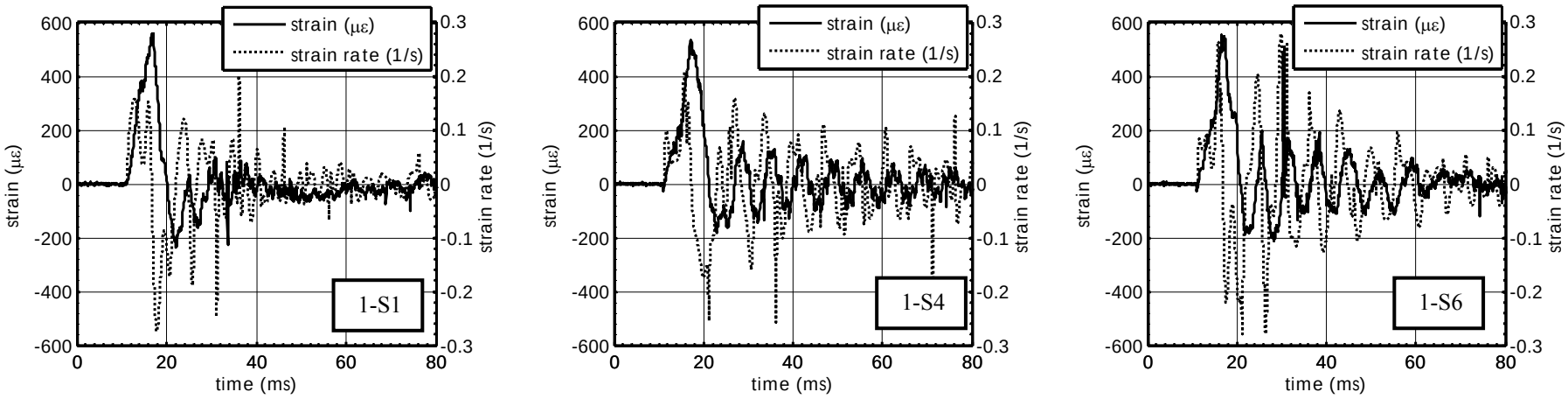

(a) SHOT 1: W=50 kg, SD= 10.3 m, Z=2.80 m/kg$^{1/3}$

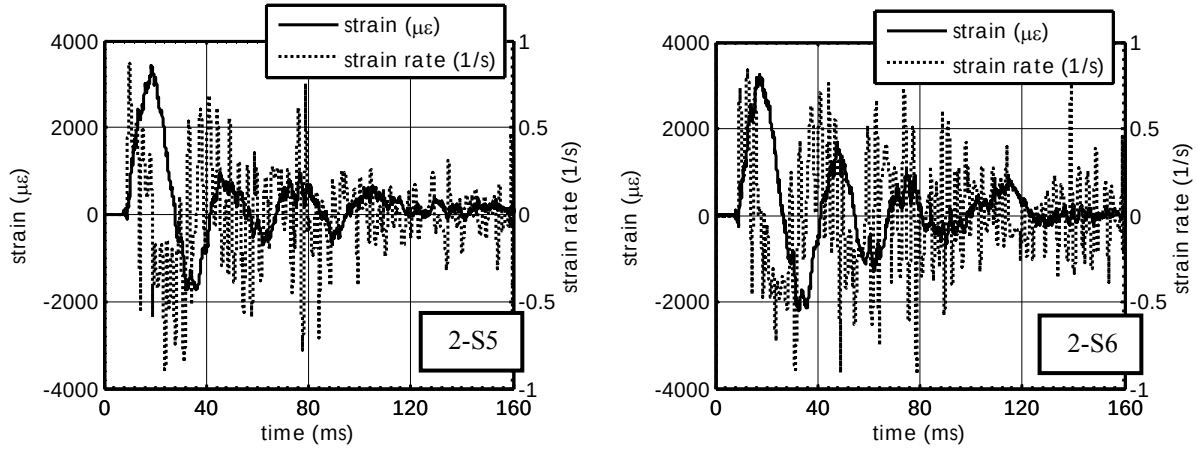

(b) SHOT 2: W=100 kg, SD= 10.3 m, Z=2.22 m/kg$^{1/3}$

Fig. 2.11: Mid-span strain time histories of test beams

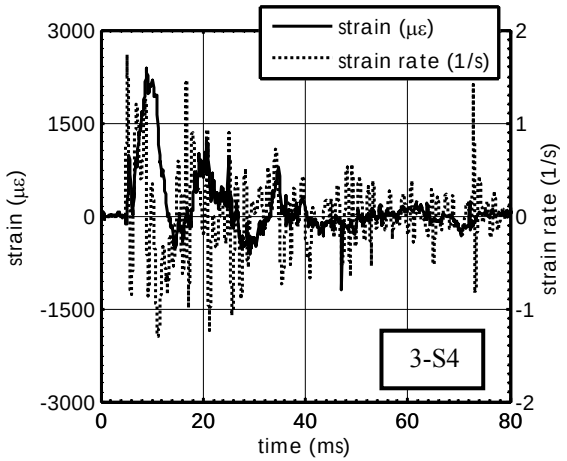

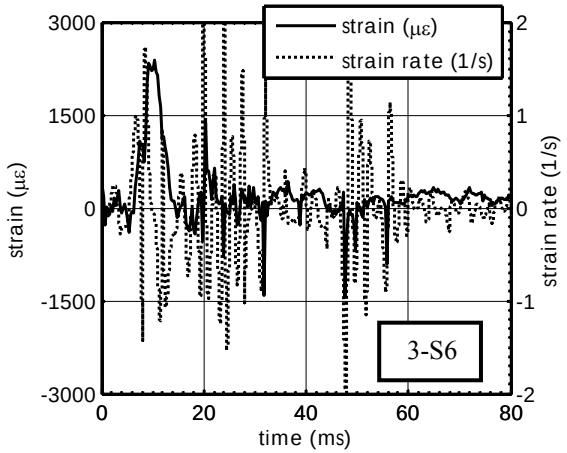

(c) SHOT 3: W=150 kg, SD= 9 m, Z=1.69 m/kg$^{1/3}$

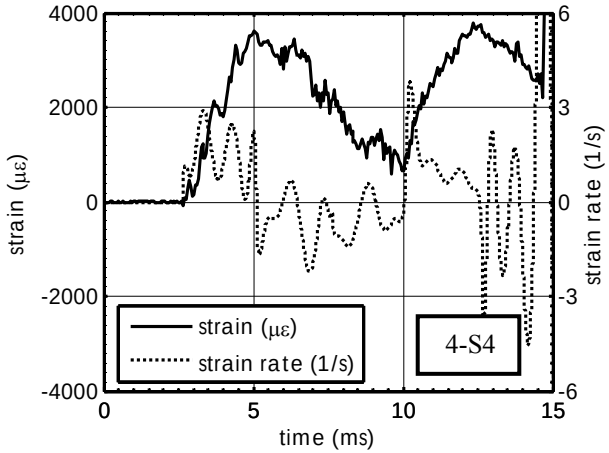

(d) SHOT 4: W=250 kg, SD= 7.0 m, Z=1.11 m/kg$^{1/3}$

Fig. 2.11: Cont.

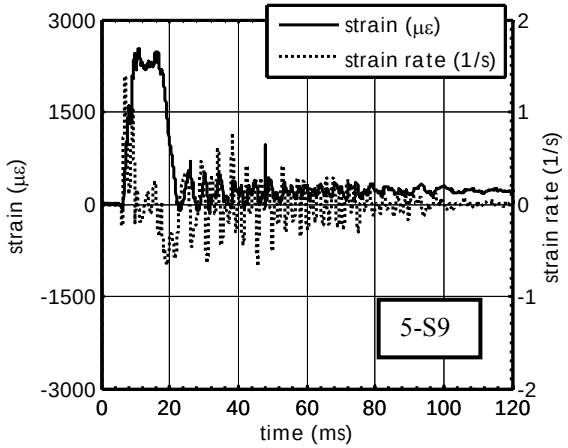

(e) SHOT 5: W=250 kg, SD= 9.5 m, Z=1.51 m/kg$^{1/3}$

Fig. 2.11: Cont.

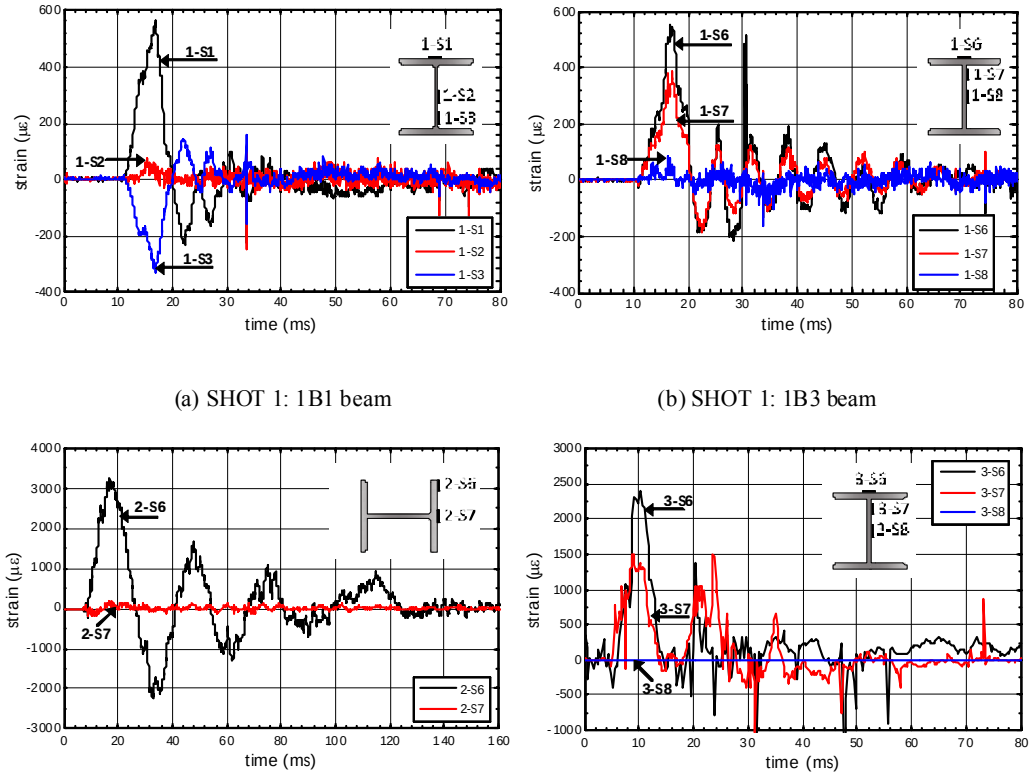

(a) SHOT 1: 1B1 beam

(b) SHOT 1: 1B3 beam

(c) SHOT 2: 2B3 beam

(d) SHOT 3: 3B3 beam

Fig. 2.12: Strain time histories at different locations over the cross-sections

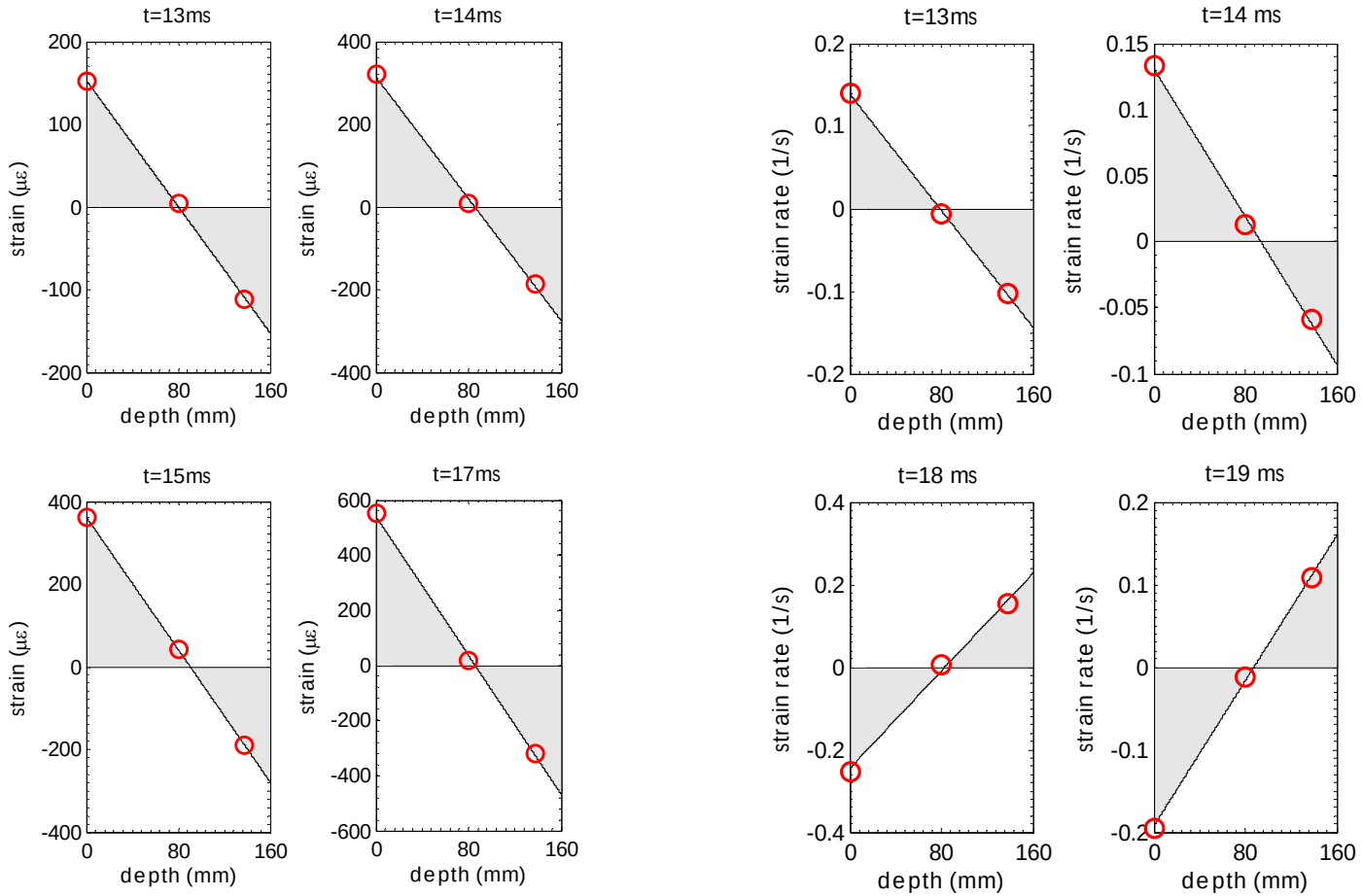

(a) (b)

Fig. 2.13: Strain and strain rate profile over the mid-span of beam 1B1

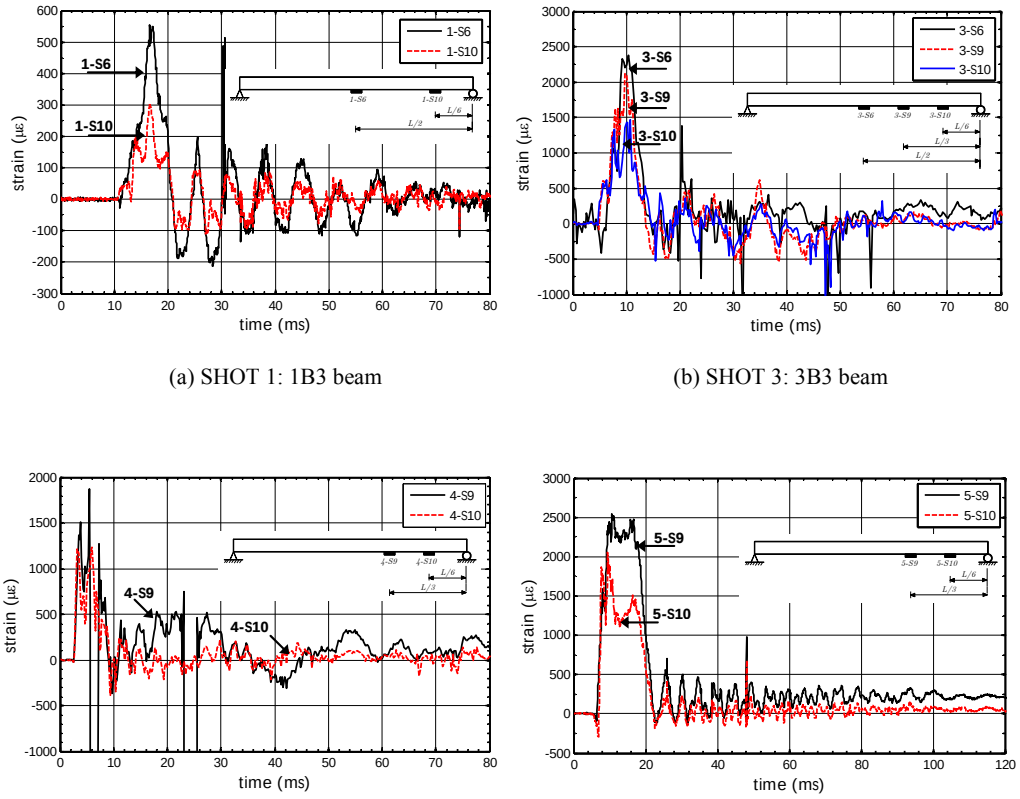

(a) SHOT 1: 1B3 beam

(b) SHOT 3: 3B3 beam

(c) SHOT 4: 4B3 beam

(d) SHOT 5: 5B1 beam

Fig. 2.14: Strain time histories along the length of the test beams

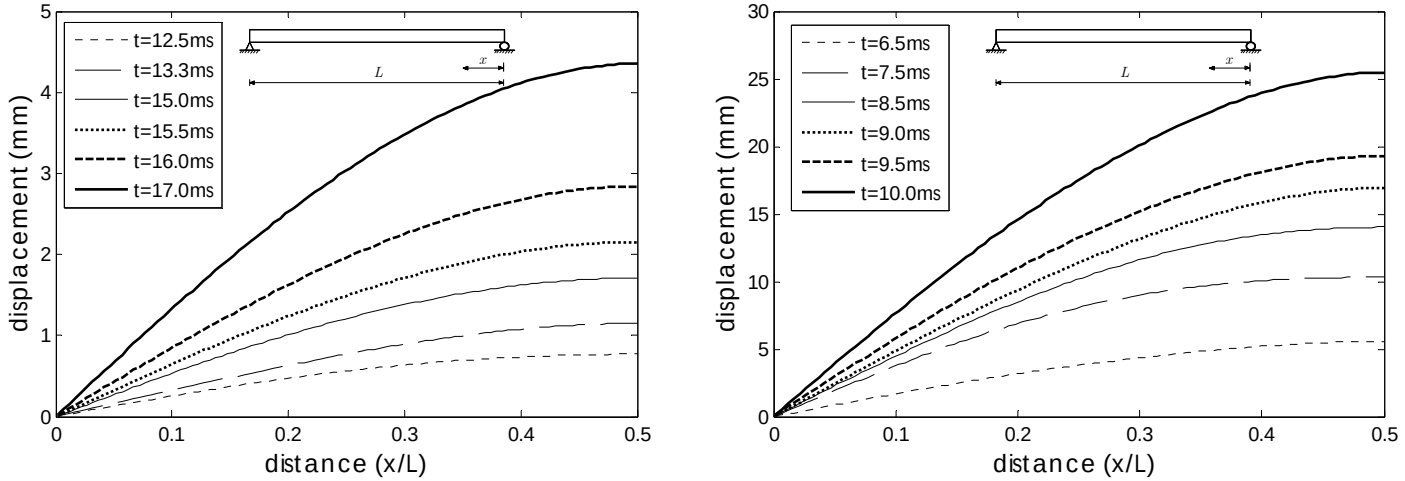

(a) SHOT 1: 1B3 beam

(b) SHOT 3: 3B3 beam

Fig. 2.15: Deflected shapes at different instants of time

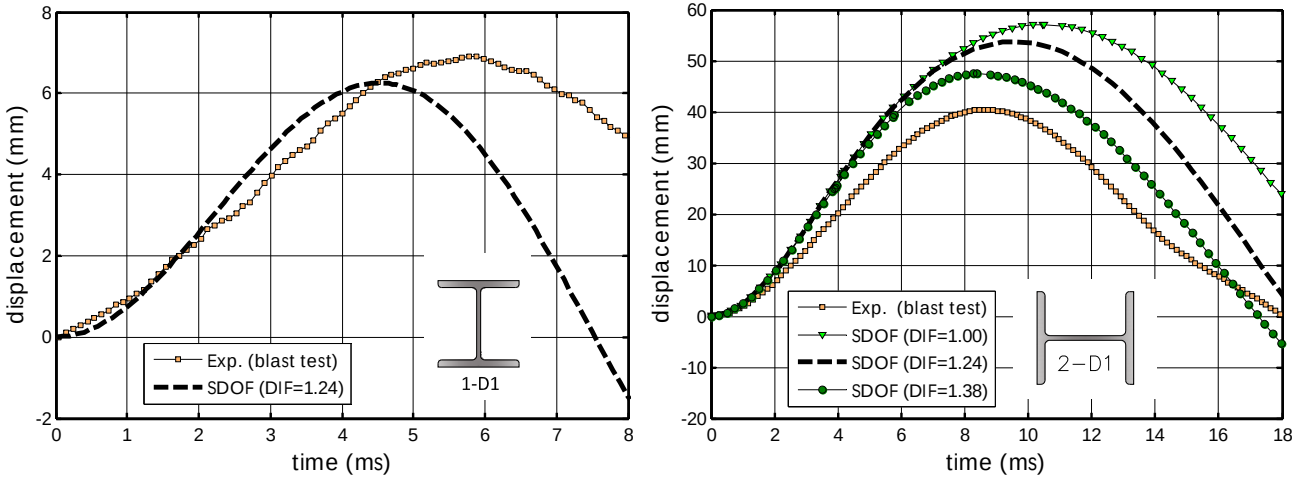

(a) SHOT 1: 1B3 beam (b) SHOT 2: 2B3 beam

Fig. 2.16: Mid-span displacement time histories of test beams

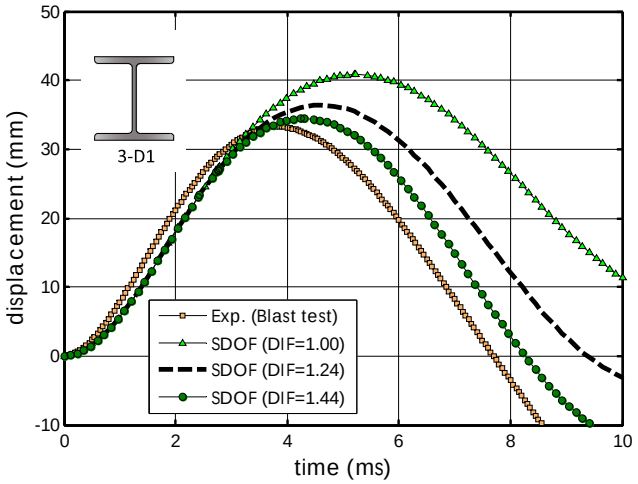

(c) SHOT 3: 3B3 beam

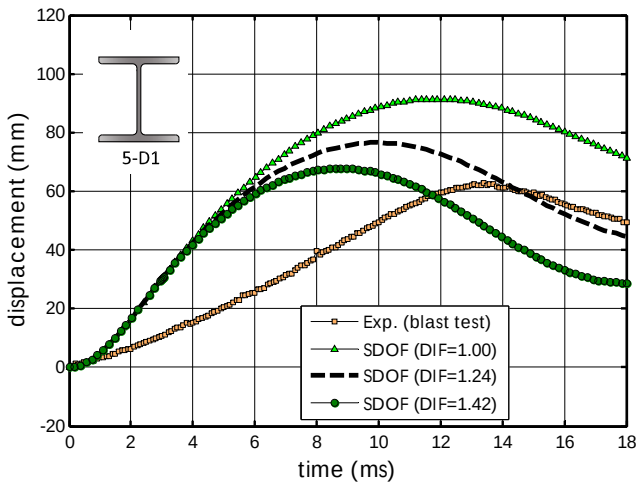

(d) SHOT 5: 5B1 beam

Fig. 2.16: Cont.

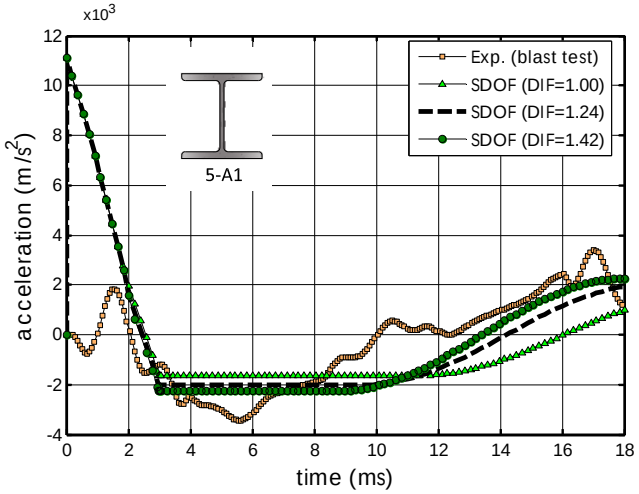

Fig. 2.17: Mid-span acceleration-time histories of beam 5B1

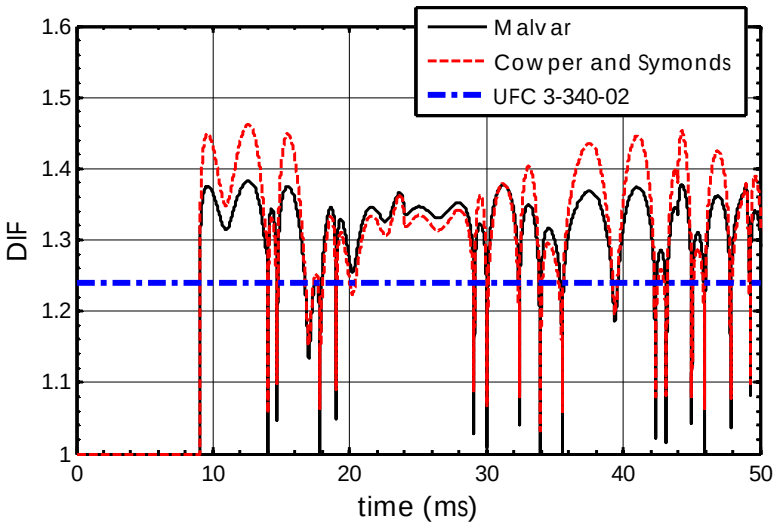

(a) SHOT 2: W=100 kg, SD= 10.3 m, Z=2.22 m/kg$^{1/3}$

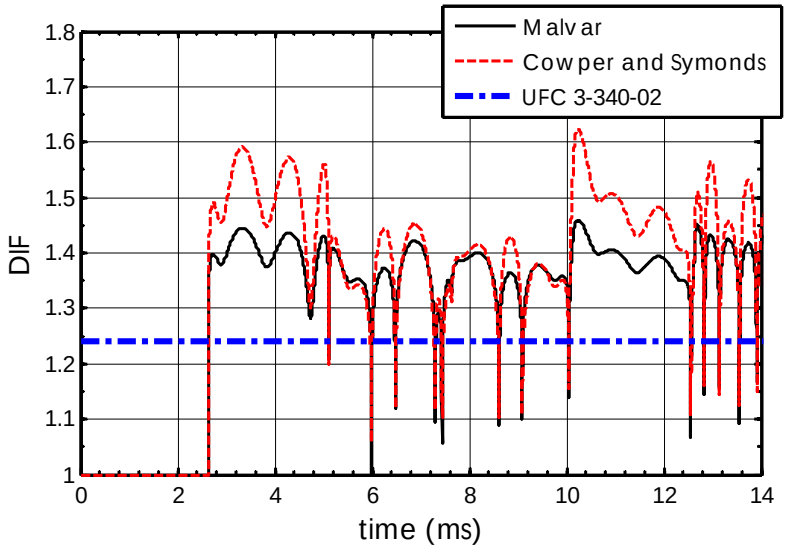

(b) SHOT 4: W=250 kg, SD= 7.0 m, Z=1.11 m/kg$^{1/3}$

Fig. 2.18: DIF-time histories for mid-span of test beams

Chapter 3: Single and Multi Degree of Freedom Analysis of Steel Beams under Blast Loading

3.1 Abstract

This paper presents detailed analysis of the results of field tests on 13 full scale wide flange steel beams subjected to blast loads generated by the detonation of up to 250 kg of ANFO explosive. The experimental results are analyzed using an equivalent Single-Degree-of-Freedom (SDOF) model of a beam, which includes material nonlinearity and strain rate effects. To account for strain rate effect on beam stiffness and strength, its full moment-curvature response is determined by dividing its cross-section into a number of layers and a strain rate-dependent stress-strain relationship, based on the Cowper-Symonds strain rate model, is used to capture the nonlinear stress distribution over the section. To determine the effects of higher modes of vibration and the variation of beam mechanical properties along its length on its dynamic response, the test beams are also analyzed using a Multi-Degree-of-Freedom (MDOF) model involving beam finite elements. Each element has two nodes and three degrees of freedom and is again divided into a number of layers to capture the strain rate effect and nonlinear stress distribution over its depth. The predicted displacements and strains by the two models are compared with the corresponding experimental data and the results show that for the given beams, the time-dependant deformations, internal forces, and moments can be adequately predicted by either model because the first mode of vibration is found to dominate their response; however, the use of a constant strain rate through the so-called Dynamic Increase Factor (DIF) can lead to highly conservative estimate of the actual strength of such members.

Keywords: Blast loads; Damage; Dynamic response; Explosions; Steel beams; Field tests.

3.2 Introduction

Modern steel buildings designed under the provisions of current codes, particularly lighter frame structures with non-moment resisting connections, may be incapable of maintaining structural integrity under severe blast loads. In the American Institute of Steel Construction specifications for steel structures in nuclear facilities (AISC 2006), it is stated that impactive and impulsive loads shall be considered concurrent with other loads in determining the required strength of structural steel elements, where impulsive loads include blast loads. To ensure the safety of these structures, it is important to design them for levels of strength and ductility, which would be adequate to resist the expected design-based threat level. The attainment of this goal requires the development of suitable blast-resistant design procedures and construction techniques.

Studies have been carried out to predict the response of structures under blast and impact loading in order to assess damage and mitigate the associated risk (Biggs 1964; Boutros 2000; Krauthammer et al. 1986; Krauthammer et al. 1990; Schleyer and Hsu 2000). These studies have focused on methods of analysis in which it is assumed that the first mode of vibration governs the dynamic response of structural members; however, there is not sufficiently detailed empirical data available from actual blast tests on full scale members to justify the generality of this assumption, particularly in the inelastic and plastic deformation ranges. The notion that a member can suddenly change its behaviour from an elastic deformed shape to a plastic one appears counterintuitive but is widely accepted and used in the development of Single-Degree-of- Freedom (SDOF) models in blast analysis (Biggs 1964, Baker et al. 1983, Krauthammer et al. 1990). Other analytical and numerical models with various degrees of sophistication are also available (Chen and Liew 2005; Liew 2008; Lee et al. 2009) to analyze the full dynamic response of steel members under blast loading, experimental validation of the results of these models by means of data from actual blast tests is also necessary, in particular of those aspects of the models that

are aimed at capturing the response of structural members over the inelastic range. It is important that detailed aspects of the response, such as spatial and temporal variation of member strains are captured during the test and compared with their predicted variations. The latter is necessary to confirm that the simple beam displacement function that is often used in the derivation of SDOF models can also represent strain variation with sufficient accuracy, given that strain is a function of the second derivative of the displacement function.

Based on the information available in the open literature, most research programs and government sponsored tests have focused on understanding the response of reinforced concrete and masonry structures to blast loading (Magnusson 2007; Oesterle et al. 2009; Schenker et al. 2008). The response of Fibre Reinforced Polymer (FRP) retrofitted concrete and masonry structures to blast loading has been also experimentally investigated (Davidson et al. 2004; Razaqpur et al. 2007; Tan and Patoary 2009; Wu et al. 2009). However, there are few studies that have experimentally investigated the resistance of structural steel members under blast loading (Lawver et al. 2003). Magallanes et al. (2006) investigated the behaviour of a W360X347 column with a clear height of 5730 mm (18'-9") subjected to 1818 kg (4000 pounds) of TNT-equivalent ANFO with a ground stand-off distance of 4750 mm (15'-6"). Only the peak residual deformation of the column above its base in the strong axis direction was reported after the test. Detailed experimental data for steel members subjected to blast loading is lacking partly due to security concerns in some countries and the desire to limit the dissemination of such information and partly due to the difficulty of obtaining reliable and detailed data in blast tests which are inherently destructive and make it difficult to protect the instrumentation (Jama et al. 2009). This lack of detailed experimental data makes it difficult to judge the validity and/or limitations of the assumptions made in various theoretical and numerical models.

One of the key characteristics of blast loading is the inducement of high strain rates in structural members. While a number of empirical models exist for

predicting the effect of strain rate on steel stress-strain behaviour, these models have been developed based mainly on data obtained from either split Hopkinson pressure bar tests on small steel specimens or from impact tests on steel members (Bassim and Panic 1999; Krafft et al. 1954; Malvar 1998; Manjoine and Pittsuburgh 1944; Soroushian and Choi 1987). These studies have shown that the yield strength exhibits an apparent increase with the increase of loading rate, the ultimate tensile strength increases only slightly, and the elastic modulus generally remains insensitive to the strain rate. Aspden and Campbell (1966) tested a set of low-carbon steel beams with rectangular cross-section in pure dynamic bending with maximum strain rate up to 20 /s. They also conducted dynamic axial compression tests on cylindrical specimens made of the same steel in order to correlate their results with those obtained from dynamic bending tests. The results showed that the curvature rate had a large influence on the behaviour of steel beams as demonstrated by the fact that the dynamic upper yield moment at strain rate of 12 /s increased by 80% compared to the static yield moment. The moment resistance subsequently decreased by 30% relative to the upper yield moment before increasing again as work-hardening commenced. This study showed that the dynamic flexural behaviour cannot be fully explained by using the data obtained from uni-axial compression tests in conjunction with elementary theory of plastic bending since such calculations would result in a much smaller upper yield moment and a constant moment resistance prior to initiation of work-hardening.

In order to account for the effect of strain rate on the strength of a beam, in current practice the material static strength is increased by multiplying it by the so-called Dynamic Increase Factor (DIF). The DIF is given as function of the strain rate using rate sensitive models (Jones 1988; Malvar 1998), which are based on data obtained from small steel specimens tested in uni-axial tension. For instance, the use of DIF is recommended by ASCE (1997) and UFC 3-340-02 (USDOD 2008) design guidelines to calculate the resistance of structural

members . In a SDOF model only one DIF value is used to represent the strain rate effect on the entire member while in reality it varies both over the member depth and length. This might result in overestimating the effect of the strain rate on a member ultimate resistance, especially in the case of sections with high A_w/A_f ratio, where A_w and A_f are the cross-sectional areas of the web and the flange, respectively. In statically indeterminate beams, variations in stiffness and strength caused by stress-strain nonlinearity and strain rate effects could lead to internal force distributions quite different from those based on the assumptions of uniform stiffness along such members.

Multi-Degree-of-Freedom (MDOF) models, similar to the one used in the current analysis, can account for the actual spatial and temporal variations of strain rate, albeit they are more complex and time-consuming to use, but does the expected higher accuracy justify the extra effort? To answer this question and to ascertain the relative accuracy of each method, in this paper two dynamic analysis models are applied to analyze a series of beams tested by Nassr et al. (2011) under blast loads generated by the explosion of up to 250 kg of ANFO explosive at different scaled-distances. Verification of such models by detailed experimental data has not been previously reported in the literature, yet this is necessary in order to gain confidence in their predictions.

3.3 Experimental program

The experimental results used in this investigation were obtained from a test program conducted by Nassr et al. (2011). The full details of the program will not be repeated here, but for clarity and completeness, a brief description is necessary and is therefore provided. Thirteen typical wide flange steel beams, with either a W150X24 or W200X71 section, and with span length of 2413 mm (95 inches), were field tested under blast loading. The nominal static yield and ultimate strength of the W150X24 section were 393 and 537 MPa, respectively, while those of the W200X71 section were 362 and 474 MPa. Table 3.1 shows the test

matrix, including the charge mass, ground stand-off distance, scaled-distance, section designation, and the orientation of each beam during the test, i.e. the axis of bending of the section under the blast pressure. The ground stand-off distance ranged from 7 to 10.3 m while the charge size varied from 50 to 250 kg. The twelve beams tested in shots 1 to 4 had W150X24 section while the one beam tested in shot 5 had W200X71 section.

Figures 3.1(a) and (b) show the front and side views of the test setup, which comprised a reinforced concrete frame and a steel container behind it. Wing walls were built on the sides and top of the frame to reduce the effect of blast wave clearance. The frame supported the test specimens while the steel container housed the instrumentations and prevented the blast wave from wrapping around the test specimens. For convenience, the beams were tested in the vertical position and simply supported. They were subjected mainly to bending caused by the blast pressure as the axial stress due to self-weight was practically negligible. All the beams were pinned at the top and roller supported at the bottom. The same setup was used for shots 1 to 4 while shot 5 had a slightly different set-up as described below.

The maximum amount of explosive that could be detonated at the particular tests site was 250 kg of ANFO. Considering this limitation and the desire to ensure a reasonably uniform pressure acting on the test specimens, a ground stand-off distance of 9.5 m was chosen for the W200X71 section, resulting in a scaled-distance of 1.51 m/kg$^{1/3}$. As the predicted reflected pressure for this scaled-distance acting on the surface of the beam flange facing the blast was deemed to be insufficient to cause sufficiently high stresses in the beam, it was decided to increase the blast load acting on it by placing a 1.18 m wide and 2.50 m high steel curtain in front of it, with the curtain designed to transfer the blast pressure acting on its surface to the beam flange, thus magnifying the blast load on the beam. Details of the steel curtain are given by Nassr et al. (2011), but it suffices to state that it had very high stiffness in the horizontal direction but

negligible stiffness in the vertical direction. The high horizontal stiffness allowed for an efficient load transfer without significant energy absorption through deformation of the curtain elements while the low vertical stiffness enabled the curtain to follow the test beam deformed shape in the in-bound displacement, without interfering with its stiffness. Given that the mass of the curtain relative to the beam was approximately 3 and the two were in initial contact, it is reasonable to assume that they would remain in contact during the in-bound motion up to at least the point of maximum displacement. This supposition is supported by the frequency response analysis of the experimental measurements later in this paper. The geometry of the curtain is not expected to play a significant role in the determination of the dynamic behaviour of the beam. Clearly a different tributary area will change the magnitude of the load and its associated impulse, resulting in a change in the amplitude of the response, but it is not expected to change the nature of either the elastic or plastic response. This can be easily shown by the fact that the response is linearly proportional to the amplitude of the pressure (Biggs 1964).

During the blast tests, reflected pressures, strains, and displacements were measured. The reflected pressure was measured by five pressure transducers that were installed at different positions on the concrete frame and are labeled as P1 to P5 in Fig. 3.1(a). The mid-span displacements were measured for one beam in each shot using potentiometers. In addition, the strain time-histories were measured at different locations along the specimen. All the data were automatically recorded by data acquisition equipment at a sampling rate of 1 MHz.

In the following, typical blast load and member response parameters measured during the test will be compared with their predicted values, using two well known blast analysis modelling methods.

3.4 Experimental versus predicted blast pressure wave parameters

The response of a structure or element to a blast event is strongly dependent on the spatial and temporal distributions of the blast pressure and its magnitude. Therefore, the relatively accurate prediction of these quantities is important for assessing a member's response to a blast event. Blast load parameters are in practice often determined by using a set of empirical relations that are plotted in the form of charts or fitted into equations. There are also some closed-form semi-empirical expressions available that can be used to estimate the blast parameters. Alternatively, numerical methods based on laws of conservation of energy, mass and momentum and a given equation of state may be used within the framework of computational fluid dynamics to obtain the blast load parameters (Lee et al. 2009). However, the latter is not widely used in structural engineering applications, particularly in the case of simple geometries such as the one in the present tests. In this study, the predictions of two blast load models will be investigated.

A typical reflected pressure time-history obtained in shot 1, which involved a charge size of 50 kg at stand-off distance of 10.3 m, is shown in Fig. 3.2. It can be seen that the blast wave is characterized by the typical rapidly rising peak pressure P_r of 270 kPa, followed by decay towards the ambient pressure, within positive phase duration t_d of approximately 20 ms, followed by a negative pressure phase. The latter phase is commonly neglected in design of structural members and therefore will not be further discussed. The area beneath the pressure time-history represents the impulse, and its variation with time is also shown in Fig. 3.2 with a maximum impulse of 780 kPa.ms, which was obtained by numerically integrating the area under the pressure time profile. For structural elements whose natural period is much greater than the positive phase duration of the blast pressure acting on them, the member response is governed by the maximum impulse rather pressure, therefore, knowing the maximum impulse

becomes more important than knowing the actual pressure variation with time (Baker et al. 1983; Smith and Hetherington 1994).

In empirical and semi-empirical methods, blast wave parameters namely the pressure, impulse, and positive phase duration, are commonly expressed in terms of the scaled-distance Z

$$Z = \frac{SD}{\sqrt[3]{W}} \tag{3.1}$$

where SD is the stand-off distance in meters and W is the charge mass in kilogram (kg). Kinney and Graham (1985) proposed the following semi-empirical equation for the reflected pressure P_r expressed in kPa

$$P_r = 0.20 P_s \left(\frac{7P_o + 4P_s}{7P_o + P_s} \right) \tag{3.2}$$

in which P_o is the atmospheric pressure and P_s is the incident overpressure which is given in terms of Z as (Kinney and Graham 1985)

$$\frac{P_s}{P_o} = \frac{808\left[1 + \left(\frac{Z}{4.5}\right)^2\right]}{\sqrt{1 + \left(\frac{Z}{0.048}\right)^2}\sqrt{1 + \left(\frac{Z}{0.32}\right)^2}\sqrt{1 + \left(\frac{Z}{1.35}\right)^2}} \tag{3.3}$$

Similarly, the positive phase duration t_d, expressed in milliseconds (ms), was given as (Kinney and Graham 1985)

$$\frac{t_d}{W} = \frac{980\left[1 + \left(\frac{Z}{0.54}\right)^{10}\right]}{\left[1 + \left(\frac{Z}{0.02}\right)^3\right] + \left[1 + \left(\frac{Z}{0.74}\right)^6\right] + \sqrt{1 + \left(\frac{Z}{6.9}\right)^2}} \tag{3.4}$$

On the other hand, Prugh (1999) expressed positive reflected impulse I_r in kPa.ms as follows

$$\frac{I_r}{W^{1/3}} = 8.97\left(\frac{200}{Z^{1.5}} + \frac{125}{Z}\right) \tag{3.5}$$

In addition, all blast wave parameters are compared with results obtained using an empirical relationship by fitting a high order polynomial to the data points reported in UFC-3-340-02 (USDOD 2008). This relationship gives results that are practically identical to those given by the relationships developed by Kingery and Bulmash (1984), which is the basis for the well known blast prediction software CONWEP (Hyde 1990). For the sake of clarity, the relationship used in this study will be referred to as the UFC-Model (UFCM).

To assess the accuracy of the predictions of these approaches, the reflected pressure, positive impulse and positive phase duration obtained from all the transducers in the five blast shots in this study are compared with UFCM predictions and with those obtained from Eq. (3.2), (3.5), and (3.4) in Figs 3.3(a), (b), and (c), respectively. As can be noticed in Fig. 3.3(a), the reflected pressure predictions deviate noticeably from the corresponding experimental results. The UFCM predicted values agree relatively better than those obtained by using Eq. (3.2). The mean value of experimental/predicted pressures ratio is 1.06 and 1.63, with Coefficient of Variation (COV) of 13% and 12% for UFCM and Eq. (3.2), respectively. On the other hand, as shown in Fig. 3.3(b), both UFCM and Eq. (3.5) predict reasonably well the experimental reflected impulse values. The mean values of the ratio of measured/predicted impulse are 1.02 and 0.98, with COV of 15% and 15% for UFCM and Eq. (3.5), respectively. Based on these results, Eq. (3.5), provides a quick and reasonably accurate means to predict the impulse for far range blast loading scenarios. The positive phase duration predictions are shown in Fig. 3.3(c). As can be noticed, both the UFCM and Eq. (3.4) predictions poorly compare with the experimental results. The mean values of the ratio of measured/predicted positive phase duration are 0.66 and 1.22 with COV of 15% and 20% for UFCM and Eq. (3.4), respectively.

It is generally understood that there is a certain degree of uncertainty inherent in the computed values of wavefront parameters due to some random and/or disregarded factors, which may affect the predicted structural response.

These factors include atmospheric pressure, charge shape, ground characteristics, detonation process, charge height, etc. (Baker et al. 1983). For instance, the form of the shockwave front may be affected by the shape of the explosive charge, although for surface bursts and relatively large scaled-distances, it is customary to assume a hemispherical wave front (Bogosian et al. 2002).

For far range explosions, usually a uniform pressure is assumed on surfaces of small to medium height impinged by the blast. In order to investigate the degree of uniformity of the reflected pressure and impulse acting on the tested steel beams, Figs 3.4(a) and (b) show the reflected pressure and impulse contours, predicted by UFCM, over the face of the test frame in shots 1 and 4, shots which in the current tests had the maximum and minimum scaled-distance, respectively. In these figures, the beam locations are indicated by the dashed lines. As expected, the non-uniformity of the blast pressure distribution tends to increase with decreased values of scaled-distance. The reflected peak pressure and impulse varied by 6% and 18% along the beam length for shots 1 and 4, respectively. However, in the tests by Nassr et al. (2011), the pressure and impulse variations along the test beams did not exhibit a consistent trend, i.e. being highest at the point with the smallest scaled-distances and lowest at the point with largest scaled-distances. Given this fact and the relatively small differences between the recorded pressures and impulses from the five pressure transducers in each blast shot, it can be reasonably assumed that uniform pressure and impulse acted along each beam, which is represented by the average of the five pressure time-histories recorded in each shot.

3.5 Models for predicting the response of structures to blast loads

One of the key objectives of the present investigation was to ascertain the level of accuracy of SDOF model versus the MDOF model in predicting the detailed response of steel beams subjected to different blast intensities. In the following,

the SDOF and MDOF models used in the current investigation are described, followed by the comparison of their predictions with the experimental data.

3.5.1 Single-degree-of-freedom model

The key assumption of a SDOF model is that the real beam can be represented by an equivalent spring-mass system, as shown in Fig. 3.5. The dynamic response of the beam is approximated by its first mode shape, and typically a shape function ϕ is assumed to represent the actual deformed shape taken by the member during its motion. For the model developed and used in the current study, ϕ was chosen as the deflected shape of a simply supported prismatic beam under uniform static load. Thus the following shape functions were used for the elastic and plastic deformed shapes

$$\phi(\xi) = \begin{cases} 1 - \frac{24}{5}\xi^2 + \frac{16}{5}\xi^4 \; ; \quad \xi = \frac{z}{L} - \frac{1}{2} & \text{(elastic range)} \\ 1 - 2|\xi| & \text{(plastic range)} \end{cases} \tag{3.6}$$

where $\xi = (z/L\text{-}1/2)$ is a natural coordinate, z is the Cartesian axial coordinate of a point on the beam measured from the left support and L is the beam length (Fig. 3.5(a)). In the plastic range, in conformity with the usual assumption of plastic analysis, it is assumed that under uniform pressure beam deformation is concentrated at the location of the plastic hinge at mid-span of the beam and the rest of the beam only experiences rigid body motion.

In order to define an equivalent SDOF system, it is necessary to evaluate the parameters of the system, namely, the equivalent mass M_e, spring constant K_e, and load $F_e(t)$. Following Biggs (1964), the mass and load transformation factors K_M and K_L , respectively, can be easily derived based on the assumed shape functions and the concept of energy equivalency between the actual beam and its idealized SDOF model. These factors are listed in Table 3.2 for both the elastic and plastic states. Since the transformations factors are based on the integration of the deformed shape over the member span, the choice of a specific deflected

shape has no significant effect on their value, provided that the assumed shape satisfies the kinetic boundary conditions of the member (Baker et al. 1983; Smith and Hetherington 1994). For instance, the shape function associated with uniformly distributed and linearly varying static loads would lead to practically equal transformation factors. Consequently, the dynamic equation of motion of the equivalent SDOF system can be written as

$$K_M M \ddot{y} + K_L R = K_L P(t) \tag{3.7}$$

or

$$K_{LM} M \ddot{y} + R(y) = P(t) \tag{3.8}$$

where $\ddot{y}$ is the equivalent mass acceleration and is equal to the actual beam mid-span acceleration, M, $R(y)$, and $P(t)$ are the beam mass, resistance, and load, respectively. K_{LM} is the so-called load-mass factor given by $K_{LM}=K_M/K_L$, and its values are listed in Table 3.2. The resistance $R(y)$ of the beam is idealized by an elastic-perfectly plastic relationship, which is equal to Ky in the elastic stage and $R_{\mathrm{m}} = {}^{8M_p}\!/_{L}$ in the plastic stage. Quantities y, $K = {}^{384}\!/_{5L^2}.{}^{EI}\!/_{L}$, and M_p are the beam mid-span displacement, elastic stiffness, and plastic moment capacity, respectively (Biggs 1964).

In this study the moment M_p was determined by assuming an elastic-perfectly plastic stress-strain relationship for steel and by including the strain rate effect on its yield strength. This relationship was used to determine the full strain rate-dependent moment-curvature response of each section. The beam cross-section was divided into a number of layers, Fig. 3.6, and based on the assumption of linear strain and strain rate distribution over the depth of the section, the stress in each layer was determined. Accordingly, the resultant axial force in the i^{th} layer was written as

$$F_i = \sigma_i(\varepsilon_i)\mathrm{DIF}(\dot{\varepsilon}_i) w_i \Delta s \tag{3.9}$$

where w_i, Δs, $\sigma_i(\varepsilon_i)$, and $\mathrm{DIF}(\dot{\varepsilon}_i)$ are the layer width, thickness, stress and strain rate-dependent dynamic increase factor, respectively. The DIF was

determined as function of its strain rate using the Cowper and Symonds strain rate model (Jones 1988)

$$\text{DIF} = 1 + \left(\frac{\dot{\varepsilon}}{D} \right)^{1/q} \tag{3.10}$$

where D and q are constants for the particular material, and were taken as $D = 40$, and $q = 5$ for steel (Jones 1988). The resulting moment resistance of the cross-section was obtained by summing the moments of the layer forces about the centroid of the section. The maximum moment resistance thus calculated was used in the SDOF model to define the plastic limit of the resistance function.

The strain rate at any time was obtained by differentiating, using the central difference method, the recorded strain time-histories of the mid-span of each beam. As reported by Nassr et al. (2011), the maximum strain rates in shots 1 to 4 ranged from 0.28 to 2.89 /s, which appear to follow a linear relationship with scaled-distance as shown in Fig. 3.7. The mid-span strain gauge in shot 5 failed to capture any data; therefore, the maximum strain rate computed from strain time-history measured at 1/3 of beam span was reported as 1.40, which does not follow the linear relationship in Fig. 3.7. Figures 3.8(a) and (b), respectively, show the strong (x-x axis), and weak (y-y axis), moment-curvature relationships for section W150X24 corresponding to the maximum strain rates measured in the current tests.

Figure 3.8(c) shows the x-x axis moment-curvature relationship for section W200X71, corresponding to the maximum strain rate measured in this beam. The moment-curvature diagrams of the two sections based on an average DIF=1.24, as recommended by UFC 3-340-02 (USDOD 2008) and as commonly assumed in practice, are also shown in Fig. 3.8. It can be observed in the latter figure that the strain rate has noticeable influence on the maximum capacity of the section. It can also be noticed that the DIF recommended by UFC 3-340-02 (USDOD 2008) underestimates the maximum moment capacity in each case in the present test beams. This may have an adverse effect on the design of supporting members and

connections for beams under blast loads. In a subsequent section, the detailed measured response parameters of the test beams will be compared with the predictions of the above SDOF model.

3.5.2 Multi-degree-of-freedom model

In this case, as shown in Fig. 3.9, the test beams were discretized by using a number of two-dimensional beam elements with six degrees of freedom. Each beam was idealized as a layered element through its depth in order to capture its detailed response and to account for strain rate variation through its cross-section and along its length. The following nonlinear dynamic equation of motion was solved

$$[M]\ddot{y}+[K]y=\{F(t)\} \tag{3.11}$$

where $[M]$ and $[K]$ are the mass and stiffness matrices, and $\{F(t)\}$ is the load vector. Each beam was divided into 24 elements along its length and 16 layers or filaments through its depth. A diagonal lumped mass matrix was used and shear deformation and rotational inertia were neglected as they do not significantly influence the natural frequency and structural response for ratios of the radius of gyration to the span length of the order of 10^{-3} or less (Chopra 2001). The element stiffness matrix was obtained by summing the contribution of each layer to the total axial and flexural rigidity of the section. As in the case of the SDOF model, the variation in strain and strain rate in each layer and their effect on section strength and rigidity at each node were included in the analysis. The Newmark (ASCE 1997) time integration method was used to solve Eq. (3.11) in an incremental fashion. ASCE (1997) recommends that the maximum time-step be chosen as either one tenth of the natural period of vibration of the member or one tenth of the duration of the blast, whichever is smaller. In the present tests, in each case the positive phase duration was significantly shorter than the beam natural vibration period; therefore, the value of one tenth of the blast duration governed. At each time step in the analysis, based on the pressure time-history,

the pressure was assumed to act uniformly over the reflecting surface; i.e. it was assumed uniformly distributed over the flange surface facing the blast wave (shot 1 to shot 4) and over the steel curtain (shot 5). It should be noted that in compliance with standard practice, structural damping was neglected because under blast loading the first cycle of response normally dominates the member behaviour. The analysis yielded the full response of each beam, including its displacement, strain, velocity, acceleration, internal shear force and moment responses.

3.6 Comparison of models predictions with the experimental data

3.6.1 Displacement time-histories

Figure 3.10 shows the measured mid-span displacement time-histories of the test beams in shots 1 to 5 and their corresponding values using the above SDOF and MDOF models. Generally, as can be seen in Fig. 3.10, both models predict reasonably well both the peak and overall displacement response of the beams in shots 1, 2, and 3. The peak displacement predicted by the SDOF model for the beams in shots 1, 2, and 3 were 6.5, 43, and 30.2 mm, differing by 6.2, 5.3, and 8.3%, respectively, from the corresponding experimental values. The same displacements predicted by the MDOF were 6.7, 46.2, and 32 mm, differing by 3.3%, 12%, and 3.5 %, respectively, from the corresponding experimental values. Note that the displacement transducer used for measuring the displacement time-history of the beam in shot 4 failed to capture any data because it was destroyed by the blast and falling debris.

In evaluating the dynamic response of the beam in shot 5, one must consider the effect of the curtain on the response of the beam. As stated earlier, due to the particular design of the blast curtain, it is reasonable to assume that the curtain had negligible bending stiffness in the vertical direction, therefore it would not have altered the beam bending stiffness, but the curtain mass would alter the total mass in both the SDOF and MDOF model. In this study the effective mass of

the SDOF system was calculated based on the sum of the masses of the beam and the curtain while in the MDOF model the curtain mass was divided into nodal masses and added to the corresponding beam nodal mass. As will be discussed later, the results of this idealization agree reasonably well with those obtained from the frequency response analysis of the experimental measurements. In Fig. 3.10(d), the experimental time-history of the beam in shot 5 is compared with the corresponding SDOF and MDOF models predictions based on the above assumption. The peak displacement predicted by the preceding models are 62 and 65.2 mm, respectively, differing by 1.8% and 3.1% from the corresponding experimental value. From these results, it is clear that both models predict the experimental displacement of each beam up to the peak displacement reasonably well and the difference between the predictions of the two models is relatively small. The latter is true even for the beams that experienced nonlinearity and relatively large displacements.

3.6.2 Strain time-histories

Since longitudinal strain due to bending is a function of the second derivative of the displacement function and since in both the SDOF and MDOF models the assumed displacement functions are not exact, it is prudent to investigate the accuracy of these functions, particularly that of the SDOF model. The relevant level of accuracy can be best gauged by comparing predicted strain responses with their experimental counterparts. Figures 3.11(a) to (i) show the measured and corresponding predicted strain time-histories at different locations on the five test beams. The strain time-histories predicted by the SDOF model were calculated on the basis of the displacement function in Eq. (3.6), which gives the beam mid-span curvature as

$$\kappa(\xi,t) = \frac{\varepsilon_{\max}(\xi,t)}{d/2} = \phi''(\xi)y(t) \tag{3.12}$$

where κ denotes the curvature of the beam, ε_{max} is the strain at the extreme fibre, d is the depth of the beam, $\phi(\xi)$ is the displacement shape function, and $y(t)$ is the mid-span displacement. If Eq. (3.12) is applied at mid-span (ξ=0, z=L/2), the maximum strain can be written as

$$\varepsilon_{\max}\big|_{z=\frac{L}{2}} = \phi''\big|_{z=\frac{L}{2}} \frac{d}{2} y(t) = 4.8 \frac{d}{L^2} y(t) \tag{3.13}$$

Based on the deflected shape of the beam and the amplitude of its maximum strain at its mid-span, its maximum strain at any other location can be determined by evaluating the curvature function at the desired location and dividing it by the corresponding mid-span curvature. For instance, the maximum strain at 1/3 and 1/6 of the span can be written as

$$\begin{aligned} \varepsilon_{\max}\big|_{z=\frac{L}{3}} &= \frac{\phi''\big|_{z=\frac{L}{3}}}{\phi''\big|_{z=\frac{L}{2}}} \varepsilon_{\max}\big|_{z=\frac{L}{2}} = 0.844\, \varepsilon_{\max}\big|_{z=\frac{L}{2}}, \\ \varepsilon_{\max}\big|_{z=\frac{L}{6}} &= \frac{\phi''\big|_{z=\frac{L}{6}}}{\phi''\big|_{z=\frac{L}{2}}} \varepsilon_{\max}\big|_{z=\frac{L}{2}} = 0.556\, \varepsilon_{\max}\big|_{z=\frac{L}{2}} \end{aligned} \tag{3.14}$$

The preceding approach for calculating strain is valid if the stress in the member does not significantly exceed the yield stress as in the case of the beams in shots 1 and 3. This can be verified by observing the strains measured at 1/2 and 1/6 of the span along the beam in shot 1, as shown in Fig. 3.11(a), (b), and at 1/2, 1/3, and 1/6 of span along the beam in shot 3, as shown in Fig. 3.11(d), (e), and (f), respectively. Even for the beams experiencing larger strains than the yield strain, such as the beams in shot 2 and shot 4, the predicted strains by the SDOF still agree reasonably well with the corresponding experimental results. This can be corroborated by observing the strains at 1/2 and 1/6 of the span along the beam in shot 4, as shown in Fig. 3.11(g) and (h), and at 1/3 of the span along the beam in shot 5, as shown in Fig. 3.11(i). In general, there is reasonable agreement between the experimental and predicted strain time-histories obtained from both the SDOF and the MDOF models in terms of the peak strain and overall response. Both

models tend to slightly overestimate the peak strain, with the predicted peak strains by the SDOF and MDOF models differing from the corresponding experimental values on average by 13% and 11%, respectively. However, the corresponding strain profiles show remarkable differences at specific times. This disagreement may be ascribed to the approximation of the loading distribution along the length of the beam. In addition, the out-of-plane modes of vibrations might have contributed to this disagreement, as will be discussed later, e.g. the effect of the second and third out-of-plane modes at 1/6 of span of the test beams, which have a pronounced effect at 1/6 of the span, where they have their maximum values, as shown in Figs. 11(b), (f), and (h).

3.6.3 Dynamic reactions and moments

Dynamic reactions are important because beams are often supported by or connected to other members whose dynamic response would depend on the reaction forces. In design of beams, the internal forces, i.e. bending moment and shear force, are used to size the section and/or to check its adequacy. Given the difference between the shape functions used in SDOF and MDOF models, it is important to compare the internal forces predicted by the two methods. Since MDOF models require much more effort to implement than SDOF, and since SDOF models are commonly used in design practice, it is useful to determine if this extra effort is justified. The dynamic reactions were not measured during the test, thus only comparison between the results of the SDOF and MDOF models are presented in Fig. 3.12. The dynamic reactions were calculated from SDOF model using the following simplified expressions which were obtained based on the dynamic equilibrium of vertical forces, including the inertia forces, acting on a simply supported beam under uniform blast loading (Biggs 1964):

$$V_o(t) = \begin{cases} 0.39R(t) + 0.11F(t), & \text{(elastic range)} \\ 0.38R(t) + 0.12F(t), & \text{(plastic range)} \end{cases} \tag{3.15}$$

where $V_o(t)$ denotes the dynamic reaction at the supports, $F(t)$ is the resultant blast force acting on the reflecting surface, and $R(t)$ is the resistance function. Despite neglecting the higher modes of vibration, the SDOF model showed reasonable agreement with the MDOF model, as can be seen in Fig. 3.12(a) and (b) for the beams in shot 1 and shot 4, respectively. As Fig. 3.12(a) shows, both models exhibit similar qualitative trend, and the vibration period of the dynamic reaction predicted by the SDOF model agrees well with that by the MDOF model. Accordingly, it appears that the shape function in Eq. (3.6) results in a good estimate of the dynamic reactions. This observation confirms the common supposition (Baker et al. 1983; Smith and Hetherington 1994) that the elastic deformed shape associated with static loading generally gives better results than other types of assumed displacement functions. In the case of plastic deformations, Fig. 3.12(b), the maximum dynamic reaction from the SDOF model compared well with that from the MDOF model, but a phase shift was observed during the free vibration phase due to the sudden change in the shape function when plastic deformation commenced. A constant value of dynamic reaction can be observed during free vibration in the plastic state, Fig. 3.12(b), as the dynamic reaction was solely function of the inertia force in accordance with Eq. (3.15), which, in turn is proportional to the defined resistance function. Table 3.3 summarizes the maximum reactions obtained from the SDOF and the MDOF models for all the tests. The average difference between the maximum dynamic reactions predicted by the two models is 9%, with a COV of 6%.

Figures 3.13(a) and (b) show the SDOF and MDOF predictions for the mid-span dynamic moment for the beams in shot 1 and 4, respectively. The mid-span dynamic moments were calculated based on the SDOF model using the following simplified expressions, which were obtained based on dynamic equilibrium:

$$M(t) = V_o \frac{L}{2} - P(t)w\frac{L^2}{8} - M\ddot{y}(t)\frac{1}{L}\int_0^{L/2}\phi(z)\left(\frac{L}{2} - z\right)dz \qquad (3.16)$$

where $P(t)$ is the blast overpressure and w is the width of the flange or, if applicable, the width of the blast curtain. Eq. (3.16) can be simplified as

$$M(t) = L\begin{cases} 129\times10^{-3}R(t) - 4\times10^{-3}F(t), & \text{(elastic range)} \\ R_m / 8, & \text{(plastic range)} \end{cases} \tag{3.17}$$

Again, reasonable agreement was found between the two models in terms of the maximum moment prediction and the overall moment response in the case of beams that experienced elastic deformation in shot 1. Although the SDOF model captured reasonably well the maximum moment and the mid-span moment history for the beam in shot 4, during the free vibration phase, it indicated a phase shift compared to the MDOF model period. Table 3.3 summarizes the predicted maximum mid-span moment of each test beam. The average difference between the predictions of the two models is 9% with a COV of 5%. By comparing the maximum moment of each beam with its yield moment from its strain rate-dependant moment-curvature diagram in Fig. 3.8, it is found that the maximum moments of the beams in shot 1 and 3 are less than their yield moment while the maximum moments of the beams in shot 2, 4, and 5 are greater than their yield moments.

Figure 3.14 shows the dynamic shear and bending moment distribution along the beam length obtained from the SDOF and MDOF models at different time instants during the initial stages of motion in shot 1. As mentioned before, the SDOF model compared well with MDOF model in terms of the maximum shear at the supports, but less agreement was found between the two models when comparing the shear force distribution along the beam length. This discrepancy is attributed to the exclusion of the higher modes of vibration in the SDOF model. The results also showed some discrepancy between the predicted moments by the two models in terms of both magnitude and distribution. Due to the high magnitude of the inertia force at the beginning of vibration, the beam bending moment seems to be negative at the mid-span section. It should be pointed out that due to the contribution of the inertia term, the shape function required to

calculate the shear and bending moment diagrams, at specific times, might be different from those under uniform static loading. This is particularly evident if one considers the reversal of the curvature of the shear and moment graphs in Fig. 3.14. However, due the relatively small magnitude of the beam internal forces at the early stages of its motion, the above differences between the results of the SDOF and MDOF are practically unimportant.

3.7 Effect of higher modes on dynamic response

In order to further investigate the reason for the adequacy of the SDOF model in predicting the response of the current test beams and to demonstrate that their responses were indeed governed by the first mode of their vibration, the frequency components and their contributions to the dynamic response of the beams were investigated. The power spectral density (PSD), which represents the signal strength at various frequencies of the response, was computed from the strain time-histories of the test beams. Figures 3.15(a) and (b), respectively, show the mid-span strain time-history and PSD response in normalized form for the beam in shot 1. The contributions of different frequency components in the response were studied by calculating the variance σ^2 of the PSD curve, as shown in Fig. 3.15(b). The transfer function (TXY) is used to identify the frequencies components related to the structural properties of the system, as shown in Fig. 3.15(c), and it is defined as the ratio of the output signal (strain frequency response) to the input signal (blast pressure frequency response). However, it only provides a linear approximation of the nonlinear system response characteristics (Bendat and Piersol, 1993). In addition, to facilitate the interpretation of different frequency components, the first three frequencies corresponding to the first three modes of vibration in both the strong (x-x axis) and the weak (y-y axis) directions of the beam were calculated and are plotted in Figs. 3.15(b) and (c). These frequencies were calculated by using the following expression for a simply supported beam (Chopra 2001):

$$f_n = \frac{n^2\pi^2}{L^2}\sqrt{\frac{EI}{m}} \qquad n=1, 2, 3,\ldots \tag{3.18}$$

where EI denotes the flexural rigidly of the beam, L is the beam length, and m is the mass per unit length.

As shown in Fig. 3.15(c), a dominant frequency component of 84 Hz can be observed, corresponding to the flexural vibration frequency of the first mode in the x-x direction. A secondary peak frequency of 717 Hz was also noticed, a frequency that corresponds to the third mode of vibration. Other frequency components were associated with the second and third modes of vibration about the y-y axis. However, as shown in Fig. 3.15(b), the contribution of the latter frequencies was only 5% to the total response. The first mode contributed 88% to the total response; on the contrary, the third mode contributed only 3%. Similarly, Figs. 3.15(d), (e), and (f) show for the beam in shot 2 its mid-span strain time-history, PSD response, and TXY, respectively. Again, the frequency of the first mode (30 Hz) was dominant with a contribution of 97% to the total response. The contribution of the third mode frequency (265 Hz) was less than 2% to the total response. The frequency response of the beam had no sign of exciting any of out-of-plane frequencies, i.e. about x-x axis in this case. Figures 3.15(g), (h), and (i) show for the beam in shot 5 at 1/3 of its span the strain time-history, PSD response, and TXY, respectively. The PSD response shows that the dominate frequency (40 Hz), which contributed 93% to the total response, is associated with the first mode of vibration of the beam, provided the frequency of the beam is calculated by considering the mass of the beam as the sum of the masses of the steel section and the blast curtain. A secondary frequency peak of 122 Hz was observed, which is associated with the first mode of vibration of the beam without the curtain, and which had a contribution of only 3% to the total response. The third mode had a small contribution of only 1% to the total response. From the above discussion, it can be concluded that the responses of the current test beams

under blast loading were dominated by the first mode of vibration, which justifies the use of the SDOF model for predicting their dynamic behaviour.

3.8 Estimation of natural frequency of test beams

The dynamic response of a beam under blast load is dependent on the ratio of the blast pressure positive phase duration to the fundamental period of the member, therefore, large discrepancy between the actual and theoretical period and frequency can affect the predicted response. To gauge the accuracy of the theoretical frequency equation, i.e. Eq. (3.18), which was used to determine the period used in the SDOF model, the actual fundamental frequency of each test beam was extracted from its strain time-history by isolating the first mode. The strain time-histories (Figs. 3.15(a), (d), and (g)) were passed through a band-pass filter whose range encompassed the predicted fundamental frequency of the test beam. The band-pass frequencies were determined such that the power contribution from the first mode to the PSD curves (Figs. 3.15(b), (c), and (h)) was sufficiently represented by a portion of the curve bracketed by the band-pass frequencies. For instance, a range of frequency of 70-90 Hz was used as band-pass frequencies to isolate the first mode as shown in Fig. 3.15(a). As shown in Fig. 3.16, when a band-pass filter was applied to the strain time-history, the reconstructed time series for the first mode resembled a consistent logarithmic decay. Once a logarithmic decay is revealed, the natural frequency (f) can be calculated using the measured period T.

The same approach was used for the strain responses shown in Fig. 3.15(a), (d), and (g). Figures 3.16(a), (b), and (c) show the filtered time-history responses. The natural frequency was found to be 83.5, 34.5, and 119 Hz for the beams with section W150X24 oriented in the x-x direction, for the beams with section W150X24 oriented in the y-y direction, and for the beams with section W200X71 oriented in x-x direction, respectively. The natural frequencies thus determined are compared in Table 3.4 with the corresponding values obtained by

using Eq. (3.18). The predicted frequencies compare well with the actual frequencies with a maximum difference of 6.8%.

3.9 Summary and conclusions

This paper contains detailed analysis of the dynamic response of a number of wide flange steel beams tested under blast loads. The measured blast wave parameters were compared with the available equations and models for blast load prediction. The test beams were analyzed by using two models, an equivalent SDOF model and a MDOF model based on beam finite elements. In the SDOF, the beam resistance function was based on a moment-curvature relationship derived from a layered sectional analysis that included the stress and strain rate variation over the depth of the beam. The MDOF finite element model accounted for stress and strain rate variation over the cross-section and along the beam. The results of both models were compared with the corresponding experimental displacement and strain time-histories. Based on the analysis of the results and their comparison with the experimental data, the following conclusions can be stated.

(1) UFCM could predict reasonably well the pressure and impulse obtained from the experimental measurements.

(2) The closed-form equation proposed by Prugh (1999) provides a good and accurate estimate of the impulse values in the current tests.

(3) The positive phase duration for the current blast tests could not be accurately estimated by either an available closed-form equation or by UFCM.

(4) When the DIF was calculated using the Cowper-Symonds strain rate model and the strain rate was assumed to vary linearly through the depth of the beam, the SDOF model adequately captured both the time dependant deformations and internal forces in the test beams.

(5) The assumption of a constant DIF based on a relatively low strain rate, as suggested by a number of available design documents, leads to rather conservative estimate of the DIF compared to that calculated based on the measured strain rates. This could lead to an underestimation of the actual forces transferred by a member to its connections or supporting members.

(6) Due to the difference between the actual displaced shape of the beam and its assumed shape in the SDOF model, at the initial stages of motion, the longitudinal variation of dynamic shear and moment based on the SDOF model differed from that based on the MDOF model.

(7) Based on power spectral density analysis, the responses of the test beams were found to be governed by the first mode of vibration, with minor contribution from the third mode. For this reason, the SDOF model provided accurate prediction of the response of the current test beams, both at the elastic and inelastic stages.

3.10 Acknowledgements

The authors wish to gratefully acknowledge the following organizations for their support towards this study: the Chemical, Biological, Radiological/Nuclear and Explosives Research and Technology Initiative (CRTI project 06-015TD), Public Works and Government Services Canada, the Centre for Effective Design of Structures (CEDS) at McMaster University, and the Natural Sciences and Engineering Research Council of Canada for their financial support, the Canadian Explosives Research Laboratory (CERL) for assisting with the blast tests, and the Canadian Armed Forces for the use of their test range. CEDS is funded through the Ontario Research and Development Challenge Fund, a program of the Ministry of Research and Innovation of Ontario.

3.11 Notation

The following symbols are used in this paper:

Δ_y = displacement at the yield load (mm);

d = section depth (mm);

f = frequency (Hz);

f_y = yield stress (MPa);

ϕ = shape function;

K = stiffness (kN/m);

K_M = mass factor;

K_L = load factor;

K_{LM} = load-mass factor;

I_r = reflected impulse (kPa.ms);

μ = ductility ratio;

M = mass (kg);

M_u = ultimate moment (kN.m);

P_s = peak incident pressure (kPa);

P_r = peak reflected pressure (kPa);

R = resistance (kN);

R_m = maximum resistance (kN);

t_a = arrival time of pressure wave (ms);

t_d = positive phase duration (ms);

W = charge mass (kg);

y = mid-span displacement (mm);

$\ddot{y}$ = mid-span acceleration (m/s^2);

Z = scaled-distance (m/kg$^{1/3}$).

3.12 References

AISC (2006). "Specification for safety-related steel structures for nuclear facilities." ANSI/AISC N690-06. American Institute for Steel Construction, Chicago, Illinois.

ASCE, (1997). "Design of blast resistant buildings in petrochemical facilities." Task Committee on Blast Resistant Design, ASCE, New York.

Aspden, R. J., and Campbell, J. D., (1966). "The effect of loading rate on the elasto-plastic flexure of steel beams." Proceedings of the Royal Society of London. Series A, Mathematical and Physical Sciences, 290(1421), 266-285.

Baker, W. E., Cox, P. A., Westine, P. S., Kulesz, J. J., and Strehlow , R. A., (1983). "Explosion hazards and evaluation." Elsevier Scientific Pub. Co., Amsterdam; New York.

Bassim, M. N., and Panic, N., (1999). "High strain rate effects on the strain of alloy steels." Journal of Materials Processing Technology, 92-93, 481-485.

Bendat and Piersol, (1993). "Engineering applications of correlation and spectral analysis." Wiley, New York.

Biggs, J. M., (1964)." Introduction to structural dynamics." McGraw-Hill Book Company, New York.

Bogosian D., Ferrito J., and Shi Y., "Measuring uncertainty and conservatism in simplified blast models." Proc 30th Explosion Safety Seminar, Atlanta, GA, August (2002).

Boutros, M. K., (2000). "Elastic-plastic model of pinned beams subjected to impulsive loading." Journal of Engineering Mechanics, 126(9), 920-927.

Chen H., and Liew, J. Y. R (2005). "Explosion and fire analysis of steel frames using mixed element approach." Journal of Engineering Mechanics, 131(6), 606-616.

Chopra, A. K., (2001). "Dynamics of structures : theory and applications to earthquake engineering." Prentice Hall, Upper Saddle River, NJ.

Davidson, J. S., Porter, J. R., Dinan, R. J., Hammons, M. I., and Connell, J. D., (2004). "Explosive testing of polymer retrofit masonry walls." Journal of Performance of Constructed Facilities, 18(2), 100-106.

Hyde, D.W., (1990). "Conventional weapons effect (CONWEP)." Application of TM5-855-1. US Army Engineer Waterways Experiment Station, Vicksburg, USA.

Jama, H. H., Bambach, M. R., Nurick, G. N., Grzebieta, R. H., and Zhao, X. L., (2009). Numerical modelling of square tubular steel beams subjected to transverse blast loads. Thin-Walled Structures, 47(12), 1523-1534.

Jones, N., (1988). "Structural impact." Cambridge University Press, Cambridge; New York.

Kingery, C.N. and Bulmash, G. (1984). "Airblast Parameters from TNT Spherical Air Burst and Hemispherical Sur-face Burst." Report ARBL-TR-02555. US Army Research and Development Centre – Ballistic Research Laboratory (BRL), Aberdeen Proving Ground, Aberdeen, MD.

Kinney, G.F., Graham, K.J., (1985). "Explosive shocks in air." Springer-Verlag, New York.

Krafft, J. M., Sullivan, A. M., and Tipper, C. F., (1954). "The effect of static and dynamic loading and temperature on the yield stress of iron and mild steel in compression." Proceedings of the Royal Society of London. Series A, Mathematical and Physical Sciences, 221(1144), 114-127.

Krauthammer, T., Bazeos, N., and Holmquist, T. J., (1986). "Modified SDOF analysis of RC box-type structures." Journal of Structural Engineering, 112(4), 726-744.

Krauthammer, T., Shahriar, S., and Shanaa, H. M., (1990). "Response of reinforced concrete elements to severe impulsive loads." Journal of Structural Engineering, 116(4), 1061-1079.

Lawver, D., Daddazio, R., Vaughan, D., Stanley, M., and Levine, W., (2003). "Response of AISC steel column sections to blast loading." Problems Involving Thermal-Hydraulics, Liquid Sloshing, and Extreme Loads on Structures ASME Pressure Vessels and Piping Conference, ASME, NY, 139-148.

Lee, L., Kim, T., and Kim, J., (2009). "Local response of W-shaped steel columns under blast loading." Structural Engineering and Mechanics, 31(1), 25-38.

Liew, J. Y., (2008). "Survivability of steel frame structures subject to blast and fire." Journal of Constructional Steel Research, 64 (7-8) 854–866.

Magallanes, J. M., Martinez, R., and Koening, J., (2006). "Experimental results of the AISC full-scale column blast test." Report TR-06-20.2, The American Institute of steel construction, Chicago.

Magnusson, J., (2007). "Structural concrete elements subjected to air blast loading." PhD Thesis, Royal Institute of Technology, Sweden.

Malvar, L. J., (1998). "Review of static and dynamic properties of steel reinforcing bars." ACI Materials Journal, 95(5), 609-616.

Manjoine, M. J., and Pittsuburgh, E., (1944). "Influence of rate of strain and temperature on yield stresses of mild steel." Journal of Applied Mechanics, 11, 211-218.

Nassr, A. A., Razaqpur, A. G., Tait, M. J., Campidelli, M., and Foo, S., (2011). "Experimental performance of steel beams under blast loading."ASCE's Journal of Performance of Constructed Facilities, accepted in Sept. 23, 2011, available online, DOI: 10.1061/(ASCE)CF.1943-5509.0000289.

Oesterle, M. G., Hegemier, G. A., and Morrill, K. B., (2009). "Response of concrete masonry walls to simulated blast loads." ASCE Conf. Proc, Austin, Texas.

Prugh, R.W. (1999). The Effects of explosive blast on structures and personnel Process Safety Progress 18(1), 5-16

Razaqpur, A. G., Tolba, A., and Contestabile, E., (2007). "Blast loading response of reinforced concrete panels reinforced with externally bonded GFRP laminates." Composites Part B: Engineering, 38(5-6), 535-546.

Schenker, A., Anteby, I., Gal, E., Kivity, Y., Nizri, E., Sadot, O., Michaelis, R., Levintant, O., and Ben-Dor, G., (2008). "Full-scale field tests of concrete slabs subjected to blast loads." International Journal of Impact Engineering, 35(3), 184-198.

Schleyer, G. K., and Hsu, S. S., (2000). "A modelling scheme for predicting the response of elastic-plastic structures to pulse pressure loading." International Journal of Impact Engineering, 24(8), 759-777.

Smith, P. D., and Hetherington, J. G., (1994). "Blast and ballistic loading of structures." Butterworth-Heinemann, Oxford; Boston.

Soroushian, P., and Choi, K.-B., (1987). "Steel mechanical properties at different strain rates." Journal of Structural Engineering, 113(4), 663-672.

Tan, K. H., and Patoary, M. K. H., (2009). "Blast resistance of FRP-strengthened masonry walls. I: approximate analysis and field explosion tests." Journal of Composites for Construction, 13(5), 422-430.

USDOD, (2008). "Structures to resist the effects of accidental explosions." Document No. UFC 3-340-02. US Department of Defense (USDOD), Washington, DC.

Wu, C., Oehlers, D. J., Rebentrost, M., Leach, J., and Whittaker, A. S., (2009). "Blast testing of ultra-high performance fibre and FRP-retrofitted concrete slabs." Engineering Structures, 31(9), 2060-2069.

3.13 List of figures

Table 3.1: Matrix of test specimens

Shot	Section designation	Charge mass (kg)	Stand-off distance (m)	Scaled-distance ($m/kg^{1/3}$)	Axis of bending
1	W150X24	50	10.30	2.80	x-x
2	W150X24	100	10.30	2.22	y-y
3	W150X24	150	9.00	1.69	x-x
4	W150X24	250	7.00	1.11	x-x
5	W200X71	250	9.50	1.51	x-x

Table 3.2: Transformation factors for simply supported beams

	Elastic range	Plastic range
Mass Factor, K_M	0.5	0.33
Load Factor, K_L	0.64	0.50
Load-Mass Factor, K_{LM}	0.78	0.66

Table 3.3: Maximum dynamic reactions and moments

Shot	Section designation	Scaled dist. Z ($m/kg^{1/3}$)	Max. reaction V_o (kN)		Max. moment M_{max} (kN.m)	
			SDOF	MDOF	SDOF	MDOF
1	W150X24	2.80	32	36	26	25
2	W150X24	2.22	40	42	33	26
3	W150X24	1.69	105	127	85	84
4	W150X24	1.11	175	195	119	110
5	W200X71	1.51	972	1020	565	541

Table 3.4: Actual and estimated values of natural frequency

Section	Orientation	Natural Frequency (Hz)		
		Actual	Estimated	%Error
W150X24	x-x	83.5	81.6	2
W150X24	y-y	32.5	30.2	6.8
W200X71	x-x	119	113.6	4.5

(a) Front view (b) Side view

Fig. 3.1: Test setup

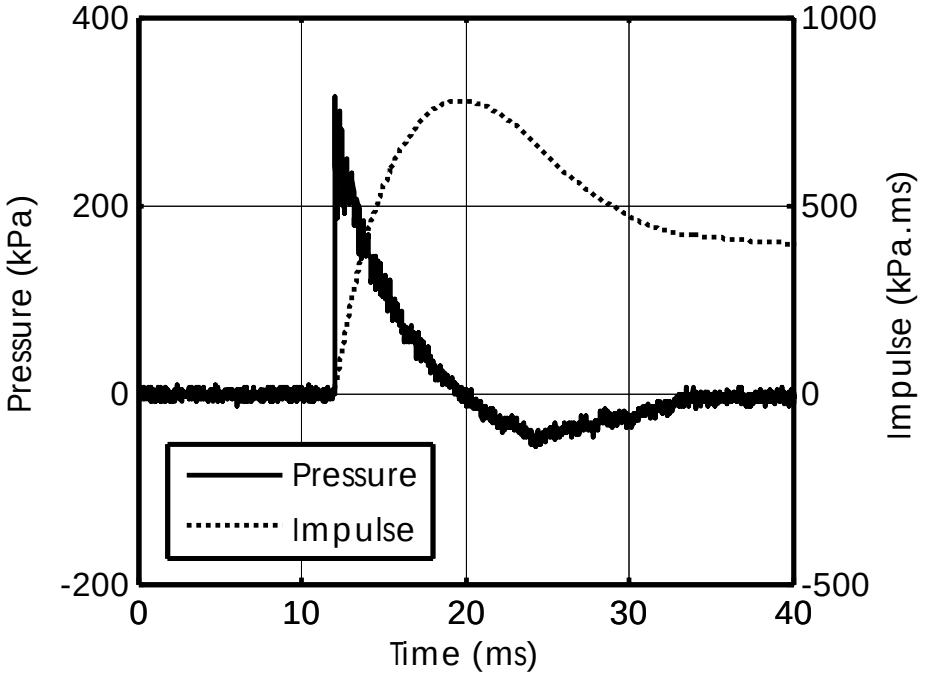

Fig. 3.2: Typical pressure and impulse time-history

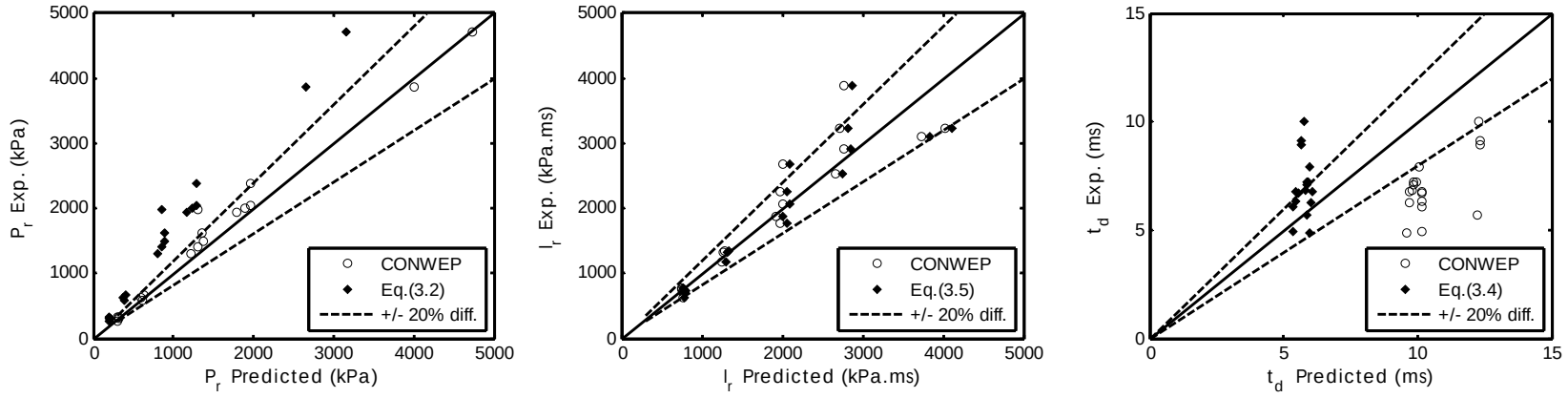

(a) Reflected pressure (P_r) (b) Reflected impulse (I_r) (c) Positive phase duration (t_d)

Fig. 3.3: Pressures, impulses, and positive phase durations for blast shots

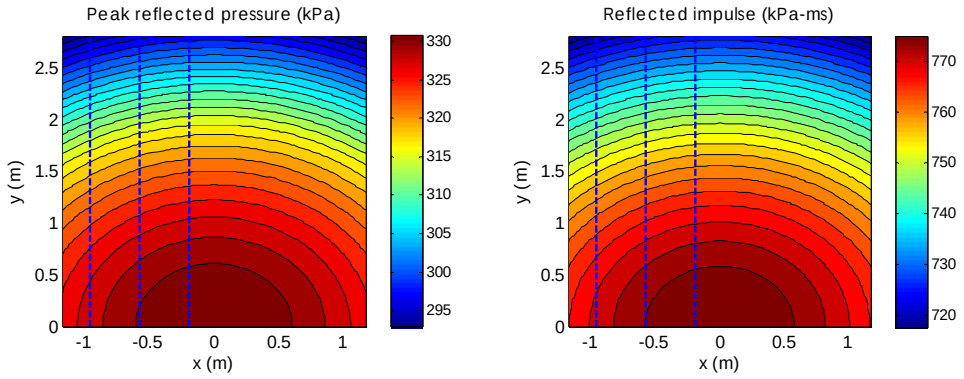

(a) Shot 1: W=50 kg, SD= 10.3 m, Z=2.80 m/kg$^{1/3}$

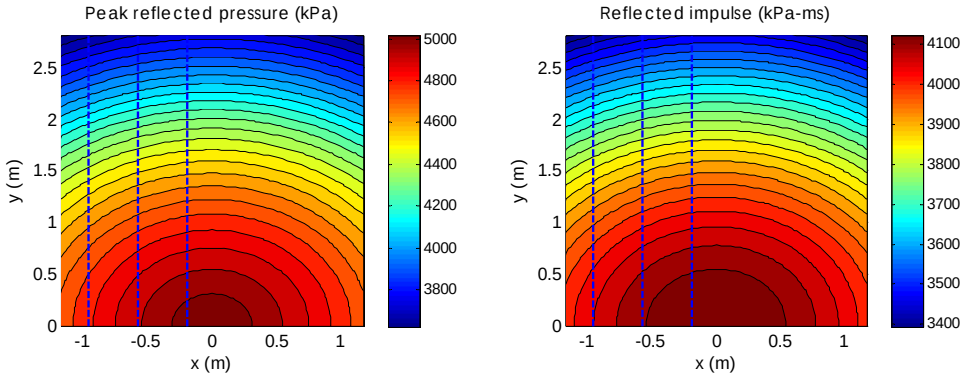

(b) Shot 4: W=250 kg, SD= 7 m, Z=1.11 m/kg$^{1/3}$

Fig. 3.4: Pressure and impulse contours

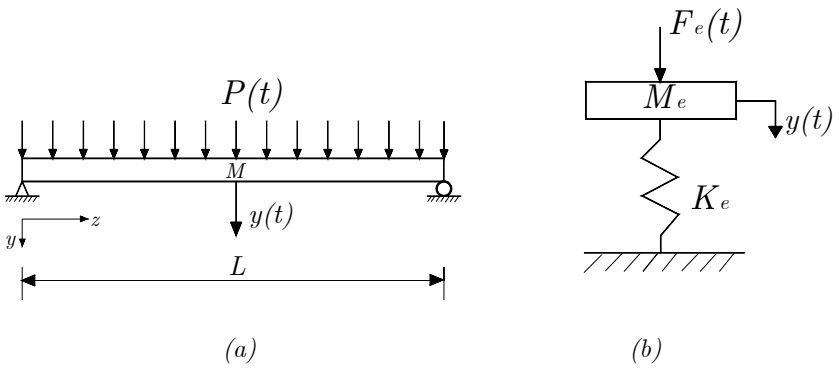

Fig. 3.5: Equivalent SDOF system, (a) real beam and (b) equivalent system

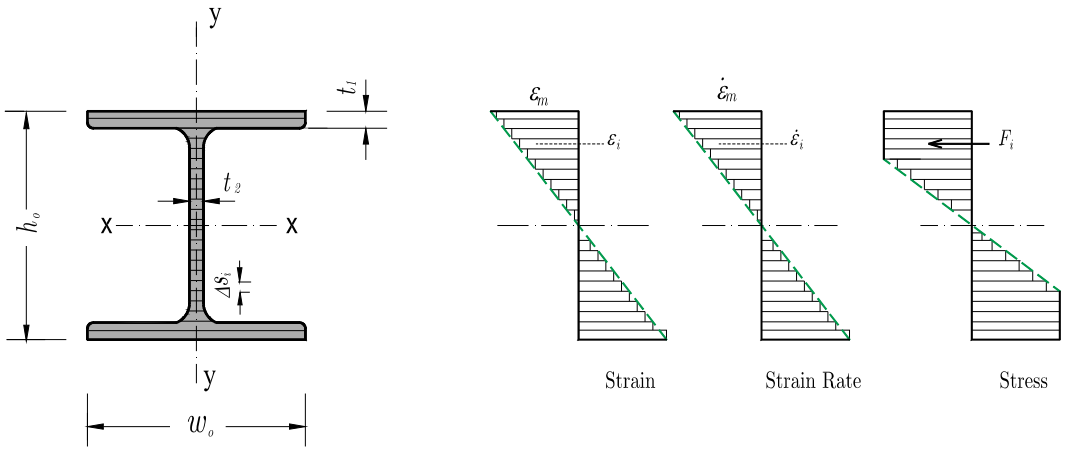

Fig. 3.6: Layered analysis of a cross-section for the plastic hinge

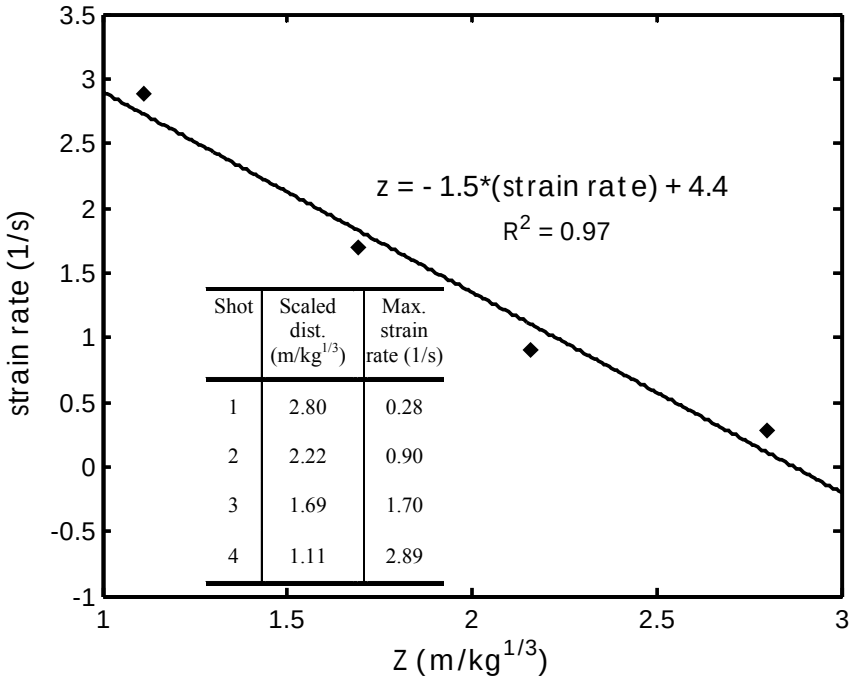

Shot	Scaled dist. ($m/kg^{1/3}$)	Max. strain rate (1/s)
1	2.80	0.28
2	2.22	0.90
3	1.69	1.70
4	1.11	2.89

Fig. 3.7: Strain rate of different blast shots

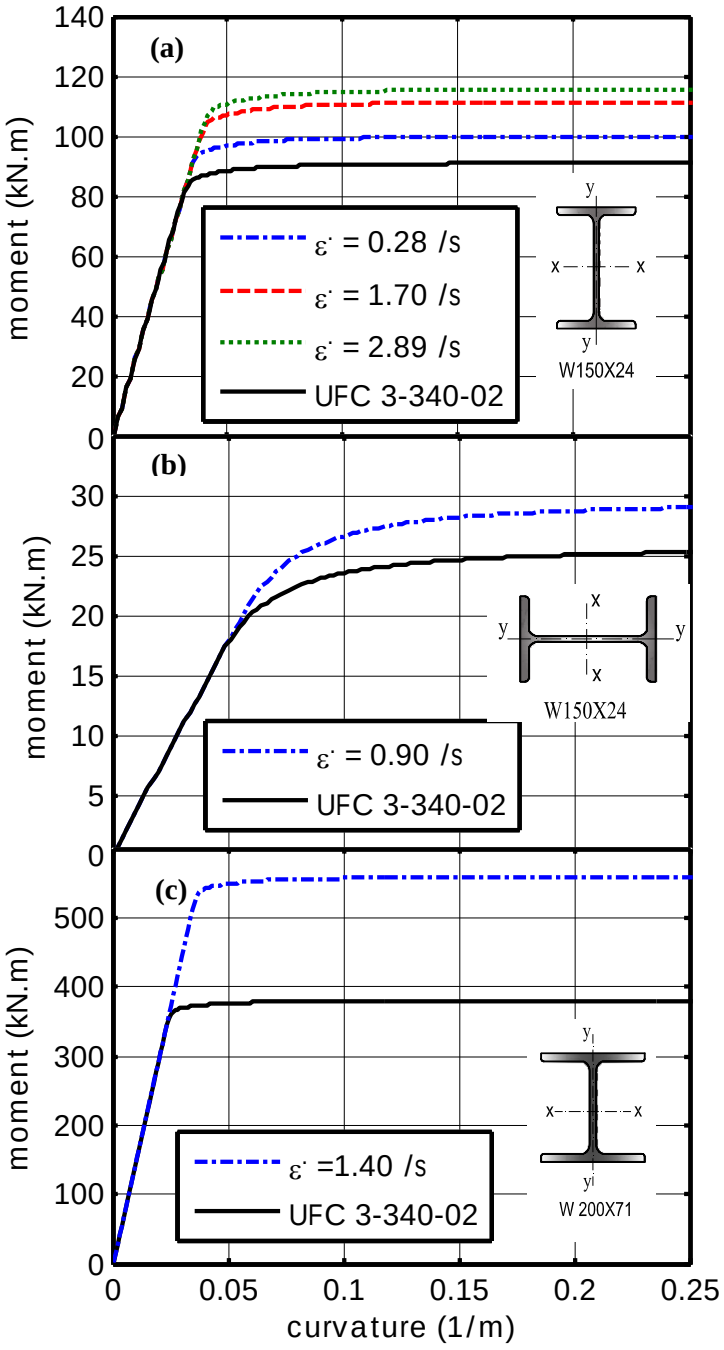

Fig. 3.8: Moment-curvature diagrams

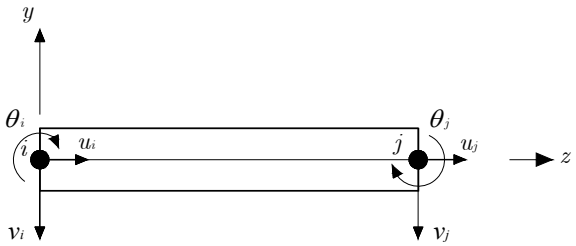

Fig. 3.9: Degrees-of-freedom in beam element

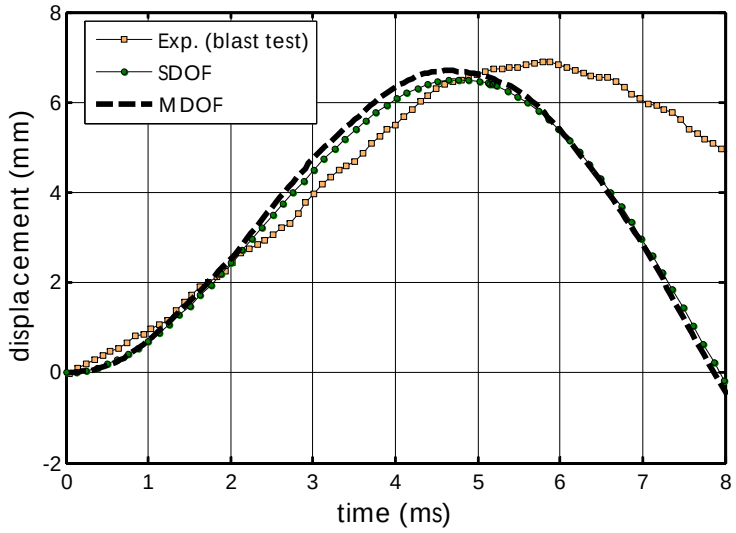

(a) Shot 1: W=50 kg, SD= 10 m, Z=2.80 m/kg$^{1/3}$

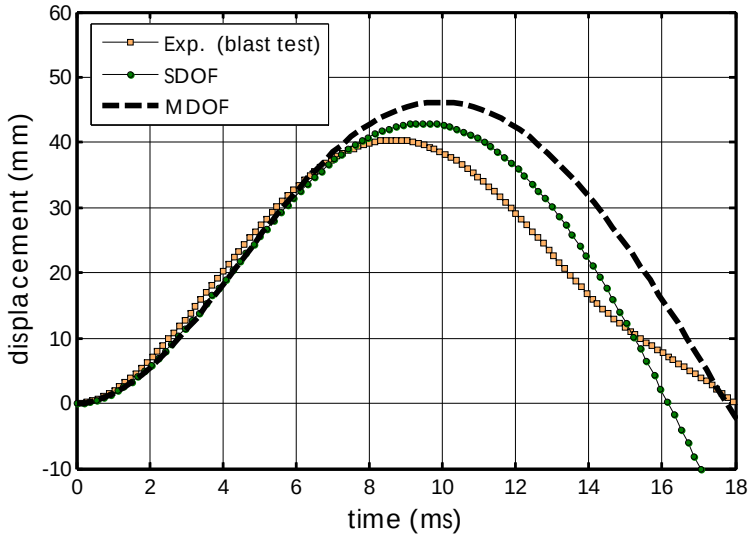

(b) Shot 2: W=100 kg, SD= 10.3 m, Z=2.22 m/kg$^{1/3}$

Fig. 3.10: Displacement time-histories for blast shots

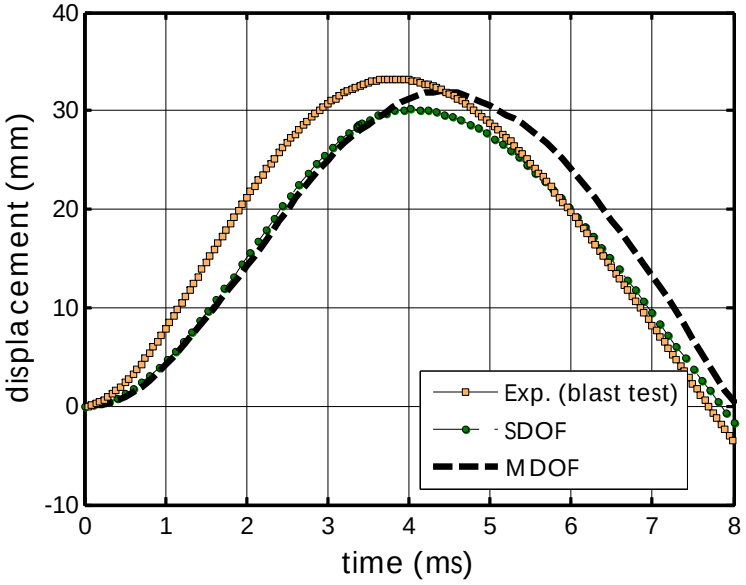

(c) Shot 3: W=150 kg, SD= 9 m, Z=1.69 m/kg$^{1/3}$

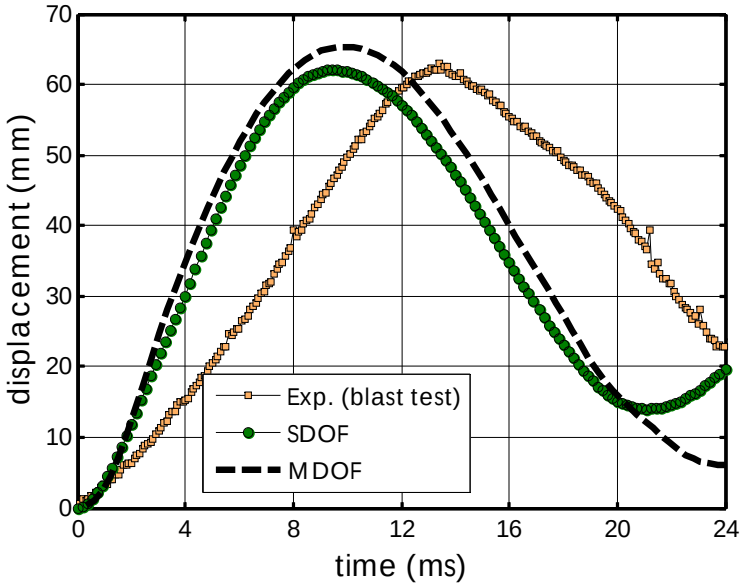

(d) Shot 5: W=250 kg, SD= 9.5 m, Z=1.51 m/kg$^{1/3}$

Fig. 3.10: Cont.

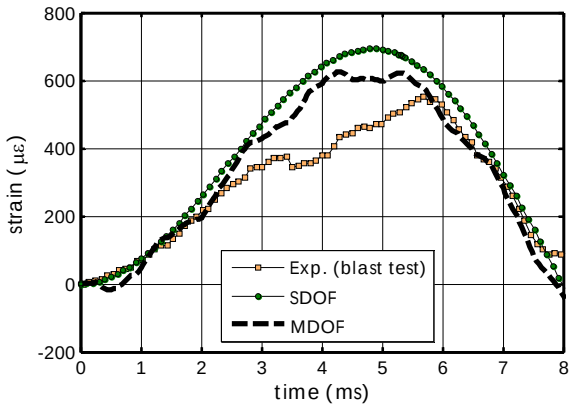

(a) SHOT 1: 1/2 span strain

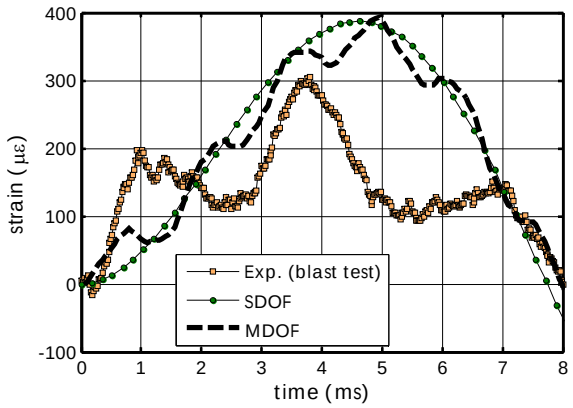

(b) SHOT 1: 1/6 span strain

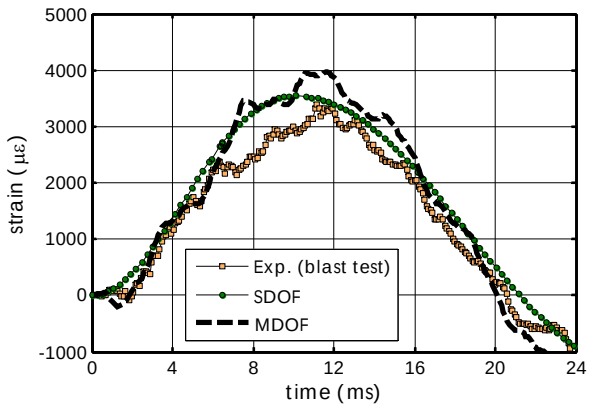

(c) SHOT 2: 1/2 span strain

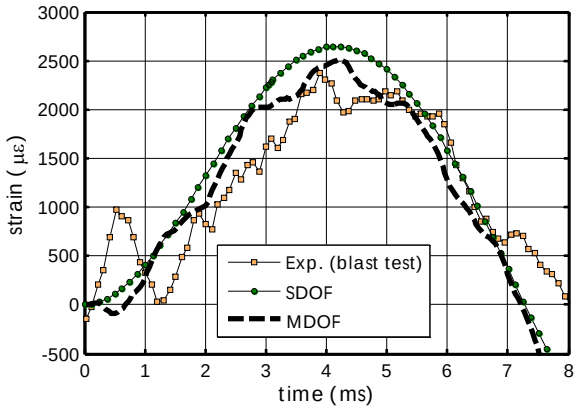

(d) SHOT 3: 1/2 span strain

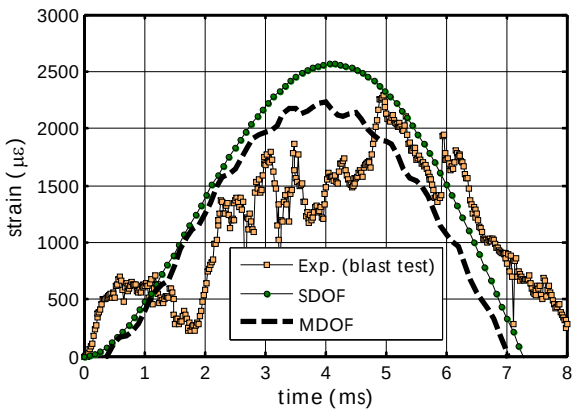

(e) SHOT 3: 1/3 span strain

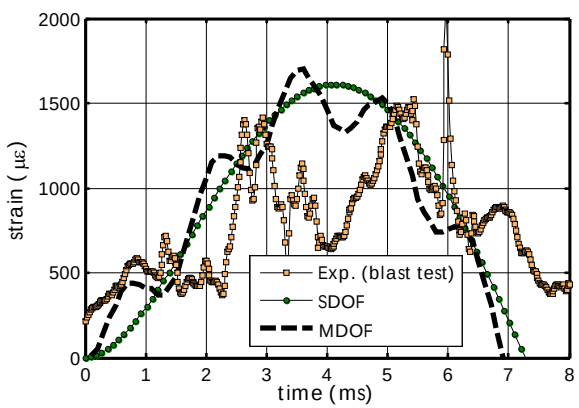

(f) SHOT 3: 1/6 span strain

Fig. 3.11: Strain time-histories for steel beams in different blast shots

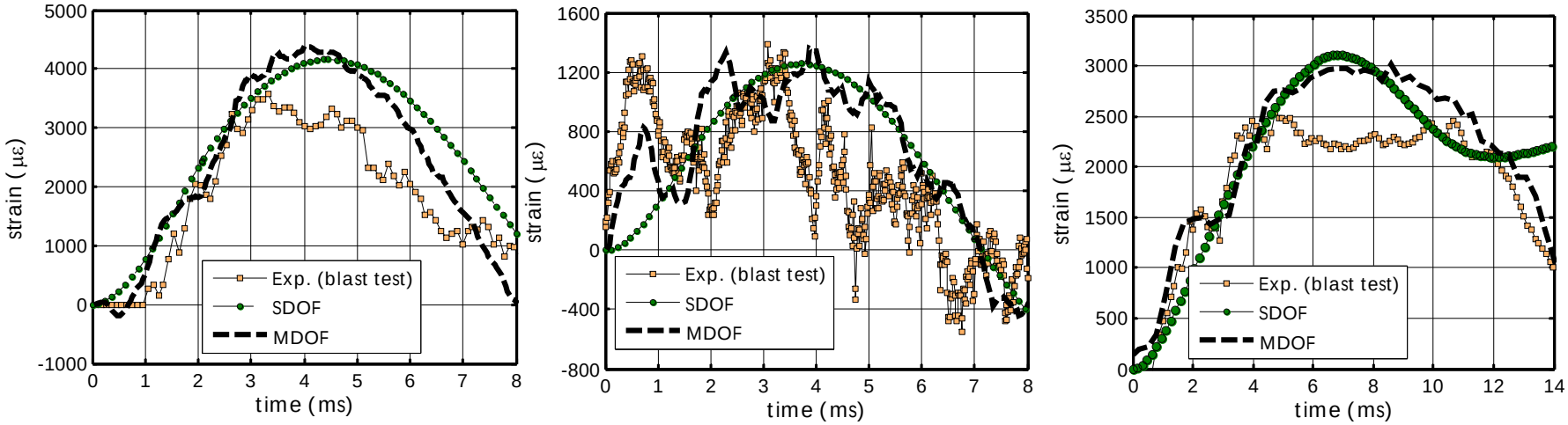

(g) SHOT 4: 1/2 span strain (h) SHOT 4: 1/6 span strain (i) SHOT 5: 1/3 span strain

Fig. 3.11: Cont.

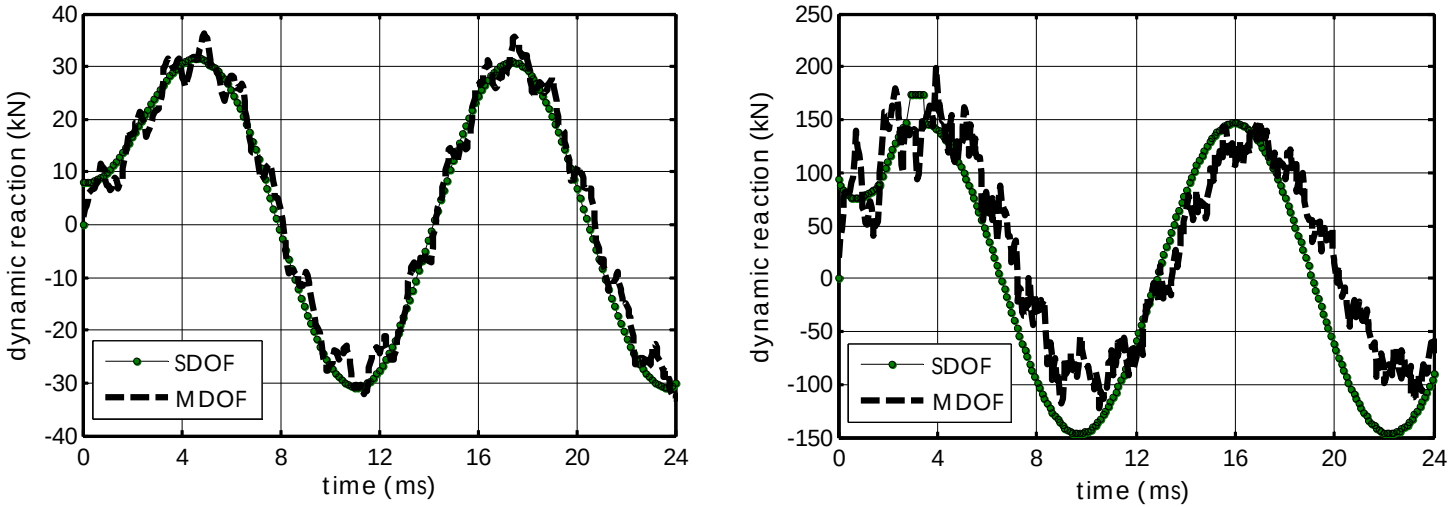

(a) Shot 1: W=50 kg, SD= 10.3 m, Z=2.80 m/kg$^{1/3}$ (b) Shot 4: W=250 kg, SD= 7.5 m, Z=1.11 m/kg$^{1/3}$

Fig. 3.12: Dynamic reactions time-histories for beams in (a) Shot 1 and (b) Shot 4

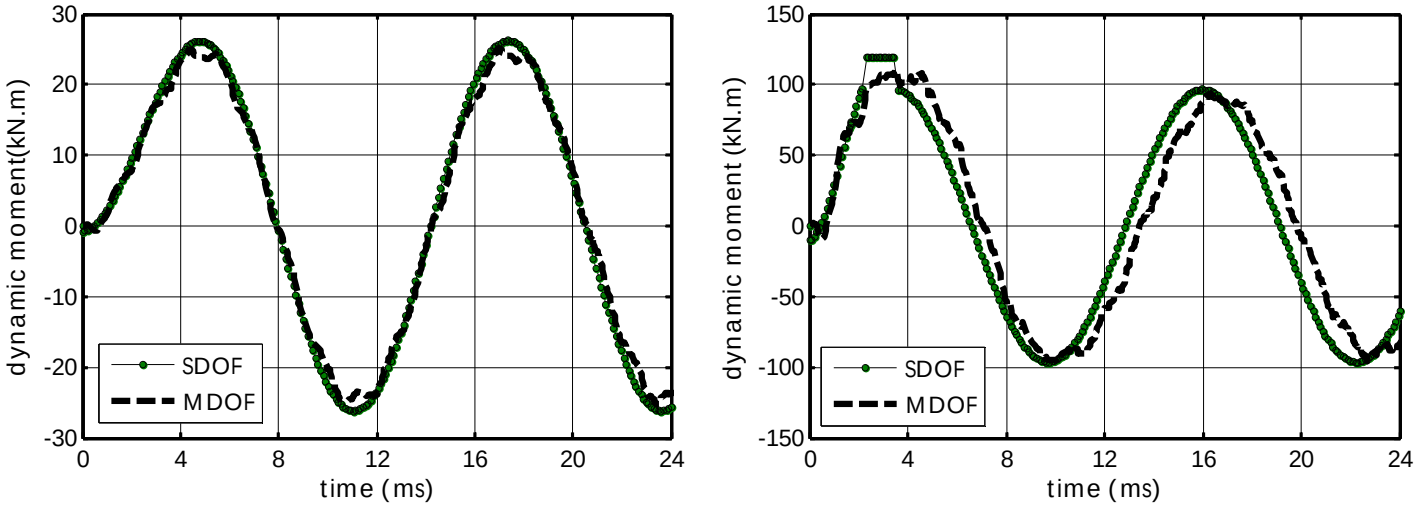

(a) Shot 1: W=50 kg, SD= 10.3 m, Z=2.71 m/kg$^{1/3}$ (b) Shot 4: W=250 kg, SD= 7.5 m, Z=1.11 m/kg$^{1/3}$

Fig. 3.13: Moment time-histories for beams in (a) Shot 1 and (b) Shot 4

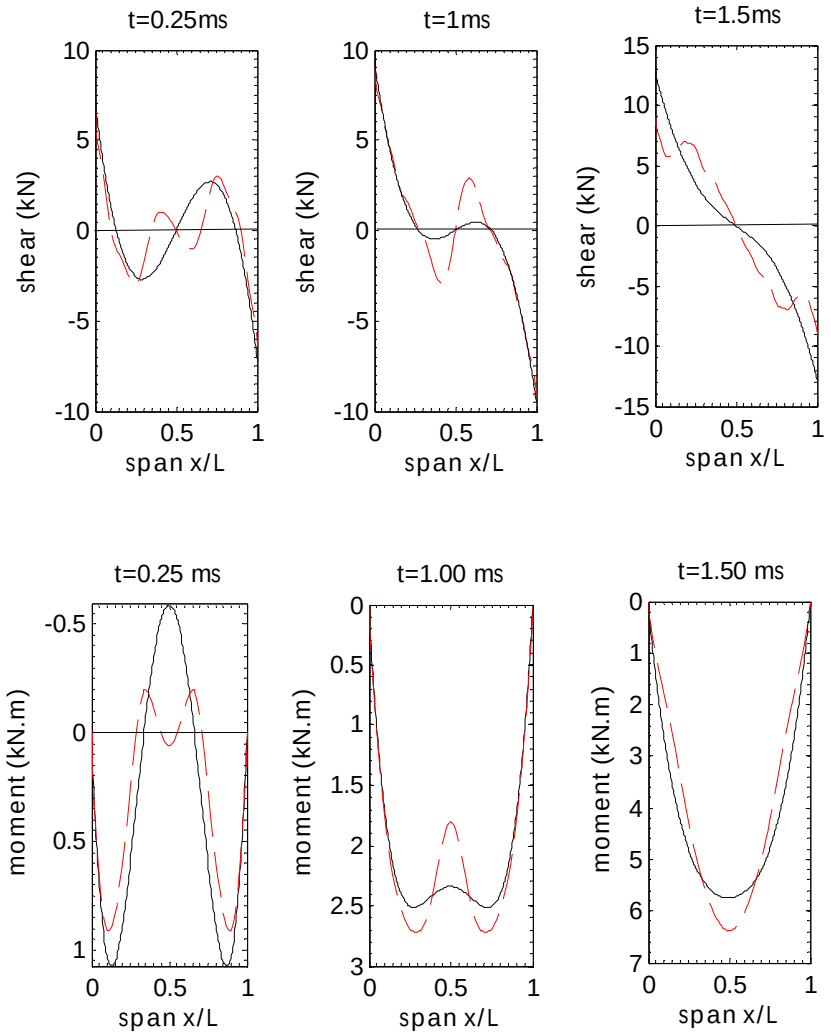

Fig. 3.14: Dynamic moment and shear of beams in shot 1, —— SDOF and – – – MDOF

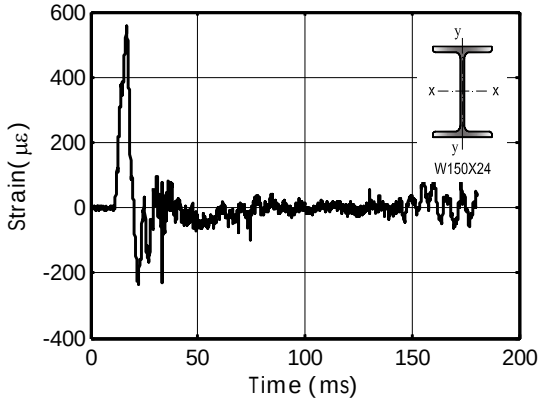

(a) Shot 1: Strain time-history

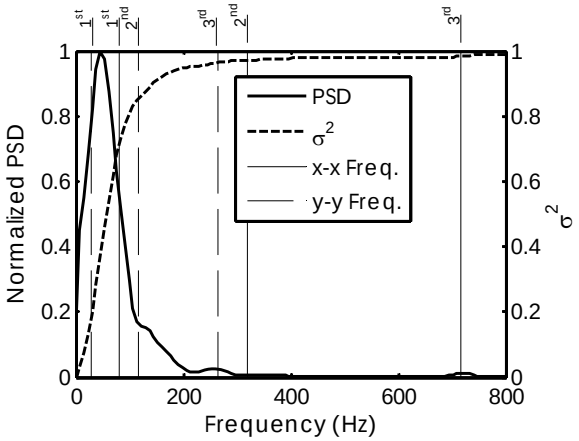

(b) Shot 1: Power spectral density (PSD)

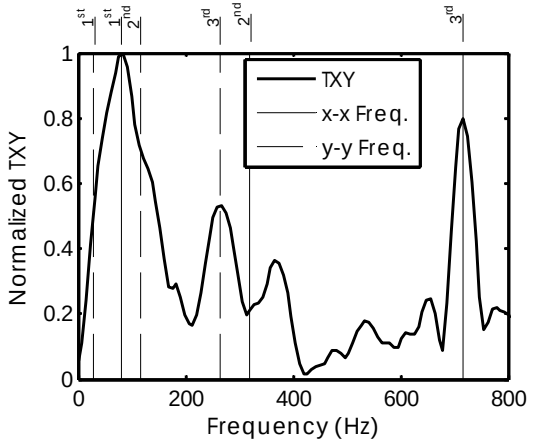

(c) Shot 1: Transfer function (TXY)

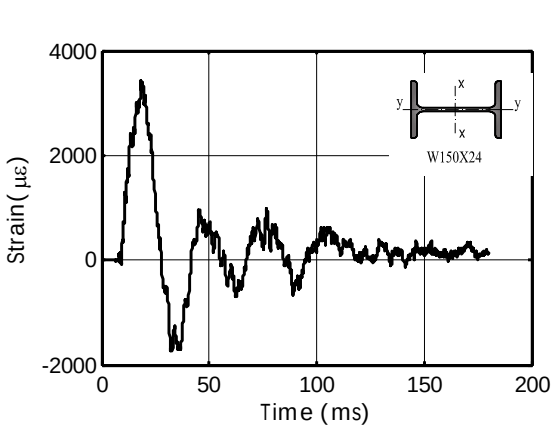

(d) Shot 2: Strain time-history

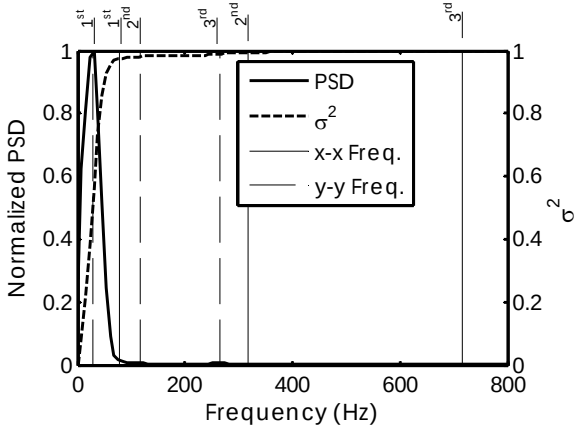

(e) Shot 2: Power spectral density (PSD)

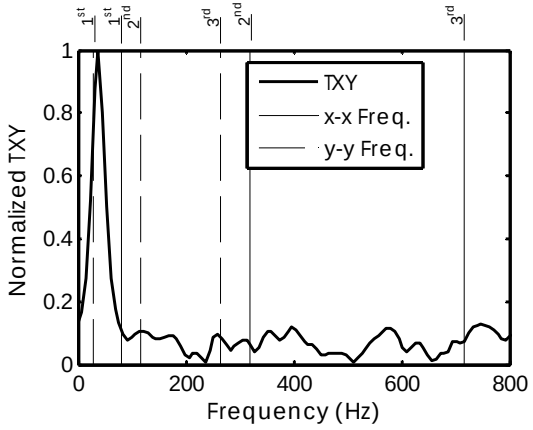

(f) Shot 2: Transfer function (TXY)

Fig. 3.15: Power spectral and transfer function of strain time-history

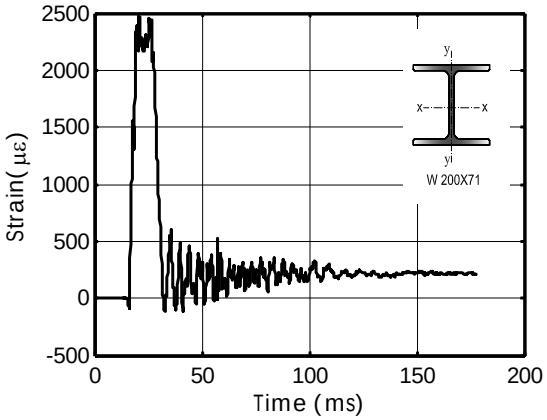

(g) Shot 5: Strain time-history

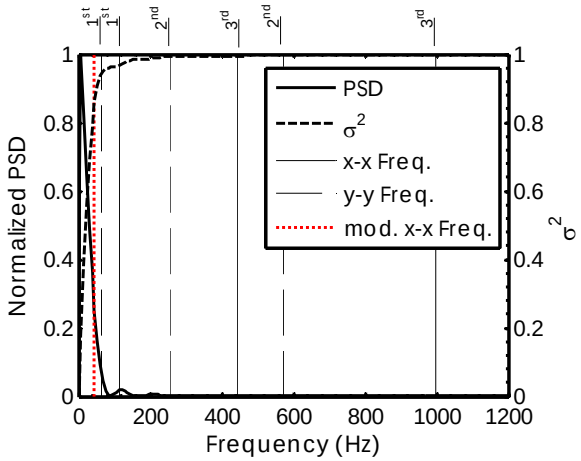

(h) Shot 5: Power spectral density (PSD)

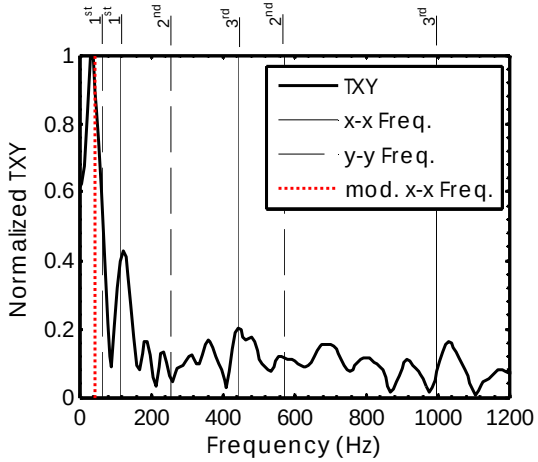

(i) Shot 5: Transfer function (TXY)

Fig. 3.15: Cont.

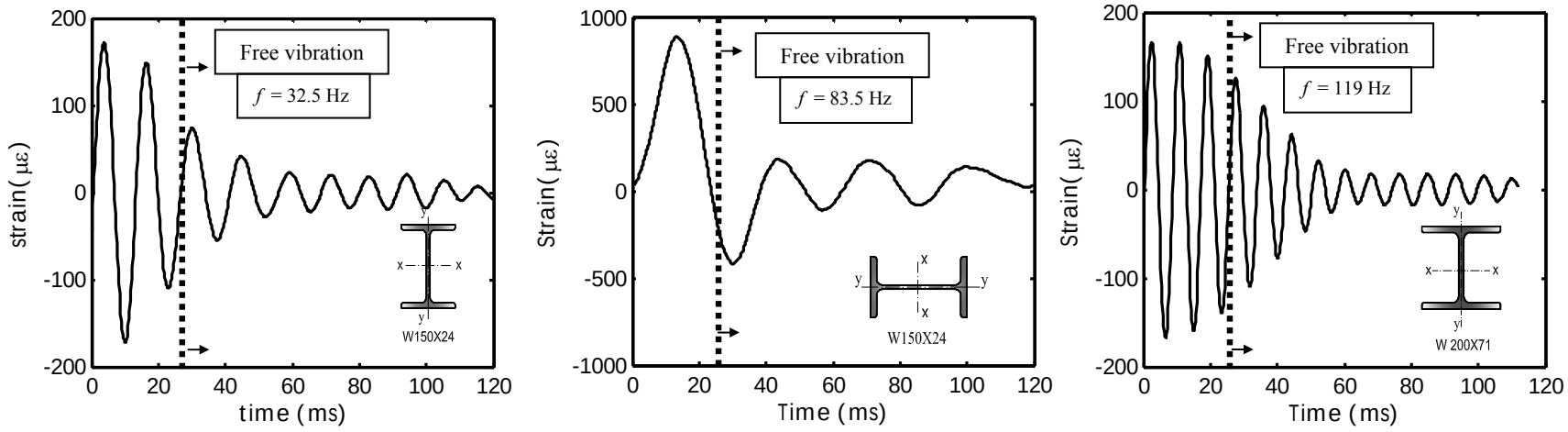

(a) Shot 1 (b) Shot 2 (c) Shot 5

Fig. 3.16: Natural frequencies for test beams

Chapter 4: Dynamic Response of Wide Flange Steel Columns Subjected to Blast Loading: Experimental Results

4.1 Abstract

Thirteen typical wide-flange steel columns, each carrying an axial load equal to 25% of its axial capacity, are field tested using live explosives, involving charge size of 50 to 250 kg of ANFO and ground stand-off distance of 7.0 to 10.3 m. The reflected pressure time histories, time-dependant displacements, accelerations, and strains of the columns are measured, and their post-blast damage and failure modes are reported. Maximum deformation, vibration period, strain rate, and contributing modes in the dynamic response of the columns are compared to those of companion steel beams (without axial load) tested in the same set-up. Results show that in columns that exhibit elastic response, due the elongation of the column period of vibration caused by the axial load, the lateral deformation caused by blast load is reduced rather than magnified by the axial load. Therefore, axial-bending interaction, or P-δ effect, may be neglected for columns with the same level of axial load of the current test, provided the column response remains within the elastic range, but if it crosses into the plastic range, the interaction cannot be ignored.

Keywords: Blast loads; Damage; Dynamics; Explosions; Steel columns; Strain rate; Field tests

4.2 Introduction

When a column is subjected to lateral load due to blast pressure, the static compressive axial load acting on the column affects the dynamic response of the column in two ways. First, the blast load induces lateral deformation in the column which causes the applied and resisting axial forces to form a couple as they are no longer colinear. The couple causes additional lateral deformation and bending in the column. This is the well known *P-δ* effect, which tends to magnify the primary bending moment due to blast pressure and reduces the column load carrying capacity. Secondly, the axial load reduces the flexural stiffness of the column and thus elongates its fundamental period T (Bazant and Cedolin 1991). The dynamic response of the column is function of the ratio of t_d/T (Biggs, 1964), where t_d is the blast pressure positive phase duration. Since the elongation of T leads to reduction of t_d/T, the consequence is a reduction in the column lateral deformation. Therefore, the latter phenomenon tends to mitigate the adverse effect of *P-δ* effect on column response.

The *P-δ* effect on columns subjected to blast load is dealt with in design manuals such as UFC3-340-02 (USDOD 2008) and other blast design guides (ASCE1997; Dusenberry, 2010). The phenomenon is primarily dealt with using slightly modified procedures from those normally applied in beam column design under static loads. The modifications involve the replacement of static column axial strength and plastic moment capacity by its corresponding dynamic values. While this approach is simple to apply, it does not recognize the mitigating effect of the axial load on the response, a phenomenon that does not exist under static conditions.

A more rigorous approach to the inclusion of both effects involves the solution of the equation of motion for beam columns given as

$$EI\frac{\partial^4 y}{\partial x^4} + P\frac{\partial^2 y}{\partial x^2} + m\frac{\partial^2 y}{\partial t^2} = w(x,t) \tag{4.1}$$

where EI is the flexural rigidity of the column, y is lateral displacement, P is the axial load, $w(x,t)$ is the blast load as a function of time t and distance x along the beam column, and m is the mass per unit length. In general, a closed form solution of Eq. (4.1) is difficult to obtain, but Montalva et al. (2007) used the Galerkin method in conjunction with an incremental time integration scheme to solve it. Their solution included the effects of damping, shear deformation, and rotational inertia, but was limited to columns undergoing only elastic deformations. For columns having slenderness ratio $\lambda=KL/r$, where KL is the effective column length and r is the modulus of gyration of cross-section, and subjected to blast and constant axial load P, they made the following recommendations:

(1) Columns with $\lambda > 75$ should not be used.

(2) For $45 \geq \lambda \geq 75$, axial effect must be considered in the analysis.

(3) For $38 \geq \lambda \geq 45$ if $P/P_e < 0.5$, axial effect may be ignored, otherwise it should be considered.

(4) For $\lambda < 38$ axial effect may be ignored, regardless of P/P_e value.

where P_e is the Euler buckling load. However, these recommendations are based on elastic analysis; they ignore the residual stresses and strain rate effect in the columns and may lack generality due to the advent and propagation of inelastic deformations before failure.

From the analytical/numerical perspectives, several other simplified studies have been carried out to predict the response of members under blast and impact loading in order to assess damage and mitigate the associated risk (Biggs 1964; Krauthammer et al. 1986; Krauthammer et al. 1990; Boutros 2000; Schleyer and Hsu 2000). These studies have focused on methods of analysis in which it is assumed that the first mode of vibration governs the dynamic response of columns, or more precisely beam columns, but the deformed shape actually used in the analysis is further simplified by taking the shape which the beam column will assume if it is subjected to only the blast pressure acting statically. Although this simplification appears reasonable, there is not sufficiently detailed empirical

data available from actual blast tests on full scale members to corroborate the generality of this assumption for beam columns in the inelastic and plastic deformation ranges. The notion that a beam column can suddenly transition from an elastic deformed shape to a fully plastic one appears counterintuitive but is usually accepted and used in the development of Single-Degree-of-Freedom (SDOF) models in blast analysis (Biggs 1964, Baker et al. 1983, Krauthammer et al. 1990).

Blast loads induce strain rate dependant stresses and deformations that differ in several respects from those caused by other types of static and dynamic loads, including seismic and wind loads. Investigations have been conducted to study the effect of strain rate caused by dynamic uni-axial loads on the mechanical properties of steel (Manjoine and Pittsuburgh 1944; Krafft et al. 1954; Soroushian and Choi 1987; Malvar 1998; Bassim and Panic 1999). These studies have used impact or split Hopkinson pressure bar test methods and have shown that under high strain rate the yield strength increases noticeably, the ultimate tensile strength increases but proportional less than the yield strength while the elastic modulus remains essentially constant. A significant increase in the yield strength due to strain rate can alter the dynamic behaviour of steel columns under blast loading as it can change traditional steel section classifications and render a compact section non-compact (Liew 2008). The prevailing practice in North America is to use the Dynamic Increase Factor (DIF) (USDOD 2008), which is independent of the actual strain rate that may be experienced by a member under a given blast scenario, to account for the effect of strain rate on column capacity, but in reality the strain rate varies over the cross-section depth and along the column. However, there is insufficient experimental data available from real blast tests to get a sense of the limitations of the assumptions that underpin the recommended DIF values and their effect on assessing the safety of steel columns.

Detailed experimental data for steel members subjected to blast loading is lacking in the open literature partly due to security concerns in some countries and

partly due to the difficulty of obtaining reliable and detailed data in blast tests, which are inherently destructive and make it difficult to protect the instrumentation (Jama et al. 2009). For instance, an experimental program was conducted by the Energetic Materials Research and Testing Centre (Magallanes et al. 2006), to investigate the behaviour of a W360X347 steel column with a clear height of 5.73 m subjected to 1818 kg (4000 pounds) of TNT-equivalent ANFO with a ground stand-off distance of 4.75 m (15'-6"). The steel section and charge/stand-off distance were selected to simulate conditions similar to those in the 1995 bomb attack on Murrah Building in Oklahoma City. This test actually involved a beam tested in the vertical position because no axial load was applied to it and only the peak residual deformation of the column was reported after the test. Such minimal data is not adequate for understanding the real behaviour of columns and/or for validating the results of theoretical models for blast analysis of structures. Since practically every model is based on some assumptions, one must compare their results with properly executed test data in order to ascertain the validity and limitations of the assumptions.

The main objective of this investigation is to provide detailed experimental data from large scale steel columns tested in the field under blast loads generated by the detonation of live explosives. Such data is necessary for validating and/or calibrating theoretical and numerical models and is believed to be currently lacking. For each column, its maximum deformation, vibration period, strain rate, and contributing modes in the dynamic response are compared to those of its companion steel beam (without axial load) tested in the same set-up. It is demonstrated that the axial load in some cases can reduce the maximum lateral deformation caused by blast pressure while in other cases it can magnify it.

4.3 Experimental program

4.3.1 Test specimens

Thirteen wide flange steel columns, each with a height of 2413 mm, were tested under blast loading. Two different section sizes, W150X24 and W200X71, were chosen for the study, which are typical of those used in low and medium-rise steel buildings. The static nominal yield stress and ultimate strength of W150×24 section were 393 and 537 MPa, respectively, and those of W200×71 section were 362 and 474 MPa, respectively. These sections conform to Canadian CSA G40.21 specifications and are classified as Class 1 according to CAN/CSA-S16-09 Standard (CISC 2011).

To simulate the static axial load on a column, the columns with W150×24 section were axially prestressed using two 7-wire prestressing strands having a 13 mm diameter and a nominal ultimate tensile strength of 1860 MPa. For the column with W200X71 section, the axial load was applied by four 13 mm diameter symmetrically prestressing strands. The strands were anchored to a 24.5 mm thick steel plate welded to each end of the column. The strands were simultaneously stressed and an axial force equal to 25% of the static axial load capacity of each section was applied. The prestressing strands were anchored at the location of the mid-height of the cross-section to avoid their extension during the column lateral vibration and thus to minimize the change in the level of the axial load during the blast event.

4.3.2 Test matrix

Each column was subjected to one of five blast shots generated by different combinations of charge weight and stand-off distance, as shown in Table 4.1. All the blast shots were conducted in the field, where the maximum charge size used was limited to 250 kg of ANFO. It is worth mentioning that extremely high pressures can be achieved by close-in explosions involving small charges, but

such blast-scenarios would result local failure modes, such as breaching and tearing, that are not intended to be the focus of this investigation. Here, the objective is to investigate the behaviour of full size column specimens subjected to plane shock waves and essentially uniform pressure. Consequently, a minimum stand-off distance of several meters had to be maintained. Table 4.1 shows the test matrix, including the charge mass, ground stand-off distance, scaled-distance, applied axial load magnitude, section designation, and column orientation with respect to bending due to blast pressure and corresponding slenderness ratio. The ground stand-off distance ranged from 7 to 10.3 m while the charge size varied from 50 to 250 kg. The stand-off distance and charge weight combinations were selected to achieve different levels of response and ductility ratio in the test columns when subjected to bending about the strong axis (x-x) or the weak axis (y-y). Note that the slenderness ratio of the test columns is 27, 38, or 100. A total of twelve W150X24 section columns were tested in shots 1 to 4 had while one W200X71 section column was tested in shot 5.

4.3.3 Test setup

Figures 4.1(a) and (b) show the front and side views of the test setup for shots 1 to 4 in the test program. A reinforced concrete (RC) supporting frame with clear opening of 2.36X2.81 m was used to support the steel specimens during the blast test. The supporting frame consisted of two RC beams and columns joined together at the 4 corners by steel sockets.

In order to confine the specimens and to prevent wrap around effect, an ISO steel container was placed behind the frame. The wrap around phenomenon has a pronounced effect on the pressure and impulse acting on a target with relatively small dimensions as shock waves would engulf the target before the pressure substantially drops on the target surface facing the charge. For convenience, the chosen steel container was a standard shipping container with nominal dimensions of 20 ft (6.1 m) long, 8 ft (2.4 m) wide, and 8 ft (2.4 m) high.

The container also provided protection to the instrumentation and wiring during each blast event. In addition, plywood panels were placed between the test specimens to prevent the pressure from wrapping around the specimens during the blast.

As shown in Fig. 4.1(a), concrete block wing walls were erected around the RC frame which provided a total reflecting surface with outer dimensions approximately equal to 5.42×3.72 m, as depicted in Fig. 4.1(c). This set-up provided reasonably uniform peak pressure and impulse over the test columns by minimizing the clearing effect, which is due to rarefaction waves travelling back from the edges of the reflecting surface and causing considerable pressure relief, which, in turn, leads to a significant loss of total specific impulse (Smith and Hetherington 1994). Figure 4.1(c) shows key dimensions of the test setup, including the frame dimensions, dimensions of the overall reflecting surface, and column spacing. This set-up was used for shots 1 to 4 and each shot involved the testing of six W150×24 members, which included 3 beams and 3 columns. Only the detailed data for the test columns are presented and discussed in this paper.

To ensure reasonably uniform pressure acting on the test specimens, a ground standoff distance of 9.5 m was chosen for the column having W200X71 section, resulting in a scale distance of 1.51 m/kg$^{1/3}$. As the predicted reflected pressure for this scaled-distance acting on the surface of the column flange facing the blast was deemed to be insufficient to cause sufficiently high stresses in the column, it was decided to increase the blast load acting on it by placing a 1.18 m wide and 2.50 m high steel curtain in front of the column. The curtain was designed to transfer the blast pressure acting on its surface to the column flange, thus magnifying the blast load on the column. The curtain consisted of twelve 1180 mm long structural steel elements made of HSS 254×152×6.4 mm section. These elements were strung by aircraft cables and cladded on one face with a thin metal sheet. The cables were firmly secured to steel rods at the top of the curtain, and the rods were supported at their ends on steel brackets welded to the reaction

frame ceiling. Figure 4.2(a) shows the dimensions and details of the steel curtain, while Fig. 4.2(b) shows its front view in the test frame. This support system allowed the entire curtain to swing freely. The curtain was designed to have very high stiffness in the horizontal direction but negligible bending rigidity in the vertical direction. The high horizontal stiffness allowed for an efficient load transfer without significant energy dissipation through plastic deformation of the curtain elements while the low vertical bending rigidity enabled the curtain to follow the test sample deformed shape without increasing its stiffness.

All the steel columns were pinned at the top and roller supported at the bottom. Steel bolts were used to pin the top of the column to the RC frame. The roller support was formed by welding a round bar to the bottom of the column and the bar reacted against a bracket welded to the bottom of the supporting frame. In addition, a steel chain was used to prevent the bottom of the column from swinging freely during the negative or rebound phase of the motion. A 100 mm vertical gap was left between the bottom end of each column and the support frame to allow free axial displacement.

4.3.4 Instrumentations

During the blast tests, the reflected pressures, columns strains, accelerations, and displacements were measured. The reflected pressure was measured by five pressure transducers that were installed at different locations on the RC frame and are labeled as P1 to P5 in Fig. 4.1(c). These gauges were coated with silicon rubber to minimize the effects of heat radiation during the explosion. All the pressure transducers had a rated capacity of 6950 kPa, a resolution of 0.021 kPa, a low frequency response of 0.5 Hz, and a resonant frequency of 500 kHz.

The displacement time-history along each test specimen was recorded using a number of linear potentiometers. The potentiometers had a maximum stroke of 600 mm, a repeatability of less than 0.01 mm, and a maximum operating speed of 5 m/s. The potentiometers were supported by wooden posts inside the

test frame at one end and attached to the specimen of the other end. The end in contact with the specimen was clamped to allow measurement of inbound and rebound displacements. As several displacement potentiometers were damaged during the test program, only the mid-span displacement time-history for columns 2C1 and 3C1 were recorded by transducers D-2C1, and D-3C1, respectively. In addition, 120 ohm strain gauges were used to capture the strain time-history at a number of locations along each column as shown in Fig. 4.3. As indicated in the latter figure, six different strain gauge arrangements were used to capture the variation of strain over the cross-section and along the span. Each strain gauge was given a designation to indicate the shot number and its location according to the particular arrangement in Fig. 4.3, e.g. strain gauge 6 in shot 3 was designated as 3-SC6.

Mid-span acceleration-time-history was recorded for column 5C1 using an accelerometer with a frequency range from 0.5 to 35000 Hz. This accelerometer is designated as A-5C1. A high speed camera was used to record a close-in view of the blast event in shot 3 and an overview of blast event in shot 4. The high speed camera could capture high-quality video at 3000 frames per second. All the data were automatically recorded at a sampling rate of 1 MHz.

The charge was made of several 25 kg bags of Ammonium Nitrate-Fuel Oil mixture (ANFO) and arranged in a prismatic shape, as shown in Fig. 4.1(a). The chemical composition of the explosive charge was of 5.7% fuel oil and 94.3% ammonium nitrate. The explosive energy of ANFO is approximately 3717 kJ/kg, which is 82% of the energy of one kilogram of TNT. It is expected that the charge shape will have some effect on the planarity and uniformity of the pressure wave acting on the test columns, but based on existing criteria, for the selected stand-off distances in this study, its effect is assumed to be relatively small (USDOD 2008).

4.4 Experimental results

4.4.1 Post-blast observations

The steel columns were carefully checked after each shot and the post-blast damage and mode of failure of each specimen were recorded. The response of the columns in shots 1, 2, 3, and 5 appeared to be flexural. The columns in shots 1 and 3 experienced only elastic deformations as no permanent deformations were observed in either in-plane or out-of-plane directions. The columns in shots 2 and 5 experienced yielding and plastic deformation, particularly visible at the mid-span section; however, no out-of-plan deformations were observed in these columns. On the other hand, in shot 4, the columns exhibited instability deformations as they experienced yielding and plastic deformation in both the in-plane and out-of-plane directions accompanied by noticeable twist at mid-span section. None of the columns exhibited local buckling or fracture at any section.

Post-blast residual in-plane and out-of-plane deformations along all the test columns were measured using a total station. The maximum permanent deflection for columns in shot 2 was found to be 29.8 mm at the mid-span section of 2C1. Columns 2C2 and 2C3 experienced lower permanent deflection than 2C1, with maximum value of 26.5 and 22.8 mm, respectively. Figure 4.4(a) shows the in-plane post-blast deflected shapes of the columns in shot 2, which appear to be nearly symmetrical about the longitudinal centreline of the column. Figure 4.4(b) shows the peak permanent deflection of 5C1 to be 32.8 mm at mid-span. The maximum in-plane and out-of-plane deflections of columns in shot 4 were 60.4 and 93.3 mm, respectively. The full post-blast deflected shape of the columns in shot 4, in both in-plane and out-of-plane directions, are plotted in Fig. 4.4(c) and (d), respectively. The difference among the deflected shapes of nominally identical columns in the same shot may be attributed to the slight difference in the stand-off distance of the columns and to the non-uniformity of the blast pressure caused by random variations in the parameters governing blast waves. As the

scaled-distance decreases, the blast pressure wave tends to deviate from a purely plane shape, which affects the blast pressure distribution on the target surface.

4.4.2 Pressure time histories

A typical reflected pressure time-history obtained in shot 1, which involved a charge size of 50 kg at stand-off distance of 10.3 m, is shown in Fig. 4.5. The pressure profile exhibited the typical rapid rising peak pressure P_r of 270 kPa from the ambient pressure, followed by decay towards the ambient pressure, within the positive phase duration t_d of approximately 20 ms, followed by a negative pressure phase. The area beneath the pressure time-history represents the impulse, and its variation with time is shown in Fig. 4.5, with a maximum impulse of 780 kPa.ms, which was obtained by numerically integrating the area under the pressure time profile. The reflected pressures, impulses, and positive phase durations measured by different transducers in all the blast shots are plotted in Fig. 4.6. It can be observed that there are variations in the measured pressure and impulse values recorded by the different gauges in the same shot. These variations may be in part due to the small differences in the scaled-distances from the charge centres to each transducer and partly due to the irregularities of the terrain that had gentle upward and downward slope, which are known to enhance or weaken the shocks (Baker 1983). The average of the measured peak reflected pressures, P_r, recorded by the different transducers in shots 1, 2, 3, 4, and 5 was 307, 623, 1560, 4283, and 2098 kPa, respectively, with coefficient of variation (COV) of 8%, 6%, 17%, 14%, and 9%, respectively. For shots 1, 2, 3, 4, and 5, respectively, the average measured reflected impulse, I_r, based on the recorded pressure profiles in each shot, was found to be 715, 1279, 2130, 3174, and 3144 kPa.ms with corresponding COV of 7%, 7%, 17%, 3%, and 18%.

The positive phase duration is a critical parameter as it affects the dynamic response of the structural member. For structural members whose natural period is greater than the positive phase duration of the blast pressure, similar to the current

test columns, their member response is governed by the maximum impulse rather pressure (Baker et al. 1983; Smith and Hetherington 1994). In the present blast shots, the positive phase duration had an average value of 7.3, 6.0, 6.2, 2.1, and 8.4 ms with COV of 5%, 16%, 12%, 9%, and 22% for shots 1, 2, 3, 4, and 5, respectively.

4.4.3 Time-dependant deformations

All strain time histories were recorded from the instant of explosion initiation. Several gauges failed to capture any data due to damage caused by the blast and falling debris. The strain time histories for different points over the depth of the columns cross-sections during shot 1 to 5 are shown in Fig. 4.7. The strain time histories for columns 1C1, 1C2, and 1C3 in shot 1, with maximum tensile strains of 413, 420, 374 $\mu\varepsilon$, are shown in Fig. 4.7(a) to (c), captured by gauges 1-SC1, 1-SC3, and 1-SC8, respectively. These gauges were mounted on the back flange at the mid-height of each column. The minor differences among the maximum strain values may be attributed to the non-uniform distribution of the reflected pressure on these specimens. The maximum strain in columns 1C1, 1C2, and 1C3 occurred at 17.8, 17.1, and 17.8 ms, respectively. By comparing these time lengths with the positive phase duration of the corresponding pressure histories (Fig. 4.5), one can observe that the maximum strain occurred in the free vibration phase at a time greater than the positive phase duration, which is indicative of the impulsive nature of the present blast loads (Biggs 1964). As expected, the gauge 1-SC5 recorded a compressive maximum strain of 250 $\mu\varepsilon$ as it was located closer to mid-height of the cross-section. The strain time histories recorded by 1-SC3 and 1-SC5 were in-phase indicating a flexural response without twisting and local deformations.

Due to the larger charge and smaller stiffness of the columns in shot 2, they experienced larger strains than those in shot 1. The strain responses for columns 2C1 and 2C2 are shown in Fig. 4.7(d) and (e). The maximum

compressive strain in column 2C2 captured by gauge 2-SC5 was 5420 $\mu\varepsilon$. Due to the limited voltage range of gauge 2-SC2 and 2-SC3, a maximum strain of 8000 $\mu\varepsilon$ was recorded at the location of these gauges; this is indicated in Fig. 4.7(d) and (e) by a plateau for strains higher than 8000 $\mu\varepsilon$. Gauge 2-SC4 recorded a smaller strain compared to the maximum strain at the mid-height of column 2C2, indicating that essentially a constant axial load was maintained during the flexural vibration of the columns. The maximum measured tensile strain in the columns in shot 3 was 1760 and 2000$\mu\varepsilon$ in 3C1, and 3C2, respectively. These strain values indicate that the latter columns responded in the elastic range only, as shown in Fig. 4.7(f) and (g). Strain gauge 3-SC5 in column 3C2 recorded a maximum compressive strain of 1600 $\mu\varepsilon$.. The strain time-history for column 4C2 in shot 4 is shown in Fig. 4.7(h), with a maximum strain of 9300 $\mu\varepsilon$, which is substantially greater than the static yield strain. Figure 4.7(h) shows only the first peak recorded during shot 4 as a signal loss occurred after the second peak and this loss was indicated in the remaining strain history by a sudden increase to a value of 12000 $\mu\varepsilon$, followed by a plateau to the end of the trace. As shown in Fig. 4.7(i), the maximum mid-span tensile strain in column 5C1 was found to be 3960 $\mu\varepsilon$.

The variations of strains at $L/2$, $L/3$, and $L/6$ from one end of the columns, where L is the column height, were also recorded, as shown in Fig. 4.8(a), (b), (c), and (d) for columns 1C2, 3C2, 4C2, and 5C1, respectively. It can be observed that the strain time histories for columns 1C1, 3C2, and 5C1 are in-phase, indicating a flexural response, with no noticeable out-of–plane deformation throughout the vibration period. The strain time histories variations along column 2C4 were incomplete due to signal loss after the first peak, thus, only the strain variations during the first peak could be plotted for column 2C4. The strain variations along the test columns provide a good indication of the deflected shape during the vibration period, as will be discussed in the next section.

The mid-span displacements for columns 2C1 and 3C1 are shown in Fig. 4.9(b) and (c) as captured by displacement potentiometers D-2C1 and D-3C1,

respectively. The maximum displacement for column 2C1 was recorded to be 56.1 mm. While the charge size used in shot 3 was larger than that in shot 2, the columns involved in this shot had higher stiffness than those in shot 2; therefore, a lower maximum displacement of 30.9 mm was recorded for column 3C1 as shown in Fig. 4.9(b). Due to the destruction of the displacement transducers D-1C1, D-4C1, and D-5C1 by the blast and falling debris, the displacement time histories were not recorded at the mid-span of the columns in these shots. The displacement time histories y_s were obtained by integrating the curvature diagrams, obtained from the strain time histories, of columns 2C1, 2C3, 2C4, and 2C5, designated as $y_{/sC2}$, $y_{s\text{-}3C2}$, $y_{s\text{-}4C2}$, and $y_{s\text{-}5C1}$, respectively. The displacement time histories measured by gauge D-3C1 in column 3C1 and the corresponding computed displacement $y_{s\text{-}3C2}$ of the replicate column 3C2 are plotted in Fig. 4.9(c). The comparison shows good agreement in terms of the maximum displacement and the overall behaviour. The maximum calculated displacements for columns 1C2, 3C2, 4C2, and 5C1 were 5.3, 29.2, 107, and 71 mm, respectively.

The mid-span acceleration-time-history for column 5C1 was recorded during shot 5. As shown in Fig. 4.10, under the effect of the blast pressure, the column exhibited an increase in acceleration to a maximum value of 1300 m/s^2 at approximately 1.5 ms after the arrival time. A second acceleration peak of 1250 m/s^2 can be observed at 5.5 ms after the arrival time. The second peak can be explained by a sudden jump in the velocity caused by the formation of the plastic hinge at mid-span (Magnusson 2007).

4.5 Discussion on test results

4.5.1 Column deflected shape

The deflected shapes at different time instants were obtained by the numerical integration of the corresponding curvature diagrams, established based on the measured strain values at three locations along the half-length of each column.

The curvature at each section was obtained by computing the slope of the strain profile at that section. Figures 4.11(a) and (b) show the deflected shapes at different instants during the in-bound displacements of column 1C2 and 5C1, respectively. The deflected shapes at different instants were also compared with the shape functions ϕ usually assumed when performing dynamic analysis based on a Single-Degree-of-Freedom (SDOF) model, where ϕ represents the deflected shape function of a simply supported prismatic member under uniform static load. For deformations within the elastic and plastic ranges, ϕ is given as (Biggs 1964; Smith and Hetherington 1994)

$$\phi(\xi) = \begin{cases} 1 - \frac{24}{5}\xi^2 + \frac{16}{5}\xi^4 & \text{(elastic range)} \\ 1 - 2|\xi| & \text{(plastic range)} \end{cases} \tag{4.2}$$

where ξ = (x/L-1/2) is a natural coordinate, and L is the member length. In the plastic range, in conformity with the usual assumption of plastic analysis, it is assumed that under uniform pressure, deformation is concentrated at the location of the plastic hinge at mid-span of the member and the rest of the member only experiences rigid body motion. Using the above elastic range shape function in conjunction with the measured mid-span displacement, for column 1C2 its elastic deformations are plotted in Fig. 4.11(a) at different the instants of time. The assumed shape function provides a good approximation of the actual deflected shape in the elastic range during the in-bound displacement. In Fig. 4.11(b), the deflected shapes of column 5C1 undergoing plastic deformations obtained by integration of curvature are compared with those based on the shape functions applicable to the elastic and the plastic ranges. The elastic shape function results in deflected shapes that compare well with the actual deflected shapes for small displacements up to 50 mm, but for larger displacements, while neither shape function gives a good estimate of the actual deflected shape, the computed deflected shapes based on the elastic shape function are in relatively better agreement with the actual deflected shape than those based on the plastic shape

function, particularly in the range of the plastic deformations experienced by column 5C1.

4.5.2 Strain rate time-histories

The strain rate time histories were obtained by differentiating the captured strain time histories using the central difference method. The strain rate time histories at the location of gauges 2-SC3, 2-SC4, and 2-SC5 are plotted in Fig. 4.12(a). The strain rate profiles over the depth of column 2C2 at different instants of time are plotted in Fig. 4.12(b). As can be observed, strain rate profiles are linear, once again, confirming the assumption of section planarity at different time instants. Table 4.2 lists the maximum mid-span strain rate for the columns in each blast shot. The highest strain rate was 5.00 /s in shot 4 and the lowest rate was 0.22 /s in shot 1. The highest mid-span strain rates associated with shots 2, 3, and 5 were calculated to be 1.50, 1.50, and 2.70 /s, respectively. It is worth mentioning that these strain rates are significantly less than the strain rate range of 100-1000 /s often cited for blast in the literature (Bischoff and Perry 1991). However, to date in the open literature, there is scant strain rate data obtained from blast tests on reasonable size steel members to confirm the validity of the above range in far range blast analysis and design. Therefore, additional tests with a wide range of scaled-distances are needed to establish the range of strain rates experienced by steel structures during unconfined explosions. Such data would assist in deriving realistic dynamic increase factors for design and evaluation purposes.

Strain rate time histories along columns 1C2 and 5C1are shown in Fig. 4.13(a) and (c), respectively. Figures 4.13(b) and (d) show the strain rate variation along columns 1C2 and 5C1 at different instants of time. Due to the contribution of higher modes of vibrations in the dynamic response, as will be discussed later, the strain rate variations do not indicate a specific trend along the test columns. The rapid variation of strains with time at locations involving higher frequencies

of vibrations leads to higher strain rates than at the mid-span sections, e.g. the effect of the second out-of-plane mode at 1/3 of span where 1-SC6 and 5-SC6 gauges were located.

4.5.3 Effect of the axial load

To study the effect of the axial load on the dynamic response of steel members under blast loading, the dynamic responses of the test columns will be compared with the results of companion beams, i.e. similar members with no axial load, previously reported by Nassr et al. (2011). These beams were tested in the same blast shots as the current columns and had identical geometric and material properties to the columns. Figures 4.14(a) and (b) show a comparison between the mid-span displacement time histories for the test columns and their companion beams in shots 2, and 3, respectively. The maximum displacement increased due to the axial load by 38% in the case of columns experiencing plastic deformations in shot 2. On the other hand, the axial load had a small effect in the case of columns experiencing only elastic deformations as in shot 3 where the maximum displacement decreased by 7%.

Figures 4.14(c) and (d) show a comparison between the mid-span strain time histories for the test columns and their companion beams in shots 1, and 4, respectively. Due to the large inelastic deformations of the columns in shot 4, the effect of axial load was significant as it increased the maximum strain by 158%. Again, a smaller effect of the axial load was observed in the case of columns that sustained only elastic deformations as in shot 1 where the maximum strain decreased by 15%. It should be noted that, unlike static beam column elements, where the applied axial load magnifies the maximum deformations due to lateral load by a magnification factor (Timoshenko and Gere, 1961), under dynamic lateral loading, the axial load appears to decrease the maximum lateral deformation in the case of columns undergoing elastic deformations as seen in shots 1 and 3. As will be shown later, this may be attributed to the effect of the

higher modes on the response of the column and the increase of its natural period in flexure by the axial load. The ratio of the positive phase duration of the reflected pressure to the natural period of the member is known to influence the member response, particularly when the response is in the impulse regime, and the decrease of this ratio leads to reduction in the maximum response (Biggs 1964). On the contrary, in the plastic state, where the *P-δ* effect tends to dominate the overall response, an increase of maximum deformation due to axial load is observed. A summary of the comparisons between each column and its companion beam responses are shown in Table 4.2. The axial load increased the maximum displacement in the case of the columns in shot 5 by 28% while it decreased the maximum displacement for the columns in shot 1 by 13%. The maximum mid-span strain was increased by 57% for the columns in shot 2, but it was decreased by 16% for the columns in shot 3.

It is evident from these results that the slenderness ratio alone cannot be used as a criterion to exclude or include the effect of axial load on bending of steel columns. For example, for column 4C2 had a slenderness ratio of 38 about the strong axis, which was the bending axis in the test, and it experienced 158% more lateral deformation than the companion beam. According to Montalva et al. (2007) the effect of the axial load on the bending of this column can be ignored, but as observed from test results it would be unconservative to do so. The current results show that the slenderness ratio, P/P_e and the advent of plastic deformation must be collectively considered to assess the significance of axial-bending interaction in columns under blast loads.

The axial load increased the permanent deformations sustained by the test columns. The effects of axial load on the maximum permanent deformations δ_p and strain rate are indicated in Table 4.2. The axial load has a noticeable effect on the strain rate of members with inelastic deformations as the strain rate increased by up to 93%, e.g. members in shots 2, 4, and 5, while its effect was less in the case of columns undergoing elastic deformations, e.g. members in shots 1 and 3.

The effect of the axial load on contributing modes in the response and natural frequencies was studied by computing the Power Spectral Density (PSD) from strain time histories of the test columns. Figures 4.15(a) and (d) show the PSD responses for mid-span strain time histories for columns 1C1 and 2C2 captured by 1-SC1 and 2-SC5, respectively. Figures 4.15(b) and 4.16(e) show the PSD for the companion beams. The contributions of different frequency components in the response were studied by calculating the variance σ^2 of the PSD curve, as shown in Fig. 4.15. The transfer function (TXY) is also used to identify the frequencies components related to the structural properties of the system as shown in Fig. 4.15(c) and (f). In addition, to facilitate the interpretation of different frequency components, the first three frequencies corresponding to the first three modes of vibration about both the strong (x-x) and the weak (y-y) axes of the member were calculated and are plotted in Figs. 4.15. These frequencies were calculated using the following expression for a simply supported member (Bazant and Cedolin 1991):

$$f_n = \frac{n^2\pi}{2L^2}\sqrt{\frac{EI}{m}}\sqrt{1-\frac{P}{n^2P_{cr}}} \qquad n=1, 2, 3,\ldots \tag{4.3}$$

where m is the mass per unit length. As shown in Fig. 4.15(a) and (c), it can be observed that the response is dominated by the frequency component of 76 Hz, representing the fundamental frequency, which contributed approximately 73% to the total response. A secondary peak frequency of 712 Hz was also noticed, a frequency that corresponds to the third mode of vibration, which contributed approximately 4% to the total response. The other frequency components corresponded to the first three out-of-plane modes of the columns, with total contribution of 16% to the response. The response of the companion beam, as shown in Fig. 4.15(b) and (c), was also dominated by a frequency of 84 Hz with an approximate contribution of 88% to the total response, the third mode contributed only 3%, while the third out-of-plane mode contributed 2% to the response. Due to the lower stiffness of the columns in shot 2, the effect of the

axial load on the fundamental frequencies is noticeable (see Eq. (4.3)), as can be noticed in Figs. 4.15(d), (e), and (f). The responses of the test columns in shot 2 were dominated by the fundamental frequency of 20 Hz with a reduction of 40% compared to the fundamental frequency of the companion beam. The fundamental modes contributed 95% to the total response of both the test column and the beam in shot 2. Table 4.2 summarizes the effect of the axial load on the fundamental frequencies of the test members.

4.6 Summary and conclusions

In this study full-scale field tests were performed on wide flange steel columns subjected to high-intensity, short duration out-of-plane blast loads in addition to a static axial load equal to 25% of the column static axial capacity. The effects of charge size and stand-off distance on columns behaviour were investigated by measuring their time-dependant deformations using a variety of measuring devices. The blast load characteristics were also measured in each blast shot. The measured response values for the columns were compared with the corresponding values for companion beams to study the effect of the axial load on the response. Based on the results of the present study the following conclusions are reached.

(1) The axial load on a column may increase or decrease the maximum lateral displacement of the column due to blast pressure. The reduction is caused by the elongation of the column fundamental period due to axial load while the increase is caused by the *P-δ* effect.

(2) For the axial load level applied in the current tests, which was 25% of the column axial capacity, the axial load decreased the lateral displacement of the columns relative to that of a similar column without axial load, as long as the column did not experience plastic deformation.

(3) In columns that experienced plastic deformation, the *P-δ* effect dominated the response and the axial load increased the column maximum lateral deformation by up to 158%.

(4) The axial-bending interaction, or P-δ effect, may be neglected for columns with the same level of axial load of the current test, provided the column response remains within the elastic range, but if it crosses into the plastic range, the interaction cannot be ignored.

(5) The axial-bending interaction affects the contributing modes of vibration in the dynamic response by exciting higher modes of vibration and thus reducing the effect of the first mode.

(6) The axial-bending interaction increases the strain rate in the plastic range of the responses by up to 93%.

(7) While the strain rate variation along the height of the test columns did not exhibit any specific trends due to the contribution of the higher modes of the dynamic response, nevertheless strain rate profiles can be reasonably approximated as linear over the cross-section of columns under blast loading.

4.7 Acknowledgements

The authors wish to gratefully acknowledge the following organizations for their support towards this study: the Chemical, Biological, Radiological/Nuclear and Explosives Research and Technology Initiative (CRTI project 06-015TD), Public Works and Government Services Canada, the Centre for Effective Design of Structures (CEDS) at McMaster University, and the Natural Sciences and Engineering Research Council of Canada for their financial support, the Canadian Explosives Research Laboratory (CERL) for assisting with the blast tests, and the Canadian Armed Forces for the use of their test range. CEDS received funding through the Ontario Research and Development Challenge Fund, a program of the Ministry of Research and Innovation of Ontario. The authors also appreciate the technical support of Messrs. Rick Guilbeault and Don Wilson of CERL during the experimental phase of this study.

4.8 Notation

The following symbols are used in this paper:

δ_p = maximum permanent displacement (mm);

$\dot{\varepsilon}$ = strain rate (/s);

I_r = reflected impulse (kPa.ms);

L = member height (m);

m = the mass per unit length (kg/m)

P = axial load (kN);

P_r = peak reflected pressure (kPa);

t_d = positive phase duration (ms);

y = mid-span displacement (mm);

Z = scaled-distance (m/kg$^{1/3}$).

4.9 References

ASCE. (1997). “Design of blast resistant buildings in petrochemical facilities.” Task Committee on Blast Resistant Design, ASCE, New York.

Baker, W. E., Cox, P. A., Westine, P. S., Kulesz, J. J., and Strehlow , R. A. (1983). "Explosion hazards and evaluation." Elsevier Scientific Pub. Co., Amsterdam; New York.

Bassim, M. N., and Panic, N. (1999). "High strain rate effects on the strain of alloy steels." Journal of Materials Processing Technology, 92-93, 481-5.

Bazant, Z. P., and Cedolin, L. (1991). "Stability of structures: elastic, inelastic, fracture, and damage theories." Oxford University Press, New York.

Biggs, J. M. (1964). "Introduction to structural dynamics." McGraw-Hill Book Company, NY.

Boutros, M. K. (2000). "Elastic-plastic model of pinned beams subjected to impulsive loading." Journal of Engineering Mechanics, 126(9), 920-927.

Bischoff, P., and Perry, S. (1991). "Compressive behaviour of concrete at high strain rates." Materials and Structures, 24(6), 425-450.

CISC. (2011). "Handbook of steel construction." Canadian Institute of Steel Construction, Willowdale, Canada.

Dusenberry, D. O. (2010). "Handbook for blast resistant design of buildings." J. Wiley, Hoboken, N.J.

Jama, H. H., Bambach, M. R., Nurick, G. N., Grzebieta, R. H., and Zhao, X. L. (2009). "Numerical modelling of square tubular steel beams subjected to transverse blast loads." Thin-Walled Structures, 47(12), 1523-1534.

Krafft, J. M., Sullivan, A. M., and Tipper, C. F. (1954). "The effect of static and dynamic loading and temperature on the yield stress of iron and mild steel in compression." Proceedings of the Royal Society of London. Series A, Mathematical and Physical Sciences, 221(1144), 114-127.

Krauthammer, T., Bazeos, N., and Holmquist, T. J. (1986). "Modified SDOF analysis of RC box-type structures." Journal of Structural Engineering, 112(4), 726-744.

Krauthammer, T., Shahriar, S., and Shanaa, H. M. (1990). "Response of reinforced concrete elements to severe impulsive loads." Journal of Structural Engineering, 116(4), 1.061-1079.

Liew, J. Y. R. (2008). "Survivability of steel frame structures subject to blast and fire." Journal of Constructional Steel Research, 64(7-8), 854-866.

Magallanes, J. M., Martinez, R., and Koening, J. (2006). "Experimental results of the AISC full-scale column blast test." Report TR-06-20.2, The American Institute of steel construction, Chicago.

Magnusson, J. (2007). "Structural concrete elements subjected to air blast loading," PhD Thesis, Royal Institute of Technology, Sweden.

Malvar, L. J. (1998). "Review of static and dynamic properties of steel reinforcing bars." ACI Materials Journal, 95(5), 609-616.

Manjoine, M. J., and Pittsuburgh, E. (1944). "Influence of rate of strain and temperature on yield stresses of mild steel." Journal of Applied Mechanics, 11, 211-18.

Montalva, A., Loukaides, E., Long, M., and Gallant, S. (2007). "Analysis of steel columns for air-blast loads. In Proceedings of the International Symposium on Interaction of the Effects of Munitions with Structures, ISIEMS 12.1, Orlando,FL, 18-21 September 2007.

Nassr, A. A., Razaqpur, A. G., Tait, M. J., Campidelli, M., and Foo, S. (2011). "Experimental performance of steel beams under blast loading" ASCE's Journal of Performance of Constructed Facilities. (Accepted, September, 2011). DOI: 10.1061/(ASCE)CF.1943-5509.0000289.

Schleyer, G. K., and Hsu, S. S. (2000). "A modelling scheme for predicting the response of elastic-plastic structures to pulse pressure loading." International Journal of Impact Engineering, 24(8), 759-777.

Smith, P. D., and Hetherington, J. G. (1994). Blast and ballistic loading of structures, Butterworth-Heinemann, Oxford; Boston.

Soroushian, P., and Choi, K.-B. (1987). "Steel mechanical properties at different strain rates." Journal of Structural Engineering, 113(4), 663-672.

Timoshenko, S.P., and Gere, J.M. (1961). "Theory of elastic stability." McGraw-Hill Inc., New York.

USDOD. (2008). "Structures to resist the effects of accidental explosions." Document No. UFC3-340-02. US Department of Defense (USDOD), Washington, DC.

4.10 List of figures

Table 4.1: Matrix of test specimens

Shot	Section designation	Axial load (P) (kN)	Charge mass (kg)	Stand-off distance (m)	Scaled-distance ($m/kg^{1/3}$)	Axis of bending	Slenderness ratio (KL/r)*	Test columns
1	W150X24	270	50	10.30	2.80	x-x	38	1C1, 1C2, 1C3
2	W150X24	270	100	10.30	2.22	y-y	100	2C1, 2C2, 2C3
3	W150X24	270	150	9.00	1.69	x-x	38	3C1, 3C2, 3C3
4	W150X24	270	250	7.00	1.11	x-x	38	4C1, 4C2, 4C3
5	W200X71	640	250	9.50	1.51	x-x	27	5C1

Table 4.2: Effect of the axial load on the dynamic responses of steel members

Shot	Max. disp. (mm)			Max. strain ($\mu\varepsilon$)			Max. strain rate (/s)		
	Axial load = 0	Axial load = P	Ratio[2]	Axial load = 0	Axial load = P	Ratio	Axial load = 0	Axial load = P	Ratio
1	6.9	5.3	0.77	559	420	0.75	0.28	0.22	0.79
2	40.8	56.1	1.38	3435	5390[4]	1.57	0.90	1.50	1.67
3	33.2	30.9	0.93	2384	2000	0.84	1.70	1.50	0.88
4	NC[1]	107	---	3610	9300	2.58	2.89	5.00	1.73
5	62.8	71	1.13	2536[3]	3008[3]	1.19	1.40	2.70	1.93

Shot	Max. δ_p(mm)			Frequency f (Hz)		
	Axial load = 0	Axial load = P	Ratio	Axial load = 0	Axial load = P	Ratio
1	0	0	1.00	84	76	0.90
2	2.4	29.8	12.42	33	19	0.58
3	0	0	1.00	84	76	0.90
4	3.8	60.2	15.84	84	76	0.90
5	30.7	32.8	1.07	119	109	0.92

(1) NC= Not Captured

(2) Ratio=column (Axial load=P)/beam (Axial load=0)

(3)The strain was measured at 1/3 of the span from the bottom

(4) Maximum mid-span at the compression flange of the column

(a) Front view of test setup

(b) Side view of test setup

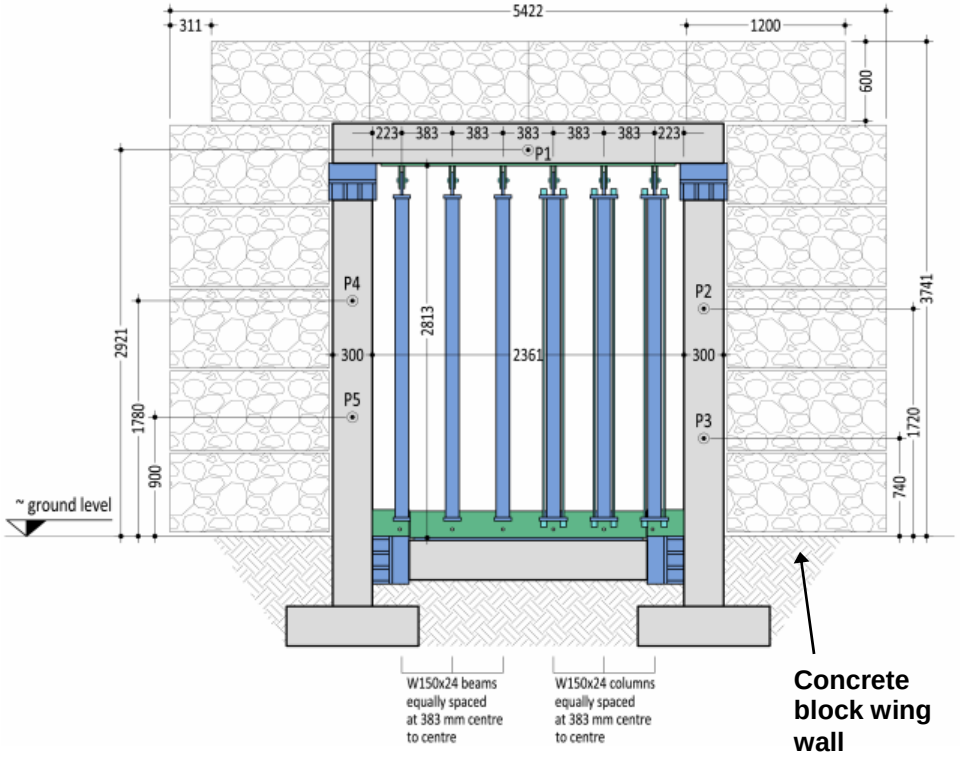

(c) Dimensions of the reflecting surface (in mm)

Fig. 4.1: Blast test setup

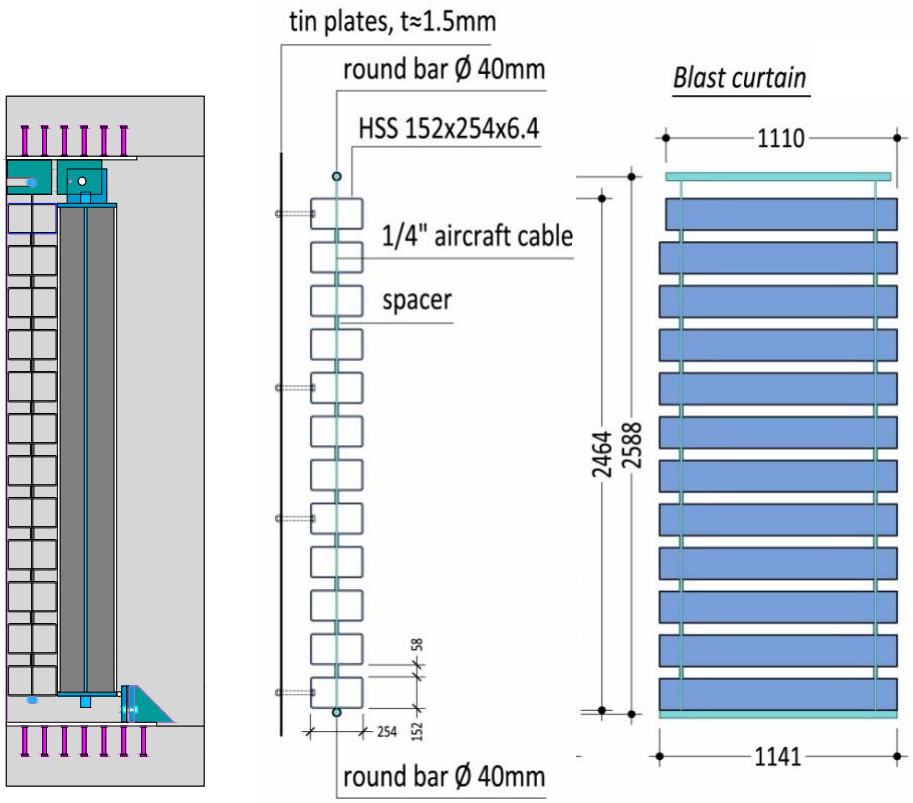

(a) Steel curtain dimensions (in mm)

(b) Test setup for shot 5

Fig. 4.2: Blast curtain dimensions

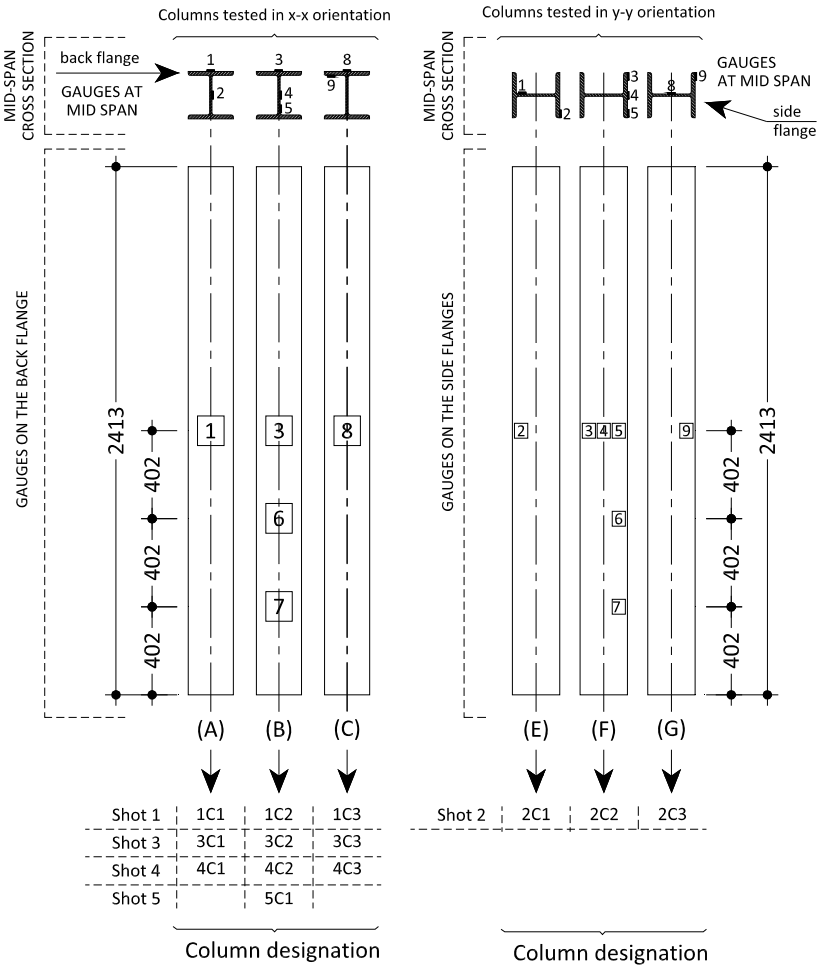

ig. 4.3: The strain gauge layout arrangement for test columns

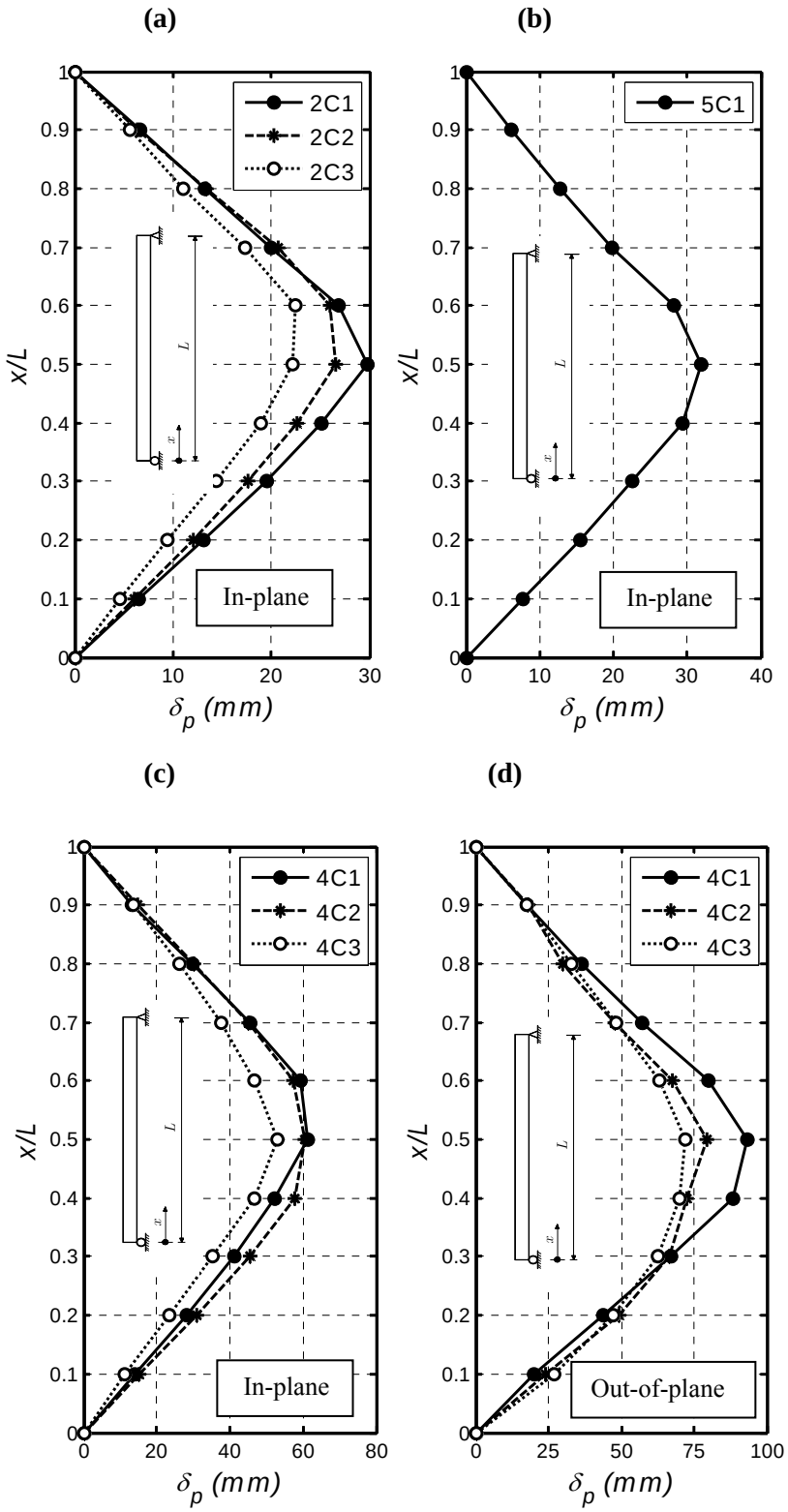

Fig. 4.4: Permanent deflected shape of steel columns after the blast shots

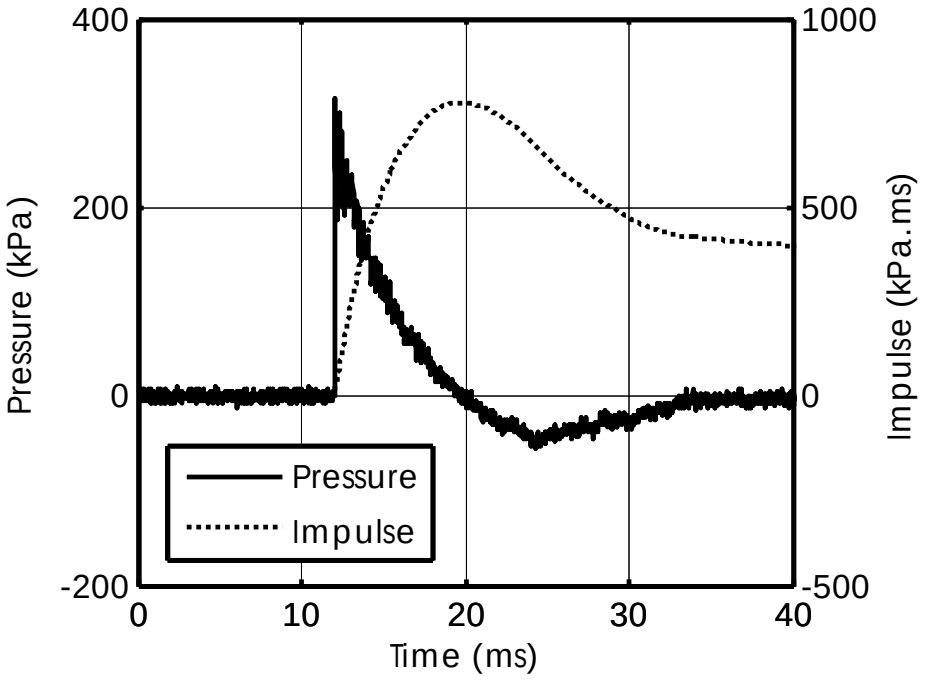

Fig. 4.5: Typical reflected pressure and impulse time-history

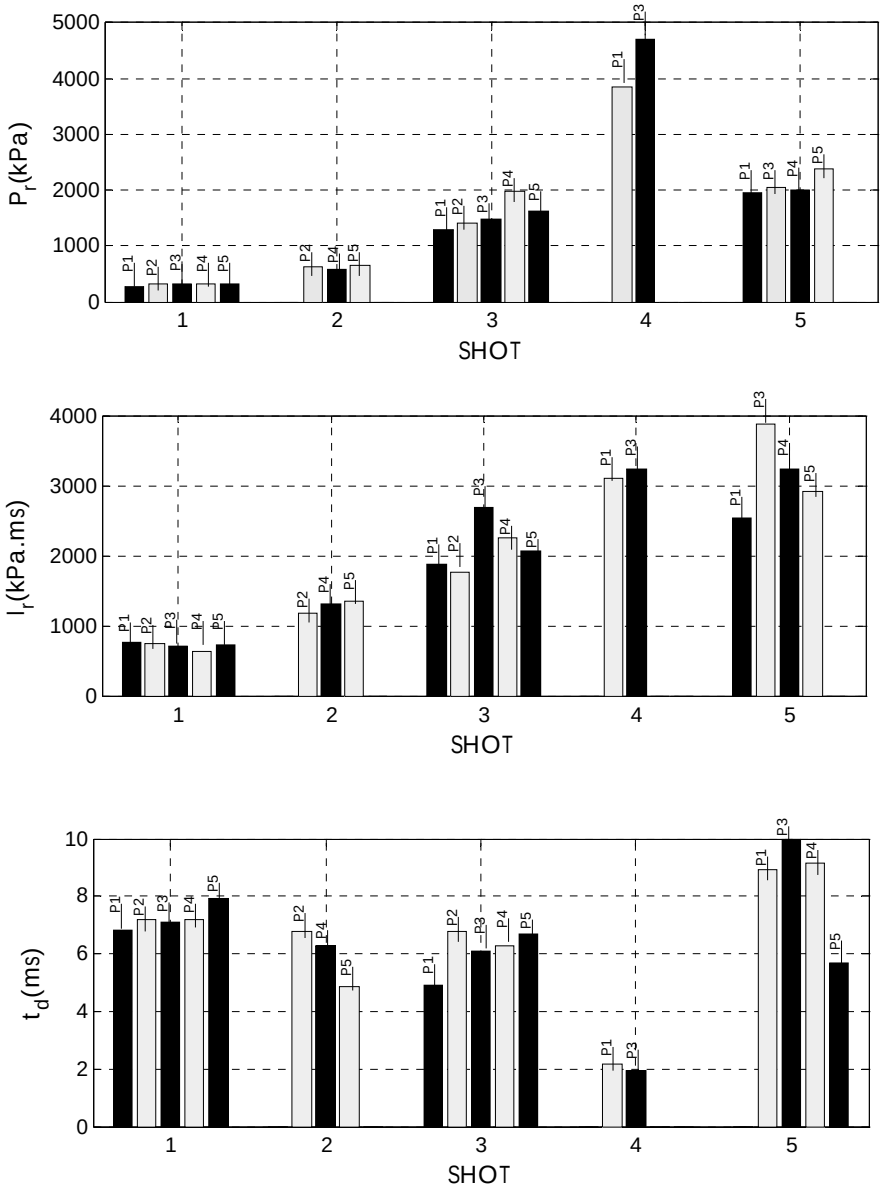

Fig. 4.6: The reflected pressures, impulses, and positive phase durations measured by different transducers

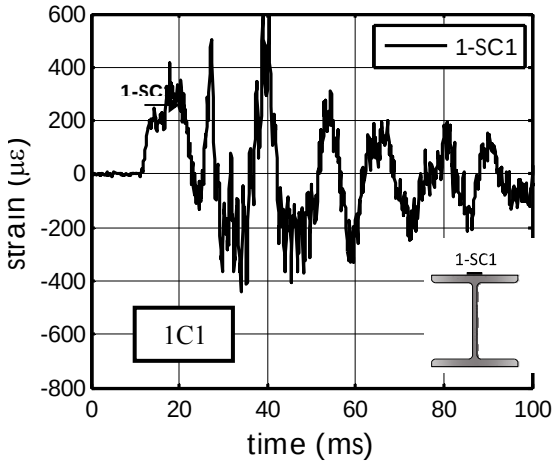

(a) Column 1C1

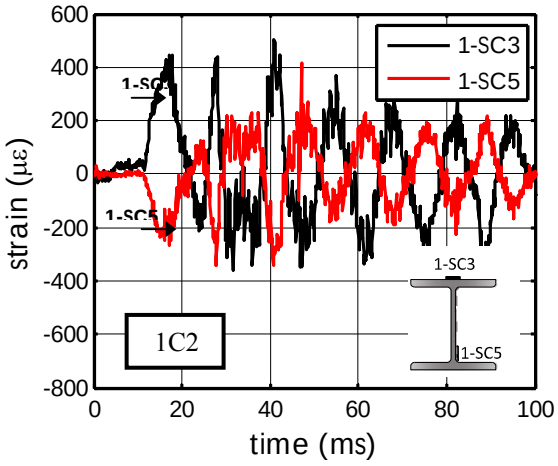

(b) Column 1C2

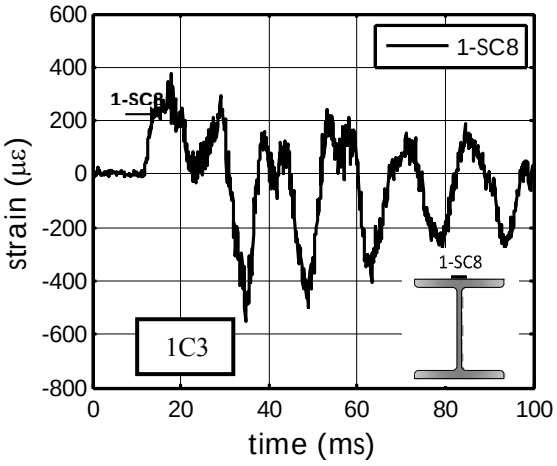

(c) Column 1C3

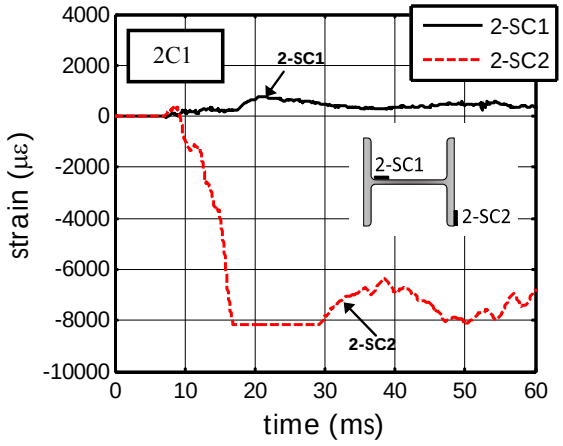

(d) Column 2C1

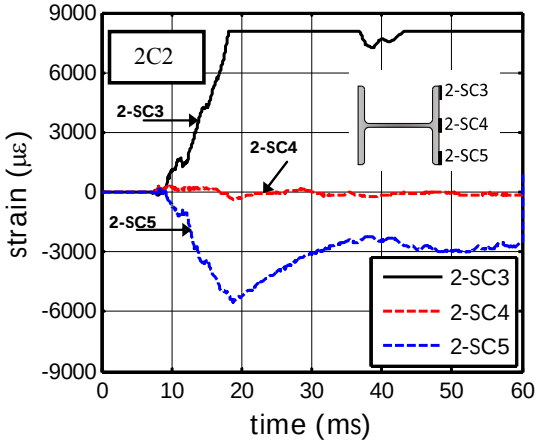

(e) Column 2C2

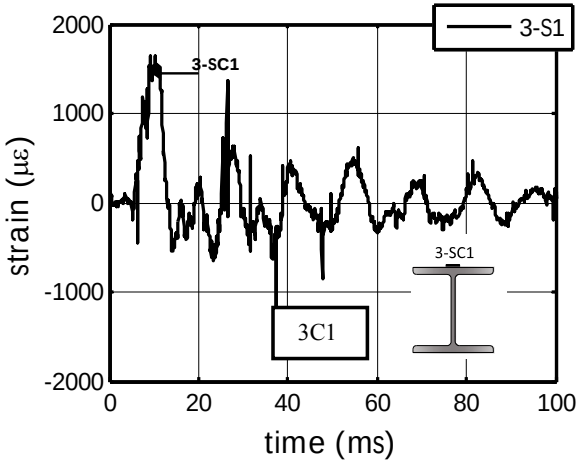

(f) Column 3C1

Fig. 4.7: Strain time histories at different locations over the cross-sections

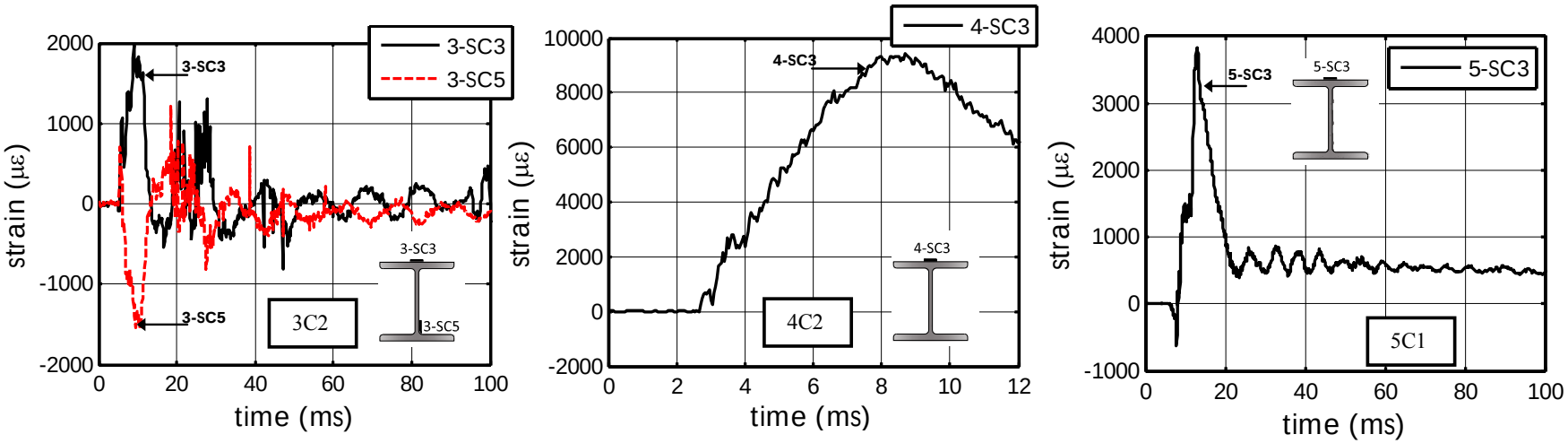

(g) Column 3C2 (h) Column 4C2 (i) Column 5C1

Fig. 4.7: Cont.

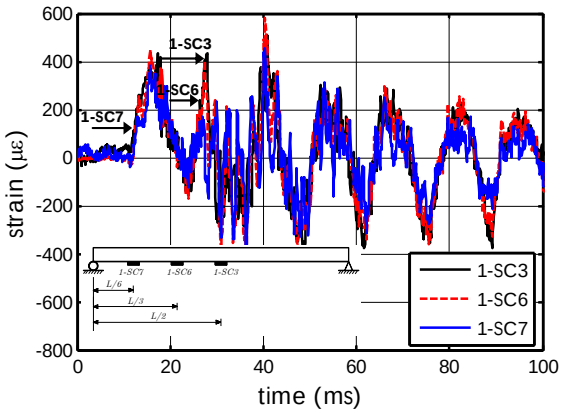

(a) SHOT 1: 1C2 column

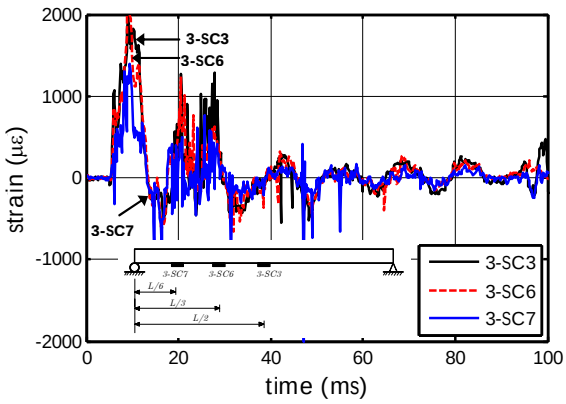

(b) SHOT 3: 2C2 column

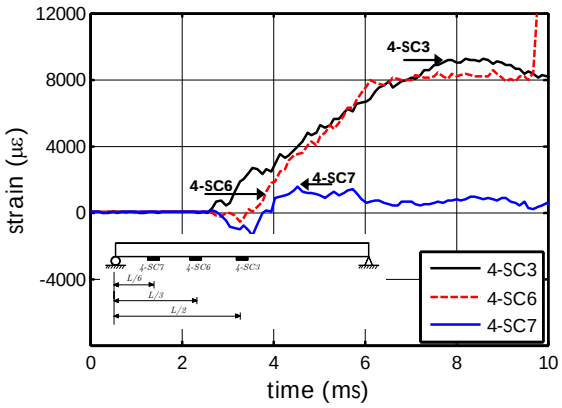

(c) SHOT 4: 3C2 column

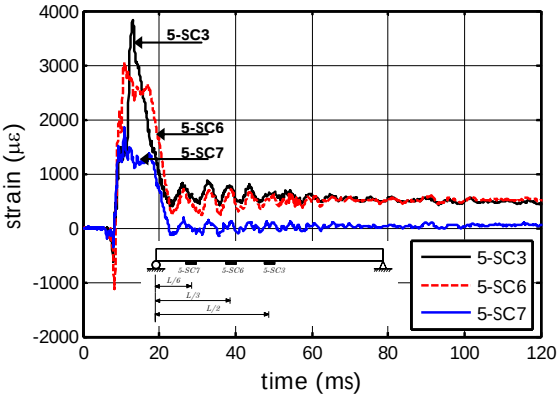

(d) SHOT 5: 5C1 column

Fig. 4.8: Strain time histories along the height of the test columns

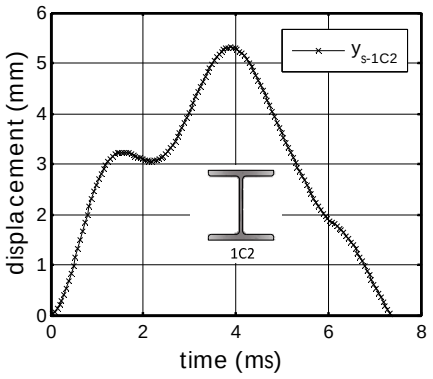

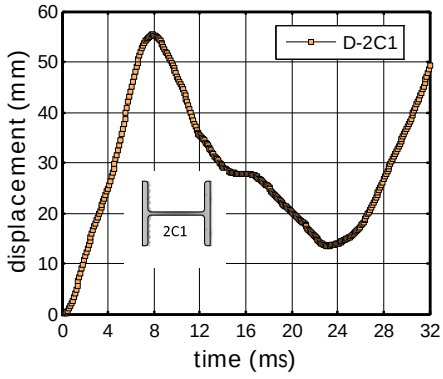

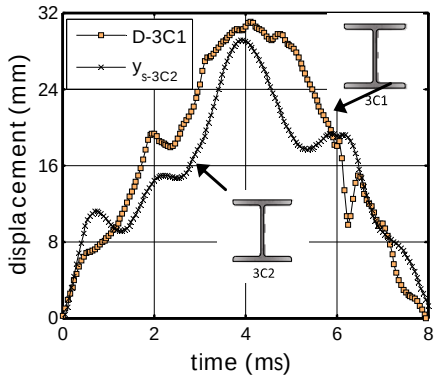

(c) SHOT 3: Z=1.69 m/kg$^{1/3}$

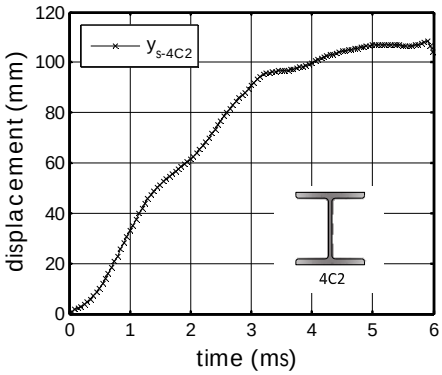

(d) SHOT 4: Z=1.11 m/kg$^{1/3}$

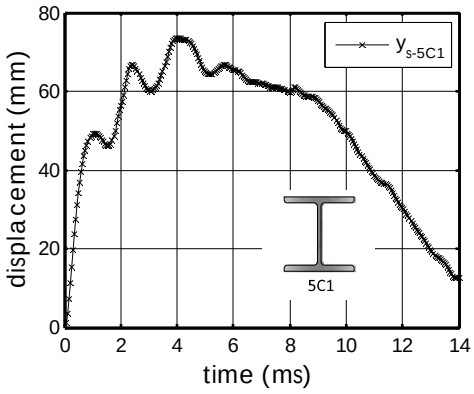

(e) SHOT 5: Z=1.51 m/kg$^{1/3}$

Fig. 4.9: Mid-span displacement time histories of test columns

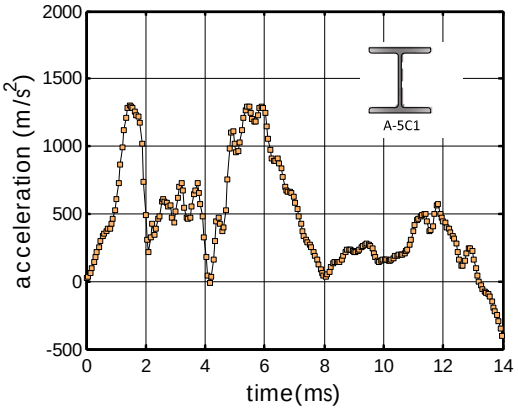

Fig. 4.10: Mid-span acceleration-time-history of 5C1 column

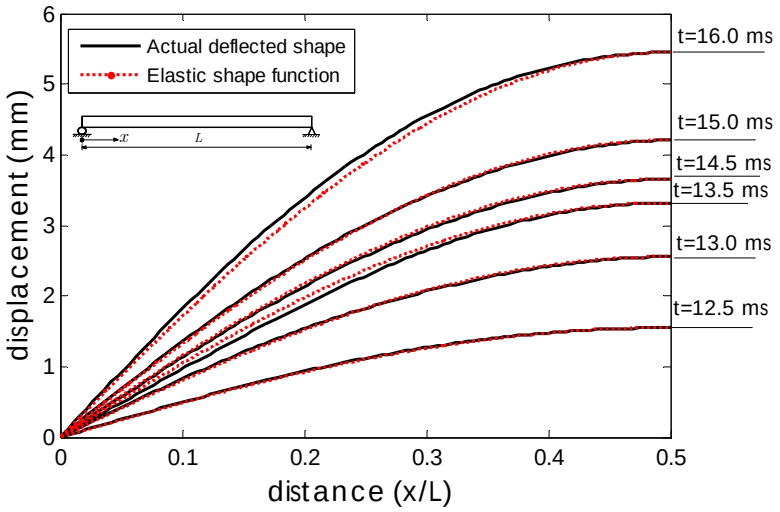

(a) SHOT 1: 1C2 column

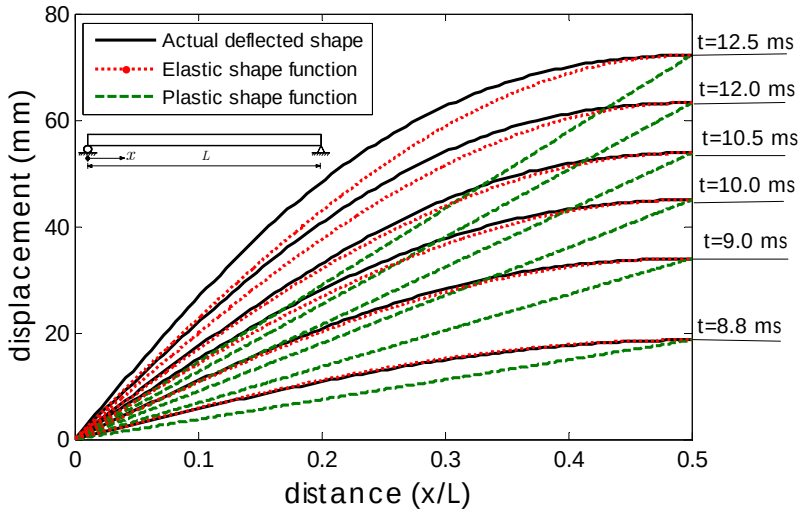

(b) SHOT 5: 5C1 column

Fig. 4.11: Deflected shapes at different instants of time

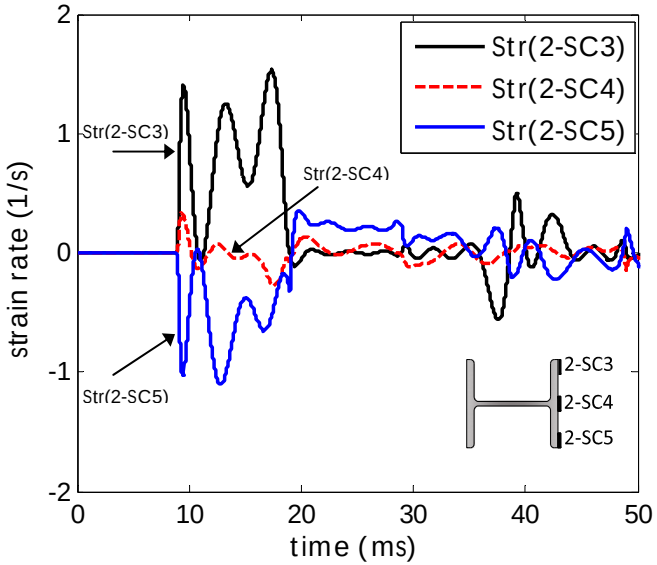

(a)

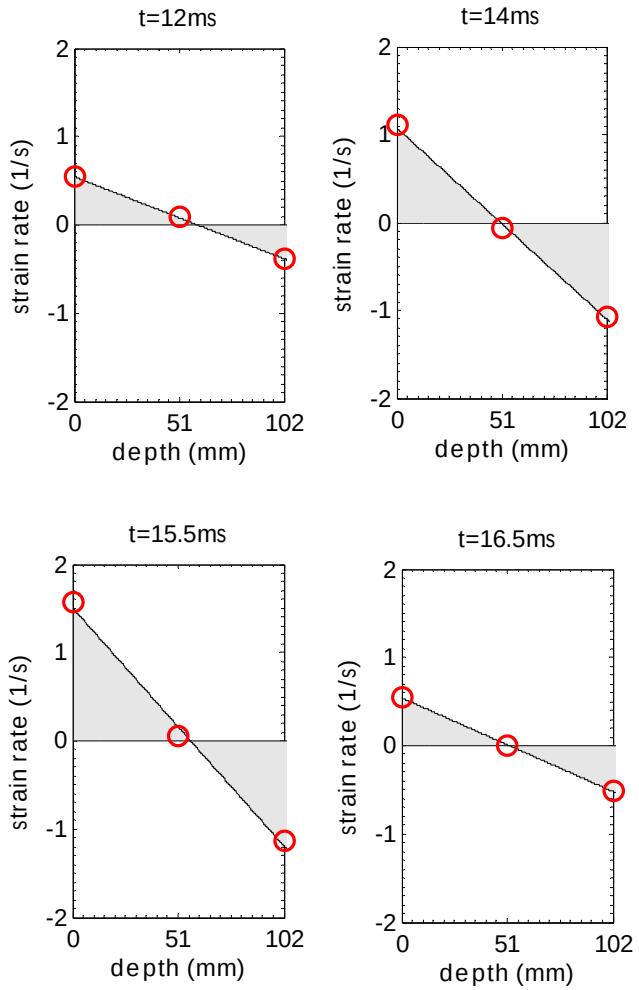

(b)

Fig. 4.12: Strain rate time histories at different locations over the cross-section for column 2C2

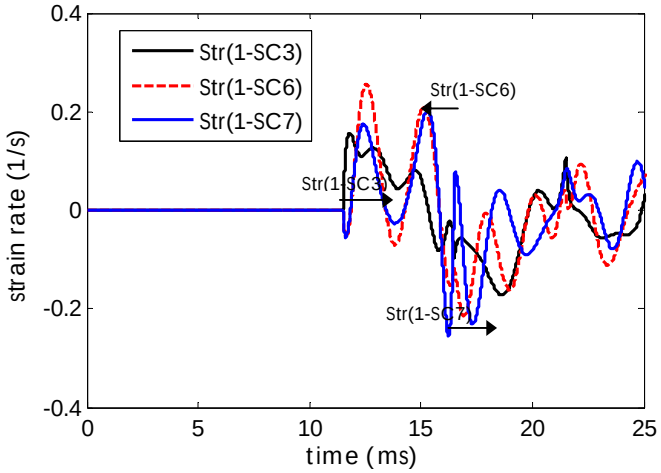

(a) SHOT 1: Strain rate histories along 1C2

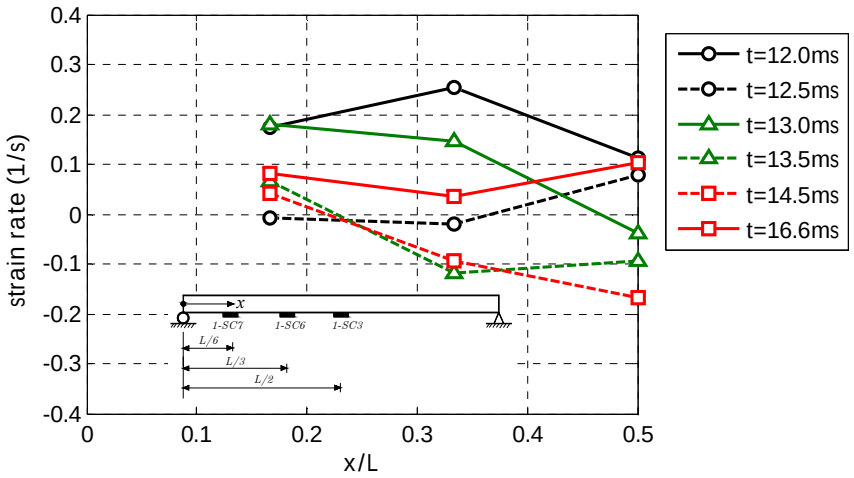

(b) SHOT 1: Strain rate along 1C2 at different instants

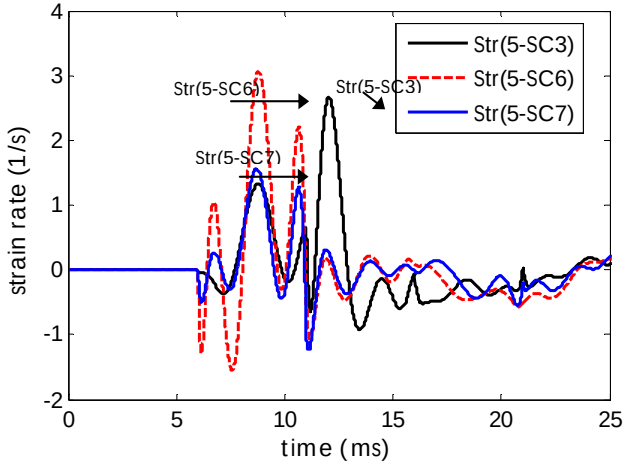

(c) SHOT 5: Strain rate histories along 5C1

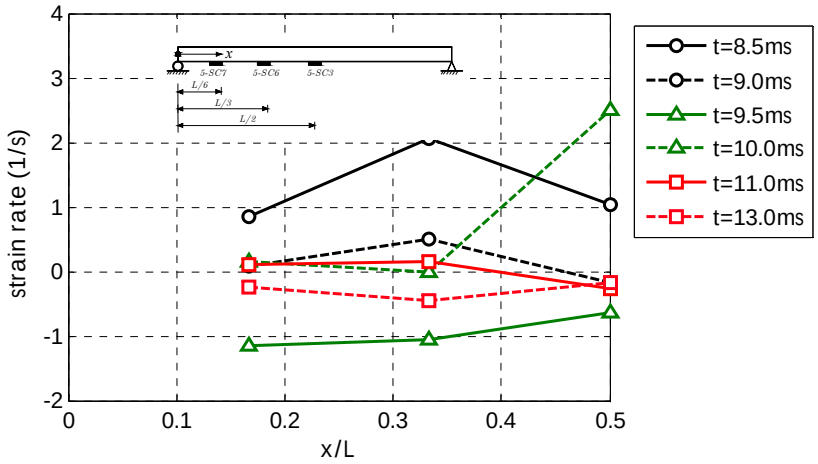

(d) SHOT 5: Strain rate along 5C1 at different instants

Fig. 4.13: Strain rate time histories along the height of the test columns

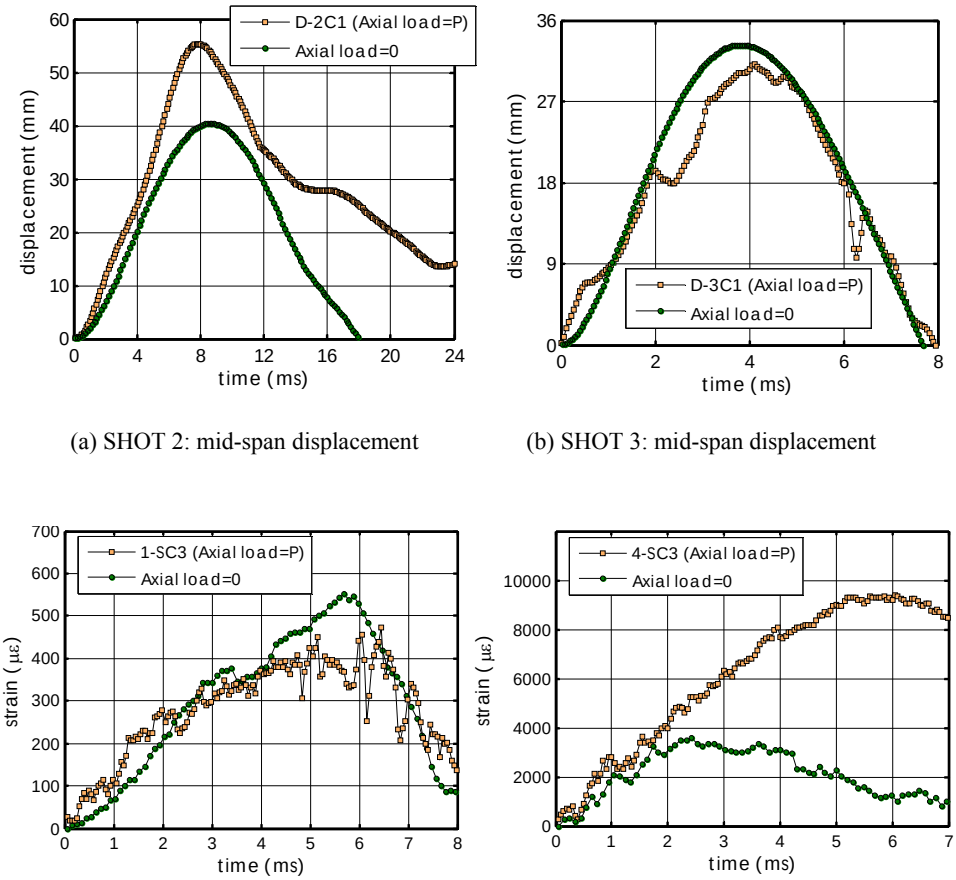

(a) SHOT 2: mid-span displacement

(b) SHOT 3: mid-span displacement

(c) SHOT 1: mid-span strain

(d) SHOT 4: mid-span strain

Fig. 4.14: Effect of axial load on the displacement and strain time histories

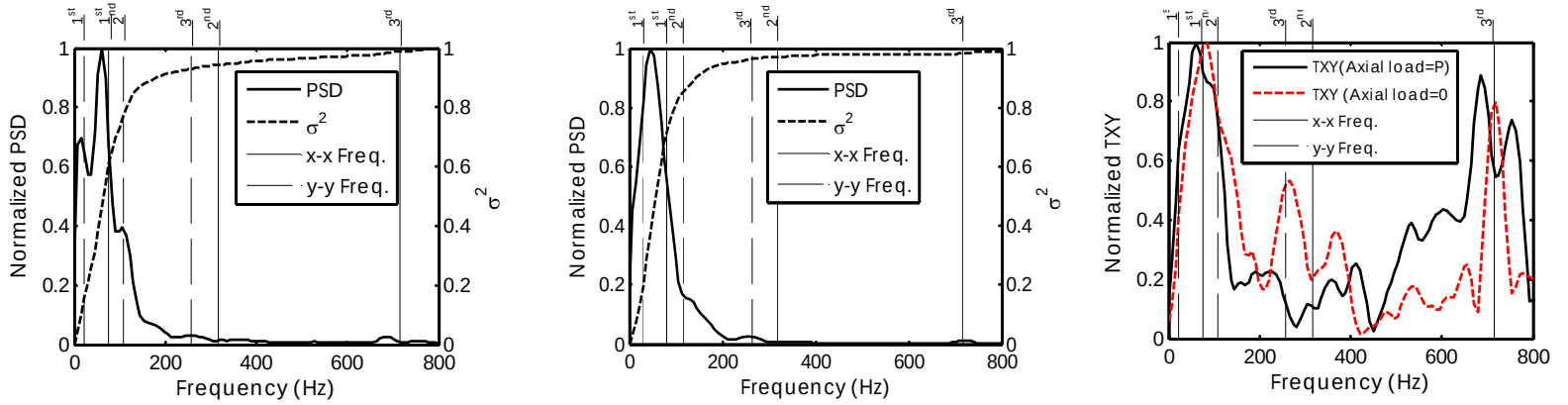

(a) SHOT 1: PSD response (Axial Load=P)

(b) SHOT 1: PSD response (Axial Load=0)

(c) SHOT 1: Transfer function (TXY)

(d) SHOT 2: PSD response (Axial Load=P)

(e) SHOT 2: PSD response (Axial Load=0)

(f) SHOT 2: Transfer function (TXY)

Fig. 4.15: Effect of axial load on the fundamental frequencies and contributing modes in the response

Chapter 5: Strength and Stability of Steel Beam Columns under Blast Load

5.1 Abstract

A Single-Degree-of-Freedom (SDOF) model is used to determine the effect of axial load on column strength and stability during a blast event. The model, which accounts for the axial load-bending interaction (P-δ effect) and strain rate effect on the column dynamic response, is validated by comparing its results with experimental data from blast tests on full scale steel columns and with the results of the finite element software LS-DYNA. Maximum displacements and moments obtained from SDOF analysis are also compared with the results of the interaction formulas recommended by the Unified Facilities Criteria (UFC 3-340-02) design manual for steel structures. It is shown that the UFC method overestimates the column capacity for ductility ratios μ greater than one, irrespective of the axial load to Euler elastic buckling load ratio (P/P_e). Also for $P/P_e > 0.5$, even if $\mu < 1.0$, the UFC method still overestimates the actual column capacity. For dealing with this problem in practical applications, non-dimensional beam column curves are developed to include the effects of the blast load and column properties on both its strength and stability.

Keywords: Blast loads; Buckling; Damage; Dynamics; Explosions; Steel columns; Strain rate

5.2 Introduction

Axial load acting concurrently with the lateral load on a beam column, for example, column subjected to blast loading, results in secondary moments that diminish its pure moment resistance. This interaction between the two loads is commonly known as P-δ effect, and for static loads it is accounted for using the so-called Moment Magnification Factor (MMF) (Salmon et al. 2009). Basically, the maximum moment due to the lateral load is multiplied or magnified by this factor and the column capacity is checked against the combined effects of the axial load and the magnified moment. The factor is function of type of lateral load, i.e. uniform, concentrated, triangular, etc., the end boundary conditions of the column, and the ratio P/P_e, where P is the applied axial load, and P_e is the Euler elastic buckling load for the column.

The factor is derived either by solving the governing equation of an elastic beam column, leading to the so-called secant formula (Timoshenko and Gere 1961), or more simply by finding the maximum lateral deflection of the beam column due to the applied lateral load and the secondary moment (Salmon et al. 2009). The two approaches give essentially the same result; therefore, in practice the magnification factor is based on the deflection approach because it is easier to apply.

Since the magnification method is convenient to use in design work and has been found to lead to the satisfactory design of beam columns under static loads, in the UFC design guide (UFC-3-340-02, USDOD 2008), it is recommended that it be applied, with slight modification, to beam columns subjected to axial gravity load and lateral blast load. The modification essentially involves the determination of the maximum moment due to lateral blast pressure by dynamic analysis methods and the use of dynamic rather than static steel strength values in the calculation of the axial load and moment capacity of the column. Thus the magnification factor is assumed to be independent of the

dynamic nature of the lateral load. Although this procedure is convenient to apply, it is not applicable to a beam column under blast loading, as elaborated in the following section, if it experiences maximum lateral deflection greater than its elastic deflection limit.

Previous studies on beam columns have dealt with some aspects of the dynamic response and capacity of beam columns, but have not directly dealt with the limitations of the moment magnification method in the form recommended by UFC. To ensure member stability, ASCE Standard (2011) states that *P-δ* effects must be considered in the case of all structural members under combined axial load and bending, but it makes no reference to any specific method of analysis to satisfy this requirement. Since the UFC method includes the combined effects of axial load and bending, one might presume that it satisfies the requirements of the ASCE Standard, but this assumption would be incorrect when the column deflection exceeds its elastic limit. Montalva et al. (2007) used the Galerkin method in conjunction with a time-step integration scheme to solve the governing equation of motion of a beam column. The solution, which included the effects of damping, shear deformation, and rotary inertia, showed that the beam column capacity is strongly affected by its ductility ratio, μ, defined as the ratio of the maximum deflection of the column to its maximum elastic deflection. However, their solution was based on the assumption of constant flexural and shear rigidity, therefore, it is not applicable to columns with $\mu > 1.0$; consequently, it suffers from the same limitation as the UFC method. The governing dynamic equation for a beam column with an elastic-perfectly plastic resistance function and $\mu > 1.0$ is different from the one used by Montavala et al. because in their equation the column resistance is linearly proportional to its deflection at all times while in fact once the column deflection exceeds its elastic limit, its plastic resistance is constant and independent of its deflection.

Other methods of analysis of columns under blast load are based on numerical methods, involving Single-Degree-of-Freedom (SDOF) or Multi-

Degree-of- Freedom (MDOF) models. In the SDOF formulation presented in ASCE (1997), the dynamic effect of the axial load on the structural response is not considered directly, but its effect on the reduced capacity of the column cross-section due to combined axial load and bending moment, as in the case of static loads, is considered. On the other hand, the software SBEDS (USACE 2008a) explicitly includes the P-δ effects through the application of an equivalent uniform lateral load to the column. For a given maximum deflection, this load is obtained by equating its associated maximum moment to the maximum moment caused by the applied axial load with an eccentricity equal to the given deflection. SBEDS also includes the effects of strain rate on column strength and deformations through the application of a constant Dynamic Increase Factor (DIF) (USDOD 2008), which is based on the assumption of a constant strain rate through the depth of the cross-section. In reality the strain rate varies both over the member depth and length and the effects of these variations on beam column strength has not been sufficiently investigated, but neglecting them and assuming a constant strain rate may result in an overestimate of the ultimate resistance of a column in some cases, especially in the case of sections with high A_w/A_f ratio, where A_w and A_f are the cross-sectional areas of the web and the flange, respectively. Furthermore, as a consequence of strain rate effect on column yield strength, its failure mode could change from a ductile flexural mode to another less ductile or brittle mode.

More advanced MDOF analyses utilize the nonlinear Finite Element Method (FEM), which can be used to model complex geometric and material nonlinearities, including strain rate effect, and blast wave-structure interaction (Shi et al., 2008; Lee et al., 2009), but this technique is significantly more complex and costly, therefore, SDOF models are commonly used in routine structural design applications.

As stated earlier, SDOF models are based on certain assumptions which need validation before they can be reliably applied. Although theoretically they

can be validated by comparing their results with those from the more sophisticated FEM analyses, experimental verification of the results of both types of models is necessary because both models are based on certain assumptions. By comparing the experimental displacement and strain responses for test specimens with their corresponding predicted values, one can gauge the level of accuracy of each model. Comparing strains is important because failure criteria are based on strain or stress and since stress is a computed quantity as function of strain, good agreement between measured and computed strains, versus measured and computed displacements, more strongly validates the underlying assumptions and accuracy of these models.

In this paper experimental data from blast tests on full scale steel beam columns are compared with the results of two dynamic analysis models. The first is a SDOF model, developed by the authors, which accounts for both the effect of strain rate and secondary moment due to axial load. The P-δ effect is modelled similarly to SBED through equivalent lateral load, but contrary to SBED, the column resistance function is determined based on its strain rate-dependent moment-curvature response, which is obtained by dividing its cross-section into a number of layers, and by applying a strain rate-dependent stress-strain relationship to capture the nonlinear stress distribution over its depth. The second model is based on three-dimensional FEM idealization and the full dynamic analysis of the beam column using the software LS-DYNA (Hallquist, 2006 and LSTC. 2007), which accounts for large displacements and strains and utilizes a plastic-kinematic constitutive model to capture material nonlinearities and strain rate effects. Reasonable agreement is observed between the measured and computed responses using either model. In light of this observation, the SDOF model is subsequently utilized to further investigate the effect of axial-bending interaction on the dynamic failure of beam columns. The results are used to generate stability diagrams for the assessment of the critical load, and Pressure-

Impulse (PI) diagrams to check the column performance against specified deflection or ductility limits.

5.3 *P-δ* effect assessment for beam columns under blast load

According to UFC, the resistance of a beam column subjected to combined axial load and bending about the principal x-axis of the column cross-section can be calculated using the following interaction formulas, provided all other failure modes are prevented

$$\frac{P}{P_u}+\frac{C_{mx}M_x}{M_{px}\left(1-\frac{P}{P_{ex}}\right)}\le 1.0 \tag{5.1}$$

$$\frac{P}{P_P}+\frac{M_x}{1.18M_{Px}}\le 1.0 \text{ for } \frac{P}{P_P}\ge 0.15 \tag{5.2}$$

$$\frac{M_x}{M_{Px}}\le 1.0 \text{ for } \frac{P}{P_P}\le 0.15 \tag{5.3}$$

where

C_{mx} = coefficient dependent upon beam column curvature caused by applied moment (C_{mx} =1.0 for pinned beam column under uniform load)

P = applied axial load

P_u = ultimate compression capacity of beam column

P_{ex} = Euler elastic buckling load of the beam column about x-axis

P_p = cross-sectional axial compression capacity

M_x = maximum applied moments about the x-axis

M_{Px}= beam column plastic moment capacity about x-axis in the absence of axial load

Equations (5.2) and (5.3) neglect the *P-δ* effect, which means that they are based on the assumption that column failure is initiated by the section reaching its full plastic capacity without experiencing instability. Equation (5.3) permits

neglecting the effect of axial load on the column resistance for values of $P/P_p \leq 0.15$. These conditions are identical in form to those in AISC (1994) for beam columns under static loads, but the moment M_x in the case of blast loads must be obtained from a dynamic analysis and the maximum resistance or capacity of the section must be calculated based on its dynamic material properties. The term $C_m/(1-P/P_e)$ is the moment magnification factor (MMF) and it accounts for the *P-δ* effect.

Equations (5.1) to (5.3) cannot be applied to columns with $\mu > 1.0$ because they are derived based on the assumption of $\mu \leq 1.0$. In the derivation of all three equations, it is implicitly assumed that the column flexural stiffness is constant and equal to its elastic stiffness. In the ASCE Standard (2011), for beam columns with compact section, a maximum ductility ratio of 3 is permitted while for non-compact sections it is limited to 0.85. A problem arises when the UFC formulas are applied to compact sections with $\mu > 1.0$. It will be demonstrated later that depending on the values of P/P_e and μ, these formulas will predict significantly different displacement, and accordingly maximum amplified moment, than that predicted by the nonlinear SDOF model. This difference is caused by the fact that under blast load the magnification factor is function of both P/P_e and μ in the post-elastic state, a fact that is not reflected by the UFC formulas. Before discussing the results of the SDOF analyses, details of the SDOF model developed to perform the analyses and its verification by experimental data will be presented.

5.4 Single-degree-of-freedom (SDOF) model for beam column analysis

In the SDOF model, the real system, as shown in Fig. 5.1(a), can be replaced by an equivalent spring-mass system as shown in Fig. 5.1(b). The SDOF model used in this analysis is based on the solution of the following equation of motion

$$K_M M \ddot{y} + K_L R(y) = K_L F(t) + K_L \eta(t) \tag{5.4}$$

or

$$K_{LM} M \ddot{y} + R(y) = F(t) + \eta(t) \tag{5.5}$$

where $\ddot{y}$ and y are the mass acceleration and displacement, respectively, and they are equal to the column mid-span acceleration and displacement; M is the column mass and $F(t)$ is the total lateral load acting on it, i.e. the load due to the blast pressure $P_r(t)$ multiplied by the area of the column surface directly facing the blast. In the present analyses, the results for time-varying reflected blast pressure acting on steel columns, obtained from measured pressure time-history curves during blast tests, will be compared with those obtained from an assumed equivalent linearly decaying pressure profile. The term $\eta(t)$ represents the equivalent lateral load (ELL) due to the secondary moment caused by the eccentricity of the applied axial load, and according to Timoshenko and Gere (1961), it can be written as

$$\eta(t) = \frac{8P}{L} y(t) \tag{5.6}$$

where L is the column length and P is the applied axial load. The coefficient K_{LM} is the so-called load-mass factor given by $K_{LM}=K_M/K_L$, where K_M and K_L are the mass and load factors, respectively. Coefficient K_{LM} is equal to 0.78 and 0.66 for the elastic and plastic states, respectively (Biggs 1964). The term $R(y)$ represents the moment resistance function of the steel column under blast loading and includes strain rate effect. In an elastic perfectly-plastic column, $R(y)$ is equal to $Ky(t)$ in the elastic state and to $R_m = {}^{8M_p}\!/_{L}$ in the plastic state, where M_p is the plastic moment capacity of the column. As indicated by Eq. (5.7), the spatial displacement of the column in the elastic state is represented by the deflected shape of a simply supported beam under uniform load and in the plastic state by a linear function corresponding to the deflected shape of the column deforming as a mechanism with a plastic hinge at its mid-span

$$\phi(\xi) = \begin{cases} 1 - \frac{24}{5}\xi^2 + \frac{16}{5}\xi^4 \; ; \quad \xi = \frac{z}{L} - \frac{1}{2} & \text{(elastic range)} \\ 1 - 2|\xi| & \text{(plastic range)} \end{cases} \tag{5.7}$$

where ξ = (z/L-1/2) is a natural coordinate and z is the Cartesian axial coordinate, as shown in Fig. 5.1(a).

5.4.1 Plastic moment capacity of the beam column

To account for the effects of axial load and strain rate on the column moment capacity, the moment M_p was determined by assuming an elastic-perfectly plastic stress-strain relationship for steel and by including the strain rate effect on its yield strength. This relationship was used to determine the full strain rate-dependent moment-curvature response of the cross-section. The column cross-section was divided into a number of layers (see Fig. 5.2) and based on the Euler-Bernoulli beam theory, the strain and strain rate variations over the depth of the section were assumed linear and the stress in each layer was accordingly determined. The axial load was assumed to produce a uniform strain over the cross-section, thus, the resultant axial force in the i^{th} layer was written as

$$F_i = \sigma_i(\varepsilon_i)\mathrm{DIF}(\dot{\varepsilon}_i)w_i\Delta s \tag{5.8}$$

where w_i, Δs, $\sigma_i(\varepsilon_i)$, and $\mathrm{DIF}(\dot{\varepsilon}_i)$ are the layer width, thickness, stress and strain rate-dependent dynamic increase factor, respectively. The DIF was determined as function of the column axial strain rate, $\dot{\varepsilon}$, using the Cowper-Symonds strain rate model (Jones 1988)

$$\mathrm{DIF} = 1 + \left(\frac{\dot{\varepsilon}}{D}\right)^{1/q} \tag{5.9}$$

where D and q are constants for the particular material, and were taken as D = 40, and q =5 for steel (Jones 1988). The average strain rate for the top fibre was assumed according to the strain rate model proposed by Nassr et al. (2012), which gives the maximum strain rate $\dot{\varepsilon}_{\max}$ in terms of scaled distance Z as

$$\dot{\varepsilon} = 2.93 - 0.67Z \tag{5.10}$$

The neutral axis depth was iteratively determined based on the equilibrium of forces acting on the beam column cross-section. The resulting moment resistance

at a specific curvature of the cross-section was obtained by summing the moments of the layer forces about the section centroid. The maximum moment resistance thus calculated was used in the SDOF model to define the elastic limit of the resistance function $R(y)$.

To check the accuracy of the steel properties used in the calculation and the methodology described for calculating the plastic moment capacity of the columns, the plastic moment resistances of the test columns were determined experimentally, as described later in this paper, and were compared with the corresponding computed values.

5.5 Finite Element Modelling (FEM)

The FEM software LS-DYNA (Hallquist, 2006 and LSTC. 2007) was used in this study to analyze steel columns and to compare its results with those obtained from the simplified SDOF model. Figure 5.3(a) shows a three-dimensional model of a 2413 mm long wide flange steel column of W150×24 section. The column was modelled with a finite element mesh consisting of 13014 nodes and 6416 eight-node solid hexahedron fully integrated elements using the ELEMENT_SOLID input card. The column was modelled as pinned at one end and roller supported at the other end. In conformity with the test columns described in the following section, a rigid plate at each end of the steel column was included in the model and all the nodes located on the horizontal centerline of the external surface of one end plate were constrained, so that all translations and rotations were prevented ($\delta_x = \delta_y = \delta_z = 0,\ \theta_y = \theta_z = 0$) with the exception of rotation around the x-axis (hinge end, see Fig. 5.3(b)). Similarly, all the nodes located on the horizontal centerline of the external surface of the other end plate (($\delta_x = \delta_y = 0,\ \theta_y = \theta_z = 0$) were constrained, so that all translations and rotations were prevented, with the exception of translation in the z-direction and rotation around the x-axis (roller end).

The steel material was modelled using the MAT_PLASTIC_KINEMATIC input card in LS-DYNA. The effect of the strain rate was taken into account by using the Cowper-Symonds model (Jones 1988) to scale up the yield stress by the strain rate dependent factor as in Eq. (5.9). In this material model, the required input material properties included the steel yield stress, density, fracture strain, and Poisson's ratio, which were taken as 470 MPa, 7850 kg/m^3, 0.20, and 0.30, respectively. In addition, the values of the two constants included in Cowper-Symonds model were chosen according to Jones's (1988) suggestion as D=40 and q=5. The above yield stress was obtained from static flexural tests performed on beam column specimens.

The blast pressure was defined using LS-DYNA input card DEFINE_CURVE and subsequently applied to the surface of the flange facing the explosive charge using LOAD_SEGEMENT card. Any pressure variation along the column length was ignored thus uniform pressure was assumed. The axial load was defined as nodal forces at the roller supported end of the column. It was applied as a ramp function over a period of 0.05 s and was maintained constant thereafter up to the end of the analysis. The blast loading was assumed to commence immediately after the axial load reached its steady state, as shown in Fig. 5.4.

LS-DYNA uses an explicit time integration algorithm for solving the problem, which is less sensitive to machine precision than the implicit method. The explicit finite element analysis solves the equation of motion in an incremental fashion and updates the stiffness matrix at the end of each increment of load and displacement based on changes in geometry and material. The termination time of 30 ms was set in order to obtain a more complete picture of the response of the column. The time step was automatically selected by LS-DYNA, which was calculated based on the speed of sound in steel behaving as an elastic material (Hallquist, 2006). In this model, the time step was calculated to be approximately 5×10^{-6} s.

5.6 Experimental evaluation of the plastic resistance of beam columns

The accuracy of the nominal static yield strength of steel and the resistance function used in the SDOF model as well as the suitability of using prestressing to simulate the axial load on the beam column were investigated by conducting static tests on six wide flange steel sections, each with span length of 2413 mm. The test specimens were divided into three groups. Each group involved two specimens with identical geometric and material properties. One specimen was tested as beam, with zero axial load, and the other as beam column, where a constant axial load was applied to the member before applying the lateral load. Groups I and III columns were subjected to bending about their strong or x-x axis, with Group I columns having W150×24 section and Group III columns W200×71 section. Columns in Group II had W150×24 section and were subjected to bending about their weak or y-y axis.

The static tests were conducted under four-point bending, as shown in Fig. 5.5. The axial load was simulated by concentric prestressing using 7-wire prestressing strands having a 13 mm diameter and a nominal ultimate tensile strength of 1860 MPa. The beam columns with W200×71 section were prestressed by four symmetrically positioned strands while the W150×24 beam columns were prestressed with two strands. In each case, the strands were anchored to a 24.5 mm thick steel plate welded to each end of the column and were simultaneously stressed with a total initial prestressing force equal to 25% of the static axial load capacity of the column. The lateral load was increased monotonically and the beam column central deflection was measured using a displacement transducer.

Figures 5.5(b) and (c) show the beam and beam column during the test, respectively. Figures 5.6(a)-(c) show the load versus mid-span deflection curves for the three groups. Both the beams and beam columns exhibit the typical ductile behavior of steel members under combined axial load and bending. The effect of the axial load on the static response of the beam columns is manifested by the

reduction of their elastic stiffness, yield load, and ultimate load compared to their companion beams. The mid-span deflection curves for beams-columns exhibit smooth continuity in both the elastic and plastic stages, which indicates that the prestressing force did not noticeably diminish with increasing deformation and was practically constant during the test.

Table 5.1 shows a comparison between the predicted and measured yield moment M_y and maximum plastic moment M_p of the test beams and beam columns. The predicted yield and plastic moments for beam columns were calculated based on MMF and the column section nominal properties. The comparison shows that the MMF method generally underestimates the moment capacity of the beams and beams-columns, with difference of 3% for the low P/P_e ratio as in Group I and III beam columns. The difference becomes larger with increased P/P_e ratio, with a difference of 45% in the case of Group II beam columns. The above differences between the calculated and predicted moment capacities broadly agree with the findings of Duan et al. (1989), who analyzed a large number of beam columns tested by many researches. Table 5.1 also gives the flexural stiffness EI/L, of each test specimens, its equivalent stiffness K, and maximum resistance R_m, as used in the SDOF model. Note that although Group I and II beam columns have the same length and cross section, the P_e for each group is different because of the difference between the axes of bending in the two groups.

5.7 Comparison of dynamic analysis models results with experimental data

In order to evaluate the accuracy of the above SDOF and FEM models, the models results are compared with the experimental data for the steel columns tested by Nassr et al. (2011a). The test columns were 2413 mm (95 inches) long and were field tested under blast loading as simply supported members. The nominal static yield and ultimate strength of the steel section were 393 and 537 MPa, respectively. Table 5.2 shows the test matrix, including column and section

designation, the charge mass *W*, ground stand-off distance (SD), scaled distance *Z*, applied axial load magnitude, and column bending axis. The blast pressure was defined in both models according to the actual pressure time-histories recorded during the test (Nassr et al. 2011a and Nassr et al. 2011b). In order to investigate the sensitivity of the dynamic response to the blast loading profile, the blast pressure was also modelled in the SDOF model as a linearly decaying pressure pulse.

Figure 5.7 shows the measured mid-span displacement time-histories of the test columns 2C2 and 2C3 and their comparison with the corresponding histories predicted by the SDOF and FEM models. Generally, as can be observed, both models predict both the peak value and overall displacement response reasonably well. The peak displacement predicted by the SDOF model for the columns 2C2 and 2C3 were 60 and 32 mm, differing by 8% and less than 1% from the corresponding experimental values, respectively. The same displacements predicted by the FEM were 62 and 31 mm, differing by 9% and less than 1% from the corresponding experimental values, respectively. Figure 5.7 also shows the predictions of SDOF model for the linearly decaying blast pressure profile. In general reasonable agreement can be observed between the predicted and measured responses, whether the actual blast pressure profile or its linear approximation is used, which is indicative of the impulsive nature of the blast loading in the these tests.

The recorded strain time-histories obtained from SDOF and FEM models are also compared with the experimental results. The strain time-histories predicted by the SDOF model were calculated on the basis of the curvature of the displacement function and mid-span displacement as described in Nassr et al. (2012). Since longitudinal strain due to bending is a function of the second derivative of the displacement function and since the assumed displacement functions are not exact, it is prudent to investigate the accuracy of these functions.

The relevant level of accuracy can be best gauged by comparing predicted strain responses with their experimental counterparts.

Figures 5.8(a), (b), and (c) show the measured and corresponding predicted mid-span maximum strain time-histories for columns 2C1, 3C1, and 4C2, respectively. The predicted and the measured strain responses compare reasonably well in terms of the peak strain and overall trend. Due to the simplicity of the assumed shape function employed in SDOF model and the use of approximate DIF values, the differences between the predicted peak strain values and their corresponding experimental values are larger than the differences between the displacements. The two strain values differ by 18%, 11%, and 7% for columns 2C1, 3C1, and 4C2, respectively, while the corresponding differences for the FEM model are 9%, 5%, and 7%, respectively. Although the effect of the higher modes was noticeable in the recorded strain responses, which were captured by the FEM model, nevertheless, despite the exclusion of the higher modes effect in the SDOF model, it predicted the peak response and the overall trend of the strain response reasonably well. From the structural design point of view, given the large amount of uncertainty in blast load prediction, the SDOF model results are considered quite acceptable. Therefore, it can be used to investigate in more detail the response of beam columns to different axial load levels and blast intensities.

5.8 Effects of ductility ratio and axial load on dynamic strength of beam columns

As stated earlier, the UFC formulas cannot be used to design beam columns in certain situations. To demonstrate this problem, consider columns 2C1 and 3C1 in Table 5.2, which were subjected to axial load with P/P_e ratio of 0.067 and 0.49, and reflected impulse, I_r, values of 1280 and 2130 MPa.ms, respectively, during the blast tests described earlier. Here these elements are analyzed by subjecting them to the same axial load values as in the blast tests, but to increasingly higher

impulse values as indicated in Table 5.3. The applied impulse for each element is expressed as fraction or multiple of the experimentally measured impulse I_r.

The maximum deflection y_{max} and moment M_{max} in each element is determined using both the SDOF model and the MMF formulas recommended by UFC, and the results are shown in Table 5.3. The table also shows the ratio of $y_{\max}^{SDOF}$ and $M_{\max}^{SDOF}$ by the SDOF model to the corresponding $y_{\max}^{MMF}$ and $M_{\max}^{MMF}$ values calculated by the MMF method. It can be noticed that for column 3C1 when the ductility ratio is below 1.0, the difference between results of the SDOF and MMF method is relatively small because the P/P_e has practically negligible effect on the column stiffness and dynamic response. However, once the column begins to experience maximum deflection noticeably greater than its elastic deflection limit, the difference between the results of the two methods becomes large. This is due to the fact that beyond the elastic limit, the column stiffness is theoretical zero, therefore under dynamic load; it is expected to experience greater deflection than that assumed in the derivation of the MMF method. This leads to higher moment due to the P-δ effect, and to reduction in the moment resistance of the beam column to lateral load. This reduction can be quite dramatic as in the case of column 3C1 experiencing ductility ratios of 3.0 and 10.5.

Next let us consider results for the beam column 2C1. This column has a high P/P_e of 0.49. We observe that in this case the difference between the maximum deflection and moment values computed by the two methods is greater than 40% even for $\mu < 1.0$, but the difference is not sensitive to the actual value of μ as long as it remains below 1.0 because the beam column remains elastic and therefore its stiffness is insensitive to the actual value of μ. The reason for the above difference is the fact that the MMF method disregards the effect of P/P_e on the prolongation of the period of vibration of the beam column. This change results in greater amount of deflection due to the blast pressure than predicted by the recommended MMF method. Note that the effect of P/P_e on the beam column

dynamic deflection is twofold: (1) it increases its period and thus increases its deflection compared to an identical companion beam column with zero axial load but subjected to the same blast load, and (2) it reduces its stiffness and thus increases its deflection due the blast load compared to the companion beam. The MMF method neglects the first effect completely, but includes the second effect relatively accurately as long as $\mu \leq 1.0$, otherwise, it essentially ignores both effects.

A reasonable approach to solving the problem is to limit the use of the MMF formulas to beam columns with $\mu \leq 1.0$ and to $P/P_e \leq 0.15$. For beam columns with $\mu \leq 1.0$ and $P/P_e > 0.15$, the change in the period of vibration of the beam column T due to applied axial load P can be calculated using (Bazant and Cedolin 1991)

$$T = \frac{T_o}{\sqrt{1 - \frac{P}{P_e}}} \tag{5.11}$$

where T_o is the period of vibration of member in the absence of axial load. Using the period according to Eq. (5.11) and the associated Dynamic Load Factor (Biggs 1964), the maximum moment of the beam column due to the lateral blast load, i.e. moment M_{mx} in the MMF formula, may be determined and then magnified in accordance with Eq. (5.12)

$$M_{mx}^{*} = M_{mx} \cdot MMF \frac{\mathrm{DLF}}{\mathrm{DLF}_o} \tag{5.12}$$

where $\mathrm{DLF_o}$ is the dynamic load factor in the absence of axial load. Similarly, the maximum displacement can be calculated using

$$y^{*} = y_o \cdot MMF \frac{\mathrm{DLF}}{\mathrm{DLF}_o} \tag{5.13}$$

where y_o is the maximum displacement in the absence of axial load. Applying this procedure to column 2C1 subjected to impulse of $0.4I_r$ (see Table 5.3), the maximum moment obtained is equal to 19.2 kN.m, which differs by 1% from the 19.4 kN.m moment obtained from the detailed SODF model described earlier.

Similarly, the maximum displacement obtained is equal to 35.7 mm, which is the same as obtained from the detailed SDOF model. This modification is not sufficient for obtaining the correct strength of beam columns with $\mu > 1.0$. In the latter case full dynamic analysis is needed.

In the next section, the results of some detailed dynamic analyses related to axial load-moment interaction and beam column stability under blast load is presented. These results shed more light on the strength and stability of steel beam columns under blast loads.

5.9 Beam column overall stability under blast loads

Column 2C1 is analyzed considering two scenarios. In the first scenario, five loading cases were considered. In each case the lateral load, or its impulse, was kept constant and equal to I_r while the axial load was increased from 1.0P in case one to 2.0P in case 5, where I_r and P are, respectively, the maximum impulse and axial load applied to this column during the blast test. The analysis was performed by both the SDOF model applying ELL and by LS-DYNA. The column mid-span displacement response for each case is shown in Fig. 5.9(a). Reasonable agreement can be observed between the LS-DYNA and SDOF results. Both models show that for axial load equal to 1.4P, or greater, the column experiences large deflections due to instability.

In the second scenario, the axial load was kept constant and equal to 1.0P while the applied impulse was increased from 1.0I_r to 2.0I_r in going from case 1 to 5. The column mid-span displacement responses for these cases are shown in Fig. 5.9(b). Once again, column instability is observed for values of impulse greater than or equal to 1.4I_r. These results clearly demonstrate that instability can be triggered by either the blast load or by the axial load.

The results of such analyses can be used to generate beam column stability curves similar to those used to determine the static stability of beam columns (Salmon et al. 2009). Figures 5.10(a) and (b) show such curves that were obtained

using the ELL SDOF model. Figure 5.10(a) shows the variation of P_{cr}/P_y ratio with the column slenderness parameter λ_c for different levels of specific impulse i acting on the column. The slenderness parameter λ_c is calculated, in compliance with the CAN/CSA-S16-09 standard (CISC 2011) and AISC LRFD design specifications (AISC 1994), in terms of the effective column length KL, section radius of gyration r, the yield strength F_y, and the elastic modulus E as

$$\lambda_c = \sqrt{\frac{F_y}{F_e}} \tag{5.14}$$

where

$$F_e = \frac{\pi^2 E}{\left(\frac{KL}{r}\right)^2} \tag{5.15}$$

The specific impulse is defined as the blast reflected impulse I_r divided by the flange or tributary width b, i.e. $i = I_r/b$. Using the SDOF model, these curves were obtained by varying the axial load for a particular slenderness λ_c and specific impulse i until instability occurred. The instability criterion was selected as tenfold increase in maximum displacement due to 1% increase in the axial load. Choosing a slightly different criterion will not alter the conclusions of the study. Different specific blast impulses i were computed by increasing the peak pressure for a linearly decaying blast pulse of fixed duration.

As shown in Fig. 5.10(a), the critical axial load significantly decreases with the increase of the slenderness λ_c for the same specific impulse. The critical axial load increases with the decrease of the specific blast impulse acting on columns with the same slenderness parameter. Figure 5.10(a) shows the combinations of specific impulse and axial which would not cause column instability. Points above a curve indicate instability while those below represent stable configuration. For instance, the column with cross-section W150×24 and slenderness ratio of 0.9 can sustain a combinations of 0.2 P_{cr}/P_y and 40

MPa.ms/m, while the same column can sustain up to 0.6 P_{cr}/P_y when subjected to specific impulse of 10 MPa.ms/m.

Figure 5.10(b) shows the variation of the ratio of critical load to static Euler buckling load P_e with the slenderness parameter λ_c. Again, for a given column the critical load is reduced by the increase in the specific impulse. It can be noticed that the P_{cr}/P_e ratio is also greatly affected by the column slenderness parameter as it increases with the increase of the slenderness parameter and the specific impulse. This ratio approaches 1.0 for columns with high slenderness parameters and low lateral blast load. The results in Fig. 5.10 demonstrate that even an axial load equal to a small fraction of a column Euler buckling load can induce a response due to blast load that can cause the column to fail due to instability. Therefore, one must carefully consider this interaction between the applied axial load and the lateral load due to blast when designing blast resistant columns.

5.10 Local stability of steel columns under blast loading

The SDOF is a simple tool for estimating the response of members to blast loading, particularly their flexural response and failure. When other modes of failure and deformation are of interest, the SDOF model cannot provide the full picture. Blast resistant design of steel members usually requires that members reach their full plastic moment capacity without incurring local instability (ASCE 2011). According to CAN/CSA-S16-09 standard (CISC, 2011), a class 1 cross-section must be able to attain its plastic moment and allow the subsequent redistribution of the bending moments without the occurrence of local buckling, but the increase of the yield strength due to the high strain rate induced by blast load might affect section classification (see Table 5.4), because member failure might be triggered by local buckling rather than global instability or flexure. Figure 5.11 shows the SDOF and LS-DYNA predicted displacement response of a steel column having W150×18 cross section, with the same loading condition,

length, and material properties as column 4C1. According to CAN/CSA-S16-09 standard (CISC, 2011), W150×18 is a class 1 section; however, due to the occurrence of local buckling, LS-DYNA predicted the column maximum displacement to be 25% higher than that obtained from the SDOF model. The local buckling occurred in the compression flange as indicated in Fig. 5.11, and preceded the yielding of the column due to the increase of yield stress by the effect of high strain rate. Consequently, this changed the section classification.

Assuming ideal elastic-plastic material and no residual stresses, Fig. 5.12 shows the effect of the strain rate on the critical buckling stress F_{cr} of a flange in compression as a function of the flange slenderness parameter λ_{cp} (Salmon et al. 2009)

$$\lambda_{cp} = \frac{b}{2t_o}\sqrt{\frac{F_y(12)(1-\mu_o^2)}{\pi^2 Ek}} \tag{5.16}$$

where k is a constant depending on type of stress and flange aspect ratio and its edge condition; μ_o is the steel Poisson's ratio, and $b/2t_o$ is the width/thickness ratio of the flange. As shown in Fig. 5.12, at low strain rate ($\dot{\varepsilon}$<0.001/s), the flange plate strength is governed by its yield strength for low values of flange slenderness parameter up to λ_{cp}=1.0, a limit at which the flange could reach its yield strength before experiencing local buckling. For λ_{cp} >1.0, the flange plate buckles prior to reaching its yield strength. Due to the increase of the yield strength under higher strain rates, the F_{cr}/F_y ratio becomes larger, leading to a decrease in the limit at which local buckling occurs. Table 5.4 shows the reduction in the slenderness limits of both the flanges and the web in Class 1 sections under high strain rates. According to Eq. (5.9), the yield strength increases by a factor of 1.30-2.22 when the strain rate increases from 0.1 to 100 /s. The slenderness limit for the flange decreases by 33% when the strain rate increases from 0.001 to 100 /s.

From the above discussion it is clear that underestimating the dynamic increase factor (DIF) is a conservative practice for evaluating global behaviour;

the opposite is true insofar as local instability of the steel member is concerned. Given the need for ductile response under blast load, it is necessary to investigate the effect of high strain rates on all modes of failure of a section under such load.

5.11 Pressure-impulse diagrams

The stability of a steel column under blast loading does not guarantee its acceptable performance since it may be accompanied by deflections that exceed the normally specified acceptable limits (USACE, 2008b; Dusenberry, 2010). Flexural members under compression are required not to exceed a ductility ratio μ=3.0 for medium to very low Level of Protection (LOP) (USACE, 2008b).

Pressure-impulse (P-I) diagrams are widely used in structural blast resistant design to compare the actual response of a member to pre-defined ductility ratios (Baker et al. 1983). Figure 5.13 shows P-I diagrams for ductility ratios of 1.0 and 3.0 generated using the ELL SDOF model and assuming a linearly decaying blast pulse. Each P-I diagram has two asymptotes, one is termed the pressure and the other the impulse asymptote, each defining the limiting value for the particular quantity. P-I diagrams are presented here in non-dimensional form, in which the peak pressure and impulse delivered by the blast are normalized in terms of the system properties as follows (Li and Meng, 2002; Fallah and Louca, 2007)

$$P_o = \frac{F_0}{R_m} \tag{5.17}$$

$$I_o = \frac{I_r}{y_{el}\sqrt{KM}\sqrt{K_{LM}}} \tag{5.18}$$

where F_o is the maximum force of the equivalent linearly decaying blast pulse with zero rise time and y_{el} is the yield displacement.

Figure 5.13(a) shows a three-dimensional (3D) P/P_e-P-I diagram for μ=1.0 and P/P_e ratio values ranging from 0 to 0.95. Figure 5.13(b) shows a two-dimensional (2D) P-I curves for ductility ratio μ=1.0 at six particular P/P_e ratio values. It can be observed from these two plots that an increase in the axial load

ratio results in a decrease in both the pressure and impulse asymptotes of the pressure-impulse curves. This indicates that as the axial load ratio is increased, the ability of a steel column to resist quasi-static or impulsive blast loads is reduced. As the axial load P approaches P_e, the pressure and impulse asymptotes approach zero. The pressure asymptote decreases from 0.50 to 0.03, when P/P_e goes from 0 to 0.95, i.e. 16 times less pressure is required under $0.95P_e$ to reach the plastic capacity of the cross section (μ=1.0) when compared with the corresponding pressure under no axial load. The impulsive asymptote shows a 2.5 fold decrease, from 1.0 to 0.4, for the same range of axial load ratio. Figures 5.13(c) and (d) show 3D and 2D P/P_e-P-I and P-I diagrams, respectively, corresponding to different P/P_e ratios for a ductility ratio of μ=3.0. It can be observed that due to the axial-bending interaction, the column can achieve only a certain ductility ratio before experiencing instability under a particular P/P_e ratio. For example, the ductility ratio μ=3.0 can only be achieved when P/P_e is less than 32%; if the P/P_e ratio exceeds 32%, then the column will experience instability before reaching a yield displacement corresponding to μ=3.0.

To study the effect of ductility ratio on P-I diagrams and to investigate the limits of the achievable ductility ratio for a given P/P_e ratio, i.e. without the column experiencing instability, Figs. 5.14(a), (b), (c), and (d) show the effect of μ on P-I diagrams for P/P_e ratios of 0, 10%, 32%, and 60%, respectively. The ductility ratio has a significant influence on both the quasi-static and impulsive asymptotes as they increase with increased μ values. As shown in Fig. 5.14(a), when P/P_e equals zero, both asymptotes increase with μ, and the increase continues up to the limiting value of μ, i.e., the maximum ductility ratio μ_{max} permitted in the resistance function R. On the other hand, when axial load is included, depending on the P/P_e ratio, a lower level of ductility is attained due to instability. This is clear in Figs. 5.14(b) to (d), which show the limiting P-I stability curves for columns subjected to various P/P_e ratios. As shown in Fig. 5.14(c) and (d), under P/P_e ratios larger than 32%, the system cannot attain a

ductility ratio larger than μ=3. Thus even though under blast loading μ=3 is permitted for compression members with compact sections in the ASCE standard, it cannot be attained when P/P_e is larger than 0.32. Therefore, in order to be able to attain μ=3, P/P_e must not exceed 0.32. Using Fig. 5.15, which shows the P-I diagrams separating stable columns from unstable columns, for different P/P_e ratios, and the maximum attainable ductility ratio without incurring instability, a designer could rapidly check for column stability under blast loading using given combinations of P_o, I_o, and P/P_e ratio values. As shown in Fig. 5.15, for P/P_e ratios of 40% and 60%, the maximum ductility ratio that can be attained in a beam column under blast load, without experiencing instability, is 2.5 and 1.6, respectively.

5.12 Summary and conclusions

Two models were applied to study the stability of beam columns under blast loads. The first model was based on SDOF approximation, which accounts for both the effect of the secondary-moment (P-δ effect) due to axial load and strain rate. In the SDOF model the concept of equivalent lateral load was applied to simulate beam column interaction. In order to account for strain rate variation over the column cross-section, a full moment-curvature relationship, derived by using a layered sectional analysis that included the stress and strain rate variation over the depth of the column, was used in the SDOF analysis. The second model was based on three-dimensional FEM using LS-DYNA software. The results of both models were compared with experimental data to gauge their accuracy and to validate their assumptions. The SDOF maximum displacements and moments were also compared with the results of the interaction formulas given in UFC design manual. The SDOF model was used to generate a set of non-dimensional curves to obtain the critical load and to check the maximum deflection or ductility limit before the onset of column instability, curves that can be used in design standards for steel structures under blast loading. The effect of strain rate caused

by the blast loading on the local buckling behaviour of steel columns was also evaluated. Based on the analysis of the results and their comparison with the experimental data, the following conclusions can be stated.

(1) The P-δ effect in steel columns bending in single curvature due to blast load can be modelled accurately using the SDOF model in conjunction with the equivalent lateral load concept, provided the strain rate effect on column moment and axial capacity is included in the SDOF model.

(2) The use of beam column interaction formulas commonly used in design for static loads may overestimate the actual column capacity under blast load.

(3) The above interaction formulas will overestimate the strength of columns with maximum ductility ratio, μ_{max}, larger than one, regardless of the P/P_e ratio.

(4) For columns with small P/P_e ratio and $\mu_{max} \leq 1.0$, the application of the interaction formulas in design should be acceptable.

(5) For column with $P/P_e > 0.15$, the column strength predicted by the interaction formula would be greater than its actual value and it would be unacceptable even if $\mu_{max} < 1.0$. The degree of overestimation will increase as P/P_e or μ_{max} increases.

(6) The reason for the overestimation described in conclusion (5) is ignoring the effect of P/P_e on the elongation of the period of vibration of the beam column.Therefore, for accurate analysis of beam columns under blast load, the effect of P/P_e on the change in the period of vibration and on the moment magnification must be considered.

(7) Underestimating the DIF is a conservative practice for evaluating global behavior of columns; the opposite is true when local instability of the steel member is concerned. Given the need for the

plastic design, all qualifying criteria for a Class 1 cross-section should be met under the high strain rates associated with blast loads

(8) Due to strain rate effect, the maximum allowable flange slenderness limits for Class 1 cross-section might decrease by 33% when the strain rates varies from 0.001 /s to 100 /s, and this would result in a change in the cross-section classification.

(9) While the axial load greatly affects the pressure asymptote in the P-I diagrams, it has less effect on the impulsive asymptote for the same ductility ratio.

(10) There is a direct relationship between the P/P_e ratio and the maximum achievable ductility in a beam column under blast load. For a maximum ductility ratio of 3.0, the P/P_e ratio cannot exceed 32%.

5.13 Acknowledgements

The authors wish to gratefully acknowledge the following organizations for their support towards this study: the Chemical, Biological, Radiological/Nuclear and Explosives Research and Technology Initiative (CRTI project 06-015TD), Public Works and Government Services Canada, the Centre for Effective Design of Structures (CEDS) at McMaster University, and the Natural Sciences and Engineering Research Council of Canada for their financial support, the Canadian Explosives Research Laboratory (CERL) for assisting with the blast tests, and the Canadian Armed Forces for the use of their test range. CEDS received funding through the Ontario Research and Development Challenge Fund, a program of the Ministry of Research and Innovation of Ontario. The authors also appreciate the technical support of Messrs. Rick Guilbeault and Don Wilson of CERL during the experimental phase of this study.

5.14 Notation

The following symbols are used in this paper:

b = flange or tributary width (mm);

ε = strain;

$\varepsilon_{\max}$ = maximum strain;

$\dot{\varepsilon}$ = strain rate (/s);

$\dot{\varepsilon}_{\max}$ = maximum strain rate (/s);

$\eta(t)$ = equivalent lateral load (kN);

f_y = yield stress (MPa);

ϕ = shape function;

k = compressive plate constant

K^* = reduced stiffness (kN/m);

K_M = mass factor;

K_L = load factor;

K_{LM} = load-mass factor;

i= specific impulse (kPa.ms/m);

I_r = reflected impulse (kPa.ms);

I_o = normalized impulse;

μ = ductility ratio;

μ_o = the Poisson's ratio

M = the mass per unit length (kg/m)

M = mass (kg);

M_u = ultimate moment (kN.m);

P_r = peak reflected pressure (kPa);

P_o = normalized reflected pressure;

R = resistance (kN);

R_m = maximum resistance (kN);

I_r = reflected impulse (kPa.ms);

L = member height (m);

λ_c = column slenderness parameter;

λ_{cp} = flange slenderness parameter;

P = axial load (kN);

P_e= Euler buckling load (kN);

P_p= cross-section axial capacity (kN);

P_r = peak reflected pressure (kPa);

t_d = positive phase duration (ms);

W = charge mass (kg);

y = mid-span displacement (mm);

y_{el} =yield displacement (mm);

$\dot{y}$ = mid-span velocity (m/s);

$\ddot{y}$ = mid-span acceleration (m/s^2);

Z = scaled-distance (m/kg$^{1/3}$).

5.15 References

ASCE. (2011). "Blast Protection of Buildings: ASCE/SEI 59-11." American Society of Civil Engineers.

ASCE. (1997). "Design of blast resistant buildings in petrochemical facilities." Task Committee on Blast Resistant Design, ASCE, New York.

AISC. (1994). "Manual of steel construction. Load and resistance factor design (LRFD)." American Institute of Steel Construction, Chicago, IL.

Baker, W. E., Cox, P. A., Westine, P. S., Kulesz, J. J., and Strehlow , R. A., (1983). "Explosion hazards and evaluation." Elsevier Scientific Pub. Co., Amsterdam; New York.

Bazant, Z. P., and Cedolin, L. (1991). "Stability of structures: elastic, inelastic, fracture, and damage theories." Oxford University Press, New York.

Biggs, J. M., (1964). "Introduction to structural dynamics." McGraw-Hill Book Company, New York.

CISC. (2011). "Handbook of steel construction." Canadian Institute of Steel Construction, Willowdale, Canada.

Duan, L. and Chen, W. F., "Design interaction equation for steel beam columns." ASCE's Journal of Structural Engineering, 115 (1989) 1225-43.

Dusenberry, D. O. (2010). "Handbook for blast resistant design of buildings." J. Wiley, Hoboken, N.J.

Fallah, A. S. and Louca, L. A. (2007) "Pressure–impulse diagrams for elastic-plastic-hardening and softening single-degree-of-freedom models subjected to blast loading." International Journal of Impact Engineering. 34(4), 823-842.

Hallquist, J.O. (2006). "Ls-Dyna theory manual." Livermore Software Technology Corporation (LSTC), Livermore, CA.

Jones, N., (1988). "Structural impact." Cambridge University Press, Cambridge; New York.

Lee, L., Kim, T., and Kim, J., (2009). "Local response of W-shaped steel columns under blast loading." Structural Engineering and Mechanics, 31(1), 25-38.

Li, Q.M. and Meng H. (2002), Pressure-impulse diagram for blast loads based on dimensional analysis and single-degree-of-freedom model. Journal of Engineering Mechanics, 128(1), 87-92.

LSTC. (2007). “Ls-Dyna keyword user's manual.” Version 971. Livermore Software Technology Corporation (LSTC), Livermore, California.

Montalva, A., Loukaides, E., Long, M., and Gallant, S. (2007). “Analysis of Steel Columns for Air-Blast Loads.” In Proceedings of the International Symposium on Interaction of the Effects of Munitions with Structures, ISIEMS 12.1, Orlando,FL, 18-21 September 2007.

Nassr, A. A., Razaqpur, A. G., Tait, M. J., Campidelli, M., and Foo, S. (2011a). “Dynamic response of wide flange steel columns subjected to blast loading: Experimental results.” Submitted to ASCE's Journal of Structural Engineering in Oct. 2011.

Nassr, A. A., Razaqpur, A. G., Tait, M. J., Campidelli, M., and Foo, S., (2011b). “Experimental performance of steel beams under blast loading.” ASCE's Journal of Performance of Constructed Facilities, accepted in Sept. 23, 2011. Available online [DOI: 10.1061/(ASCE)CF.1943-5509.0000289].

Nassr, A. A., Razaqpur, A. G., Tait, M. J., Campidelli, M., and Foo, S. (2012). “Single and multi degree of freedom analysis of steel beams under blast loading.” Nuclear Engineering and Design, 242(1), 63-77.

Salmon, C. G. Johnson, J. E., and Malhas, F. A. (2009). “Steel structures: design and behaviour.” Pearson Prentice Hall, New Jersey.

Shi, Y., Hao H., and Li, Z. X. (2008) “Numerical derivation of pressure-impulse diagrams for prediction of RC column damage to blast loads.” International Journal of Impact Engineering 35(11). 1213-1227.

Shope, R. L. (2006). "Response of wide flange steel columns subjected to constant axial load and lateral blast load." Virginia Polytechnic Institute, Virginia, USA.

Timoshenko, S.P., and Gere, J.M. (1961). "Theory of elastic stability." McGraw-Hill Inc., New York.

USACE, (2008a). "Methodology manual for the single-degree-of-freedom blast effect design spreadsheet (SBEDS)." Tech. Rep. No. PDC TR-06-01, Rev. 1. US Army Corps of Engineers-Protective Design Centre (USACE-PDC), Omaha, NE. Available online.

USACE. (2008b). "Single degree of freedom structural response limits for antiterrorism Design." Tech. Rep. No. PDC TR–06–08, Rev. 1. US Army Corps of Engineers–Protective Design Centre (USACE–PDC), Omaha, NE. Available online.

USDOD, (2008). "Structures to resist the effects of accidental explosions." Document No. UFC 3-340-02. US Department of Defense (USDOD), Washington, DC.

5.16 List of figures

Table 5.1: Static resistance parameters of test beams and beam columns

	Group	Section	Orientation	M_y (kN.m)		M_u (kN.m)		EI/L	K	R_m
				Predicted	Measured	Predicted	Measured	(kN.m)	(kN/m)	(kN)
Beams	I	W150×24	x-x	66	67	75	72	1001	13206	230
	II	W150×24	y-y	14	17	21	22	148	1955	65
	III	W200×71	x-x	256	285	291	311	5017	66179	988
Beam columns	I	W150×24	x-x	62	63	70	67	832	10985	215
	II	W150×24	y-y	7	13	11	13	112	1475	43
	III	W200×71	x-x	248	272	282	300	4444	58625	903

Table 2.2: Test Matrix of test columns

Column	Section designation	Axis of bending	Charge mass (W) (kg)	Stand-off distance (SD) (m)	Scaled-distance (Z) ($m/kg^{1/3}$)	Axial load (P) (kN)
2C1	W150×24	y-y	100	10.30	2.22	270
3C1	W150×24	x-x	150	9.00	1.69	270
4C1	W150×24	x-x	250	7.00	1.11	270

Table 5.3: Comparison of the maximum displacement and moment using SDOF and MMF

Column	P/P_e	Impulse	Ductility (μ)	SDOF		MMF		%Δy	%ΔM
				y_{max}^{SDOF} (mm)	M_{max}^{SDOF} (kN.m)	y_{max}^{MMF} (mm)	M_{max}^{MMF} (kN.m)		
3C1	0.067	$0.2I_r$	0.30	6.4	25.6	6.6	26.5	3.0	3.0
		$0.5I_r$	0.75	15.9	63.9	16.4	66.3	3.0	4.0
		$1.5I_r$	3.00	62.4	84.6	56.5	101.7	-10.0	20.0
		$2.5I_r$	10.5	221.4	83.7	138.9	101.7	-37.0	22.0
2C1	0.49	$0.1I_r$	0.23	8.9	4.9	12.7	7.0	43.0	43.0
		$0.2I_r$	0.46	17.9	9.7	25.5	14.0	43.0	44.0
		$0.4I_r$	0.91	35.7	19.4	50.9	28.6	43.0	47.0
		$0.5I_r$	1.13	44.5	21.3	63.7	35.0	43.0	64.0

Δy is the complement to one of the ratio between y_{max}^{SDOF} and y_{max}^{MMF}

ΔM is the complement of one of the ratio between M_{max}^{SDOF} and M_{max}^{MMF}

Table 5.4: Slenderness limits for class 1 steel columns under higher strain rates

Element *Description*	$\dot{\varepsilon}$ *< 0.001 /s* DIF=*1.00*	$\dot{\varepsilon}$ *=0.1/s* DIF=*1.30*	$\dot{\varepsilon}$ *=10 /s* DIF=*1.76*	$\dot{\varepsilon}$ *=100 /s* DIF=*2.20*
Flanges of I-sections	$\frac{b}{2t_o} \le \frac{145}{\sqrt{F_y^1}}$	$\frac{b}{2t_o} \le \frac{127}{\sqrt{F_y}}$	$\frac{b}{2t_o} \le \frac{109}{\sqrt{F_y}}$	$\frac{b}{2t_o} \le \frac{97}{\sqrt{F_y}}$
Webs of I-sections	$\frac{h}{w} \le \frac{1100}{\sqrt{F_y}}\left(1-0.39\frac{P}{P_y}\right)$	$\frac{h}{w} \le \frac{965}{\sqrt{F_y}}\left(1-0.30\frac{P}{P_y}\right)$	$\frac{h}{w} \le \frac{829}{\sqrt{F_y}}\left(1-0.26\frac{P}{P_y}\right)$	$\frac{h}{w} \le \frac{742}{\sqrt{F_y}}\left(1-0.18\frac{P}{P_y}\right)$

F_y = static yield strength (MPa)

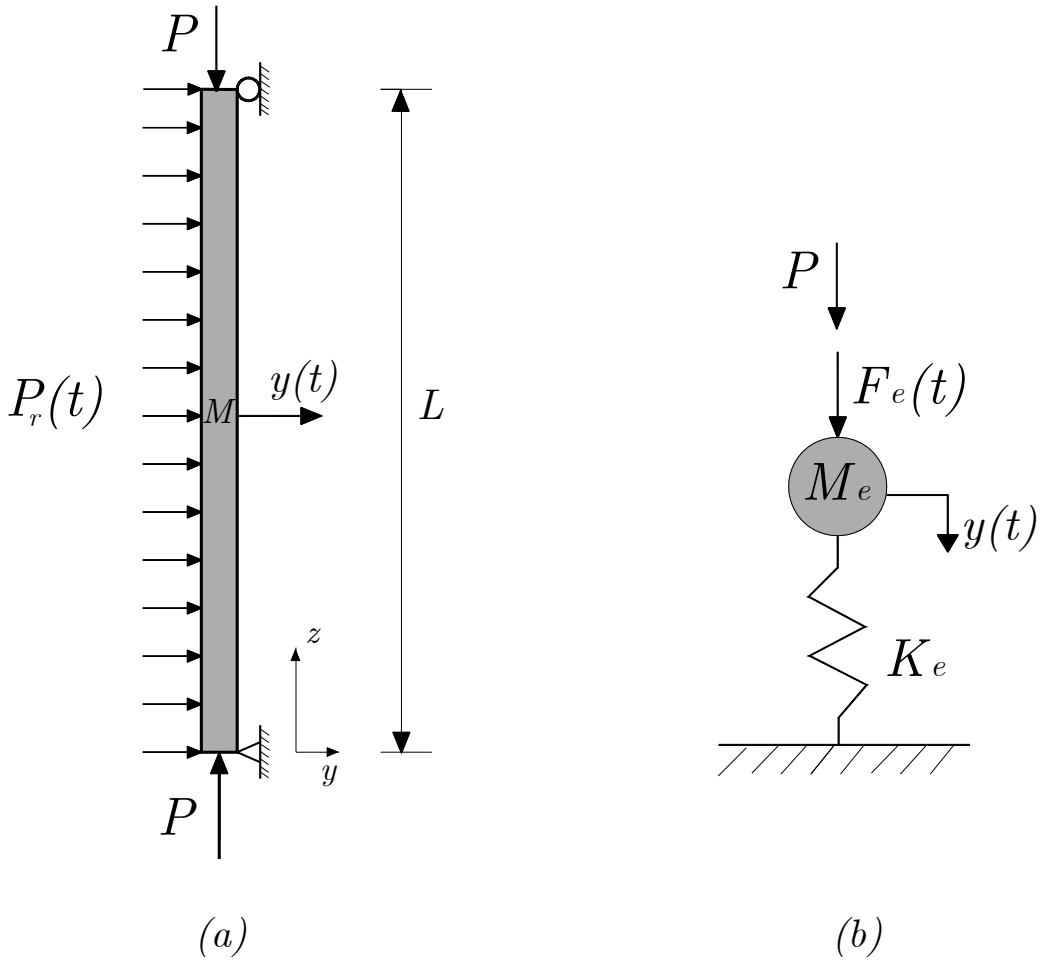

Fig. 5.1: Equivalent SDOF system, (a) real column under blast loading and (b) equivalent system

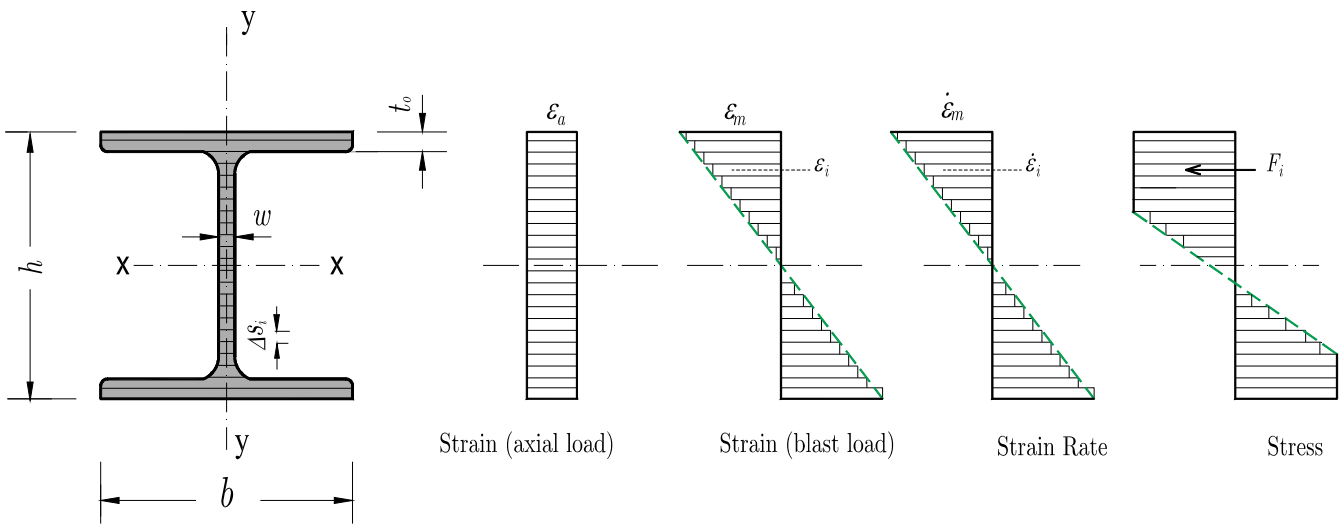

Fig. 5.2: Layered analysis of a cross-section for the plastic hinge

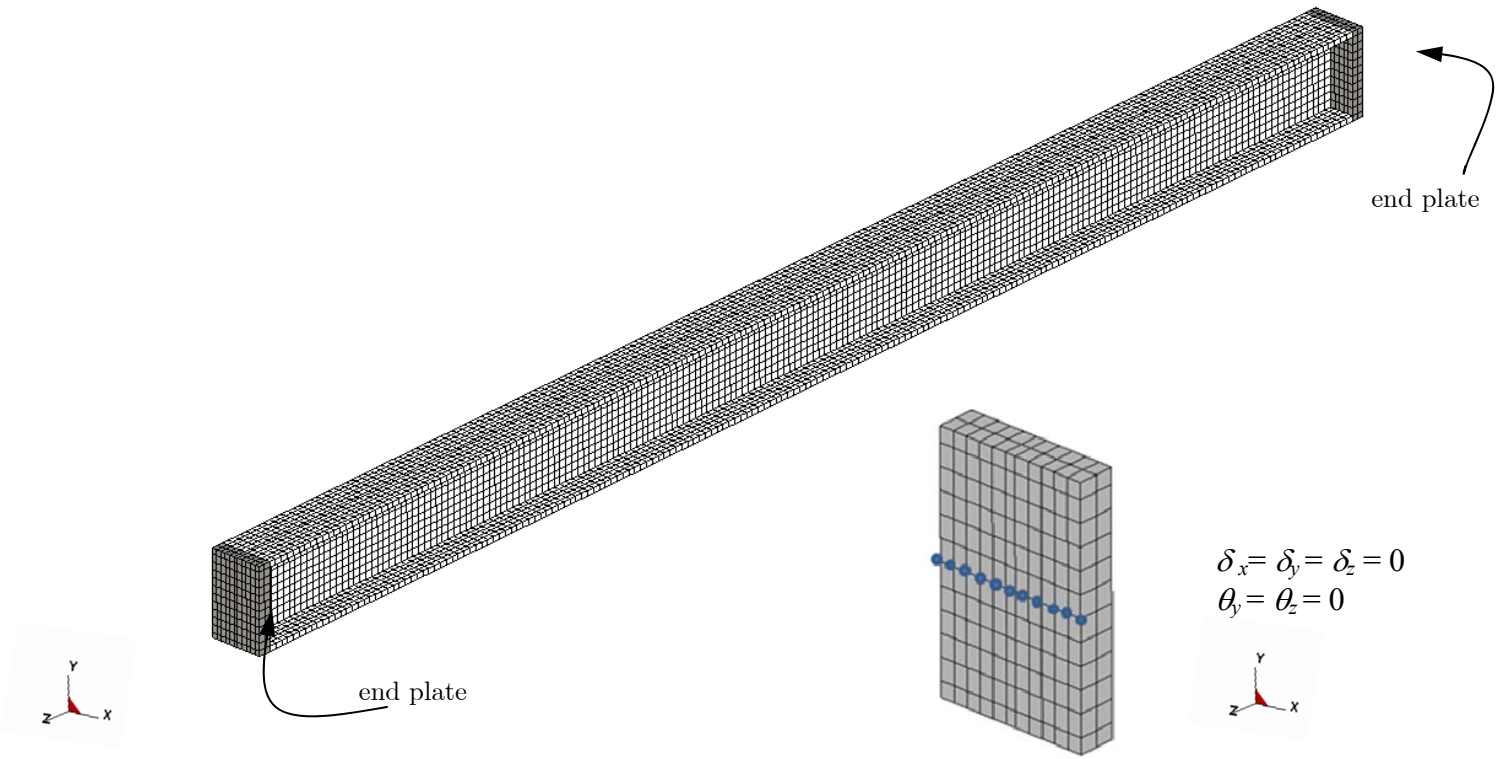

(a) (b)

Fig. 5.3: FEM column model (a) FEM mesh, (b) hinge end

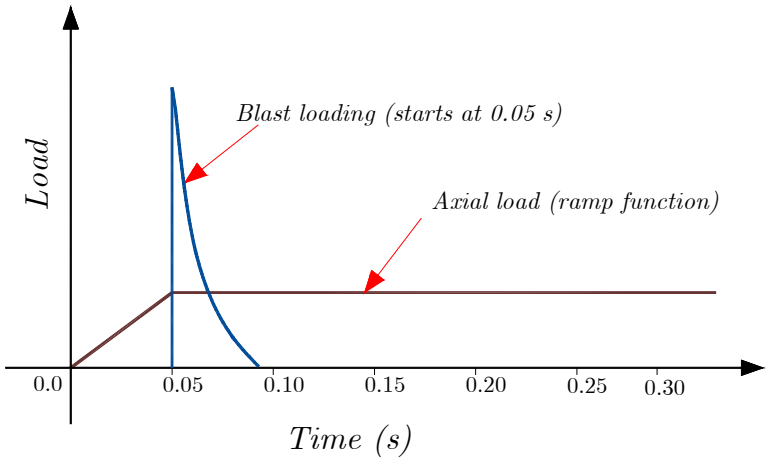

Fig. 5.4: Loading procedure for axial and blast loading in FEM

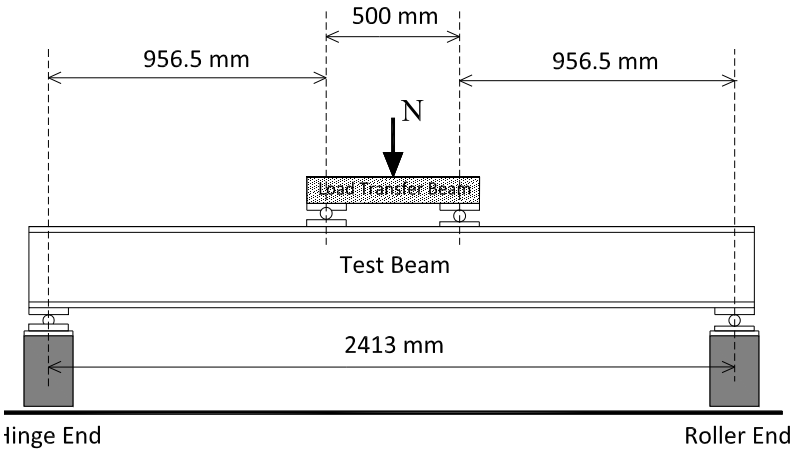

(a)

(b) Beam

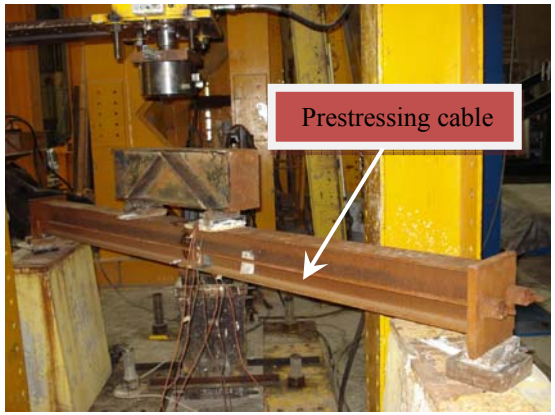

(c) Beam-columns

Fig. 5.5: Test setup for static testing of steel specimens

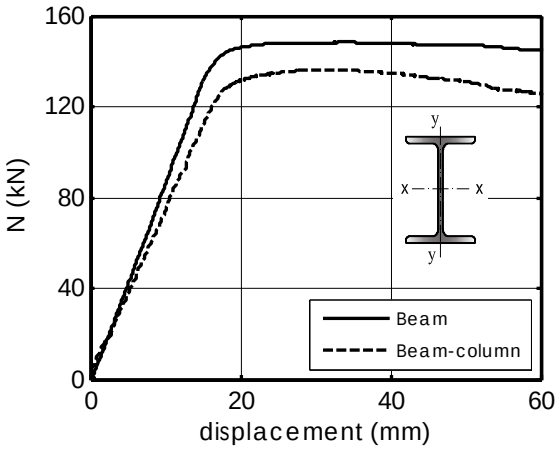

(a) Group I: W150×24 (x-x axis)

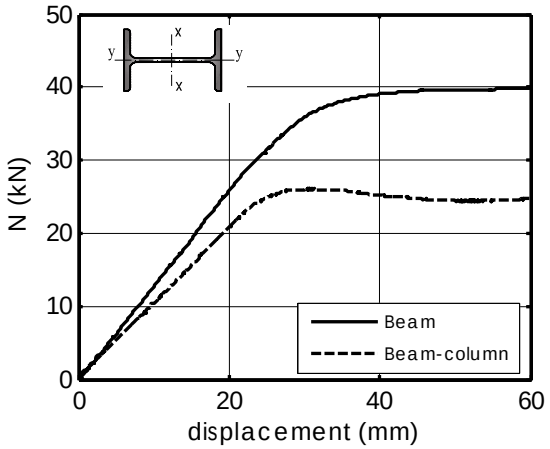

(b) Group II: W150×24 (y-y axis)

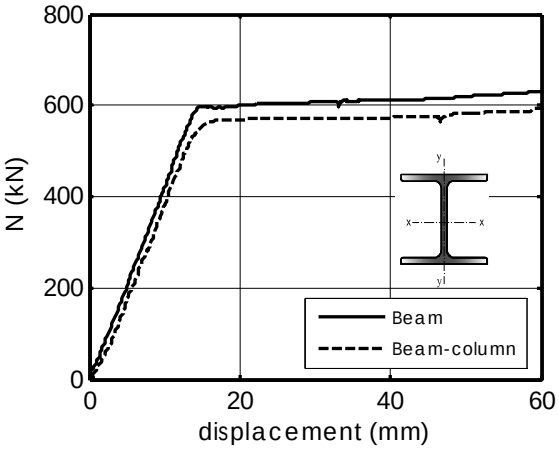

(c) Group III: W200×71 (x-x axis)

Fig. 5.6: Load versus mid-span deflection curves

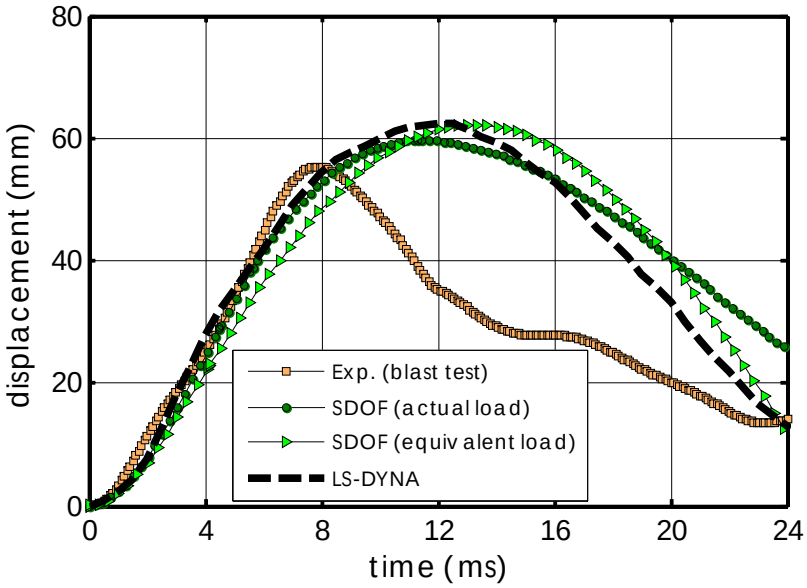

(a) 2C1 column: W=100 kg, SD=10.3 m, Z=2.22 m/kg$^{1/3}$

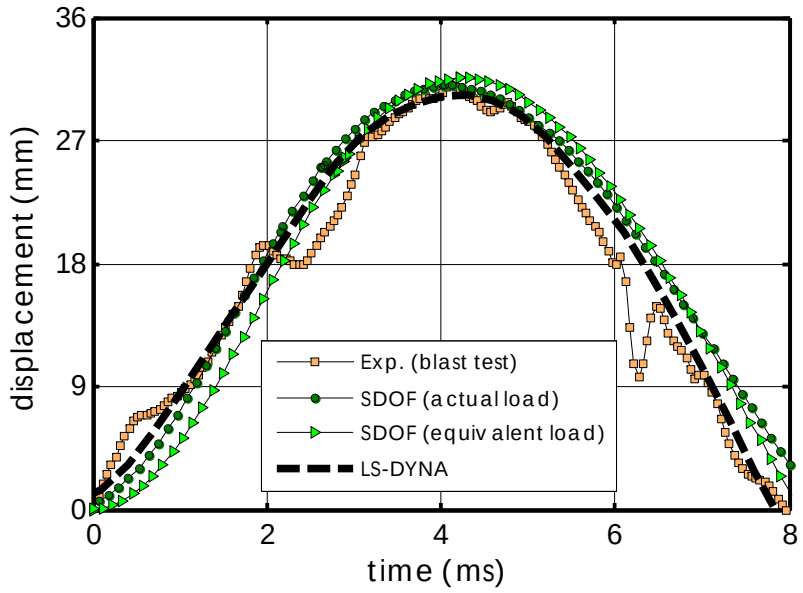

(b) 3C1 column: W=150 kg, SD=9 m, Z=1.69 m/kg$^{1/3}$

Fig. 5.7: Mid-span displacement time-histories comparisons

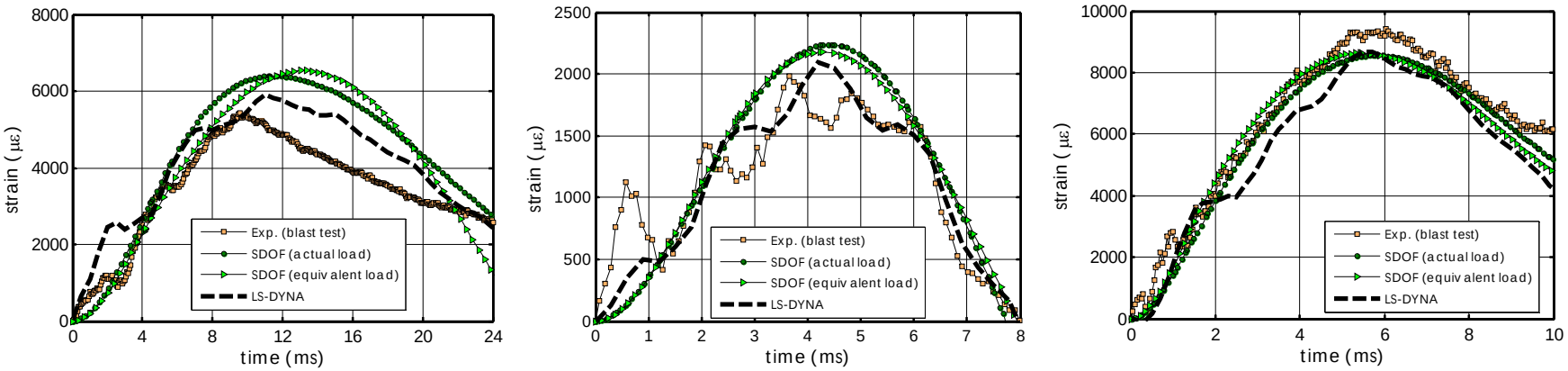

(a) 2C1 column: W=100 kg, SD= 10.3 m, Z=2.22 m/kg$^{1/3}$ (b) 3C1 column: W=150 kg, SD= 9 m, Z=1.69 m/kg$^{1/3}$ (c) 4C1 column: W=250 kg, SD= 7.5 m, Z=1.11 m/kg$^{1/3}$

Fig. 5.8: Mid-span strain time-histories comparisons

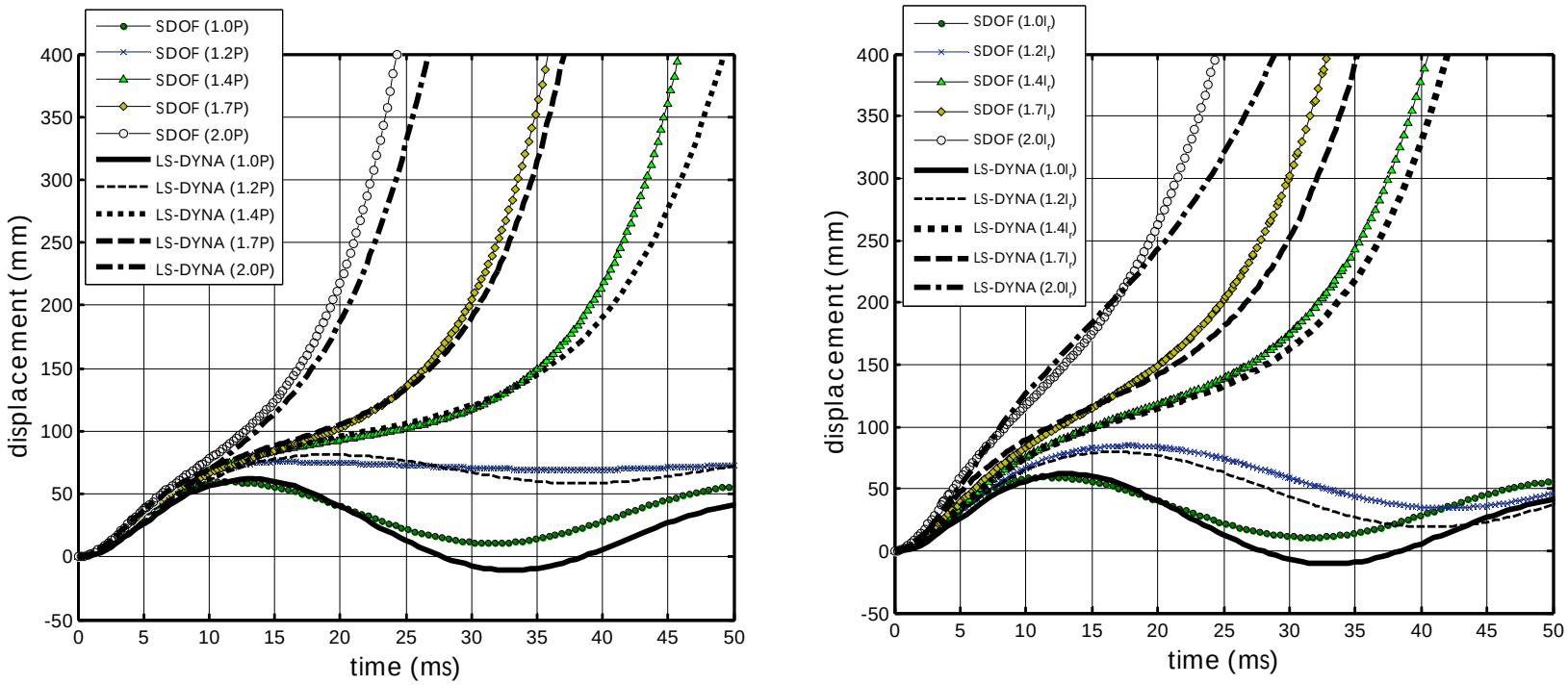

(a) (b)

Fig. 5.9: Effect of axial and blast load on stability behaviour of steel columns

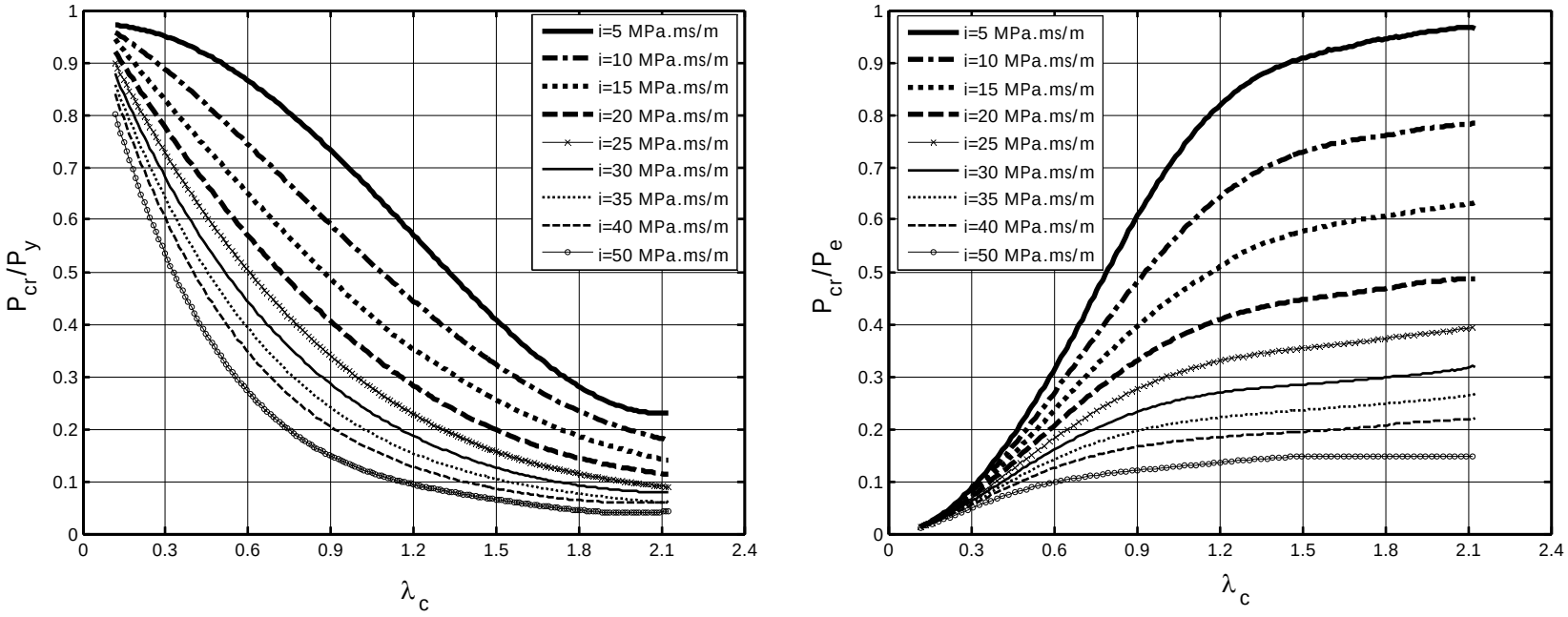

(a) (b)

Fig. 5.10: Non-dimensional curves for critical axial load of steel columns under blast loading

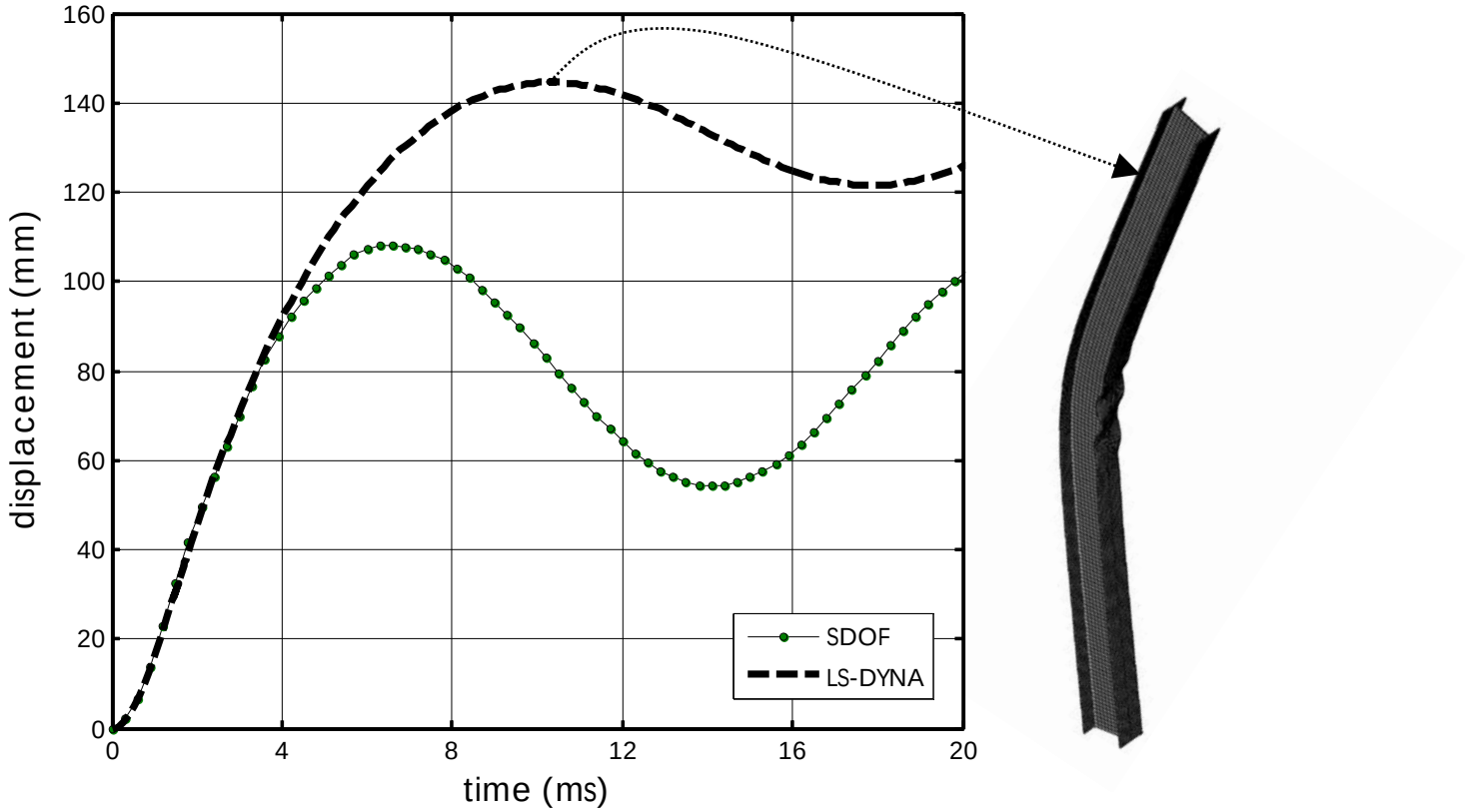

Fig. 5.11: Effect of local buckling on response predictions

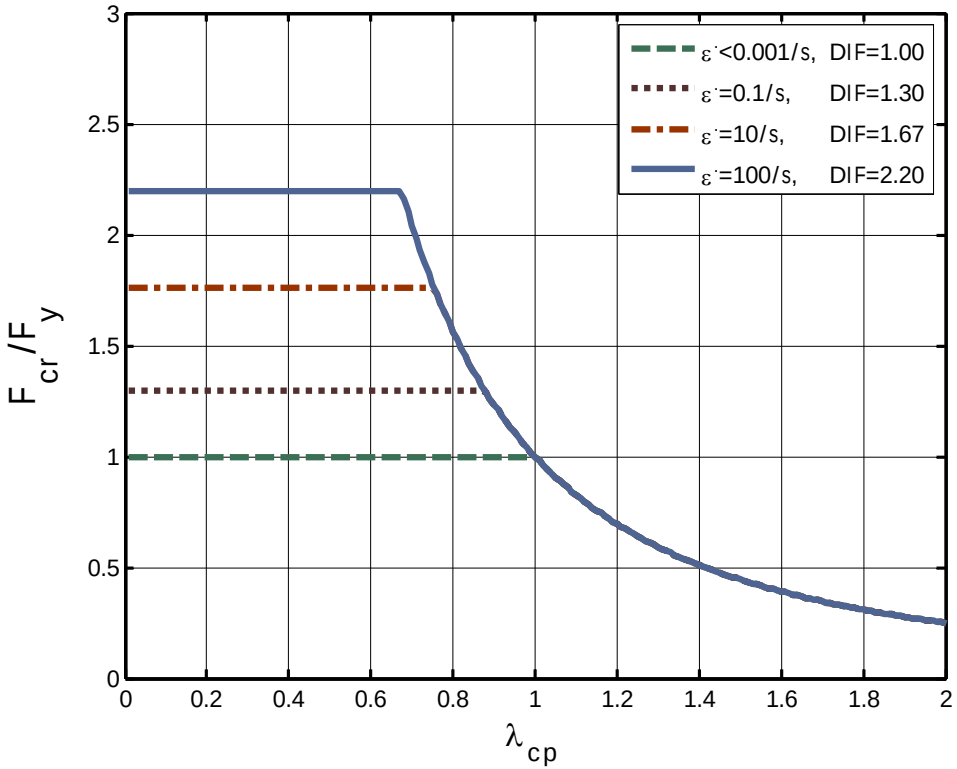

Fig.5.12: Non-dimensional representation of flange strength in compression under high strain rates

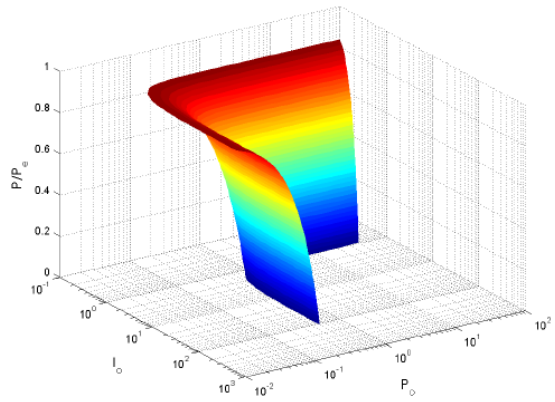

(a) 3D P/P_e-P-I diagram (μ =1.0)

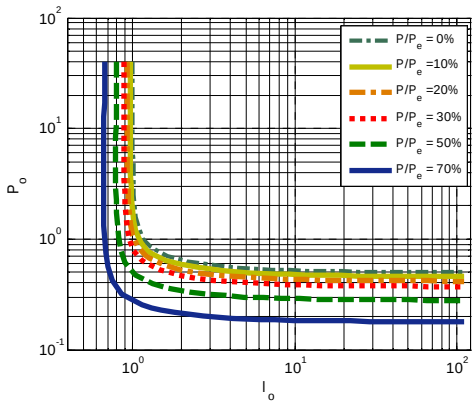

(b) 2D P-I diagrams (μ =1.0)

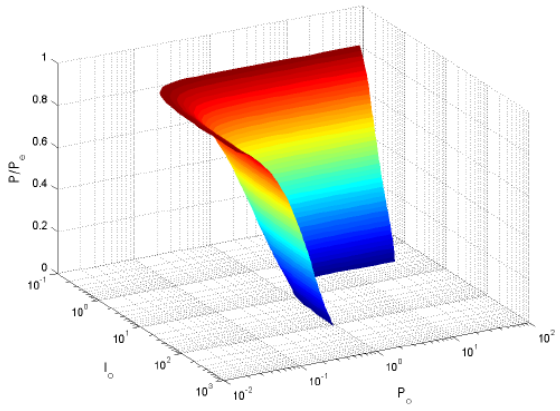

(c) 3D P/P_e-P-I diagram (μ =3.0)

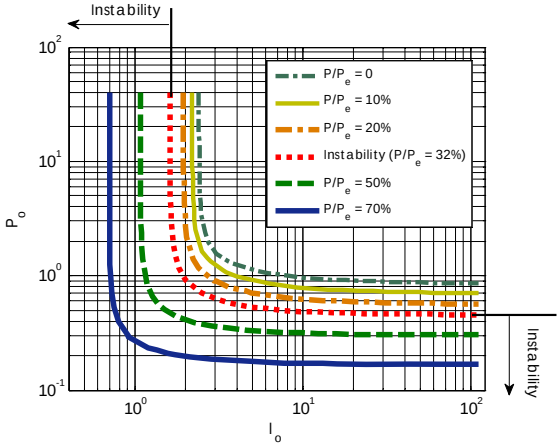

(d) 2D P-I diagrams (μ =3.0)

Fig. 5.13: Effect of axial load on P-I diagrams

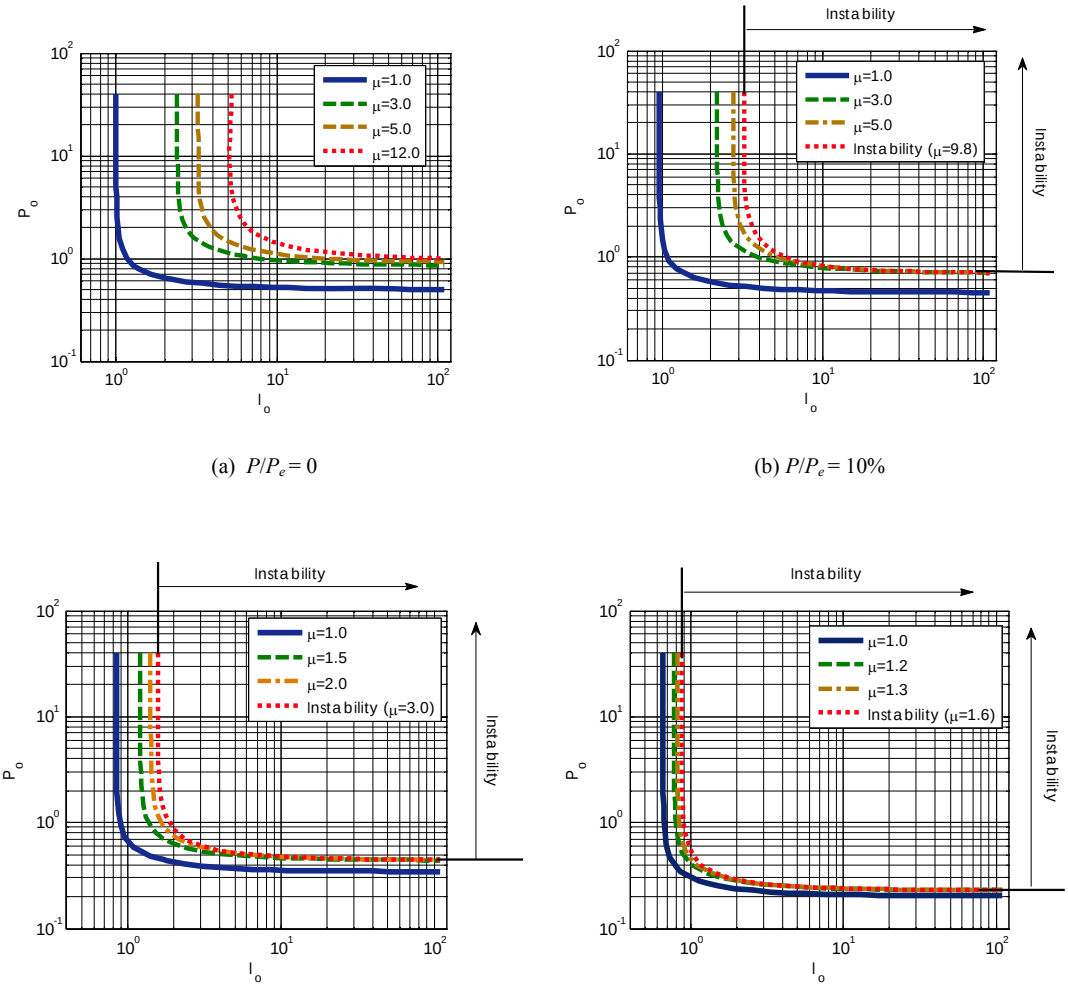

(a) $P/P_e = 0$ (b) $P/P_e = 10\%$

(c) $P/P_e = 32\%$ (d) $P/P_e = 60\%$

Fig. 5.14: Effect of ductility ratio on P-I diagrams

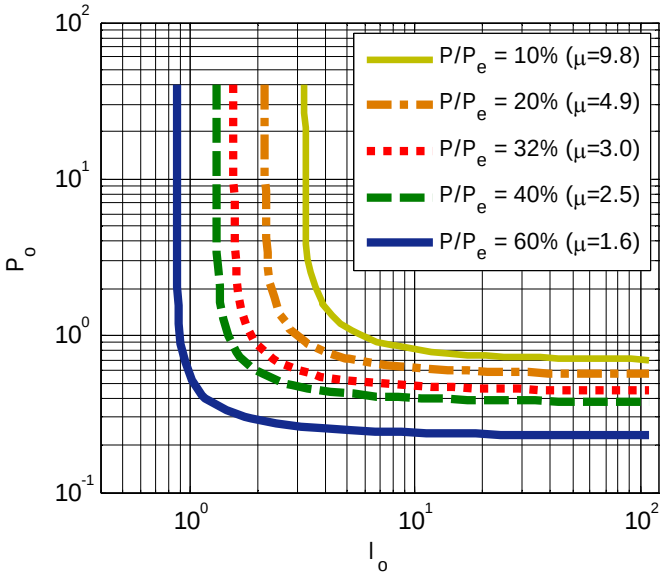

Fig. 5.15: Stability P-I limits for different P/P_e ratios

Chapter 6: Summary, Conclusions, and Recommendations for Future Research

6.1 Summary

In this study full-scale field tests were performed on wide flange steel beams and columns under blast loading. The effects of charge size and stand-off distance were investigated by measuring steel member responses using a variety of measuring devices. The study also presented detailed analysis of the results of the experimental data. The blast load characteristics were compared with those obtained using Unified Facilities Criteria (UFC 3-340-02) model (UFCM). The spatial and temporal variations of strain rate were computed from the recorded strain time histories and analyzed. In addition, time-dependant deformations were analyzed to study the contributing modes of vibration in the dynamic response using Power Spectral Density (PSD) function. Moreover, the effect of the axial load on the maximum deformation, vibration period, strain rate, and contributing modes to the dynamic response were investigated by comparing the beam results with the column results tested in the same blast shots.

Single-Degree-of-Freedom (SDOF) model was developed and its results were compared to the experimental data. In the SDOF model, the resistance function was based on a moment-curvature relationship derived from a layered sectional analysis that included the stress and strain rate variation over the depth of the cross-section. The P-δ effect was modelled using the equivalent lateral load (ELL) method to simulate the secondary moment due to axial load. To determine the effects of higher modes of vibration and the variation of steel member mechanical properties along its length on its dynamic response, the test steel members were also analyzed using Multi-Degree-of-Freedom (MDOF) models, based on Finite Element Modelling (FEM). These dynamic models were also used to investigate the effect of axial-bending interaction and dynamic stability of

columns. In addition, the results of the dynamic models were used to evaluate the results of the Moment Magnification Factor (MMF) usually used in the interaction formulas to design steel beam columns under blast. Moreover, the effect of strain rate caused by the blast loading on the local stability of steel columns was also evaluated insofar as it might lead to a shift in the governing mode of failure.

6.2 Conclusions

The following conclusions were drawn from the research reported in the preceding chapters:

1. The UFCM is able to predict the peak blast pressures and impulses for the current blast tests with differences of 18% and 19%, respectively, when compared with the average experimental reflected pressure and impulse values.
2. The closed-form equation proposed by Prugh (1999) provides a good estimate of the impulse values.
3. The positive phase duration for the current blast tests cannot be accurately estimated by either available closed-form equations or UFCM.
4. Using the commonly assumed DIF of 1.24, the SDOF model predicts the response of the current steel beams undergoing elastic deformation reasonably well, with a maximum difference of 9% between the measured and computed maximum displacements values. However, the maximum difference in the case of beams experiencing plastic deformation is 30%.
5. Using a constant DIF to estimate the material strength due to strain rate might not provide a realistic assessment of the actual effect of the strain rate on the dynamic response of beams, particularly if the actual response remains elastic while the predicted response is plastic. Therefore, the effect of the strain rate on a member response should be more accurately accounted for in SDOF analysis in order to achieve higher accuracy and better agreement with the experimental results.

6. Underestimating the actual capacity of a member due to inaccurate consideration of strain rate effect does not always lead to a conservative design. This could lead to an underestimation of the actual forces transferred by a member to its connections or supporting members.
7. When the DIF is calculated using the Cowper-Symonds strain rate model and the strain rate is assumed to vary linearly through the depth of the beam, the SDOF model adequately captures both the time dependant deformations and internal forces in the test beams.
8. Due to the difference between the actual displaced shape of the beam and its assumed shape in the SDOF model, at the initial stages of motion, the longitudinal variation of dynamic shear and moment based on the SDOF model differ from that based on the MDOF model.
9. Based on power spectral density analysis, the responses of the test beams are found to be governed by the first mode of vibration, with minor contribution from the third mode. For this reason, the SDOF model provides accurate prediction of the response of the current test beams, both at the elastic and inelastic stages.
10. While the strain rate variation along the height of the test columns did not exhibit any specific trends due to the contribution of the higher modes of the dynamic response, nevertheless strain rate profiles can be reasonably approximated as linear over the cross-section of columns under blast loading.
11. The axial load on a column may increase or decrease the maximum lateral displacement of the column due to blast pressure. The reduction is caused by the elongation of the column fundamental period due to axial load while the increase is caused by the P-δ effect.
12. For the axial load level applied in the current tests, which was 25% of the column axial capacity, the axial load decreased the lateral displacement of

the columns relative to that of a similar column without axial load, as long as the column did not experience plastic deformation.

13. In columns that experienced plastic deformation, the *P-δ* effect dominated the response and the axial load increased the column maximum lateral deformation by up to 158% in the current blast tests.
14. The axial-bending interaction affects the contributing modes of vibration in the dynamic response by exciting higher modes of vibration and thus reducing the effect of the first mode.
15. The axial-bending interaction increases the strain rate in the plastic range of the responses by up to 93%.
16. The *P-δ* effect in steel columns bending in single curvature due to blast loads can be modelled accurately using the SDOF model in conjunction with the equivalent lateral load concept, provided the strain rate effect on column moment capacity is included in the SDOF model.
17. The use of beam column interaction formulas commonly used in design for static loads can overestimate the actual column capacity under blast loads.
18. The moment magnification factor (MMF) method generally overestimates the strength of columns with maximum ductility ratio μ_{max} larger than one, regardless of the P/P_e ratio.
19. For columns with small P/P_e ratio and $\mu_{max} \leq 1.0$, the application of the interaction formulas in design should be acceptable.
20. For column with $P/P_e > 0.15$, the column strength predicted using MMF method becomes much greater than its actual value and would be unacceptable even if $\mu_{max} < 1.0$. The degree of overestimation becomes increasingly large as P/P_e or μ_{max} increases.
21. The reason for the overestimation described in conclusion (20) is due to ignoring the effect of P/P_e on the elongation of the period of vibration of the beam column. Therefore, for accurate analysis of beam columns under

blast load, the effect of P/P_e on the change in the period of vibration and on the moment magnification must be considered.

22. Underestimating the DIF is a conservative practice for evaluating global behaviour; the opposite is true when local instability of the steel member is concerned. Given the need for the plastic design, all qualifying criteria of a Class 1 cross-section should be met under the high strain rate of blast loading.
23. Due to strain rate effect, the maximum allowable flange slenderness limits for Class 1 cross-section might decrease by 33% when the strain rates varies from 0.001 /s to 100 /s.
24. While the axial load greatly affects the pressure asymptote in the P-I diagrams, it has less effect on the impulsive asymptote for the same ductility ratio.
25. There is a direct relationship between the P/P_e ratio and the maximum achievable ductility in a beam column under blast load. For a maximum ductility ratio of 3.0, the P/P_e ratio cannot exceed 32%.

6.3 Recommendations for future research

The research presented in this thesis included experimental testing of steel beams and columns under different charge weight and stand-off distance combinations. Detailed analyses of the experimental results were provided for use by researchers, practicing engineers, and code committees. However, there are still many questions that remain to be answered with regard to the dynamic response of steel members subjected to blast loads. This section attempts to address possible extensions to the research to expand the knowledge related to the response of steel members and structures to blast loading as follows

1. In the present experimental program, wide flange steel beams and columns were investigated. To ascertain the generality of the simplified methods and the conclusions of this study, steel members of different cross-section

shapes, boundary conditions, and slenderness ratios should be tested under blast loading. A wide range of scaled-distances needs to be selected to study the dynamic response of such members with different loading regimes, i.e. impulsive, dynamic and quasi-static, and to establish the range of strain rates experienced by steel structures during unconfined explosions. In addition, testing of steel columns with different axial load levels would provide good data on the dependency of the dynamic response on the axial load and verify the findings of this thesis with respect to the P/P_e ratio effect on columns strength and stability.

2. The effect of residual stresses on both material and member responses should be investigated.
3. The effect of time-varying axial load on steel column during the blast lateral response of the column should be studied. This kind of axial load occurs when the roof and beams connected to the column are also excited by the blast.
4. The interaction of the steel members with surrounding non-structural elements and cladding in buildings under blast loading and its effect on the transferable reflected pressure need be investigated. Studies should cover different arrangements of non-structural and cladding elements which would result in different loading conditions on these steel members, e.g. biaxial bending of corner elements and torsion due to unsymmetrically loaded panels.